UNIVERSITÉ DE STRASBOURG

ÉCOLE DOCTORALE DES SCIENCES CHIMIQUES

UMR 7006 - Institut de Science et d'Ingénierie Supramoléculaires

THÈSE

présentée par :

Stefano IPPOLITO

soutenue le : **13 Septembre 2021**

pour obtenir le grade de : **Docteur de l'Université de Strasbourg**

Discipline / Spécialité : Chimie Physique / Science des Matériaux

---

Ingénierie des défauts dans les semi-conducteurs 2D : fabrication de dispositifs hybrides multifonctionnels

---

THÈSE dirigée par :

M. Paolo SAMORÌ Professeur, Université de Strasbourg, France

RAPPORTEURS :

M. Artur STEFANKIEWICZ Professeur, Université Adam-Mickiewicz de Poznań, Pologne

M. Felice TORRISI Professeur, Imperial College London, Royaume-Uni

---

AUTRES MEMBRES DU JURY :

M. Bernard DOUDIN Professeur, Université de Strasbourg, France

Résumé

La découverte de nouveaux matériaux aux propriétés exploitables a toujours stimulé le progrès scientifique et sociétal dans l'histoire de l'humanité. De la préhistoire à nos jours, nous pouvons citer quelques exemples notables qui ont défini notre évolution : la pierre, les métaux (bronze et fer), l'acier et, plus récemment, les plastiques, les céramiques et les composites. À cet égard, la dernière pierre angulaire à laquelle nous avons été confrontés au cours des quinze dernières années concerne la découverte des propriétés physiques et chimiques exceptionnelles du graphène, par Geim et Novoselov en 2004[1]. Le graphène, une couche d'épaisseur atomique d'atomes de carbone hybridés sp^2 et structurellement analogues au graphite, représente une véritable percée dans la science des matériaux : ses propriétés uniques et polyvalentes[2] peuvent être la clé pour révolutionner les technologies existantes et encourager le développement de nouvelles technologies. À cet égard, la facilité d'isolement du graphène par clivage micromécanique, également connu sous le nom de méthode du ruban adhésif, a encouragé les scientifiques du monde entier à isoler de nouveaux matériaux bidimensionnels (2DM) à partir de leurs homologues massifs[3]. En conséquence, divers nanosystèmes atomiquement minces ont été produits à partir de structures de van der Waals (vdW) en couches, comme le phosphore noir, le nitrure de bore hexagonal et les dichalcogénures de métaux de transition (TMD). Contrairement au graphène qui présente un comportement semi-métallique et ne possède pas de bande interdite dans sa forme d'origine[2], les TMD offrent un large éventail de propriétés électriques, électroniques et optiques, comme par exemple des bandes interdites ajustables dans tout le spectre[4], une caractéristique essentielle pour des applications en électronique et en optoélectronique. Il est remarquable que les propriétés des matériaux monocouches soient très différentes de celles de leurs homologues massifs en raison d'un fort confinement quantique et d'effets d'écrantage et de surface réduits[5]. Par conséquent, la découverte d'effets et de phénomènes quantiques exotiques dans la limite de l'épaisseur atomique a favorisé la diffusion croissante des 2DM, et des TMD en particulier, pour des applications allant de l'électronique, l'optoélectronique et la (photo)catalyse à la (bio)détection et la biomédecine[6,7].

Cependant, les performances des dispositifs à base de TMD sont strictement liées aux propriétés inhérentes et à la qualité des matériaux, qui jouent un rôle crucial dans la détermination des applications finales. À cette fin, des efforts de recherche ont été consacrés au développement de techniques de production et d'étapes successives de fonctionnalisation pour respectivement augmenter la qualité des matériaux et améliorer leurs performances[8]. Les premières étapes de la recherche sur les TMD se sont exclusivement appuyées sur

I

l'exfoliation micromécanique, bien que cette technique présente deux inconvénients majeurs : le manque de contrôle lors de la production d'échantillons avec un nombre spécifique de couches et le fait qu'elle ne soit pas adaptée à la production à grande échelle (industrielle)[9]. Par conséquent, pour surmonter les limitations susmentionnées, diverses stratégies ont été développées et poursuivies au cours des dernières années pour favoriser la production de 2DM de haute qualité. De façon remarquable, les approches de traitement en solution sont apparues comme des méthodes efficaces pour la synthèse et l'exfoliation des TMD. Bien que les étapes de production affectent déjà la qualité et les caractéristiques des matériaux TMD traités en solution, de nombreux efforts de recherche ont été consacrés au développement de stratégies moléculaires pour ajuster finement leurs propriétés physico-chimiques[8]. Ceci est réalisé en tirant parti du rapport surface/volume le plus élevé des 2DM et de la sensibilité de leurs propriétés à l'environnement local. Les approches développées exploitent les interactions covalentes et non covalentes par lesquelles de petites molécules[10], des nanoparticules (NP) de métaux nobles[11] ou des (bio)polymères[12] interagissent avec le plan basal et/ou les bords des nanofeuillets de TMD. En fait, les processus de physisorption ou de chimisorption sont dirigés par une variété de mécanismes, dont la polyvalence représente un outil puissant dans le domaine de la science des 2DM.

L'exfoliation en phase liquide (LPE) représente la voie principale pour produire des dispersions de TMD de haute concentration et de grand volume, où les cristaux massifs sont dispersés et exfoliés dans un solvant spécifique par un transfert d'énergie mécanique qui surmonte les interactions de vdW au sein des structures en couches. Le débit élevé atteint par la LPE favorise l'utilisation des TMD dans de nombreuses applications différentes, en exploitant des matériaux vierges ou hybrides sous la forme de dispersions, de revêtements et de couches minces produits par diverses techniques de dépôt, dont l'impression à jet d'encre, la pulvérisation, le procédé rouleau à rouleau, le dépôt à la goutte, etc[13]. Bien que la LPE offre le meilleur compromis entre le coût, la pureté et le rendement, elle présente certaines limites lorsque l'application finale concerne l'(opto)électronique, où les défauts de structure du matériau jouent un rôle néfaste. En effet, la procédure d'exfoliation énergétique entraîne une légère formation de nouveaux défauts et une propagation importante des défauts de structure inhérents dans les couches exfoliées. Comme le suggèrent des considérations thermodynamiques, les défauts de dimension zéro sont les défauts stœchiométriques les plus abondants dans les TMD, en particulier les lacunes de chalcogènes principalement situées aux bords des nanofeuillets et dont l'énergie de formation est de quelques eV (~2 eV dans le cas des lacunes de soufre, désormais appelées V_S)[14].

Cette thèse se concentre sur les stratégies d'ingénierie des défauts pour améliorer les performances des dispositifs hybrides à base de TMD pour des applications en électronique, en électrocatalyse et en détection. Après une brève introduction soulignant le contexte et la

motivation de ce projet de recherche (Chapitre 1), l'accent sera mis sur la production et les propriétés des TMD traités en solution (Chapitre 2), ainsi que sur la défectuosité associée en tant qu'outil unique pour ajuster leurs caractéristiques inhérentes (Chapitre 3). La partie expérimentale sera consacrée à une description précise des matériaux et des techniques de caractérisation (Chapitre 4) employés dans les deux principaux projets présentés dans cette thèse (Chapitre 5 et Chapitre 6), dont les principaux résultats sont discutés ci-dessous.

Dans notre premier projet, nous avons développé une nouvelle stratégie moléculaire pour simultanément remédier aux V_S dans les MS_2 traités en solution (M = Mo, W, Re) et augmenter la connectivité électronique inter-flocons au moyen de systèmes moléculaires dithiolés[15]. En particulier, en utilisant des molécules dithiolées π-conjuguées (HS-R-SH), nous avons prouvé par diverses analyses multi-échelles la simultanéité de : (i) la guérison des V_S pour restaurer la structure cristalline de MS_2 et diminuer les déficiences stœchiométriques associées qui agissent comme des centres de diffusion des charges ; (ii) le pontage covalent de flocons adjacents, conduisant à une amélioration du transport des porteurs de charge à travers un réseau interconnecté. Nous avons tiré parti de l'approche de fonctionnalisation in situ des TMD en exposant les matériaux inorganiques aux connecteurs moléculaires juste après leur dépôt sur un substrat. Ceci est crucial pour la formation de voies à longue distance qui présentent des caractéristiques de transport de charge supérieures, tout comme le pontage de régions désordonnées dans les chaînes de polymères conjugués[16]. Notre approche constitue une méthode de fonctionnalisation innovante et universelle, capable d'améliorer les performances des dispositifs à base de MS_2 traités en solution pour des applications en électronique de grande surface. Nous avons appliqué cette stratégie à des transistors à couche mince à grille liquide (LG-TFT) fabriqués en coulant des dispersions de MS_2 sur des substrats SiO_2/Si pré-modelés avec des électrodes interdigitées en or (Au-IDE), puis en les exposant à des molécules de 1,4-benzènedithiol (BDT) aromatiques et conjuguées. Cela a permis d'améliorer considérablement les caractéristiques des LG-TFT à base de MS_2 d'un ordre de grandeur, ce qui a conduit à des performances électriques de pointe en termes de mobilité à effet de champ (μ_{FE}) et de rapport de courant (I_{ON}/I_{OFF}), ainsi qu'à la vitesse de commutation la plus rapide rapportée à ce jour pour des dispositifs de ce type[17]. L'amélioration de la stabilité dans l'eau et la robustesse mécanique sont d'autres caractéristiques uniques des réseaux de MS_2 à pontage covalent.

Nous avons évalué les effets de la fonctionnalisation in situ avec des molécules de BDT à l'aide de diverses techniques multi-échelles indépendantes, dont des caractérisations spectroscopiques (par exemple, Raman, UV-visible, spectroscopie photoélectronique X, spectroscopie de résonance magnétique nucléaire), morphologiques/structurales (par exemple, microscopie à force atomique, microscopie électronique à balayage, microscopie

électronique en transmission à balayage en champ sombre annulaire à grand angle, diffraction des rayons X), mécaniques et électriques (par exemple, analyse du transport de charge, mesures en fonction de la température). Le pontage covalent de flocons de MS_2 individuels avec des molécules π-conjuguées devrait améliorer leurs propriétés électriques, en particulier la connectivité électrique, où la délocalisation électronique à longue distance est préconisée[16].
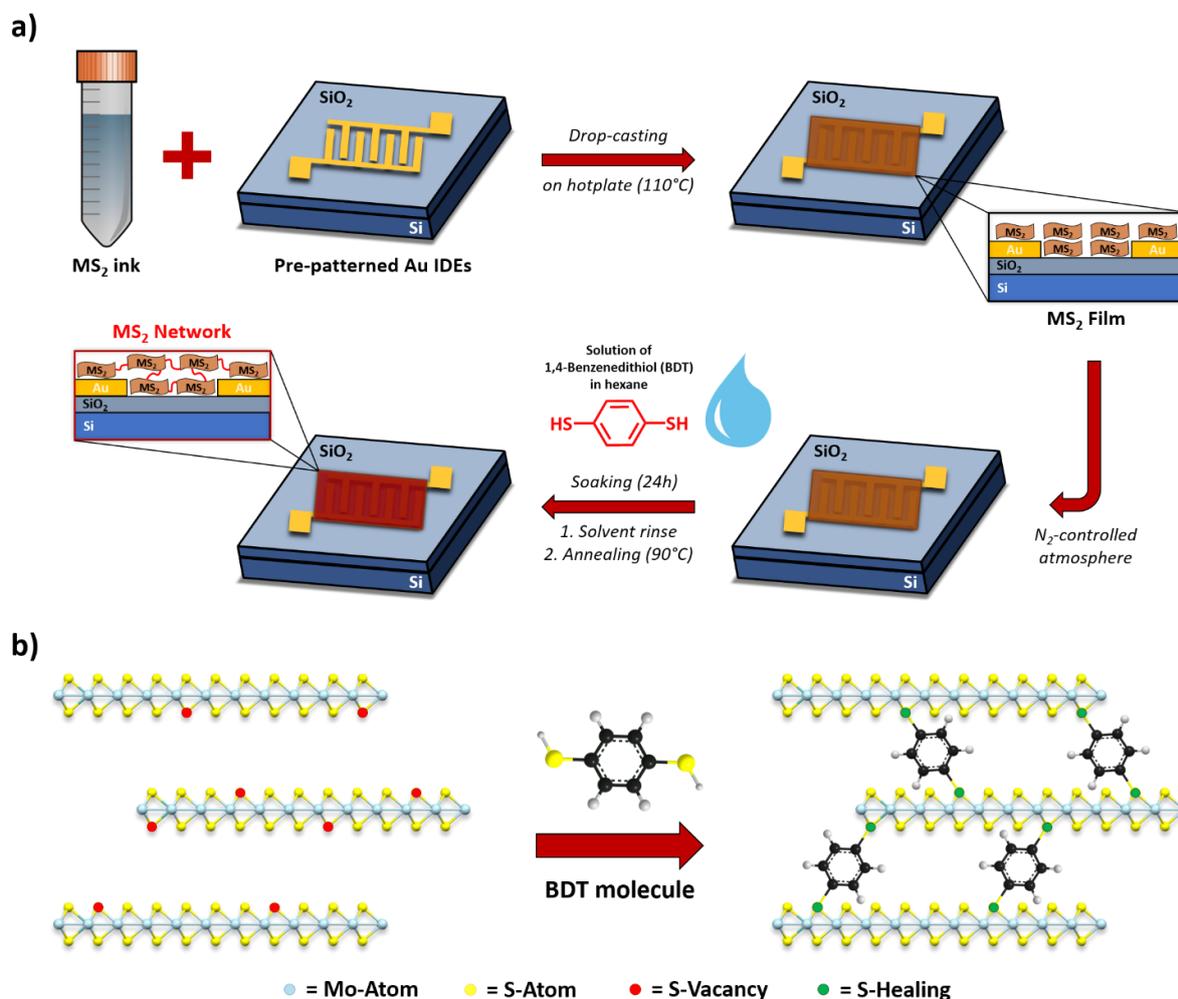

Figure I : a) Illustration du dépôt d'encre et de la fonctionnalisation in situ pour produire des réseaux de MS_2 par traitement au BDT. **b)** Esquisse du mécanisme de guérison des V_S dans les couches de MoS_2 au moyen de molécules dithiolées et de la mise en réseau inter-flocons associée

Les TFT à grille diélectrique à base de TMD traités en solution ont montré une faible commutation de courant ($I_{ON}/I_{OFF} < 10$)[18], ce qui nous a encouragé à nous concentrer sur les TFT à grille électrique au moyen d'une solution de liquide ionique, où cette dernière pénètre dans le volume libre interne du matériau semi-conducteur, la polarisation appliquée sur la grille du dispositif agissant volumétriquement. La caractérisation électrique a fourni une preuve sans ambiguïté de la formation du réseau, mettant en évidence des performances supérieures pour

les réseaux de MS$_2$; en particulier, ils ont présenté des facteurs de mérite de dispositif d'un ordre de grandeur plus élevé que les couches vierges, μ_{FE} atteignant 10^{-2} cm^2 V^{-1} s^{-1} et I_{ON}/I_{OFF} 10^4. De même, en mesurant la réponse du dispositif au courant en fonction du temps, un résultat similaire a été observé pour le temps de commutation (τ_S) des réseaux de MS$_2$: ils ont montré que τ_S atteignait ~18 ms, un ordre de grandeur inférieur à celui des couches vierges (τ_S ~170 ms), ce qui signifie que les systèmes interconnectés de manière covalente produisent des dispositifs beaucoup plus rapides que ceux à base de flocons de MS$_2$ isolés. De manière remarquable, l'amélioration décuplée des performances de dispositif enregistrée pour les réseaux de MS$_2$ s'est avérée irréalisable pour les molécules monothiolées (car elles ne permettent pas la formation de réseaux) et les molécules aliphatiques dithiolées, dont les performances ne pouvaient pas rivaliser avec celles obtenues avec les connecteurs BDT π-conjugués. De plus, en effectuant des mesures électriques en fonction de la température, nous avons observé une réponse de courant activée thermiquement avec des énergies d'activation (E_A) sensiblement différentes pour les réseaux et les films de MS$_2$, respectivement 360±10 meV et 512±12 meV. Par conséquent, comme les processus inter-flocons semblent être le principal goulot d'étranglement pour le transport de charge dans les couches minces de TMD[19], une énergie d'activation réduite indique une réduction de la résistance de jonction inter-flocons, ce qui serait cohérent avec l'augmentation de la mobilité observée lors de la formation du réseau.

Dans notre deuxième projet, nous avons développé la fabrication de systèmes multifonctionnels hybrides à base de TMD traités en solution et des nanoparticules (NP) de métaux nobles, à savoir Au, Pd et PtNP. Ce projet tire parti des principaux résultats rapportés au Chapitre 5 : les nanofeuillets de TMD traités en solution présentent une densité de défauts élevée, principalement des V_S situées sur les bords et se comportant comme des sites réactifs dans les stratégies moléculaires de fonctionnalisation suivantes. La condition *sine qua non* pour la décoration des bords des flocons de TMD avec des NP concerne une bonne adéquation des niveaux d'énergie entre le 2DM et le précurseur de sel métallique, ce qui conduit à la règle d'or suivante pour le mécanisme sous-jacent : les NP se forment spontanément si le potentiel de réduction ($E°$) du précurseur de sel métallique est inférieur à l'affinité électronique (χ) du 2DM, réduisant ainsi les atomes métalliques (Met^{n+}) jusqu'à l'état d'oxydation égal à zéro (Met^0) par transfert d'électrons à partir du 2DM. Un tel dépôt chimique, appelé déplacement galvanique, a lieu à température ambiante et sans aucun ajout d'agent réducteur[20], dont les 3 étapes principales peuvent être résumées comme suit : (i) le déplacement galvanique induit la formation de noyaux métalliques initiaux par transfert d'électrons du 2DM au précurseur de sel métallique ; (ii) le processus de mûrissement électrochimique d'Ostwald conduit à la croissance de plus grandes NP métalliques et à la

dissolution des plus petites ; (iii) la diffusion et la coalescence des NP métalliques à proximité des V_S. En particulier, la présence de V_S joue un rôle fondamental à toutes les étapes du mécanisme, puisqu'elles créent de nouveaux sites d'adsorption favorables pour les noyaux métalliques et améliorent considérablement leur diffusion vers les sites vacants. De plus, le mûrissement électrochimique d'Ostwald est entravé par les V_S en raison des effets de diffusion qui diminuent la mobilité de transfert d'électrons, affectant ainsi la taille finale des NP métalliques.
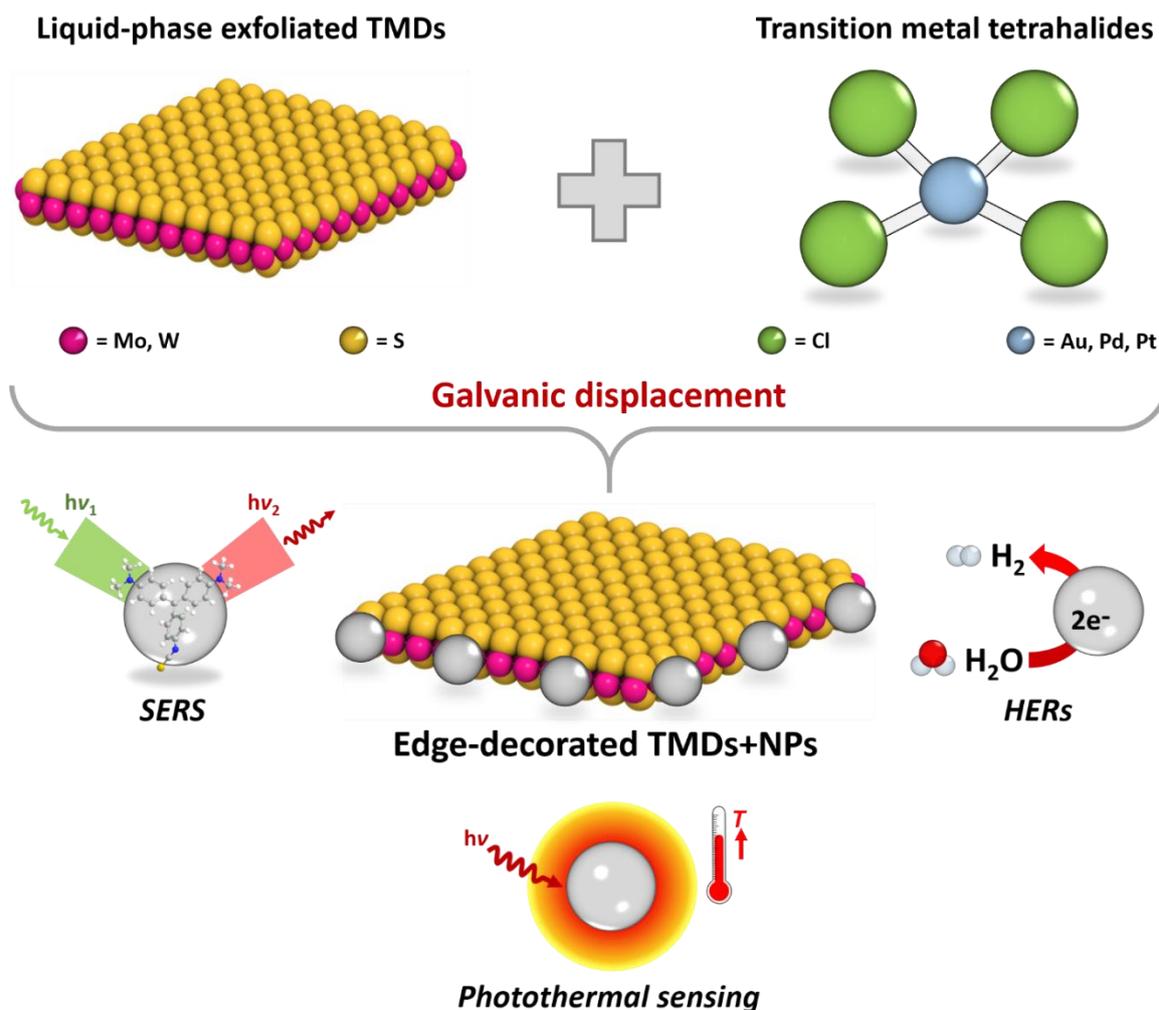
Figure II : Illustration de la stratégie de fonctionnalisation moléculaire adoptée pour la production de matériaux hybrides à base de TMD traités en solution et de NP de métaux nobles, dont les applications possibles sont également mises en évidence (SERS, HER et détection photothermique).

Nous avons évalué la formation de systèmes hybrides à base de TMD défectueux traités en solution et de NP métalliques au moyen de diverses techniques de caractérisation multi-échelles, impliquant des méthodes expérimentales ainsi que des calculs théoriques et des simulations. En particulier, l'analyse structurale et morphologique (par exemple, microscopie

électronique en transmission à balayage et à haute résolution, microscopie à force atomique, microscopie électronique à balayage) a révélé la décoration préférentielle des bords des nanofeuillets avec des Au, Pd et PtNP, confirmant le rôle crucial joué par les V_S dans le mécanisme de croissance. Nous avons utilisé des complexes tétrahalogénés plans carrés de Au(III), Pd(II) et Pt(II) comme précurseurs de sels métalliques, en étudiant leur réactivité inhérente envers les TMD semi-conducteurs, c'est-à-dire MoS_2 et WS_2, sous différents angles. Tout d'abord, nous avons effectué des calculs théoriques et des simulations sur le mécanisme de réaction entre les TMD et $HAuCl_4$, qui est utilisé comme étude de cas pour corroborer nos résultats. Plus précisément, nous avons étudié chaque étape du mécanisme de croissance, depuis l'adsorption dissociative de $HAuCl_4$ sur la surface du 2DM jusqu'à la formation de clusters et de NP, en simulant à la fois des cristaux vierges et défectueux (2% de V_S). En accord avec nos prédictions et résultats, nous avons confirmé que les V_S déclenchent et augmentent l'adsorption du précurseur de sel métallique sur la structure 2D, rendant la réaction globale plus favorable thermodynamiquement (énergies d'adsorption plus négatives). De plus, suite à l'analyse de Bader, nous avons soutenu le mécanisme de déplacement galvanique mettant en évidence un processus de transfert de charge des 2DM vers l'adsorbat à un stade très précoce, plus prononcé dans le cas de matériaux défectueux. D'un point de vue expérimental, nous avons réalisé une voltampérométrie cyclique (CV) pour déterminer le potentiel redox des 2DM et des précurseurs de sels métalliques, en utilisant une cellule composée à trois électrodes, d'une contre-électrode en fil de Pt, d'une électrode de travail en carbone vitreux (GC) et d'une électrode de référence Ag/AgCl (3 M KCl), ainsi que d'une solution aqueuse de KCl 0,1 M comme électrolyte. Les potentiels redox obtenus à partir des expériences susmentionnées étaient en accord avec le mécanisme proposé, puisque les 2DM ont montré des valeurs plus faibles que les précurseurs de sels métalliques, confirmant ainsi leur rôle d'agents réducteurs.

Nous avons testé les matériaux hybrides obtenus en décorant les bords des TMD traités en solution avec des NP de métaux nobles pour des applications en détection et en électrocatalyse. En particulier, en ce qui concerne la détection, nous avons étudié l'activité de la spectroscopie Raman exaltée de surface (SERS) (à l'état solide) et la réponse photothermique (en solution) de nos systèmes. Nous avons découvert que les TMD-AuNP présentent une augmentation significative du signal SERS (en utilisant une longueur d'onde d'excitation, λ_{ex}, de 532 nm), à la fois en condition de résonance et de non-résonance, ainsi qu'une réponse photothermique améliorée lorsqu'une λ_{ex} de 808 nm est utilisée. En outre, les systèmes hybrides ont montré une meilleure performance électrocatalytique dans les réactions de dégagement d'hydrogène (HER), comme le confirment la pente de Tafel et la résistance au transfert de charge plus faibles par rapport aux 2DM vierges.

Résumé

En conclusion, nous avons tiré profit de la défectuosité inhérente des TMD traités en solution, développant ainsi de nouvelles réactions de fonctionnalisation par des approches moléculaires. En ce qui concerne les réseaux interconnectés de manière covalente, nous avons prouvé que l'ingénierie des défauts représente une stratégie de fonctionnalisation optimale pour les MS_2 traités en solution, où les V_S peuvent subir une guérison au moyen de molécules thiolées. Plus précisément, l'utilisation de systèmes moléculaires π-conjugués dithiolés permet simultanément la guérison des V_S et le pontage de flocons adjacents dans les couches minces, ce qui conduit à une interconnectivité électronique accrue et, par conséquent, à un meilleur transport de charge dans les réseaux. Nos résultats ouvrent la voie au développement de l'électronique imprimée de haute performance et de grande surface, où une conception moléculaire appropriée des connecteurs de pontage pourrait doter les réseaux de TMD de diverses fonctionnalités, en ajustant les propriétés ultimes à la demande en fonction des applications finales. En outre, les V_S peuvent également être exploitées comme sites réactifs dans des stratégies de fonctionnalisation supplémentaires, comme rapporté dans notre deuxième projet, où nous avons développé la fabrication de matériaux multifonctionnels hybrides à base de nanofeuillets de TMD décorés sur les bords. En particulier, les V_S déclenchent l'adsorption de précurseurs de sels métalliques sur les cristaux 2D, où les premiers sont réduits en NP métalliques par un mécanisme de déplacement galvanique. Les systèmes hybrides ainsi formés présentent des performances électrocatalytiques, SERS et photothermiques améliorées par rapport aux TMD vierges, ce qui met en évidence la contribution fondamentale des NP de métaux nobles. Nos résultats offrent des lignes directrices précieuses pour la production de telles structures multifonctionnelles hybrides polyvalentes à base de MS_2 traités en solution, dont les propriétés physico-chimiques ultimes pourraient être ajustées à la carte par une conception appropriée de la composition, de la taille et de la forme des NP métalliques.

Abstract

The discovery of new materials with exploitable properties has always boosted the scientific and societal progress in the history of mankind. From prehistory to the present, we can highlight few notable examples that defined our evolution: stone, metals (bronze and iron), steel and lately plastics, ceramics and composites. In this regard, the latest cornerstone that we have faced during the past fifteen years concerns the discovery of the outstanding physical and chemical properties of graphene, by Geim and Novoselov in 2004[1]. Graphene, an atom-thick layer of carbon atoms hybridized sp^2 and structurally analogous to graphite, represents a veritable breakthrough in materials science: its unique and versatile properties[2] may be the key to revolutionize existing technologies and promote the development of new ones. In this regard, the ease of graphene isolation *via* micromechanical cleavage, also known as scotch-tape method, has encouraged worldwide scientists to isolate new two-dimensional materials (2DMs) starting from the related bulk counterparts[3]. As a result, a variety of atomically-thin nanosystems have been produced from layered van der Waals (vdW) structures, such as black phosphorus, hexagonal boron nitride and transition metal dichalcogenides (TMDs). Unlike graphene that exhibits a semimetallic behavior and does not possess a band-gap in its pristine form[2], TMDs offer a wide-range portfolio of electrical, electronic and optical properties, including, for instance, tunable band-gaps in the whole spectrum[4], a pivotal feature for electronic and optoelectronic applications. Remarkably, the properties of the single-layer materials are markedly different from those of their bulk counterparts because of strong quantum confinement, reduced screening and surface effects[5]. Therefore, the discovery of exotic quantum effects and phenomena in the atomically thin limit has promoted the ever growing diffusion of 2DMs, and TMDs in particular, for applications spanning from electronics, optoelectronics and (photo)catalysis to (bio)sensing and biomedicine[6,7].

However, the performance of TMD-based devices is strictly related to the inherent properties and quality of the materials, which play a crucial role in determining the final applications. To this end, research endeavours have been devoted to the development of production techniques and successive functionalization steps to increase the materials' quality and enhance their performance, respectively[8]. The early stages of the research on TMDs have exclusively relied on micromechanical exfoliation, despite this technique has two major drawbacks concerning the lack of control during the production of samples with a specific number of layers and it is not suitable for the production at large (industrial) scale[9]. Therefore, to overcome the aforementioned limitations, various strategies have been developed and pursued during the last few years to foster the production of high-quality 2DMs. Remarkably,

solution-processing approaches have emerged as efficient methods for the synthesis and exfoliation of TMDs. Although the production steps already affect the quality and characteristics of solution-processed TMD materials, many research efforts have been devoted to the development of molecular strategies to finely tune their physicochemical properties[8]. This is accomplished by taking advantage of the highest surface-to-volume ratio of 2DMs and their properties' susceptibility to the local environment. The developed approaches exploit covalent and non-covalent interactions through which small molecules[10], noble metal nanoparticles (NPs)[11] or (bio)polymers[12] interact with the basal plane and/or edges of TMD nanosheets. In fact, the physisorption or chemisorption processes are driven by a variety of mechanisms, whose versatility represents a powerful tool in the area of 2DM science.

Liquid-phase exfoliation (LPE) embodies the main route to produce high-concentration and high-volume TMD dispersions, where bulk crystals are dispersed and exfoliated in a specific solvent *via* mechanical energy transfer that overcomes the vdW interactions within the layered structures. The high throughput achieved by LPE promotes the use of TMDs in many different applications, exploiting pristine or hybrid materials in the form of dispersions, coatings and thin-films produced by diverse deposition techniques, including inkjet printing, spray coating, roll-to-roll, drop casting and so on[13]. Although LPE provides the best trade-off amongst cost, purity and yield, it has some limitations when the final application concerns (opto)electronics, where structural defects in the material play a detrimental role. In fact, the energetic exfoliation procedure results in a mild formation of new defects and major propagation of inherent bulk defects in the exfoliated layers. As suggested by thermodynamic considerations, zero-dimensional defects are the most abundant stoichiometric deficiencies in TMDs, especially chalcogen vacancies mainly located at the edges of nanosheets and whose formation energy is a few eV (~2 eV in the case of sulfur vacancies, henceforth referred to as V_S)[14].

This thesis focuses on defect-engineering strategies to enhance the performance of TMD-based hybrid devices for electronic, electrocatalysis and sensing applications. After a brief introduction highlighting the background and motivation at the basis of this research project (Chapter 1), focus will be laid on the production and properties of solution-processed TMDs (Chapter 2), along with the related defectiveness as one-of-a-kind tool to tune their inherent features (Chapter 3). The experimental section will be opened up with an accurate description of the materials and characterization techniques (Chapter 4) employed in the two major projects reported in this thesis (Chapter 5 and Chapter 6), whose findings are discussed below.

Abstract

In our first project, we developed a new molecular strategy to simultaneously heal V_S in solution-processed MS_2 (M = Mo, W, Re) and increase the inter-flake electronic connectivity by means of dithiolated molecular systems[15]. In particular, by using π-conjugated dithiolated molecules (HS-R-SH), we proved *via* diverse multiscale analysis the simultaneous: (i) healing of V_S to restore the MS_2 crystal structure and decrease the related stoichiometric deficiencies acting as charge-scattering centers; (ii) covalent bridging of adjacent flakes, leading to an enhanced charge-carrier transport through an interconnected network. We capitalized on the in-situ functionalization approach of TMDs, exposing the inorganic materials to the molecular linkers just after their deposition on a substrate. This is crucial for the formation of long-range pathways that exhibit superior charge transport characteristics, likewise the bridging of disordered regions in conjugated polymer chains[16]. Our approach represents an innovative and universal functionalization method, capable of improving the performance of devices based on solution-processed MS_2 for large-area electronic applications. We applied this strategy in liquid-gated thin-film transistors (LG-TFTs) fabricated by drop casting MS_2 dispersions onto SiO_2/Si substrates pre-patterned with gold interdigitated electrodes (Au-IDEs), followed by exposure to aromatic and conjugated 1,4-benzenedithiol (BDT) molecules. This yielded a notable enhancement of the characteristics of MS_2-based LG-TFTs by one order of magnitude, leading to state-of-the-art (SoA) electrical performance in terms of field-effect mobility (μ_{FE}) and current ratio (I_{ON}/I_{OFF}), along with the fastest switching speed reported so far for devices of this kind[17]. Improved water stability and mechanical robustness are other unique features exhibited by the covalently bridged MS_2 networks.

We assessed the effects of in-situ functionalization with BDT molecules by various independent multiscale techniques, including spectroscopic (*e.g.*, Raman, UV-Visible, X-ray Photoelectron Spectroscopy, Nuclear Magnetic Resonance Spectroscopy), morphological and structural (*e.g.*, Atomic Force Microscopy, Scanning Electron Microscopy, High-Angle Annular Dark-Field Scanning Transmission Electron Microscopy, X-ray Diffraction), mechanical and electrical (*e.g.*, charge transport and temperature-dependent analysis) characterizations. The covalent bridging of individual MS_2 flakes with π-conjugated molecules is expected to improve their electrical properties, especially electrical connectivity, where long-range electronic delocalization is advocated[16].

Dielectrically gated TFTs based on solution-processed TMDs showed poor current switching ($I_{ON}/I_{OFF} < 10$)[18], encouraging one to focus on TFTs electrically gated by means of an ionic liquid solution, where the latter penetrates the internal free volume of the semiconducting material gating the device volumetrically.
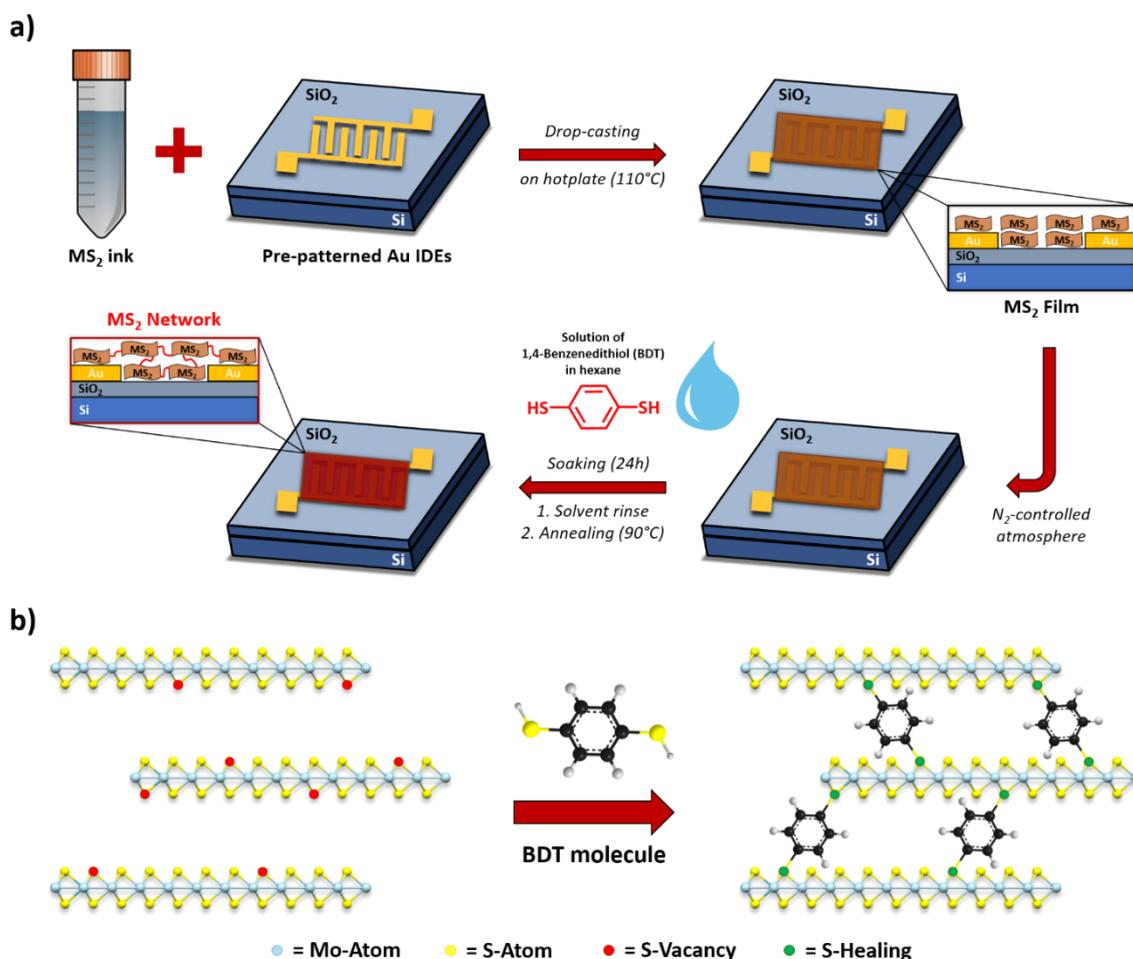
Figure I : a) Illustration of the ink deposition and in-situ functionalization to produce MS$_2$ networks *via* BDT treatment. **b)** Sketch of V$_S$ healing mechanism in MoS$_2$ films by means of dithiolated molecules and related inter-flake networking.

The electrical characterization provided unambiguous evidence of the network formation, highlighting superior performance for MS$_2$ networks; in particular, they exhibited device figures of merit one order of magnitude higher than pristine films, reaching µ$_{FE}$ up to 10^{-2} cm^2 V^{-1} s^{-1} and I$_{ON}$/I$_{OFF}$ up to 10^4. By the same token, while measuring the device time-dependent current response, a similar outcome was observed for the switching time (τ$_S$) of MS$_2$ networks: they shown τ$_S$ ~18 ms, one order of magnitude lower than pristine films (τ$_S$ ~170 ms), meaning that covalently interconnected systems result in devices much faster than those based on isolated MS$_2$ flakes. Remarkably, the ten-fold enhancement of device performance recorded for MS$_2$ networks resulted unachievable for monothiolated molecules (as they do not allow network formation) and aliphatic dithiolated molecules, whose performance could not rival those achieved with BDT π-conjugated linkers. Furthermore, by running temperature-dependent electrical measurements, we observed a thermally activated current response with noticeably different activation energies (E$_A$) for MS$_2$ networks and films, 360±10 meV and 512±12 meV

respectively. Hence, as the inter-flake processes appear to be the major bottleneck for the charge transport within TMD thin films[19], a reduced E_A points to a reduction in inter-flake junction resistance, which would be consistent with the observed mobility increase upon network formation.

In our second project, we developed the fabrication of hybrid multifunctional systems based on solution-processed TMDs and noble metal nanoparticles (NPs), namely Au, Pd and PtNPs. The project takes advantage of the major findings reported in Chapter 5: solution-processed TMD nanosheets exhibit high defect density, mainly V_S located at the edges and behaving as reactive sites in the following functionalization molecular strategies. The *sine qua non* for the edge decoration of TMD flakes with NPs concerns a proper matching of energy levels between 2DM and metal salt precursor, leading to the ensuing golden rule for the underlying mechanism: NPs are spontaneously formed if the reduction potential (E°) of the metal salt precursor lies below the electron affinity (χ) of the 2DM, thereby reducing the metal atoms (Met^{n+}) up to the oxidation state equal to zero (Met^0) by electron transfer from the 2DM. Such an electroless deposition, called galvanic displacement, takes place at room temperature and without any addition of reducing agent[20], whose 3 main stages can be summarized as follows: (i) galvanic displacement induces the formation of initial metal nuclei by electron transfer from the 2DM to the metal salt precursor; (ii) electrochemical Ostwald ripening process leads to the growth of larger metal NPs and dissolution of smaller ones; (iii) diffusion and coalescence of metal NPs close to V_S. In particular, the presence of V_S plays a fundamental role in all stages of the mechanism, since they create new favorable adsorption sites for metal nuclei and greatly enhance their diffusion towards vacancy sites. Furthermore, the electrochemical Ostwald ripening is hindered by V_S because of scattering effects that diminish the electron transfer mobility, thereby affecting the final size of metal NPs.

We assessed the formation of hybrid systems based on defective solution-processed TMDs and metal NPs by means of diverse multiscale characterization techniques, involving experimental methods corroborated by theoretical calculations and simulations. In particular, structural and morphological analysis (*e.g.*, Scanning and High-Resolution Transmission Electron Microscopy, Atomic Force Microscopy, Scanning Electron Microscopy) revealed the preferential decoration of nanosheets' edges with Au, Pd and PtNPs, confirming the crucial role played by V_S in the growth mechanism. We used square planar tetrahalides complex of Au(III), Pd(II) and Pt(II) as metal salt precursors, investigating their inherent reactivity towards semiconducting TMDs, *i.e.*, MoS$_2$ and WS$_2$, from different angles. Firstly, we performed theoretical calculations and simulations on the reaction mechanism between TMDs and HAuCl$_4$, used as case study to corroborate our findings. More specifically, we investigated each step of the growth mechanism starting from the dissociative adsorption of HAuCl$_4$ onto

the 2DM surface until the cluster and NPs formation, simulating both pristine and defective crystals (2% of V_S).
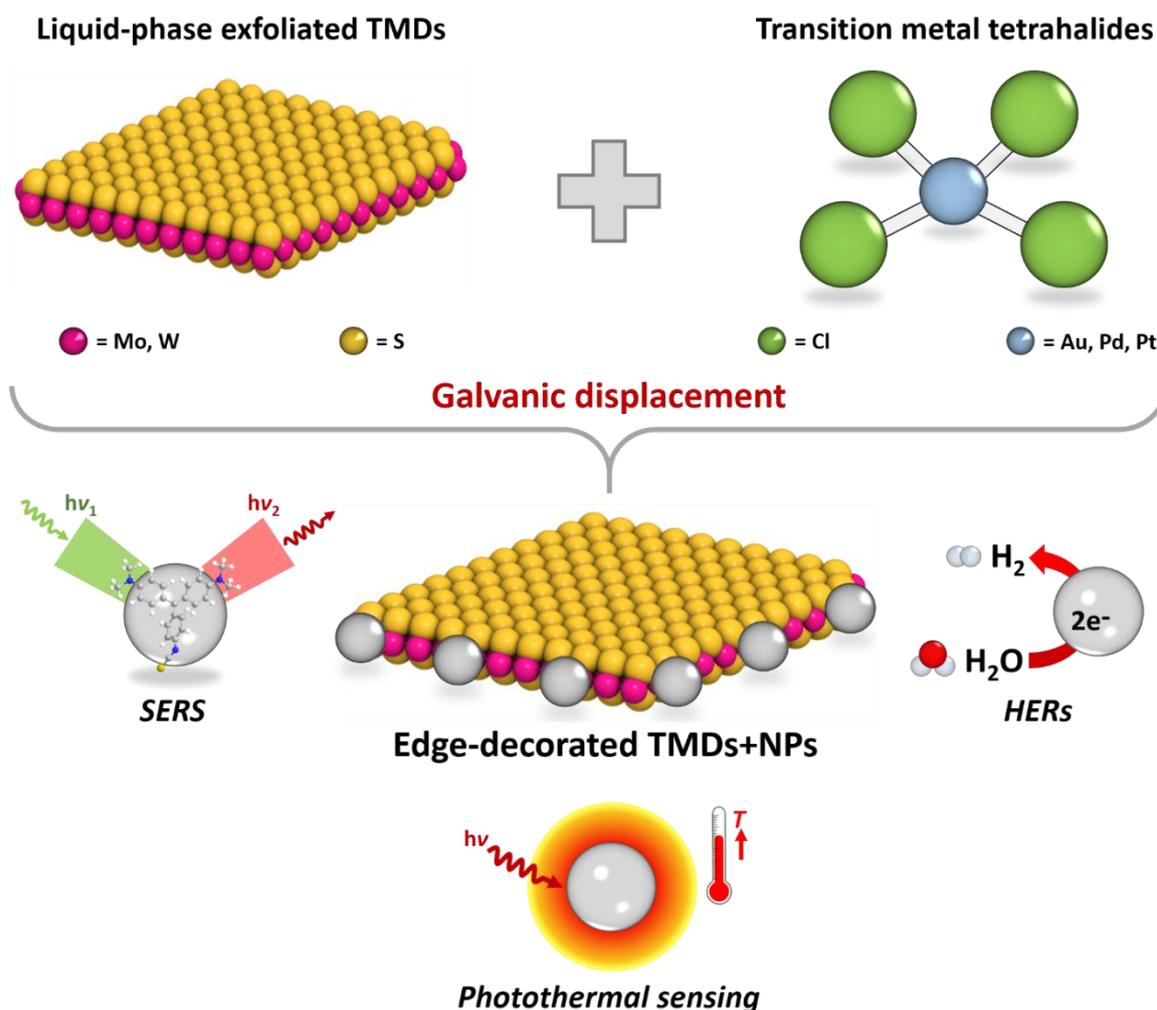
Figure II : Illustration of the molecular functionalization strategy adopted for the production of hybrid materials based on solution-processed TMDs and noble metal NPs, whose possible applications are also highlighted (SERS, HERs and photothermal sensing).

In agreement with our predictions and results, we confirmed that V_S trigger and enhance the adsorption of the metal salt precursor onto the 2D structure, making the overall reaction more thermodynamically favorable (more negative adsorption energies). Moreover, as a result of Bader analysis, we supported the galvanic displacement mechanism highlighting a charge transfer process from the 2DMs to the adsorbate in the very early stage, more pronounced in the case of defective materials. From an experimental point of view, we carried out cyclic voltammetry (CV) to determine the redox potential of 2DMs and metal salt precursors, by using a three-electrode cell consisting of a Pt wire counter electrode, glassy carbon (GC) working electrode and Ag/AgCl (3 M KCl) reference electrode, as well as aqueous KCl 0.1 M as

electrolyte solution. The redox potentials obtained from the abovementioned experiments agreed with the proposed mechanism, since the 2DMs showed lower values than metal salt precursors thus confirming their role as reducing agents.

We tested the hybrid materials obtained by decorating the edges of solution-processed TMDs with noble metal NPs for sensing and electrocatalysis applications. In particular, with regard to sensing, we investigated the Surface-Enhanced Raman Spectroscopy (SERS) activity (in solid state) and photothermal response (in solution) of our systems. We found out that TMD-AuNPs exhibit significant SERS signal enhancement (by using an excitation wavelength, λ_{ex}, of 532 nm), both in resonance and non-resonance condition, as well as improved photothermal response when a λ_{ex} of 808 nm is used. Moreover, the hybrid systems shown improved electrocatalytic performance in hydrogen evolution reactions (HERs), as confirmed by the lower Tafel slope and charge transfer resistance with respect to pristine 2DMs.

In conclusion, we took advantage of the inherent defectiveness of solution-processed TMDs, thereby developing new functionalization reactions *via* molecular approaches. In regard to the covalently interconnected networks, we proved defect-engineering represents an optimal functionalization strategy for solution-processed MS$_2$, where V$_S$ can undergo healing by means of thiolated molecules. More specifically, the use of dithiolated π-conjugated molecular systems allows the simultaneous healing of V$_S$ and bridging of adjacent flakes in thin films, leading to enhanced electron interconnectivity and, therefore, improved charge transport within the networks. Our findings pave the way for the development of high-performance, large-area and printed electronics, where an appropriate molecular design of the bridging linkers might endow the TMD networks with diverse functionalities, tuning the ultimate properties on demand according to the final applications. Furthermore, V$_S$ can also be exploited as reactive sites in additional functionalization strategies as reported in our second project, where we developed the fabrication of hybrid multifunctional materials based on edge-decorated TMD nanosheets. In particular, V$_S$ trigger the adsorption of metal salt precursors onto the 2D crystals, where the latter get reduced to metal NPs *via* galvanic displacement mechanism. The so-formed hybrid systems exhibit enhanced electrocatalytic, SERS and photothermal performance with respect to pristine TMDs, highlighting the fundamental contribution of noble metal NPs. Our results offer valuable guidelines for the production of versatile hybrid multifunctional structures based on solution-processed MS$_2$, whose ultimate physicochemical properties might be tailored *à la carte* by suitable design of composition, size and shape of metal NPs.

Abbreviations and acronyms

ε_0	Vacuum permittivity
ε_r	Dielectric constant
Φ_B	Schottky barrier
Φ_{WF}	Work function
λ_{ex}	Excitation wavelength
μ_{FE}	Field-effect mobility
τ_S	Switching time
χ	Electron affinity
2D	Two-dimensional
2DM(s)	Two-dimensional material(s)
A	Area
A*	Richardson constant
ADF	Annular dark-field microscopy
AFM	Atomic force microscopy
APW	Augmented plane wave
Au-IDE(s)	Gold interdigitated electrode(s)
BDT	1,4-Benzenedithiol
BF-TEM	Bright-field transmission electron microscopy
CB	Conduction band
CV	Cyclic voltammetry
C_V	Volumetric capacitance
CVD	Chemical vapor deposition
DFT	Density functional theory
DF-TEM	Dark-field transmission electron microscopy
DLS	Dynamic light scattering
E	Electric field
E°	Standard reduction potential
E°$_{cell}$	Standard redox potential of the cell
E_A	Activation energy
ECE	Electrochemical exfoliation
EIS	Electrochemical impedance spectroscopy
FCC	Face-centred cubic
FET(s)	Field-effect transistor(s)
FOM	Figure(s) of merit

FWHM	Full width at half maximum
GC	Glassy carbon
GGA	Generalized gradient approximation
GIXD	Grazing incident X-ray diffraction
HAADF	High-angle annular dark-field
HER(s)	Hydrogen evolution reaction(s)
HR-TEM	High-resolution transmission electron microscopy
I_{ds}	Source-drain current
IL	Ionic liquid
I_{ON}/I_{OFF}	Current ratio
IPA	Isopropanol
k_B	Boltzmann constant
LbL	Layer-by-layer
LG-TFT(s)	Liquid-gated thin-film transistor(s)
LPE	Liquid-phase exfoliation
MS_2	Transition metal disulfide
NMP	N-methyl-2-pyrrolidone
NMR	Nuclear magnetic resonance
NP(s)	Nanoparticle(s)
PAA	Poly(acrylic acid)
PDDA	Poly(diallyldimethylammonium chloride)
PDOS	Projected density of state
PDT	1,3-Propanedithiol
PESA	Photoelectron spectroscopy in air
PET	Polyethylene terephthalate
PL	Photoluminescence
PPD	Benzene-1,4-diamine
PTFE	Polytetrafluoroethylene
PVD	Physical vapor Deposition
R_{rms}	Root-mean-square roughness
SAM(s)	Self-assembled monolayer(s)
SEM	Scanning electron microscopy
SERRS	Surface-enhanced Raman scattering
SERS	Surface-enhanced raman spectroscopy
SoA	State-of-the-art
STEM	Scanning transmission electron microscopy
T	Absolute temperature

t	Thickness
TEM	Transmission electron microscopy
TFT(s)	Thin-film transistor(s)
TMD(s)	Transition metal dichalcogenide(s)
TP	Thiophenol
VASP	Vienna *ab initio* simulation package
VB	Valence band
V_{ds}	Source-drain voltage
vdW	van der Waals
V_g	Gate voltage (top-gate geometry)
V_G^{Back}	Gate voltage (back-gate geometry)
V_S	Sulfur vacancy
V_{TH}	Threshold voltage
WCA	Water contact angle
XPS	X-ray photoelectron spectroscopy
XRD	X-ray diffraction

Table of contents

Chapter 1 — Introduction

1.1. — *Background and objectives*

The discovery of graphene[1], a single atomic layer of graphite, is being regarded as a veritable breakthrough in material science, with the potential to revolutionize several existing technologies and enable the creation of new ones. Being only one carbon atom thick, graphene can be considered as the truly ancestor of 2DMs, where the strong quantum confinement, reduced screening and surface effects give rise to novel extraordinary properties[5]. For instance, graphene holds the record for the highest thermal and electrical conductivity, but it is also the strongest material ever measured[2,21].

Such an extraordinary and revolutionary discovery triggered a tremendous effort focused on the isolation and production of other 2DMs, the so-called "2DMs beyond graphene". Thus far, we embrace a large variety of atomically-thin nanosystems deriving from bulk layered vdW structures (Figure 1-1), such as black phosphorus, hexagonal boron nitride, MXenes, TMDs, and so on and so forth. Amongst them, TMDs have been attracting ever-growing interest, since they offer a broad portfolio of electronic and optical properties as an alternative to those of graphene. While the latter is a zero-gap semimetal, they possess tunable band-gaps in the whole visible spectrum, a crucial feature for applications in digital electronic switches and optoelectronic devices. However, it is probably fair to say that fundamental research on well-known 2DMs has already passed its zenith, therefore researchers have now started paying more attention to other challenging and intriguing opportunities.

Graphene family	Graphene	hBN 'white graphene'		BCN	Fluorographene	Graphene oxide
2D chalcogenides	MoS_2, WS_2, $MoSe_2$, WSe_2	Semiconducting dichalcogenides: $MoTe_2$, WTe_2, ZrS_2, $ZrSe_2$ and so on		Metallic dichalcogenides: $NbSe_2$, NbS_2, TaS_2, TiS_2, $NiSe_2$ and so on		
				Layered semiconductors: GaSe, GaTe, InSe, Bi_2Se_3 and so on		
2D oxides	Micas, BSCCO	MoO_3, WO_3	Perovskite-type: $LaNb_2O_7$, $(Ca,Sr)_2Nb_3O_{10}$, $Bi_4Ti_3O_{12}$, $Ca_2Ta_2TiO_{10}$ and so on		Hydroxides: $Ni(OH)_2$, $Eu(OH)_2$ and so on	
	Layered Cu oxides	TiO_2, MnO_2, V_2O_5, TaO_3, RuO_2 and so on			Others	

Figure 1-1 : Current library of 2DMs. Monolayers proved to be stable under ambient conditions (room temperature and air) are shaded in blue; those probably stable are shaded in green, whereas those unstable in air but that may be stable in inert atmosphere are shaded in pink. Reproduced from Ref.[22].

In particular, the first option is represented by an atomic scale Lego approach, where different 2D crystals are stacked on top of each other to fabricate vdW heterostructures (Figure 1-2). Within the latter, strong covalent bonds provide in-plane stability, whereas relatively weak vdW interactions keep the stack together[22]. The resulting artificial materials assembled in a chosen sequence show one-atomic-plane precision, whose properties can be meticulously tailored *à la carte* through an appropriate construction design. Nevertheless, the fabrication technique of such Lego architectures takes long time to master, besides dozens of complex and sophisticated procedures that have hindered the progress at industrial scale.
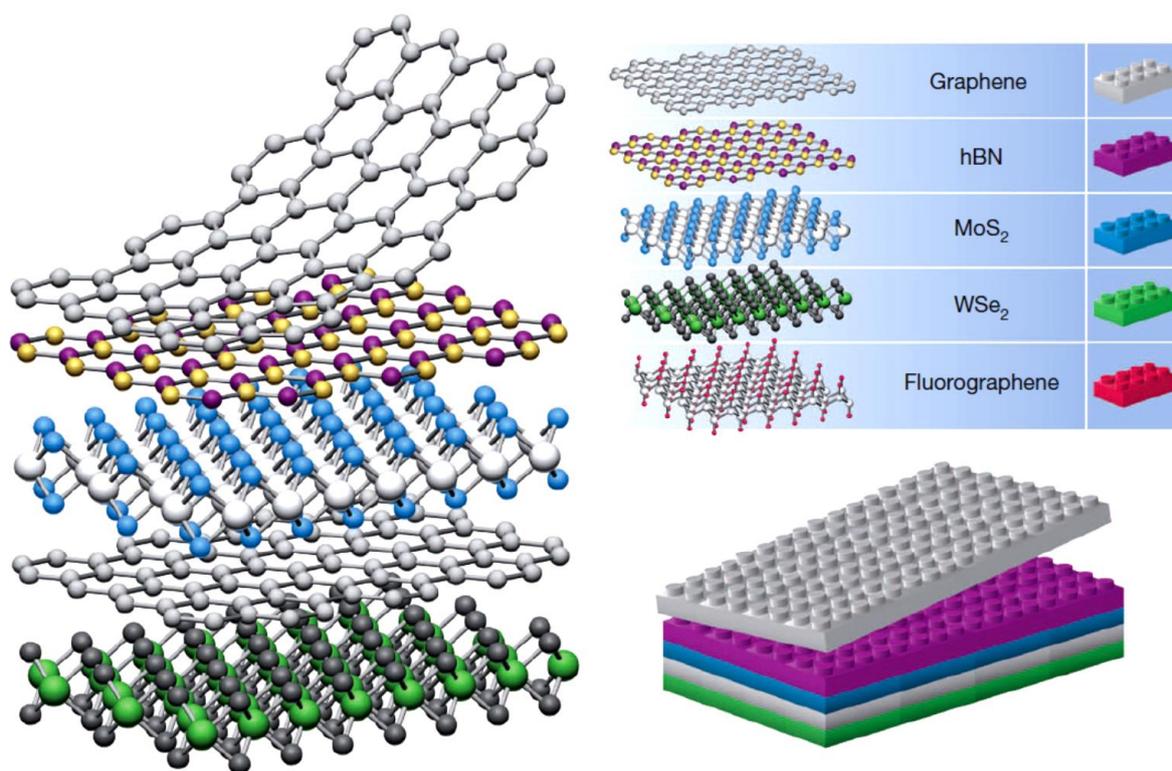

Figure 1-2 : Fabrication of van der Waals heterostructures. Considering 2D crystals analogous to Lego blocks (right panel), the production of a huge variety of layered structures becomes possible, paving the way for intriguing new opportunities in 2DM science. Reproduced from Ref.[22].

As a consequence, research endeavors have been devoted to the development of functionalization strategies[8], following the production steps, to tailor the physicochemical properties of 2DMs (Figure 1-3). The physisorption or chemisorption process of molecular systems onto 2D crystals is driven by a variety of mechanisms, whose versatility represents a powerful toolbox in such an exciting area of 2DM science. Moreover, such an appealing approach might rely on a virtually infinite number of functional molecular systems, offered by chemical synthesis, in order to boost the advance of new disrupting technologies.
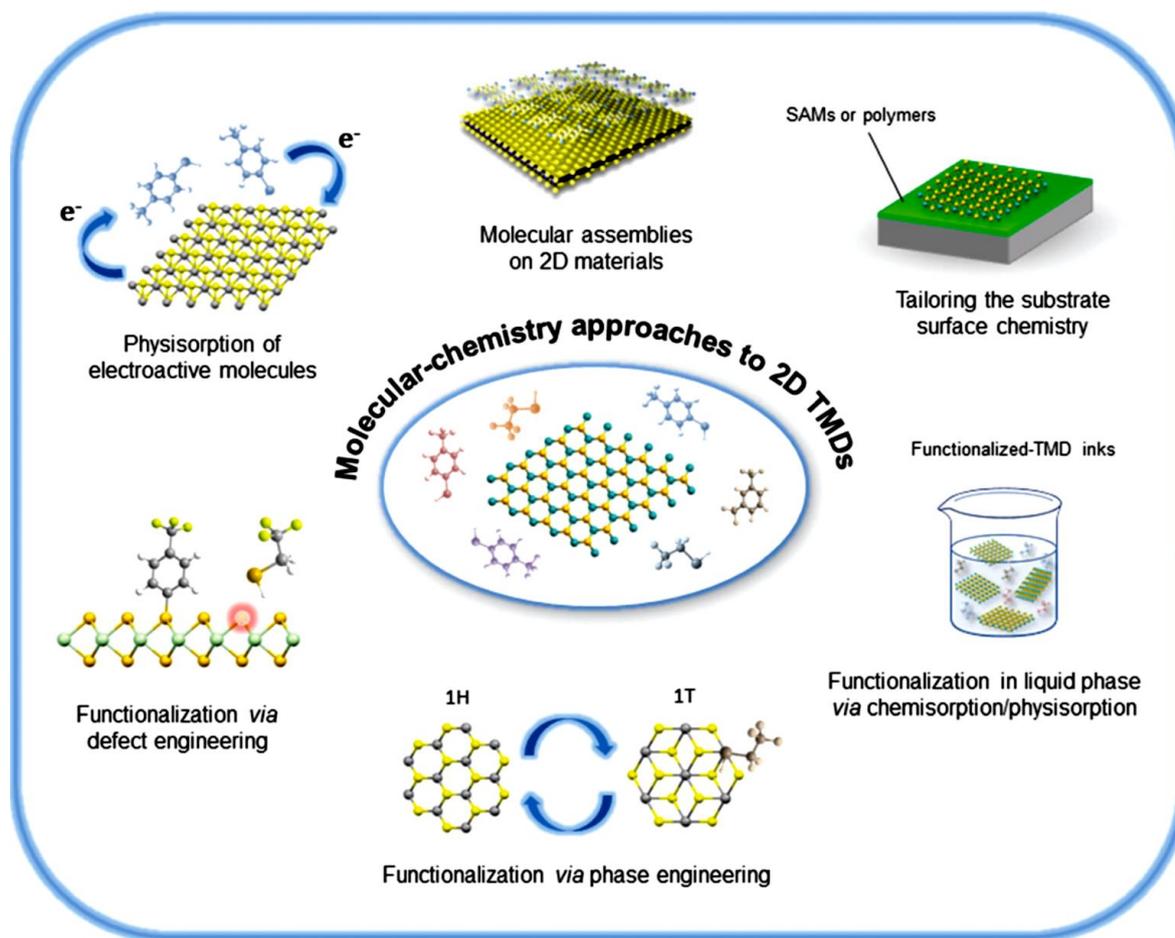
Figure 1-3 : Schematic representation of the different molecular chemistry approaches that have been investigated in the last few years for tailoring the properties of 2D TMDs. Reproduced from Ref.[8].

The successful applications of 2DMs are strictly related to their quality and exfoliation yield. To date, micromechanical cleavage remains the most straightforward source of high-quality 2DMs, even though it suffers from low yields and production rates that are not technologically suitable for upscaling at an industrial level. In light of such limitations, during the last decade intense research endeavors have been addressed towards the design and development of innovative solution-based strategies to achieve an efficient production of 2DMs, and TMDs in particular[23,24]. For a better understanding, the production methods can be classified into top-down and bottom-up approaches (Figure 1-4)[25]. Amongst them, LPE is the most commonly employed method in exfoliation (top-down) approaches, as it embodies the best trade-off among pivotal parameters to assess a production strategy in 2DM science, such as costs, purity, yield, etc[26]. More specifically, LPE entails the use of a liquid sample containing the bulk TMD crystals and an energy transfer thereto, in order to overcome the weak vdW interactions acting within the layered structures and promote their exfoliation.
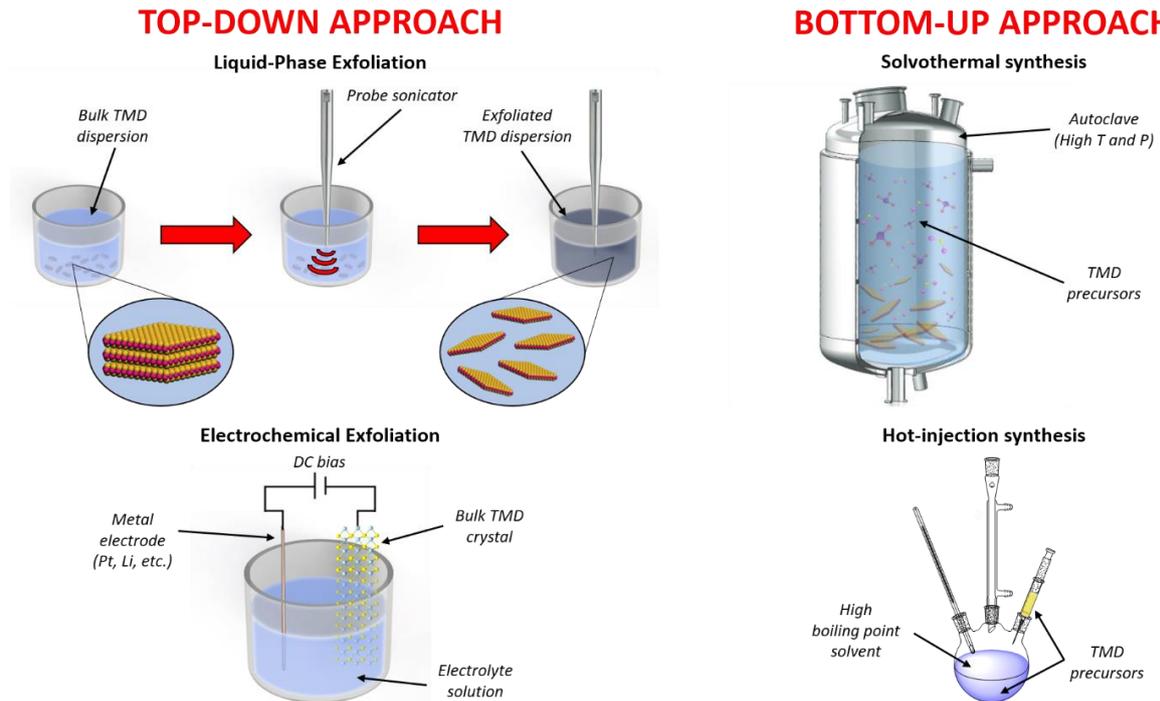
TOP-DOWN APPROACH

Liquid-Phase Exfoliation

BOTTOM-UP APPROACH

Solvothermal synthesis

Electrochemical Exfoliation

Hot-injection synthesis

Figure 1-4 : Illustration of the main production strategies to obtain solution-processed TMDs *via* top-down (left) and bottom-up approaches (right). Reproduced from Ref.[25].

As a result of thermal equilibrium and kinetics of processing, all materials possess structural defects which could significantly affect their properties. Defects residing in 2D crystals could be classified according to their dimensionality (Figure 1-5) as zero-dimensional (point defects, dopants or "non-hexagonal" rings), one-dimensional (grain boundaries, edges, and in-plane heterojunctions) and two-dimensional (layer stacking of vdW solids, wrinkling, folding, and scrolling)[27,28]. Supported by thermodynamic considerations, zero-dimensional defects are the most abundant stoichiometric deficiencies in TMDs, especially chalcogen vacancies that are mainly located at the flake edges and whose formation energy is a few eV (~2 eV in the case of V_S)[28]. In atomistic simulations, these defects are generated by removing atoms from 2D lattices, where a single vacancy involves the elimination of a single atom, whereas a double vacancy requires the removal of a pair of adjacent atoms. Finally, the atomic structure around the created vacancy is relaxed *via* geometry optimization. Defects in 2DMs can be either unintentionally formed during production steps or deliberately introduced by processing[8], altering their ultimate physicochemical properties. In this regard, they could be considered as a prime example of *Janus Bifrons* in materials science: in fact, defects can deteriorate the properties and structure of materials, but they can also enhance them with unique features that are absent in perfect solids. More importantly, defects offer one-of-a-kind opportunities for further functionalization strategies by molecular approaches, where they act as primary reactive sites in 2DMs.
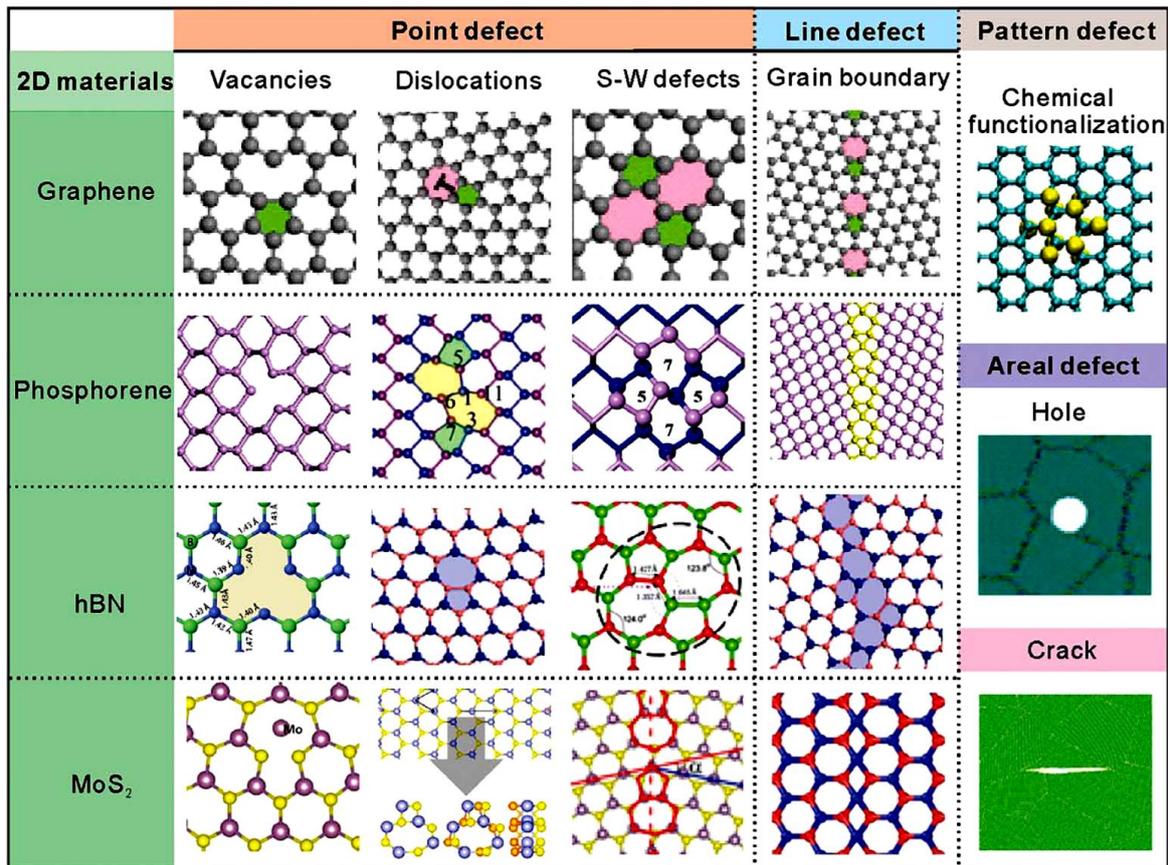
Figure 1-5 : Graphic illustration of some 2DMs with different kinds of defects. Reproduced from Ref.[27].

During the last five years, the scientific community has witnessed tremendous progress in solution-processed semiconducting TMDs, along with the use of chemical approaches to finely tune their electrical, optical, mechanical and thermal properties. Such an incredible and rapid development paved the way for the applications of TMD materials in many research areas, spanning from (opto)electronics to sensing and catalysis (Figure 1-6). In this regard, due to their atomic-scale thickness and sizable energy band-gaps (1-3 eV)[29,30], TMDs offer ideal electrostatic control in field-effect transistor (FET) geometry, minimal short-channel effects and low standby power dissipation[31], thereby representing potential alternatives to silicon for next-generation "beyond Moore" technologies[32]. Furthermore, as developments in sustainable energy are attracting global attention, it has become imperative to evaluate the efficacy of various 2DMs in these areas, such as, for instance, electrocatalysis that lies at the heart of clean energy conversion in future technologies. In particular, 2DMs represent prime candidates because of their excellent mechanical properties and conductivity (thermal and electrical), as well as high surface-to-volume ratio, providing a high density of surface active sites[33]. Finally, in view of the abovementioned features (*e.g.*, high surface-to-volume ratio, atomic thickness), 2DMs exhibit a strong response to surface adsorption events.
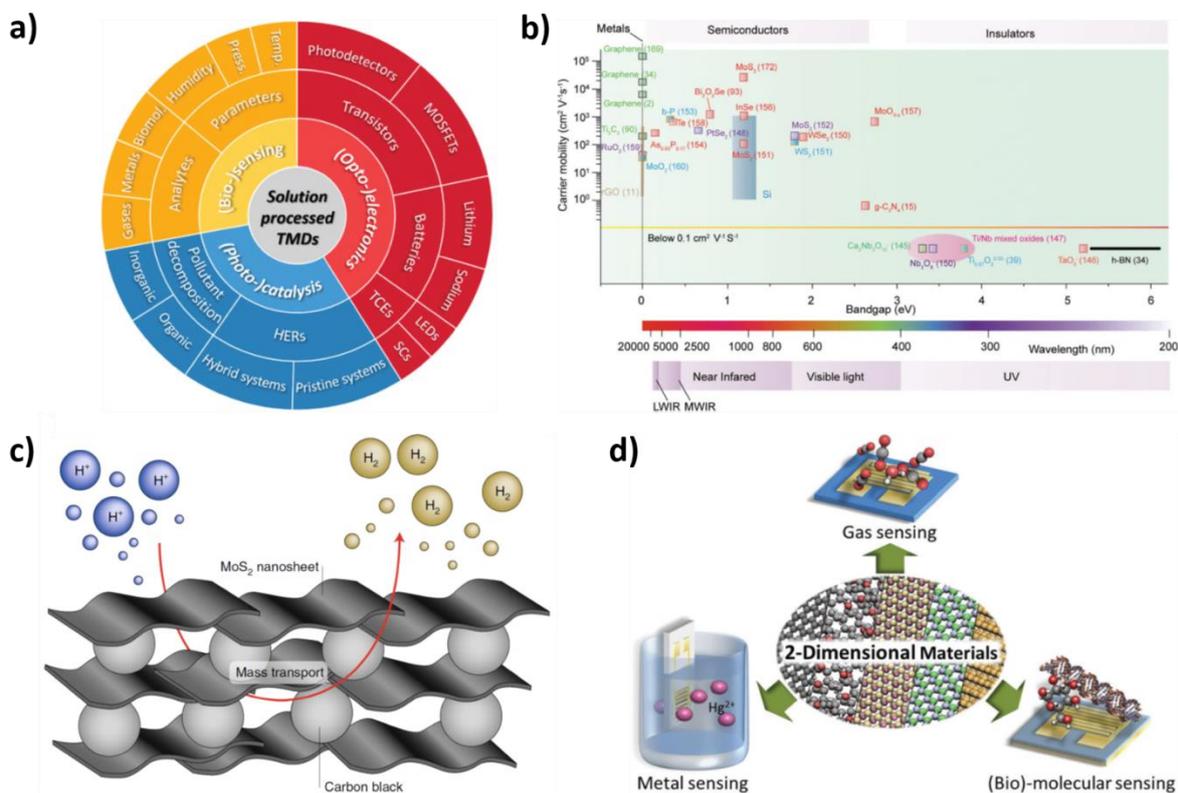
Figure 1-6 : a) Schematic illustration of the main applications envisaged for solution-processed TMDs, both in pristine and functionalized forms. Reproduced from Ref.[25]. **b)** Summary of the band-gaps and carrier mobilities of typical 2DMs, including metals, semiconductors, and insulators. Reproduced from Ref.[30]. **c)** Sketch of engineered channels in MoS_2 for HERs. Adapted from Ref.[33]. **d)** Representation of the different molecular chemical sensors based on 2DMs. Reproduced from Ref.[34].

Owing to such inherent characteristics, combined with a broad spectrum of optical/electronic properties and tunable band structures, 2D systems turn out to be optimal candidates for relevant sensing applications as well, ranging from detection of gases and metals (*e.g.*, alkali and heavy metals), to biologically relevant molecules (*e.g.*, glucose, DNA)[34]. Ultimately, the interaction between 2D structures and molecules/ions leads to detectable variations in the properties of one or both components, as a result of various mechanisms[35].

The objectives of this doctoral research target the development of new functionalization strategies *via* defect-engineering approaches, in order to produce hybrid materials based on solution-processed TMDs. The resulting 2D systems, endowed with enhanced and/or new properties, will be tested for electronic, sensing and electrocatalytic applications. In particular, this thesis work includes two main projects, whose main results and findings are thoroughly discussed afterwards. The overall manuscript is arranged as follows.

1.2. — *Outline of the thesis*

This thesis focuses on two main projects, which are correlated with the set of objectives indicated in the previous section of such an introductory chapter. Its overall organization is reported in the following bullet point.

► <u>Chapter 2</u> provides the reader with a literature review on the physicochemical properties of TMDs, as well as general overview on the SoA methods for their production. In this regard, focus is laid on the primary bottom-up and top-down approaches, highlighting their characteristic advantages and disadvantages.

► <u>Chapter 3</u> focuses on the inherent defectiveness of solution-processed TMDs, pointing out its crucial role in following chemical strategies *via* molecular approaches. In particular, the landscape of defects in 2DMs will be discussed all around, highlighting the unique features and related opportunities offered by SoA functionalization strategies.

► <u>Chapter 4</u> introduces the reader to the experimental part and core of this thesis. It offers a comprehensive report on the main characterization techniques, materials and chemicals employed in the two projects presented afterwards. More specifically, the production steps of solution-processed TMDs will be listed, as well as molecules and precursors used during the successive functionalization procedures. Finally, for the sake of completeness, a brief description of the principal characterization methods will be provided as well.

► <u>Chapter 5</u> discusses one of the two main works of this doctoral research. It deals with the production of covalently interconnected MS_2 networks *via* defect engineering approach, where dithiolated molecules are exploited to simultaneously heal V_S and bridge adjacent flakes. The networks will be tested for electronic applications, by fabricating electronic devices whose performance and properties will be compared with those of pristine films.

► <u>Chapter 6</u> presents the second major project of this doctoral work. It concerns the production of multifunctional hybrid materials based on solution-processed MS_2 and noble metal NPs. The selective edge-decoration of TMD flakes with NPs, driven by the presence of V_S, guarantees enhanced performance in sensing and electrocatalytic applications.

► <u>Chapter 7</u> summarizes the main findings of this doctoral research. Moreover, it discusses challenges and opportunities ahead in 2DM science in light of the results reported in Chapter 5 and Chapter 6, emphasizing the potential of this work as a general guideline for further investigations about defect engineering strategies in solution-processed TMDs.

Chapter 2 — TMDs: A brief overview of their physicochemical properties and production methods

2.1. — *Structure-property relationship in TMDs*

The lamellar structure of TMDs, commonly indicated with the formula MX_2, consists of an atomic layer of transition metals (M = Mo, W, Nb, Re, Sn, Pt, etc.) sandwiched between two atomic layers of chalcogens (X = S, Se, Te). Research endeavors in isolating atomically thin systems, starting from bulk systems, have revealed more than 40 possible and different layered structures (Figure 2-1)[36]. More specifically, group 4-7 TMDs are predominantly layered structures, unlike some of groups 8-10 which are non-layered. The atoms within individual nanosheets (typically 6-7 Å thick) are held together *via* strong M-X covalent bonds, whereas adjacent nanosheets interact through weak vdW forces, in the range of 10 and 10^{-2} eV per atom, respectively[37].

Among all TMDs, the most known one is certainly MoS_2, commonly used as dry lubricant in racing car engines and ultrahigh-vacuum technology[38]. It is interesting to notice that the ancient Greeks could not distinguish two different minerals and employed the same world, *μόλυβδος* (*molybdos,* meaning lead-like), to refer to, for instance, lead, graphite and MoS_2. Nowadays, we know that, despite some common structural features, the different nature of C and Mo-S chemistry gives rise to dramatic differences in the physicochemical properties.
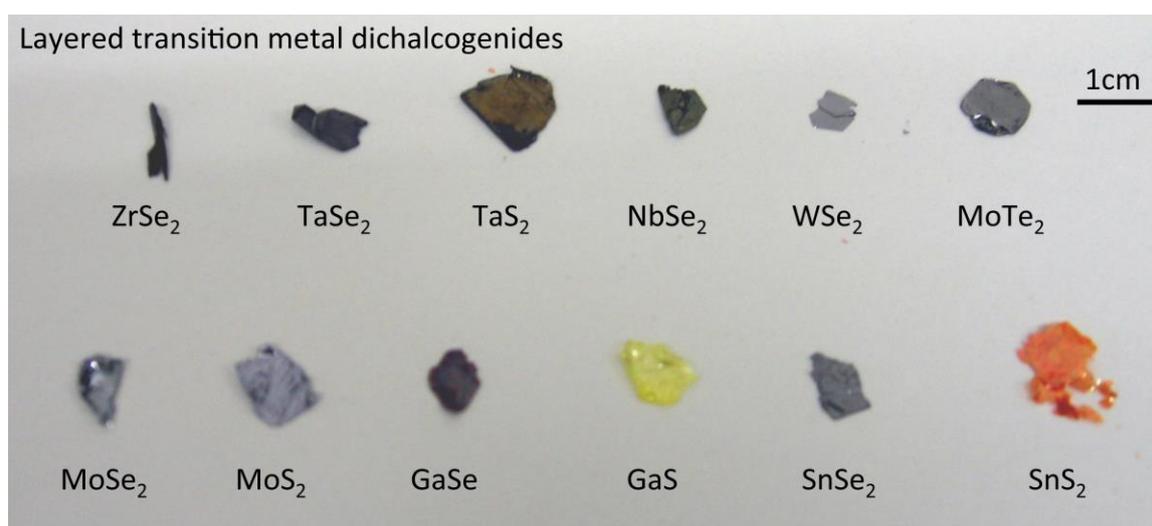

Figure 2-1 : Photograph displaying the different aspect of bulk crystals for some TMDs. Usually, such systems are employed during the exfoliation procedures performed by micromechanical cleavage using adhesive tape, also known as Scotch-tape approach. Reproduced from the following website: *van-der-waals-epitaxy.info.*

According to the mutual coordination geometry between M and X atoms within individual nanosheets, TMDs might exhibit multiple crystal lattices and undergo phase transition among these polymorphs *via* external stimuli[39,40]. In particular, TMDs show a polymorphism involving three different crystal lattices (Figure 2-2): hexagonal, generally indicated as 1H for a single layer and 2H for multilayers (trigonal prismatic coordination for the metal centre, *D3h*), tetragonal 1T (octahedral coordination for the metal centre, *Oₕ*), and rhombohedral 3R (trigonal prismatic coordination for the metal centre, *D3h*). It is worth mentioning that the numerical digits in 1T, 2H, and 3R indicate the number of layers in the stacking sequence, whereas the letters refer to the kind of crystal lattice. Besides general considerations about the structure of TMDs, they possess extremely versatile properties related to their electronic structure, strongly affected by the constituent transition metal and chalcogen atoms[41].

Moreover, the electronic properties of TMDs are heavily influenced by the progressive filling of the non-bonding *d* bands from group 4 to group 10, located within the gap between the bonding and anti-bonding bands of M-X bonds[41]. In cases where the orbitals are partially filled, *e.g.*, $2H-NbSe_2$ and $1T-ReS_2$, TMDs exhibit metallic conductivity, whereas when they are fully occupied, *e.g.*, $2H-MoS_2$ and $1T-PtS_2$, the materials possess semiconducting properties. Remarkably, even though the transition metal atoms have a major effect on the electronic properties, the band-gap between the valence and conduction band decreases when the atomic number of the chalcogen atoms increases. For instance, the band-gap of bulk $2H-MoS_2$, $2H-MoSe_2$, and $2H-MoTe_2$ gradually decreases from 1.2 eV up to 1.0 eV[42].

a) Stacking sequence (side view)
2H polymorph *1T polymorph* *3R polymorph*

b) Metal coordination geometry (top view)
Trigonal prismatic — Chalcogen atom — *2H and 3R polymorphs*
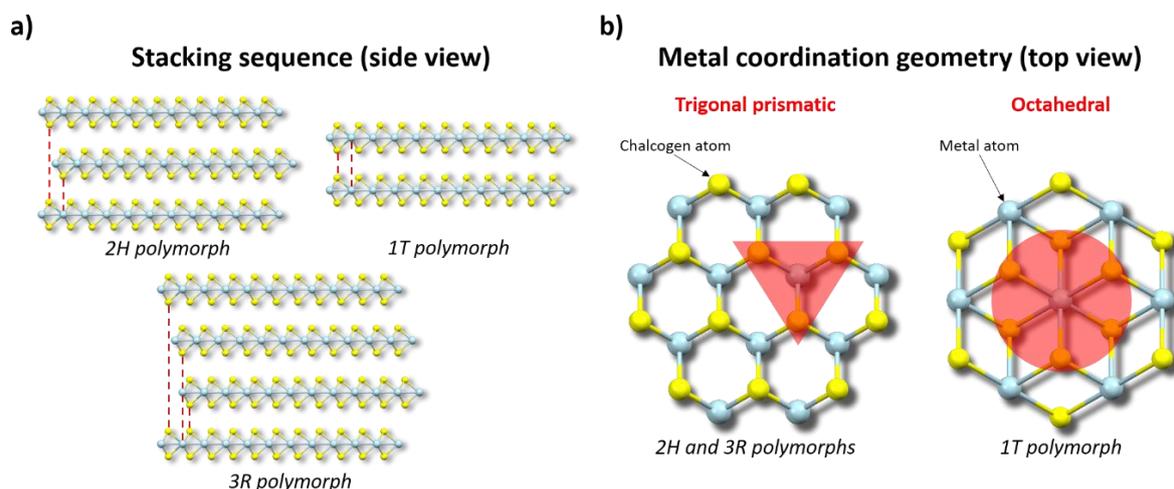Octahedral — Metal atom — *1T polymorph*

Figure 2-2 : Illustration of the different polymorph structures for TMDs. **a)** Depiction, in side view, of the three possible TMD polymorphs obtained *via* different stacking sequence of individual layers. **b)** Representation, in top view, of the metal coordination geometry for the three possible TMD polymorphs. Atom color legend: light blue, transition metal atom; yellow, chalcogen atom. Reproduced from Ref.[25].
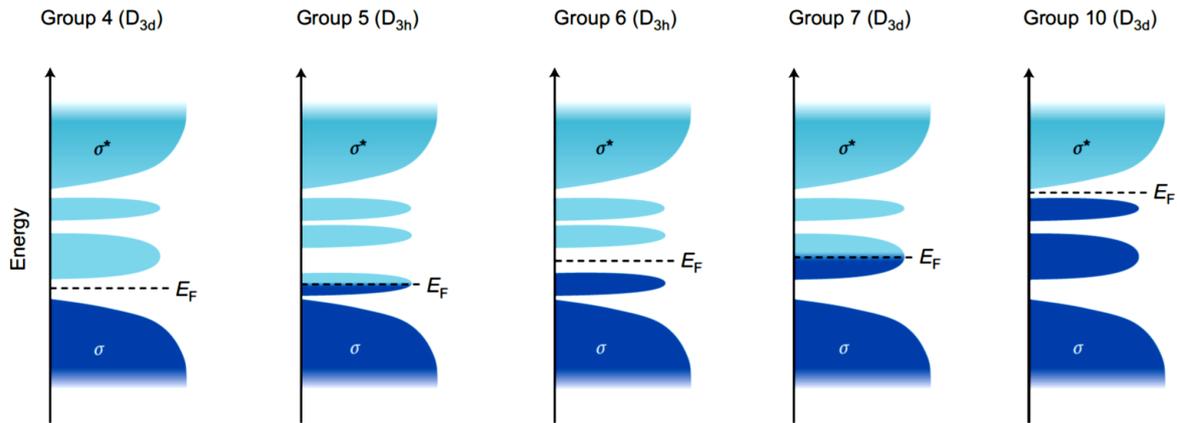
Figure 2-3 : Schematic illustration showing the progressive filling of the d bands located between the bonding (σ) and anti-bonding (σ*) states in group 4, 5, 7, and 10 TMDs. D_{3h} and D_{3d} indicate the point groups matching the 1H and 1T polymorphs, respectively. Reproduced from Ref.[41].

A prominent example of structure-property relationship in TMDs concerns the stability of the different polymorphs as a function of the d-electron count (Figure 2-3) in transition metal atoms. In this regard, group 4 TMDs exhibit an octahedral structure, whereas in group 5 and 6 both the octahedral and trigonal prismatic structures are observed. Group 6 TMDs are primarily found in trigonal prismatic geometry, while group 7 are usually found in a distorted octahedral structure, unlike group 10 where they all show octahedral structure[41].

Group	M	X	Properties
4	Ti, Hf, Zr	S, Se, Te	Semiconducting (E_g = 0.2-2 eV). Diamagnetic.
5	V, Nb, Ta	S, Se, Te	Narrow band metals or semimetals. Superconductive. Paramagnetic, antiferromagnetic, or diamagnetic.
6	Mo, W	S, Se, Te	Sulfides and selenides are semiconducting ($E_g \approx 1$ eV). Tellurides are semimetallic. Diamagnetic.
7	Tc, Re	S, Se, Te	Small-gap semiconductors. Diamagnetic.
10	Pd, Pt	S, Se, Te	Sulfides and selenides are semiconducting (E_g = 0.4 eV) and diamagnetic. Tellurides are metallic and paramagnetic. $PdTe_2$ is superconducting.

M = Transition metals; X = Chalcogens; E_g = Energy band-gap.

Table 2-1 : Electronic and magnetic properties of different layered TMDs. Adapted from Ref.[41].

The ever-growing success of TMDs is particularly related to their thickness-dependent properties[43], mainly due to changes in the band structure caused by quantum confinement effects and resulting variations in the orbital composition of the electronic states[44]. In this regard, detailed analysis on MoS_2 revealed that the electronic states of the highest valence band (VB) and lowest conduction band (CB) at the *K* point of the Brillouin zone are composed nearly exclusively by localized *d* orbitals confined within the S-Mo-S layer[45]. Such orbitals are insensitive to the number of layers, supporting the data for which the direct gap at the *K* point is not influenced by the material thickness. However, the electronic states of the highest-VB at the Γ point have anti-bonding nature and consist of Mo d^2_z and $S_{p,z}$ orbitals. The energy of the latter diminishes with the decreasing interlayer interaction, which explains the increase of the indirect band-gap upon reduction of the number of layers (Figure 2-4)[46].
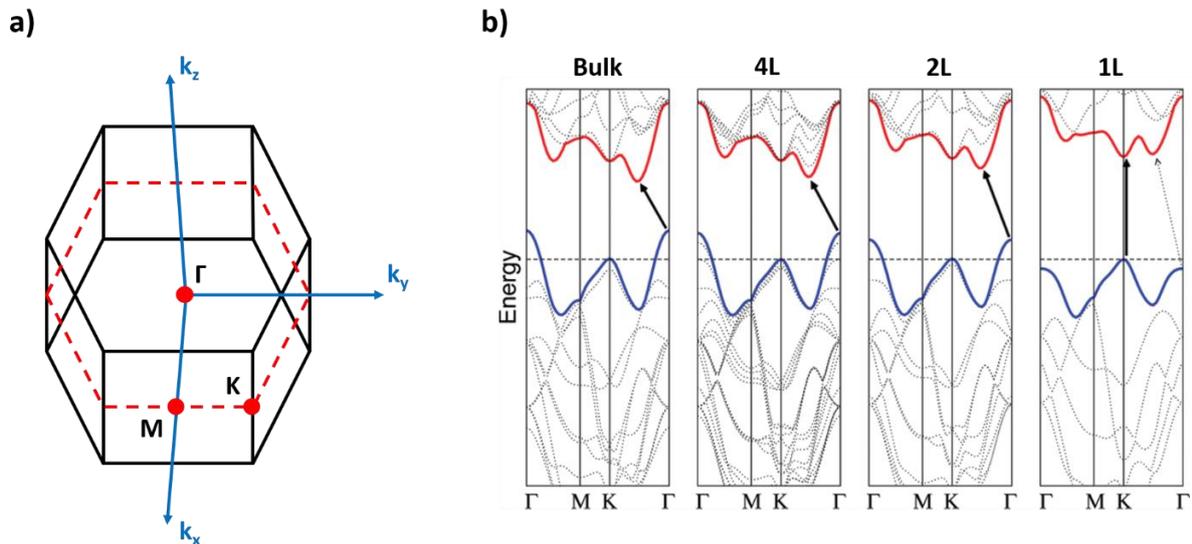
a)

b)

Figure 2-4 : a) Brillouin zone of MoS_2 highlighting the high-symmetry points in the hexagonal lattice. In particular, Γ represents the centre of the Brillouin zone; M describes the centre of a rectangular face; K represents the middle of an edge joining two rectangular faces. **b)** Evolution of the band structure of MoS_2 with decreasing thickness. From left to right: bulk crystal, four-layer (4L), bilayer (2L), and monolayer (1L). Reproduced from Ref.[43].

Besides the thickness-dependent evolution of the band structure, the optical properties of MoS_2 are also strongly influenced by the material thickness (Figure 2-5). The absorption spectra of MoS_2 show two distinctive peaks, usually referred to as A (~1.88 eV) and B (~2.06 eV) peaks[44]. They originate from the direct inter-band transitions occurring at the *K* point of the first Brillouin zone, between the double-splitted VB and the two-time degenerate CB. In particular, the spin-orbit-induced splitting of the VB at the *K* point is 0.15-0.20 eV, which reflects the average distance of 60 nm found in the MoS_2 UV-Vis spectra between A and B peaks[47].

Moreover, for bulk MoS_2 the photoluminescence (PL) signal is negligible, whereas the maximal emission is achieved for monolayer systems, where the material changes from an indirect band-gap (~1.20 eV) to a direct band-gap (~1.80 eV). In fact, the direct electronic transition allowed in monolayer MoS_2 are characterized by higher radiative recombination rate compared to indirect transitions occurring in the bulk and few-layer systems[43]. Similarly to UV-Vis, the PL spectra show two main peaks ascribed to the direct exciton transitions, *i.e.* A (~670 nm) and B (~627 nm), whose energy difference ΔE_{AB} can be related to the spin-orbit-induced splitting of the VB at the *K* point[43]. In addition, Raman spectroscopy revealed a total of four active modes for MoS_2, among which the two most investigated are E^1_{2g} and A_{1g} modes corresponding to in-plane and out-of-plane vibrations, respectively. For bulk systems, they are expected to have higher frequencies than the corresponding modes in mono or few-layer MoS_2 samples, owing to the presence of higher interlayer interactions. However, such an expectation is only confirmed for the A_{1g} mode, whereas E^1_{2g} does not agree with the previous prediction: A_{1g} mode red-shifts as the thickness is reduced from bulk to monolayer, while E^1_{2g} mode blue-shifts. In this regard, researchers revealed that the constant forces of each individual mode are determined by a complex interplay of interlayer vdW and Coulomb interactions[48]. Finally, one of the main Raman findings concerns the relationship between the difference in frequency of A_{1g}/E^1_{2g} modes and the number of layers in thin MoS_2 nanosheets.
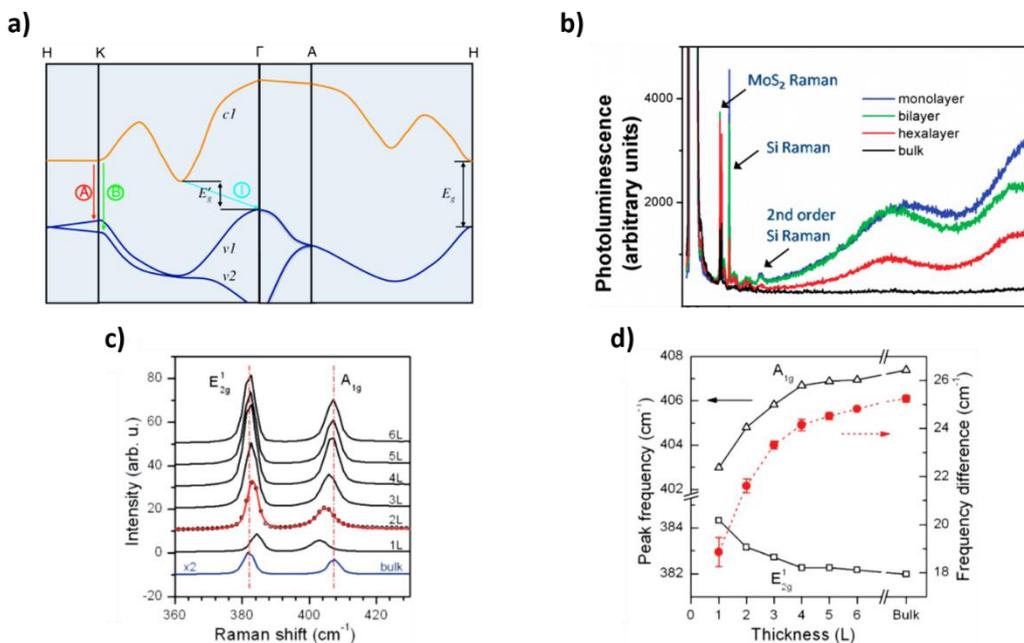

Figure 2-5 : a) Simplified band structure of bulk MoS_2. Adapted from Ref.[44]. **b)** PL and Raman spectra of MoS_2 monolayer, bilayer, hexalayer, and bulk sample. Adapted from Ref.[43]. **c)** Raman spectra of thin (nL) and bulk MoS_2 films. **d)** Frequencies of E^1_{2g} and A_{1g} Raman modes (left vertical axis) and their difference (right vertical axis) as a function of layer thickness. Adapted from Ref.[48].

2.2. — *Production methods of TMDs*

As already mentioned in Chapter 1, the successful application of 2DMs is strictly related to the quality and yield of the production methods. To date, micromechanical cleavage remains the most straightforward source of high-quality 2DMs, although it suffers from low yields and production rates that are not technologically scalable at an industrial level. In the last decade, fast-moving research has been carried out to develop novel techniques for the large-scale production of 2D crystals, where each step contributes to affect the ultimate properties of the nanomaterials as well as cost, scalability and yield of the whole process.

For the sake of clarity, the production methods can be classified as top-down and bottom-up approaches: in the former, the nanomaterials are extracted (exfoliated) from the bulk systems under specific conditions; in the latter, the atomically thin crystals are synthesized starting from suitable precursors and by connecting atoms to each other, leading to systems with high chemical homogeneity and good short- and long-range ordering. The aim of this section is to provide the reader with a brief description of the main production methods for TMDs, highlighting their inherent features and challenges.

Bottom-up: Chemical Vapor Deposition (CVD). This method is a promising approach due to the high scalability and compatibility with existing technologies. Single layer TMD nanosheets or continuous films can be obtained with lateral size ranging from few atomic units to several centimetres, according to the reaction conditions adopted during the process[49,50]. Two possible protocols can be exploited taking advantage of different physicochemical phenomena, namely physical vapor deposition (PVD) and CVD. In PVD, TMDs bulk precursors (in powder form) sublimate within a furnace by heating (800-950°C) under reduced pressure (<100 Torr), volatilizing a proper amount of material that is later deposited onto the substrate (located in the colder side of the reaction chamber) with the help of a carrier gas, usually argon or hydrogen. This method has intensely been adopted to produce mainly group 6 TMDs, such as MoS_2, WSe_2 or alloys[51,52]. In CVD, the production process is based on the volatilization and thermolysis of precursors containing the required TMD elements (Figure 2-6). The metal and chalcogen active species, produced in gaseous phase, react to form the desired TMD monomer structure, leading to the following steps of precipitation onto the substrate, nucleation and growth under the experimental conditions imposed by the user[53]. To glimpse the growth mechanism, Cao *et al.* found that the rate limiting step, in such a kind of gas-phase reactions, is represented by the precipitation of TMD monomers onto the substrate[54]. This phenomenon is strongly influenced by the partial pressure of the $TMDs_{(gas)}$ and the vapor pressure of the growing $TMD_{(s)}$ nanosheets; therefore, according to thermodynamics, in order to promote the growth, the partial pressure of the gas must exceed the vapor pressure of the nanostructures.

The latter parameter also influences the thickness of the growing TMD structure, thereby resulting a crucial feature to monitor during the overall production process. Usually, elemental sulfur is heated up inside the reaction chamber and its vapors react with gaseous metal oxide, such as MoO_3 and WO_3, characterized by high volatility and thermal stability[55].

Nevertheless, CVD technology presents some key challenges in growing high-quality wafer-scale films: (i) it is arduous to grow a continuous film with large grains. In fact, small grains necessarily imply a high density of grain boundaries, promoting the charge carrier scattering and, therefore, degrading the electronic properties of the films. (ii) The transfer of 2D films from growth substrates to target ones is usually tedious and difficult to scale up. (iii) The full understanding of the complex thermodynamic and kinetic aspects of the reaction, along with the strict growth condition requirements, still limit the scalable production of large-area 2DMs.
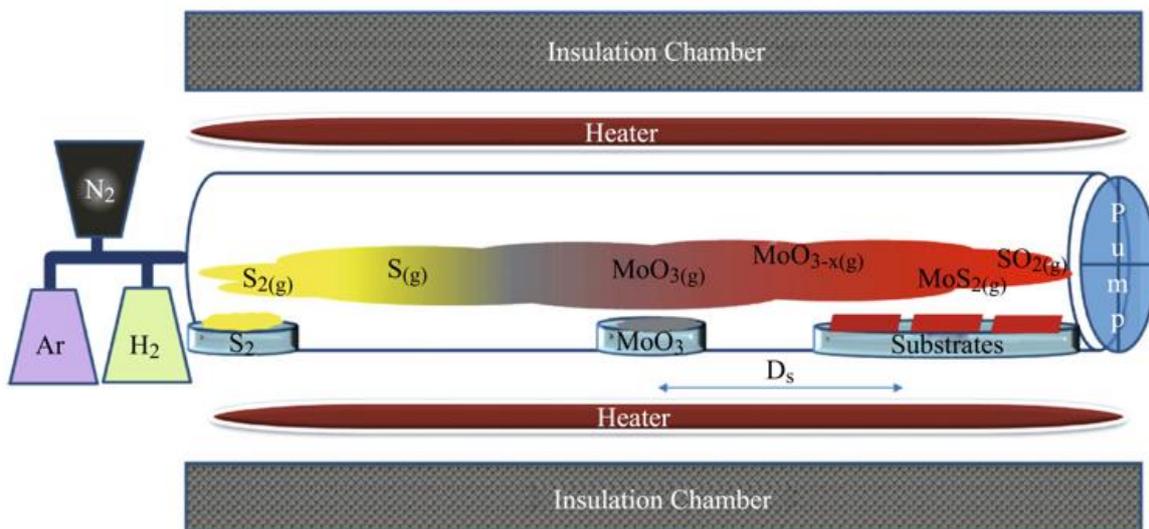

Figure 2-6 : Sketch of a CVD reactor for the production of MoS_2 nanosheets. Reproduced from Ref.[55].

Bottom-up: Chalcogenization. Another gas-phase synthesis method involves the direct sulfurization or selenization of metal containing films. The transition metal precursor is a metal or metal oxide deposited onto a certain substrate, removing the need to transport one of the two necessary agents. Then, sulfur or selenium vapors are injected inside the reaction chamber and the growth takes place onto the metallic slab. For instance, in the report by Zhan *et al.*, Mo film was deposited on a SiO_2/Si wafer and followed by thermal annealing in sulfur vapors to produce MoS_2 films[56]. However, the obtained MoS_2 presented a metallic transport property with a low current ratio, most likely due to the presence of unreacted metal impurities. Therefore, an alternative effort has been devoted to produce wafer-scale semiconducting MoS_2 thin layers, where the direct sulfurization approach is adapted by replacing the Mo metal with a MoO_3 thin layer[57]. The obtained 2D material exhibited high current ratio, rather than the

resistor-like behavior reported beforehand. Moreover, such an approach was also adopted to prepare scalable and edge-density controllable PtSe$_2$ films for HER applications, highlighting a linear relationship between edge density and catalytic activity[58]. The active materials were produced by direct selenization of Pt films deposited *via* magnetron sputtering method, using argon carrier gas to transport the chalcogen vapors (Figure 2-7).
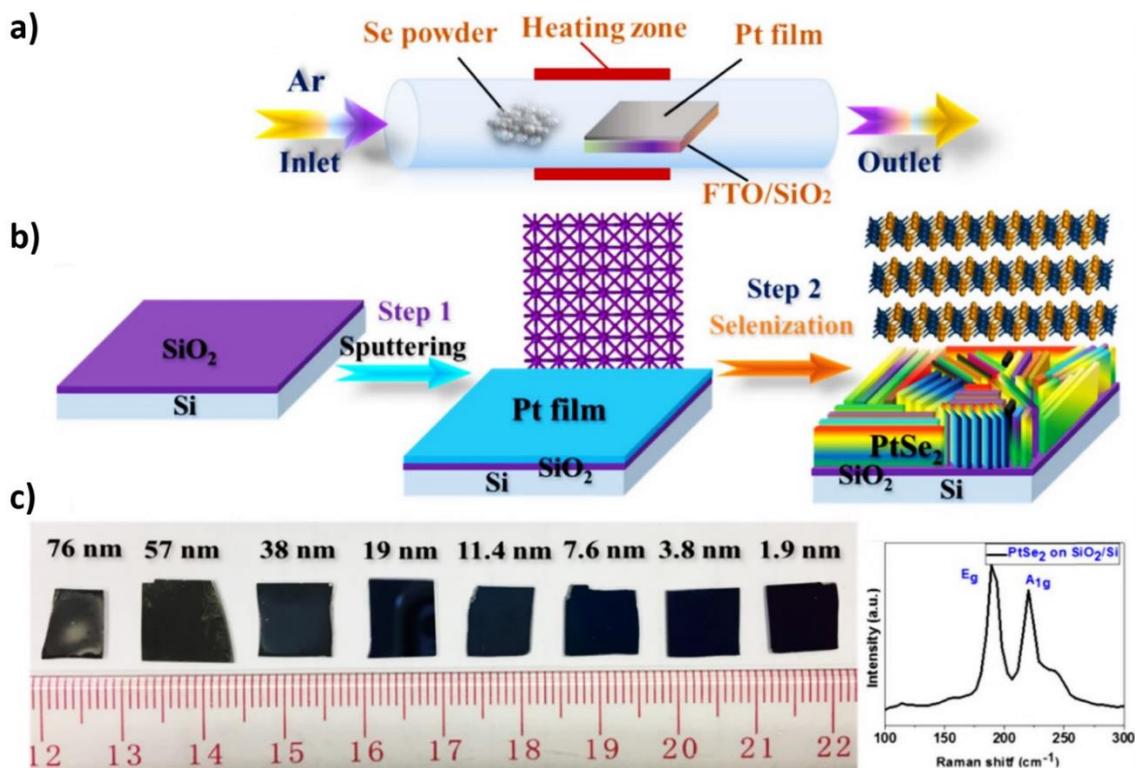

Figure 2-7 : a) Illustration of the growth process for PtSe$_2$. **b)** Two-step growth method of PtSe$_2$ film. Step 1: deposition of Pt film on SiO$_2$/Si substrate by magnetron sputtering. Step 2: selenization of the Pt film into PtSe$_2$. **c)** As-prepared PtSe$_2$ films with various thickness (left) and typical Raman spectrum of PtSe$_2$ film on SiO$_2$/Si (right). Adapted from Ref.[58].

Although it is still at its infant stage, this approach paves the way for the large-scale production of TMD films for electronic and optoelectronic applications. However, the method has several limitations and, for instance, it is hard to precisely control the thickness of the pre-deposited metal oxide or metal thin layer, limiting the wafer-scale uniformity. To tackle this issue, recent attempts have been devoted to improve the synthetic process by depositing the metal oxide layer *via* atomic layer deposition[59], taking advantage of its inherent features such as thickness controllability, high uniformity and conformality. Nevertheless, most of the metal precursors are not readily and widely available, as well as the growth could be limited to certain substrates and the strict operating conditions could hinder the scalability of the overall method.

Bottom-up: Liquid-phase synthesis. Such a method relies on the thermal decomposition and reaction of a precursor solution mixture. In liquid environment, the coordinating ligands mainly play a fundamental role in promoting the growth of TMD nanostructures within the xy plane, affecting their final properties and performance of related devices[60,61]. Temperature is a crucial parameter to monitor during the synthesis, as the thermodynamic and kinetic aspects of the reaction influence the yield and quality of the overall process. In this regard, the use of a proper solvent is mandatory to reach the prefixed thermal conditions and to form stable colloidal dispersions once the TMD structures are formed. Nevertheless, the presence of solvent molecules and additional capping agents (also used as stabilizing agents) complicates the following recovery and purification steps of the formed nanostructures.

Within this class, we can include solvothermal and hot-injection synthetic approaches. Nowadays, hydro/solvothermal synthesis represents a valuable bottom-up approach to produce TMDs, starting from specific precursors and taking advantage of sealed autoclaves operating at high temperature ($10-10^2$ °C) and controlled pressure (1-10 Pa)[62,63]. The main advantages of this strategy lie with the superior aptitude of materials in being induced to solubility *via* suitable temperature and pressure conditions, along with the more accurate control of the operating parameters, which might influence the quality and crystal structure of the final systems[64]. Nevertheless, such an approach exhibits some drawbacks related to the need of expensive autoclaves able to withstand the operating conditions, and the lack of a real-time monitoring of the crystal growth ("black box").

Hot-injection synthesis (also known as colloidal synthesis) represents an additional valuable bottom-up methods to produce TMDs. The choices concerning the precursors, the potential coordinating ligands (to ensure stability and control over the size and shape) and the solvent (which provides a homogenous reaction medium and might act as capping ligand as well)[65] are crucial. In most cases, the method involves the use of a chalcogen precursor solution rapidly injected into a hot mixture (150-300 °C) of metal precursors and capping agents, where an accurate control over the structural features of the growing materials can be achieved by adjusting the operating conditions and chemical species involved in the process. For instance, the lateral size of TMD nanosheets can be tuned by changing the reaction time while keeping the thickness constant[66] (Figure 2-8). In the same way, the final thickness of TMD nanostructures can be adjusted by either changing the precursors concentration[67], or by changing the functional groups of the capping ligands, to exploit the different binding affinities with the TMD nanosheet edges[68]. Ultimately, the colloidal synthesis represents an intriguing and versatile class of reactions towards the bottom-up production of TMDs. However, this method possesses some major drawbacks related to the use of expensive, hazardous and toxic precursors and solvents (*e.g.*, organometallic and phosphine-based compounds) that hinder the large-scale synthesis.
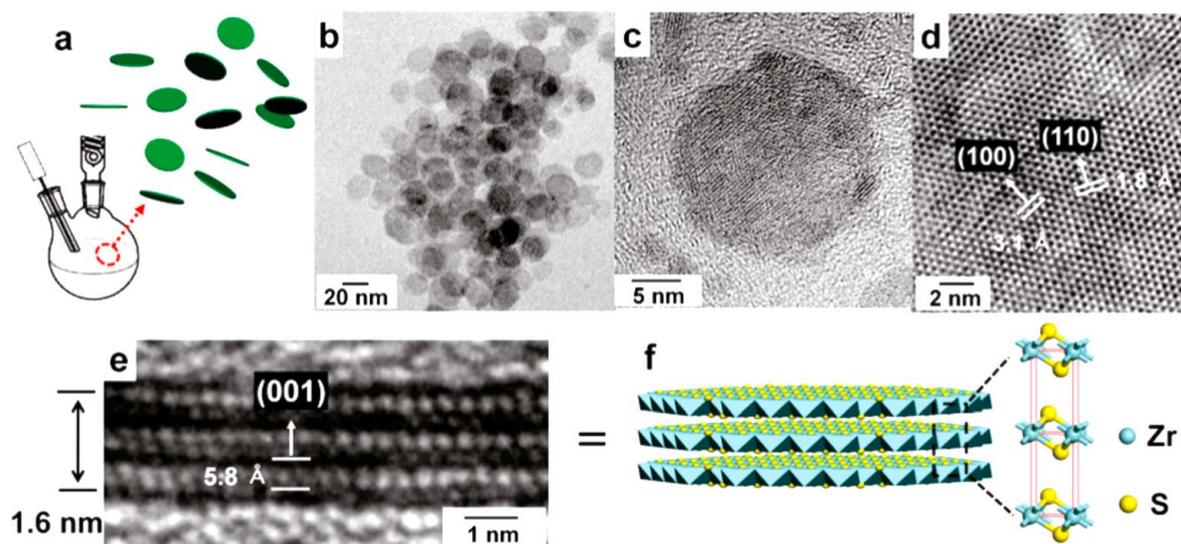
Figure 2-8 : a) Sketch of the colloidal synthesis for ZrS_2 nanodiscs dispersed in solution. **b)** Low- and **c)** high-magnification TEM images of ZrS_2 nanodiscs. **d)** HRTEM image of a nanodisc showing (100) and (110) lattice fringes. **e)** HRTEM side-view image of a nanodisc, revealing a disc thickness of 1.6 nm and 5.8 Å (001) lattice fringes. **f)** Ball-and-stick model showing a single ZrS_2 nanodisc (Zr, sky-blue; S, yellow). Reproduced from Ref.[66].

Top-down: Micromechanical cleavage. The first pioneering work using micromechanical cleavage to thin layered structures was reported by Frindt in 1966[69], where MoS_2 nanoflakes less than 10 nm thick were isolated. Geim and Novoselov improved such an approach after they succeeded in obtaining graphene from bulk graphite in 2004[1], boosting the number of related papers published afterwards for additional 2DMs. This method relies on the adhesion of crystal planes between two pieces of an adhesive tape, before peeling the tape apart to cleave the crystal. The adhesion force between the tape and the material overcomes the weak interlayer vdW interactions, thereby obtaining single- and few-layer nanosheets when the procedure is repeated more than once. Moreover, this approach allows an easy transfer of the nanosheets onto a substrate just by pushing the tape into a solid surface. Nowadays, many micromechanical techniques have been developed by taking inspiration from "Scotch tape" method, using, for instance, a three-roll mill machine with a polymeric adhesive[70] (Figure 2-9). In particular, polyvinyl chloride dissolved in dioctyl phthalate is used as adhesive, which plays a similar role to the usual tape employed in the original micromechanical cleavage. The moving rolls can drive the bulk layered crystals to run along an inverted S curve from the feed roll to the apron roll, leading to continuous exfoliation steps.

To date, this method remains the prime source of high-quality 2DMs, although it suffers from relatively low efficiency and small yields. In addition, the results of the exfoliation procedure are strongly dependent on the technical experience of the user.
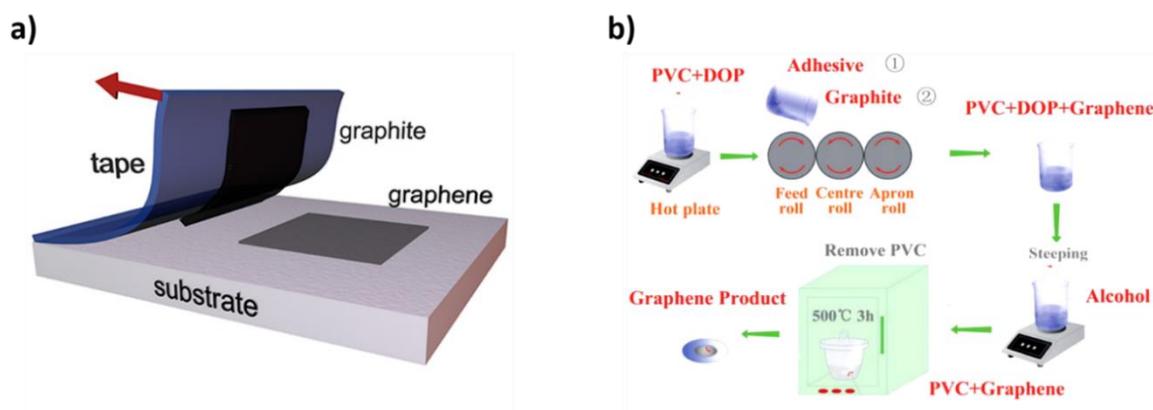

Figure 2-9 : a) Cartoon illustrating the mechanical exfoliation process of graphite to obtain graphene. **b)** Schematic illustration of the approach used to exfoliate natural graphite by three-roll mill. Reproduced from Ref.[70].

Top-down: Electrochemical exfoliation (ECE). An extremely promising and efficient top-down approach to exfoliated bulk TMD crystals takes advantage of the intercalation process of chemical species within the layers, leading to an expansion of the structure and a weakening of the interlayer vdW interactions. Lithium-ion intercalation in TMDs has been studied since the 80s[71,72], and the original method is still widely adopted to produce atomically thin structures. It involves the formation of an intercalated intermediate [Li_xMoS_2] by soaking bulk TMD powder in a solution of n-butyllithium for 2-3 days, under inert atmosphere (usually, argon or nitrogen) and increased temperature (ca. 80°C). Then, the intercalated material is transferred into an aqueous or low-boiling point solvent solution and exposed to ultrasound waves to complete the exfoliation procedure. This step also stimulates the reaction between lithium ions and water to form gaseous hydrogen, promoting the separation of thin nanosheets. However, such an approach presents considerable hazards related to the use of n-butyllithium and, therefore, safer approaches have been developed in the last few years.

In particular, the electrochemically-assisted process guarantees a fine control over the lithium intercalation within the bulk TMD crystals (Figure 2-10)[73]. A possible lithium source is represented by lithium foils, usually employed as the anode of the electrolytic cell, along with the TMD crystal acting as cathode (cathodic exfoliation). It is worth mentioning that lithium-ion intercalation is not a simple mechanical process involving the expansion of the bulk crystals; in fact, an electron transfer takes place from the metal ion to the lowest lying unoccupied energy level of the crystal, affecting the final structural and physicochemical properties of the

material[74,75]. Overall, such an approach exhibits many advantages such as more favorable operating conditions, shorter production time and safer chemicals. Ultimately, ECE is a promising tool to produce thin TMDs, despite poor compatibility with current technology for an upscaled production at industrial level.
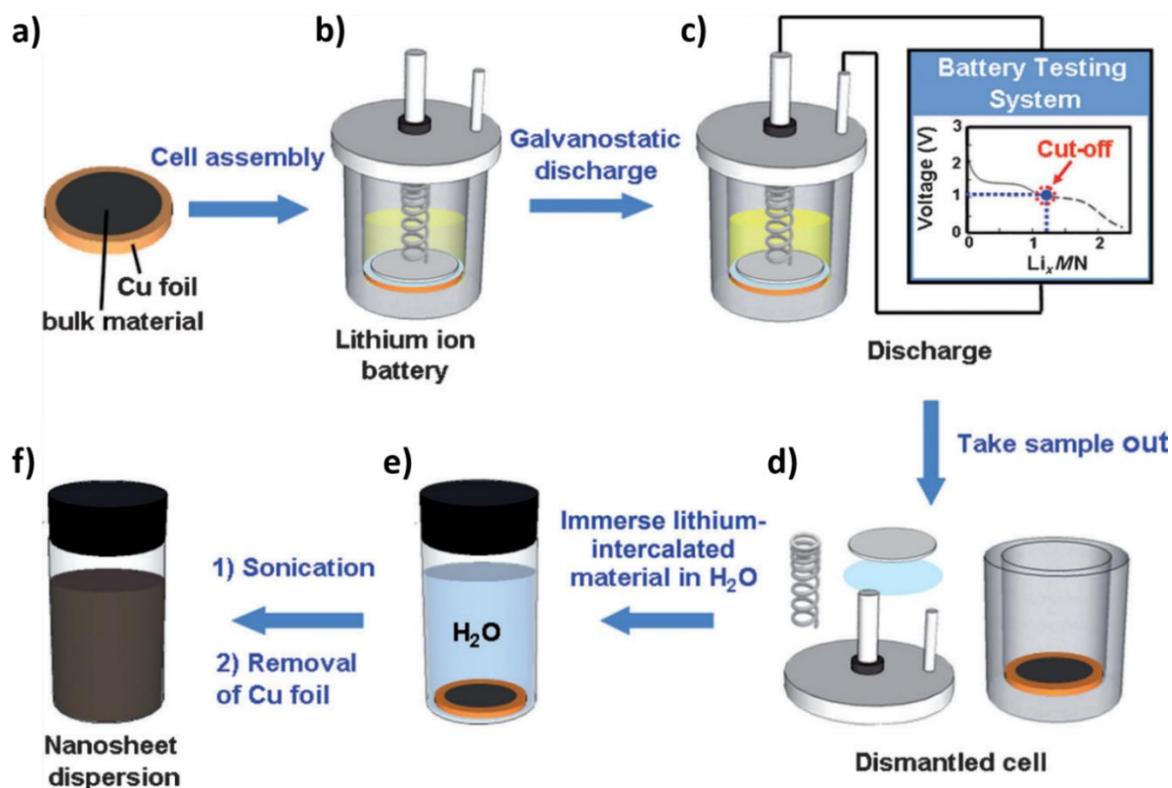

Figure 2-10 : a-f) Illustration of the electrochemical lithium intercalation and exfoliation process to produce 2D nanosheets from layered bulk materials (MN = h-BN, metal selenides, or tellurides in Li$_x$MN). Adapted from Ref.[73].

Top-down: Liquid-phase exfoliation (LPE). The overwhelming majority of top-down solution-processed TMD systems derive from LPE techniques. In fact, the seminal work published by Coleman and co-workers in 2008, about the first LPE of graphite towards graphene[76], paved the way to this new method for the production and isolation of thin 2DMs, such as TMDs. The process entails the use of a liquid sample containing the bulk TMD crystals and a transfer of energy thereto, in order to overcome the weak interlayer vdW interactions and promote their exfoliation. In this regard, mechanical energy is a suitable option due to several advantages (*e.g.,* low cost, user-friendliness, and versatility) and it can be transferred to the bulk TMD crystals *via* different strategies and forms (Figure 2-11)[77]. More specifically, shear and compression forces arise during the exfoliation steps by means of ball milling and shearing methods, promoting the separation of ultrathin nanocrystals[78,79]. In addition, ultrasonication

approaches can also be employed to guarantee an energetic agitation of the system and energy transfer; in fact, ultrasound waves propagate within the solvent, generating vibration and cavitation forces. The latter lead to the formation and implosion of cavitation bubbles, promoting high local pressure (from kPa to MPa) and temperature conditions (10^2-10^3 °C) required for the exfoliation of 2D nanosheets.
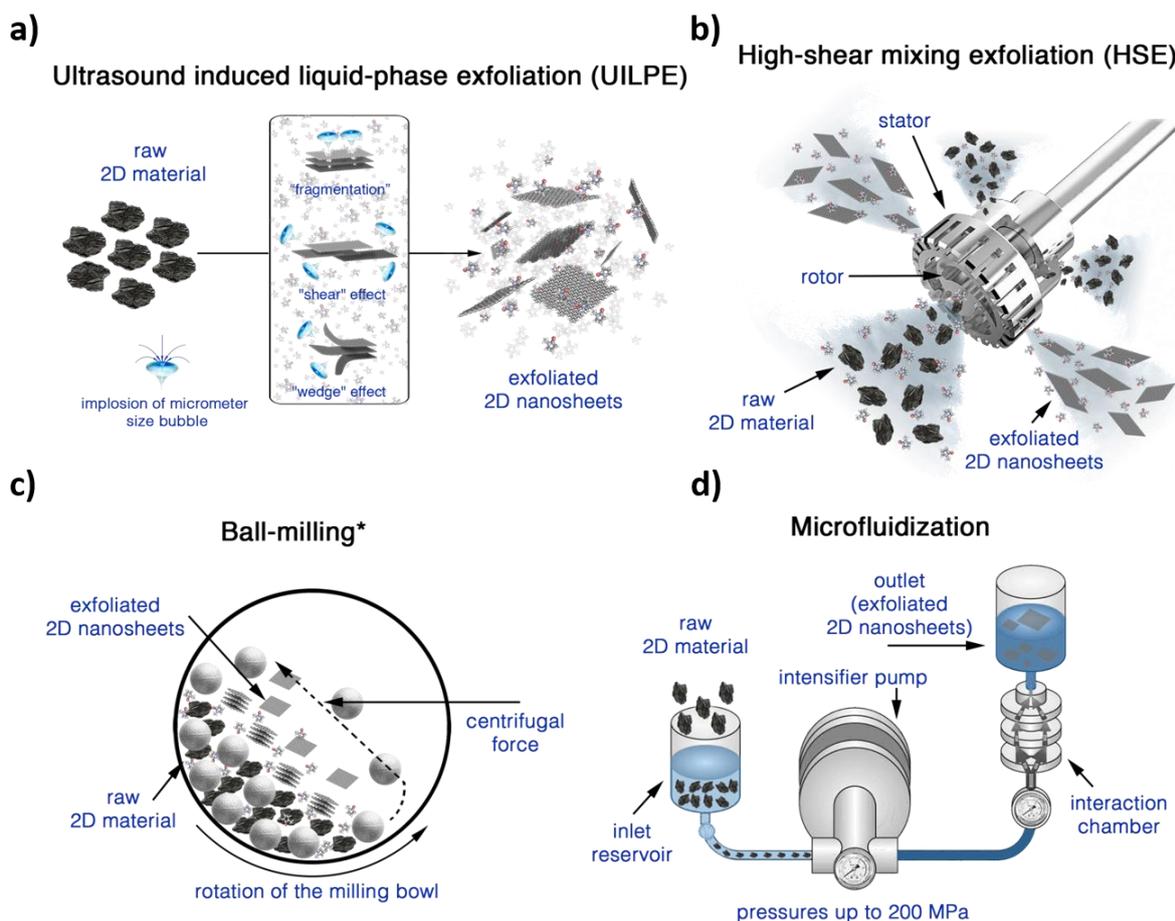

Figure 2-11 : Schematic representation of various LPE-based methods, such as **a)** ultrasound-induced LPE, **b)** high-shear mixing exfoliation, **c)** ball milling, **d)** microfluidization. Adapted from Ref.[77].

Besides mechanistic considerations, several parameters affect the overall quality and efficiency of the procedure, such as power, time and type of sonication (*e.g.*, sonic baths, sonic probes), as well as the exfoliation solvent[80,81]. LPE strategies possess good compatibility with existing technologies to scale-up the production of TMD materials to industrial level, encouraging their application in several research fields. Nevertheless, the as-exfoliated nanosheets display a broad polydispersity in terms of thickness and later size, requiring several size-sorting steps to achieve the desired structural features[82]. In addition to the lack of control over morphological properties, the common use of surfactants to improve the exfoliation and

dispersibility of the nanosheets (by modulating the surface tension of the solvent) complicates the following steps, since it results very difficult to completely get rid of such additives thereby affecting the physicochemical properties of 2DMs, especially the electrical performance[83].

Chapter 3 — Defectiveness as prime enabler of functionalization strategies in solution-processed transition metal dichalcogenides

Crystals are like people,
it is their defects which tend to make them interesting!
Professor Sir Colin Humphreys

Crystal structures are built up by repeated translation of the basic unit cell along the three crystallographic axes. However, as a result of thermal equilibrium and kinetic processing, a crystal with a perfectly regular arrangement of atoms cannot exist; imperfections, irregularities and defects are present to some extent in all crystals. For instance, some crystal's unit cells may have too few atoms, whereas others may have an extra atom or an impurity atom.
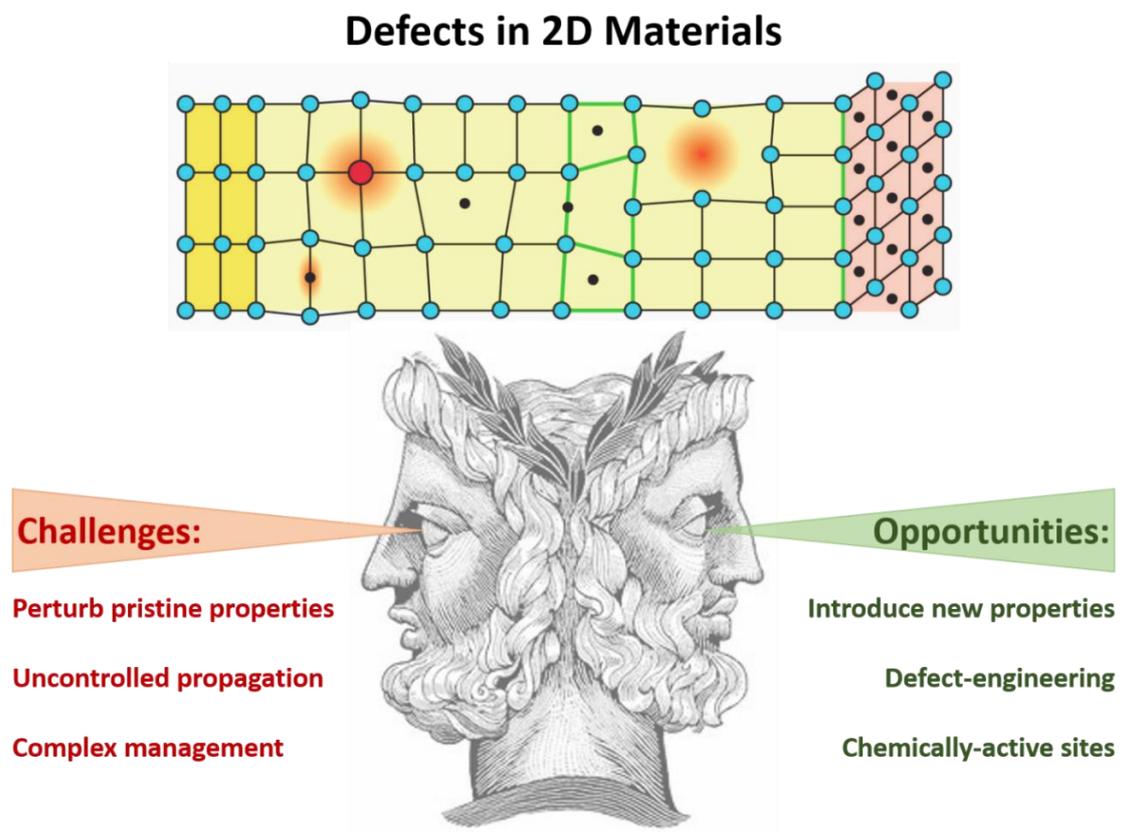

Figure 3-1 : Challenges and opportunities offered by defects in 2DMs. The defective crystal structure reported on top is reproduced from the following website: *mse.ntu.edu.tw*.

Although they are often regarded as detrimental and undesired features, defects might offer one-of-kind opportunities in materials science. Defects, in fact, represent a striking example of Janus Bifrons (Figure 3-1): they perturb the pristine material properties and structure, but they

can also be exploited in order to introduce new functionalities (enhancing the related material properties and performance), as well as being regarded as chemically-(re)active sites suitable for molecular functionalization strategies. The formation and evolution of defects becomes more critical at the nanoscale, as their interaction with interfaces plays a major role in determining the material properties, especially in 2DMs due to high surface-to-volume ratio.

The landscape of defects in solution-processed 2DMs is quite extended and complex, as a great variety of phenomena take place and contribute in affecting their properties. In fact, the exfoliated materials present topological and structural defects both inherited from the source bulk crystals and generated during the exfoliation process[9]. In this regard, the following paragraphs will present and discuss the main defects encountered in TMDs according to their atomic structure and dimensionality.

Zero-dimensional defects. A point defect is an irregularity in the crystal lattice associated with a missing atom (vacancy), an extra atom (interstitial), or an impurity atom. Above 0 K, there is a thermodynamically stable concentration of vacancies and interstitial atoms. In general, the number of defects at equilibrium for a certain temperature can be determined as:

$$N_d = N \, exp \, (\frac{-E_d}{kT})$$

where N_d is the number of defects, N the total number of atomic sites, E_d the activation energy necessary to form the defect, k the Boltzmann constant, and T the absolute temperature. Therefore, vacancy concentration increases as temperature increases; in fact, as thermal energy increases, each atom's probability of jumping out from its lowest-energy position also increases. Atoms occupying lattice positions that are unoccupied in the perfect crystals are called interstitial defects, whose related formation energy is considerably higher than a vacancy's one. Therefore, the equilibrium density of interstitials is several orders of magnitude lower than that of vacancies. Moreover, if the interstitial atom is much smaller than the rest of the atoms in the crystal, it will push the surrounding atoms further apart and distort the lattice planes. Interstitial atoms may be produced by severe local distortion during plastic deformation or by irradiating crystals with high-energy particles. Finally, when the atom occupies a nearby interstitial position, leaving a vacancy at the original lattice site, it is known as a Frenkel defect.

Because of the abovementioned thermodynamic features, the simplest and most abundant defects in TMDs are vacancies. Considering MoS_2 as a prototypical case, six different varieties are observed (Figure 3-2): single V_S, double V_S (V_{S2}), vacancy of a Mo atom and a triad of its bonded S within one plane (V_{MoS3}), vacancy of a Mo atom and all six of its nearest neighbors (V_{MoS6}), an antisite with Mo occupying a double V_S (Mo_{S2}), and a pair of S atoms occupying a Mo position ($S2_{Mo}$)[84]. Amongst them, V_S has the lowest formation (~2 eV), although the exact value depends on the chemical potentials of Mo and S atoms under different conditions[85].
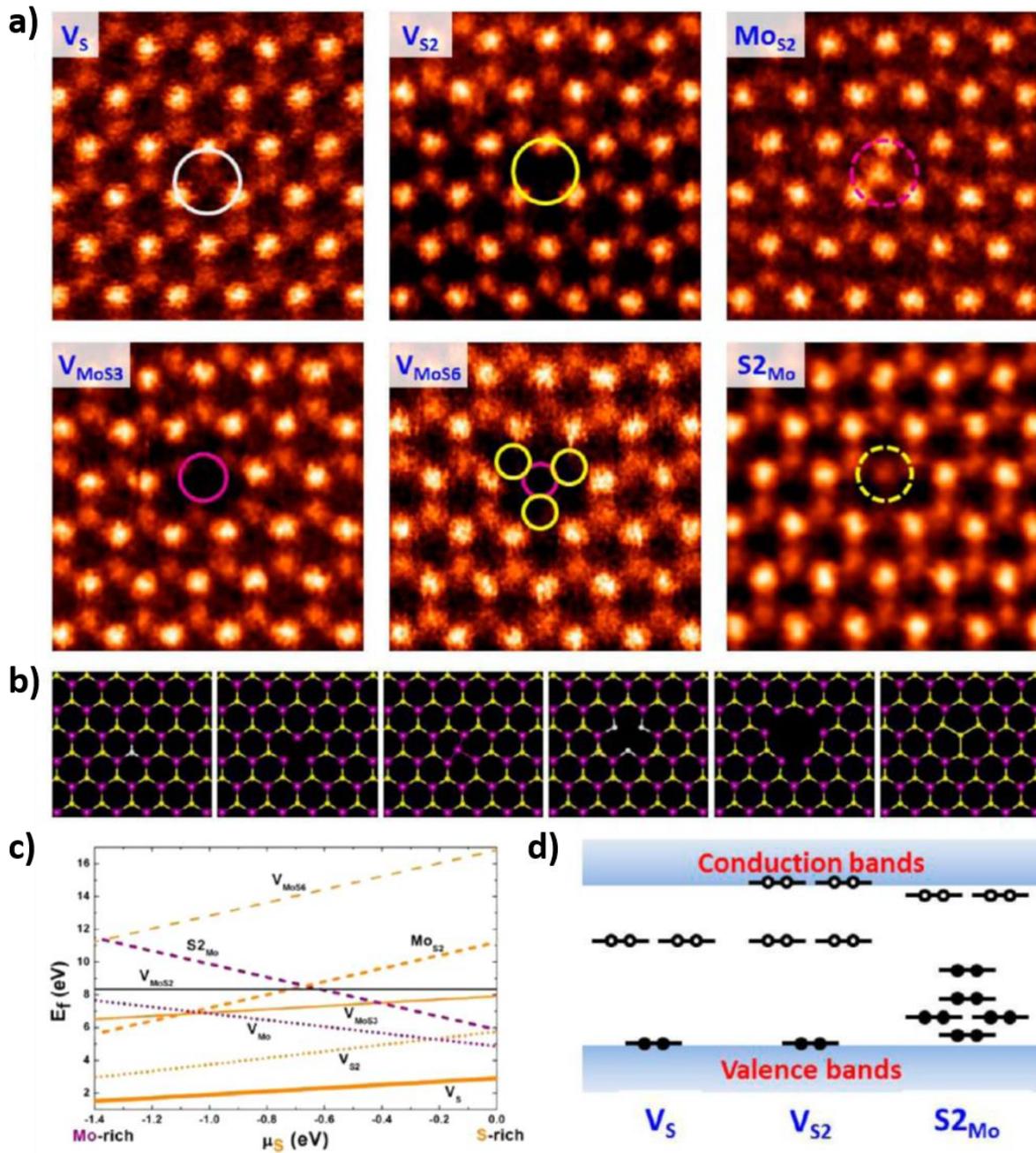
Figure 3-2 : a) Atomic resolution images of various intrinsic point defects present in monolayer MoS_2. **b)** Fully relaxed structural models of the six types of point defects observed experimentally. From left to right: V_S, V_{S2}, Mo_{S2}, V_{MoS3}, V_{MoS6}, and $S2_{Mo}$. Purple: Mo atoms; yellow: S atoms. **c)** Formation energies of different point defects as a function of sulfur chemical potential. **d)** Schematic representation of the defect levels. Adapted from Ref.[84].

One-dimensional defects. The principal one-dimensional crystal defect is the dislocation. In a perfect crystal, the atoms lie in planes within the lattice. However, if half a plane of atoms is missing, a line defect exists along the bottom edge of the half-plane that remains. Line defects are called dislocations because atoms are dislocated from their positions in a perfect crystal.

There are two fundamental types of dislocations: the pure edge and the pure screw dislocation. Edge dislocations consist of an extra half-plane of atoms in the crystal structure, whereas screw dislocations occur when one end of a crystal undergoes a shear stress and has moved at least one interplanar distance, while the other end of the crystal has not moved from its initial position. In general, dislocations are usually combinations of edge and screw, and they are either present as loops or they terminate at grain boundaries or at the crystal's free surface.

In TMDs various one-dimensional defects can be found, whose in-depth characterization and study rely on advanced electron microscopy techniques (Figure 3-3). For instance, extrinsic sulfur line vacancies result from the agglomeration of V_S usually produced by electron bombardment[86]. The formation energies of line vacancies are a function of the number of vacancies, in the range of 5-6 eV per vacancy for length of 6-16[87]. In this regard, it is worth mentioning that strain may serve as an instrument to select line vacancy orientations and, therefore, tune electronic properties[86]. In addition to sulfur line vacancies, grain boundaries and dislocations are also very common in TMDs, whose deep comprehension results intricate. When atoms are removed, the structure relaxes in three dimensions to form dislocations with a variety of motifs that are dependent on the grain boundary angle[88]. Finally, the most prominent defects in TMD nanosheets are their edges, whose energy and composition is strongly influenced by the operating conditions of the growth steps (*e.g.*, sulfur rich, sulfur poor). For instance, nanoscale calculations predict that under sulfur rich conditions Mo edges with either 50% or 100% S are the most thermodynamically stable[89], although additional compositions (0% and 50% S) have also been observed[84].
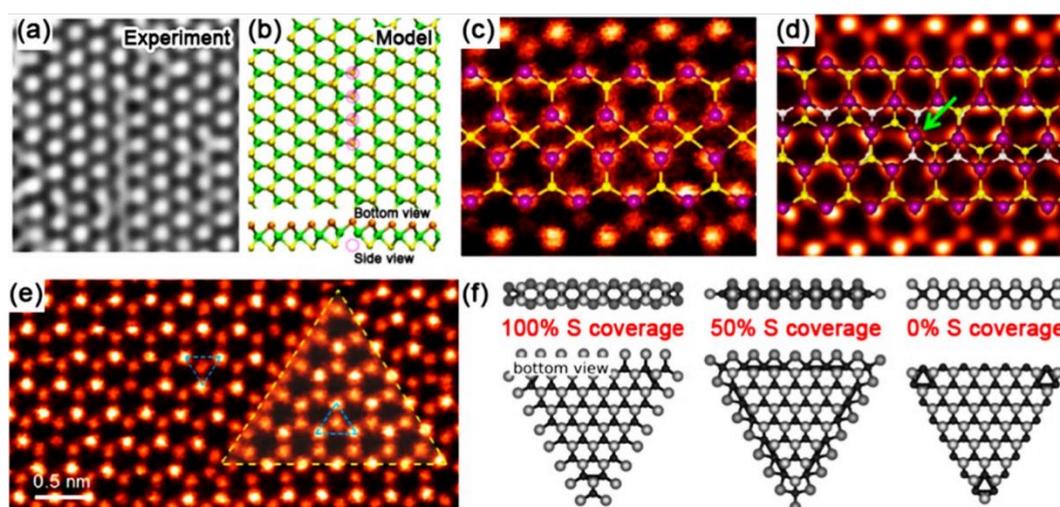

Figure 3-3 : a) HR-TEM image and **b)** structural model showing a single vacancy line in MoS$_2$ monolayer. **c-d)** ADF images of grain boundaries in CVD MoS$_2$ monolayers. **e)** ADF image showing an inversion domain in monolayer MoSe$_2$. **f)** Structural models showing Mo-terminated MoS$_2$ domains edges with different percentages of sulfur coverage. Adapted from Ref.[28].

Two-dimensional defects. The surface of 2D crystals is prone to form corrugations (or break, in the worst case, *e.g.*, cracks, holes) because of thermal fluctuations involving edge instabilities, strain, thermal vibrations, and thermal contractions (Figure 3-4). As a result, wrinkles and ripples might be formed on a two-dimensional plane influencing the overall electronic structure and altering the surface properties[90]. For the sake of clarity, the classification of such corrugations can be simplified considering their aspect ratio, topology and order. Wrinkles present a width between 1-10s nm, height below 15 nm and length above 100 nm (aspect ratio > 10); ripples are more isotropic and show feature size below 10 nm (aspect ratio ≈ 1). However, a dense formation and packing of ripples and wrinkles in two or three dimensions generates crumples. Furthermore, most synthetic few-layered TMDs materials, especially when they are stacked manually *via* transfer techniques, might fold themselves up, thereby heavily affecting their electronic and optical properties[91,92]. Finally, considering the analogies about structural features and interlayer interactions, TMD flakes can be stacked one on top of another forming vertical heterostructures, also known as vdW solids[22,93]. The interfaces among such layers can be considered as two-dimensional defects, and the overall material properties are strictly related to those of each component and their similarities (*e.g.*, lattice mismatch leading to Moiré patterns[94,95]).
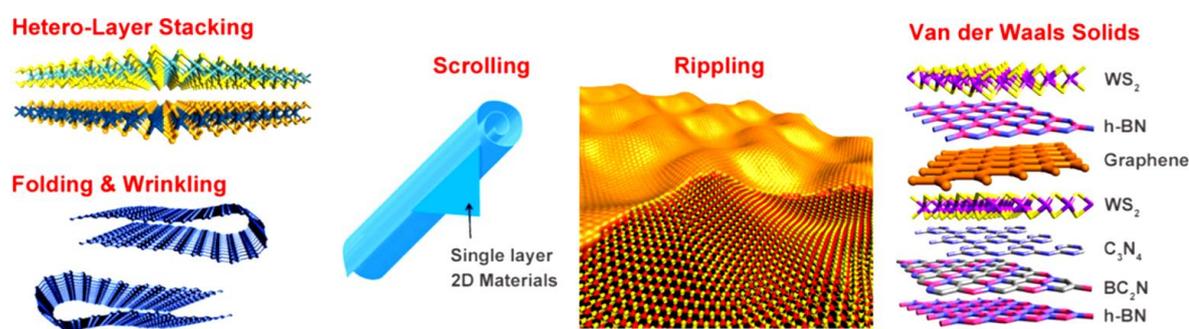

Figure 3-4 : Schematic illustration of the typical two-dimensional defects encountered in TMDs, such as folding, wrinkling, scrolling, rippling, and vertically stacked heterostructures. Adapted from Ref.[28].

As reported in the previous paragraphs, defects are ubiquitous in all materials and their critical influence on the physicochemical properties cannot be neglected. The presence of a great variety of defects in 2DMs and TMDs, in particular, has recently motivated worldwide scientists to develop new strategies in order control their nature and density, thereby customizing and tuning the properties of 2D crystals *à la carte* according to the envisioned applications. To date, we have available a long list of different approaches for TMDs, taking advantage of *in-situ* and *ex-situ* defect-engineering strategies. The former rely on synthetic steps carefully designed to achieve the material growth under precise conditions, aiming at specific stoichiometric, structural, and crystalline features; the latter, instead, exploit post-growth treatments to attain

the desired defect density/nature and related material properties. A brief description of the most common strategies to generate and control defects in TMDs is reported below.

***In-situ* generation of defects.** Production methods based on liquid and vapor phase represent versatile and appealing strategies for TMDs. As already discussed in Chapter 2, many parameters require an accurate control and monitoring throughout the whole process, offering attracting opportunities when one of them is subjected to in-depth investigation. CVD is a relatively violent (quite energetic) technique, therefore a large variety of defects can be generated and engineered. For instance, by adjusting the flow of sulfur vapor, it is possible to control the orientation of domain edges and the overall density of V_S[96,97]. Moreover, growth temperature can be tuned during the synthesis of MoS_2/WS_2 heterostructures in order to selectively promote the formation of either 2D interfaces or 1D interfaces[98] (Figure 3-5). Finally, the growth substrates (flatness, lattice constants, cleanness) play a fundamental role as well, determining the density and angle of grain boundaries, shape of domain edges, and domain orientations[99]. On the other hand, liquid-phase synthesis offers an alternative and efficient option to the abovementioned strategies, where an accurate control over defect density and nature can also be achieved. For example, the wafer-scale *in-situ* growth of vacancy-tunable TMD films was reported by Lee *et al.*[100], highlighting the vital role played by the precursor structure and molar ratio to produce V_S-modulated 2D crystals. In this regard, the presence of chalcogen vacancies induces an upshift of the Fermi level, leading to an enhancement of electrochemical catalytic activity in HER process by minimizing the energy difference with the $E^0_{H_2O/H_2}$. Similarly, Xie *et al.* reported a solvothermal synthetic approach to produce defect-rich MoS_2 nanosheets[101], highlighting a scalable pathway to accomplish the defect-engineering on TMD surfaces to expose catalytically active edge sites. The synthesis envisages the use of a high amount of precursor, hexaammonium heptamolybdate tetrahydrate $(NH_4)_6Mo_7O_{24} \cdot 4H_2O$, and different amount of thiourea, thereby achieving the defect modulation in the as-formed MoS_2 nanosheets. In fact, thiourea plays a double role, acting as reducing agent to form Mo(IV), but also as efficient additive to stabilize the dispersion upon adsorption on the surface of primary nanocrystallites, hindering the oriented crystal growth and leading to the formation of a defect-rich structure.
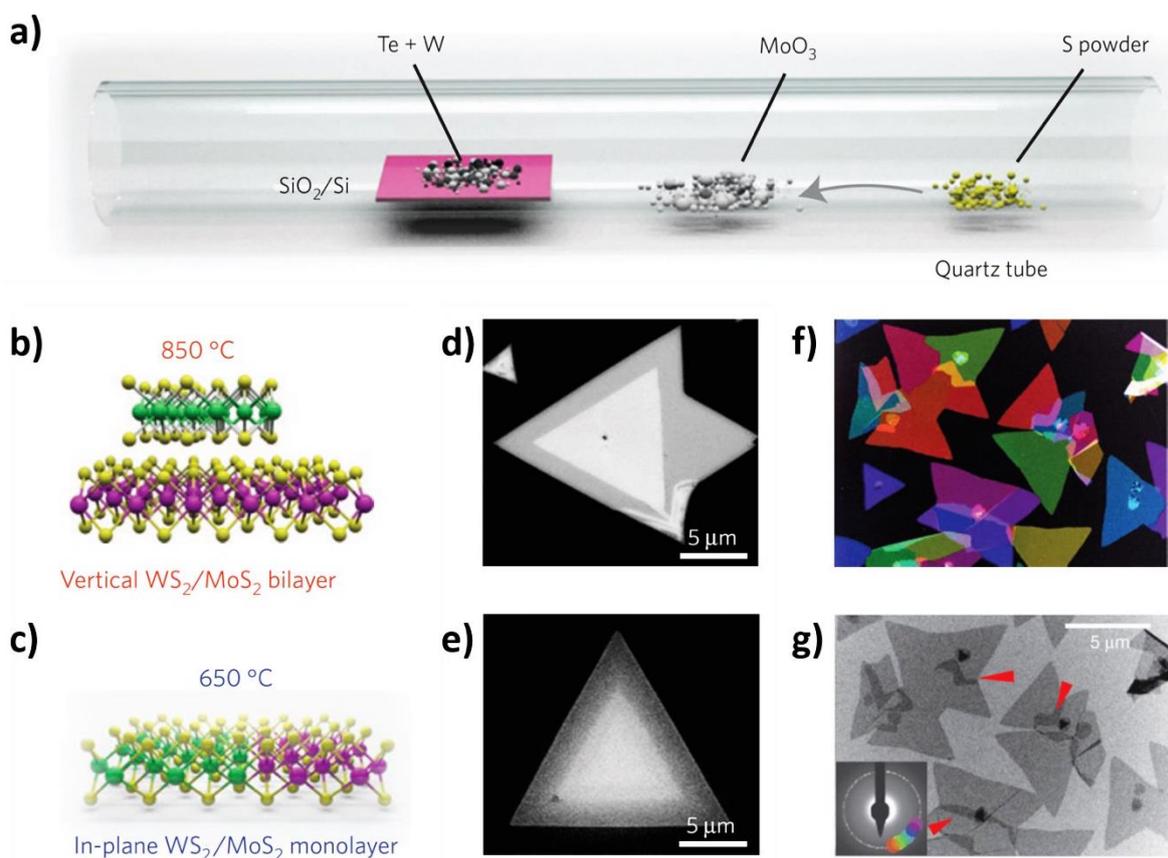
Figure 3-5 : a) Schematic of the synthesis process for WS_2/MoS_2 heterostructures. **b, d)** Schematic and SEM image of the vertically stacked WS_2/MoS_2 heterostructures synthesized at 850°C. **c, e)** Schematic and SEM image of in-plane WS_2/MoS_2 heterojunctions grown at 650 °C. Adapted from Ref.[98]. **f)** Colored DF-TEM overlay shows that irregular shapes are polycrystalline MoS_2 aggregates. **g)** BD-TEM image of a region containing irregularly shaped MoS_2 islands, with related diffraction patter as inset. Adapted from Ref.[96].

***Ex-situ* generation of defects.** Owing to the laborious and demanding control of defect formation during the synthetic steps, post-growth (*ex-situ*) treatments have been devised to guarantee a better degree of freedom for the defect-engineering of TMDs (Figure 3-6). Amongst them, thermal annealing has been proved to be a simple strategy to create chalcogen atomic defects in 2D crystals (*e.g.,* S, Te, Se)[102,103,104]. Moreover, the density of line defects can be increased with the increase of the annealing temperature, but they can also be recovered by depositing chalcogen atoms on the defective sample and following annealing, highlight the key role of temperature during the defect formation[105]. Another approach exploits laser irradiation to produce chalcogen vacancies, such as Te atomic defects that may also trigger a phase transition from 2H (semiconducting) to 1T (metallic) polymorph[106]. The aforementioned ability to perform micropatterning by laser irradiation represents one of the main advantages over thermal annealing. Furthermore, lasers can be used for the thinning of

TMDs as well, reaching single-layer 2D crystals with feature sizes down to 200 nm and arbitrary shapes and patterns[107]. Such an approach paves the way for the fabrication on demand of single- and few-layer nanosheets with different geometries to employ in (opto)electronic and photovoltaic applications, whose device performance resembles that of pristine TMD systems. A different strategy takes advantage of plasma treatments (*e.g.*, oxygen, argon, SF_6, CF_4, CHF_3)[108] to generate a great variety of defects, such as chalcogen vacancies[109,110], oxygen-transition metal bonds (promoting further chemical functionalization)[111,112], and ripples affecting the overall electrical device performance[108]. An alternative *ex-situ* approach to engineer defects in TMDs envisages the use of electron beams, where energies on the order of tens to hundreds of keV are required to generate chalcogen vacancies[86,113,114]. Remarkably, the damage induced by the electron beam can be reduced by sandwiching the TMD nanosheets (*i.e.*, encapsulation) between two graphene layers, whose high thermal and electrical conductivity decrease heat and charge accumulation[115]. Last but not least, ion bombardment represents an additional efficient and accurate method to generate and control defect density in TMDs, where different species might be adopted, such as He, Ga or Ar ions[116,117,118], α-particles[119], proton beam[120]. It is worth mentioning that such an approach promotes post-treatment processing, where the formed chalcogen vacancies, for instance, act as chemically active anchoring sites for the covalent attachment of small molecules *via* molecular functionalization strategies. In the last few year, the use of thiolated molecules has become prevalent thereby enabling a meticulous control over electronic, optical, vibrational and electrical properties[15,118,121].
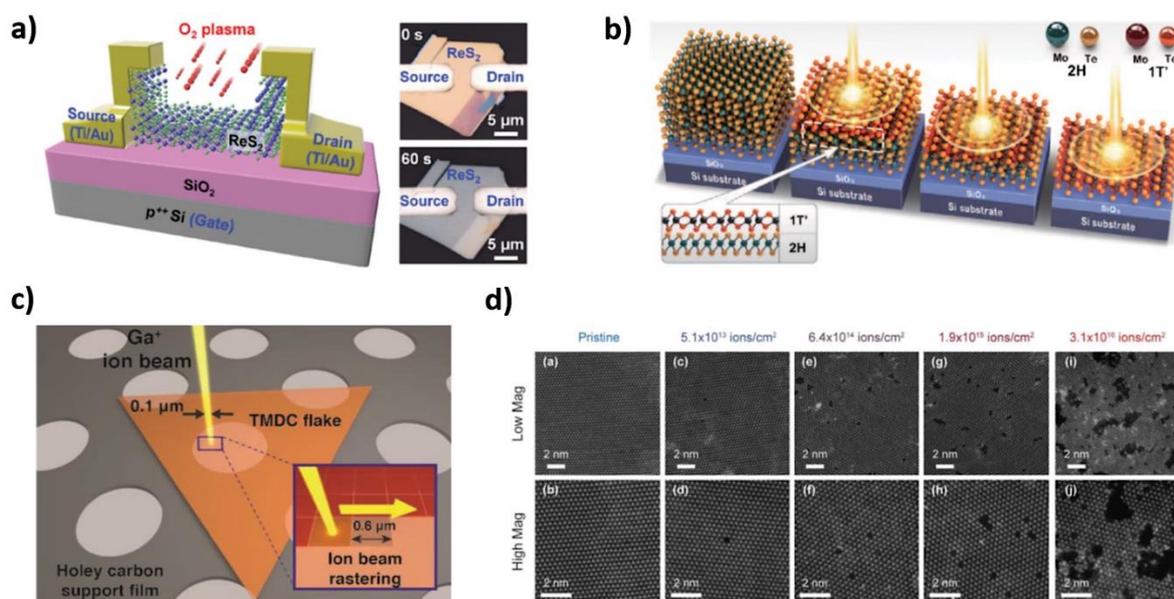
Figure 3-6 : a) Schematic illustration of O_2-plasma treated ReS_2 TFT and related optical image before and after. **b)** Schematic representation of laser-irradiation process in $MoTe_2$. **c)** Graphic of pixel-by-pixel irradiation of a TMD flake using a Ga^+ ion beam. **d)** STEM images at different magnifications of TMD flakes exposed to Ga^+ ion beam with diverse doses. Adapted from Ref.[109] **(a)**, Ref.[106] **(b)**, Ref.[117] **(c-d)**.

The previous sections of Chapter 3 are instructive about the nature and generation of defects in TMDs. By taking into account the inherent features of the production methods already discussed in Chapter 2, thus considering their characteristic thermodynamic and kinetic facets, it is conspicuous that top-down solution-processed TMDs exhibit high defect density. In fact, the exfoliation steps entail a considerable energy transfer to the bulk structures in order to peel the atomically thin layers off. However, such a process, also involves the breakage of flakes, leading to smaller and thinner crystals characterized by higher defect density, including newly formed defective edges, vacancies and grain boundaries[28,122].

In this regard, during the last decade, 2DM scientists have developed innovative molecular chemistry approaches to engineer defects in TMDs and tune *à la carte* their physicochemical properties according to the envisioned applications[8,25]. To this end, the following section will present the most important molecular functionalization strategies for the defect-engineering of solution-processed TMDs.

Molecular chemistry functionalization approaches. As extensively discussed in Chapter 2 and Chapter 3, production processes strongly contribute in affecting the final characteristics of TMD nanosheets. Nevertheless, post-production treatments have lately arisen to thoroughly tailor the physical and chemical properties of 2D TMDs, matching the requisites envisaged for a certain type of application (Figure 3-7). Modern functionalization strategies take advantage of various mechanisms and interactions, offering a plethora of possibilities in 2DM science.

One of the main approaches of defect-engineering in solution-processed TMDs exploits a coordinative-defect method, capitalizing on the unavoidable presence of chalcogen atom vacancies mainly produced during the exfoliation steps. In this regard, the seminal work was published by Dravid and co-workers in 2013[123], where chemically exfoliated MoS_2 nanosheets were subjected to reactions with different thiol-terminated polyethylene glycol derivatives bearing ionic and non-ionic headgroups. The high reactivity between thiol groups and sulfur vacancies leads to the healing process of 2D crystals, where the sulfur atoms of the molecular systems become integral part of the inorganic lattice[124]. The results of the ligand affinity tests shown that the thiol group was responsible for the observed MoS_2 modifications: changing the ligand structure (*e.g.*, polarity of the headgroup, conjugation), different colloidal stability, catalytic activity and chemical affinity towards specific molecules could be achieved. To date, the functionalization of TMD nanosheets *via* coordinative-defect approach can be performed by two distinct strategies, concerning either the direct functionalization of TMD colloidal dispersions[125,126] or the simultaneous exfoliation of bulk systems and functionalization of related exfoliated materials[127]. Nevertheless, recent studies have also capitalized on the functionalization of substrate-supported solution-processed TMD nanosheets[47]. Thus far, the majority of studies reported in literature involve the treatment of exfoliated materials with the functionalizing systems just after the exfoliation steps. In this regard, 2D MS_2 have drawn great attention because their versatility and aptitude to undergo healing reactions, in which thiolated molecules are exploited to fill V_S contained within the crystal structure. In particular, MS_2 have been studied and processed with dithiolane derivatives and thiolated molecules, in order to produce hybrid systems characterized by new and/or enhanced properties and performance, spanning from biosensing[128] to electronics[47]. However, it is worth mentioning that the sulfur healing reaction is not always the most favorable process and its mechanism is still under debate. In fact, two thiolated molecules can also interact through a TMD-mediated process and dimerize to form disulfide species that will physisorb onto the 2D crystal surface *via* weak vdW interactions[129,130].

An alternative but similar approach to the healing reaction exploits the high reactivity of chalcogen vacancies in TMDs, although the pristine crystal structure (*i.e.*, an atomic layer of transition metals sandwiched between two atomic layers of chalcogens) is not restored. More specifically, such a defect passivation method aims to deactivate the defect states without a

permanent change in the intrinsic crystal 2D structure. To this end, the adsorbed molecules should be chemically and thermally stable on TMD surfaces, avoiding any desorption and decomposition process during the fabrication steps. To date, the overwhelming majority of works reported in literature about defect deactivation rely on the formation of an organic-inorganic vdW interface, where a great variety of molecular systems can be exploited to influence and tailor the ultimate properties of TMDs. For instance, Yu *et al*. investigated the role of defects on the performance of WSe$_2$-based photoelectrodes, highlighting the effects of their passivation with silane molecules[131]. In particular, the high reactivity of Se vacancies (introduced during the exfoliation steps) promotes the interaction with the surfactant species, leading to multiple benefits. In fact, while the passivation of surface dangling bonds can reasonably reduce photogenerated charge recombination, the potential self-polymerization of silane molecules on TMD surfaces[132,133] can also improve the loading of surfactant, affecting the overall electrostatics by creating a surface dipole that might facilitate the charge extraction[134]. In the same vein, Tascón and co-workers reported the use of functional biomolecules as dispersing agents for solution-processed TMD nanosheets[135]. DNA and RNA nucleotides act as highly efficiently dispersants, favoring the preparation of stable aqueous suspension of 2D nanosheets at very high concentration (up to 5-10 mg/ml). Such an exceptional colloidal stability relies on the specific interactions of Lewis acid-base type between the biomolecules and defective TMDs, where the acidic V_S in MS$_2$ will interact with the basic nucleobases, improving stability and catalytic activity in the reduction of nitroarenes. Finally, the nucleotide-stabilized nanosheets also show high biocompatibility towards murine preosteoblasts and human sarcoma osteoblasts, paving the way for future applications in drug delivery and cancer treatments under different operating conditions (*e.g.*, temperature, pH).

The defective areas of TMD nanosheets are also prone to undergo chemisorption-based functionalization reactions, taking advantage of their inherent high reactivity towards a great variety of species. In this regard, an additional and appealing molecular strategy envisages the growth of noble metal NPs in damaged and deficient regions of 2D crystals, such as Au[136,137], Pd[138,139], Pt[140] and AgNPs[141,142]. The latter can interact with solution-processed TMDs *via* covalent and non-covalent interactions, leading to hybrid systems characterized by exceptional performance for (photo)catalysis[143,144] and biomedicine[145] applications. The growth of NPs takes place after the reduction of a noble metal precursor salt[11], induced by either the addition of reducing agent[146] or spontaneous formation[137]. In the latter case, Kim *et al*. succeeded in decorating electrochemical exfoliated MoS$_2$ and WS$_2$ nanosheets with AuNPs, using HAuCl$_4$ in water as precursor. The functionalization preferentially occurs on the defect sites, mainly located at the edges of the nanosheets and secondarily in their basal planes, more reactive than bulk crystals. A redox process takes place between [AuCl$_4$]$^-$ ions and TMD materials, and it is induced by the favorable matching of energy levels involved during the reaction, namely

the TMD ionization energy (5.4 eV and 5.2 eV for MoS_2 and WS_2, respectively[147]) lying well above the $E^0_{HAuCl_4/Au}$ (+1.0 V *vs.* SHE). It is worth mentioning that AuNPs play a double role, acting as spacers to inhibit restacking phenomena and improving the charge transport among adjacent nanosheets, thereby leading to superior electrocatalytic performance in HERs.
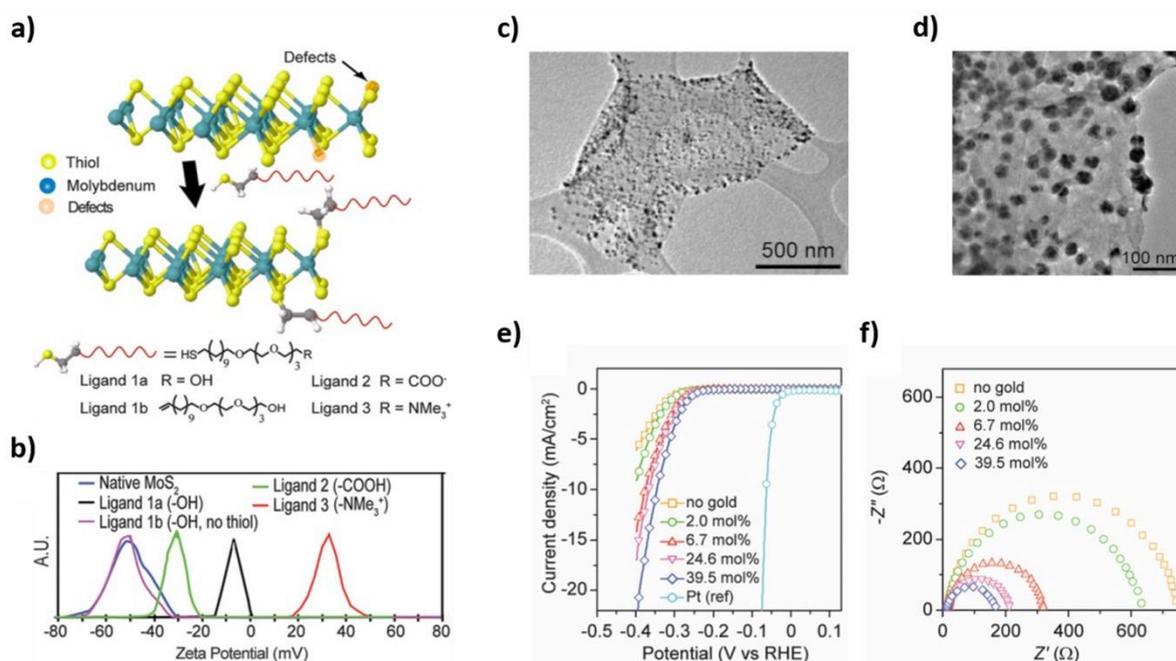

Figure 3-7 : a) Structural model illustrating the V_S healing process in chemically exfoliated MoS_2. **b)** Z-potential before and after ligand conjugation using structurally different thiolated molecules reported in **a)**. Adapted from Ref.[123]. TEM images of **c)** MoS_2 and **d)** WS_2 nanosheets decorated with AuNPs. **e)** HER performance and **f)** impedance spectroscopy of hybrid MoS_2/AuNPs. Adapted from Ref.[137].

Furthermore, the synthesis and growth of metal NPs can also be promoted by the use of suitable reducing agents. For instance, Huang *et al.* capitalized on solution-processed MoS_2 nanosheets to support the epitaxial growth of Pd, Pt and Ag nanoclusters under ambient conditions, using different reduction methods according to the chosen metal precursor[11]. Remarkably, TMD nanosheets are able to address NPs towards an epitaxial growth, resulting in preferential growth orientations such as (100) and (111). Moreover, besides providing plenty of nucleation sites in the defective areas, 2D epitaxial templates also stabilize small NPs and prevent them from aggregation. It is worth mentioning that for MoS_2/PtNPs hybrid systems, the nanomaterials exhibited much better electrocatalytic activity than commercial Pt catalyst, at the same Pt loading, likely due to the presence of additional (110) and (311) facets that promoted the catalytic reactions[148].

Finally, TMD nanosheets might also be subjected to prior functionalization reactions by exploiting organohalide[141] or thiol[142] chemistry, in order to activate the 2D structure and make it more reactive during the following steps of NP growth. Overall, such an approach represents a cutting-edge molecular strategy to produce novel and versatile hybrid functional materials based on defective solution-processed TMDs.

In light of the knowledge reported in the previous sections of this Chapter, the objectives of this doctoral work aim to develop new functionalization strategies taking advantage of the inherent defectiveness of solution-processed TMDs. To this end, the next Chapters will present and discuss the experimental results obtained during 4 years of scientific research on the topic, highlighting the main challenges and findings. In particular, two innovative and universal molecular approaches will be disclosed in Chapter 5 and Chapter 6, leading to the production of TMD-based hybrid structures characterized by new and/or enhanced properties and performance. The experimental part of this thesis will be preceded, in the following Chapter 4, by a concise but exhaustive analysis regarding the 2D materials and molecules employed throughout the two main projects, along with a description of the principal characterization techniques utilized to achieve and validate the abovementioned goals.

Chapter 4 — Materials and methods

4.1. — *Production and characterization of solution-processed TMDs*

MoS_2 and WS_2 inks are obtained by sonicating the respective powders (Sigma Aldrich, ≥99%) in N-methyl-2-pyrrolidone (NMP). An initial concentration of 20 mg/ml is processed for 1 h in 80 ml of NMP using a horn tip sonicator (Sonics Vibra-cell VCX-750 ultrasonic processor) at 60% amplitude. The dispersion is then centrifuged at 3218 g for 1 h using a Hettich Mickro 220R, after which the supernatant is discarded to remove potential contaminants from the starting powder. The sediment is then redispersed in fresh NMP and sonicated under the same conditions for 6 h. This process gives a polydisperse stock dispersion from which flakes can be size-selected by centrifugation. For each material, the polydisperse stock is first centrifuged at 106.4 g for 90 min to remove the largest aggregates, with the sediment retained for future exfoliation. The supernatant is then centrifuged at 425 g for 90 min to separate the smaller flakes. Finally, this sediment is redispersed in 30 ml of isopropanol (IPA).

ReS_2 inks are prepared by mixing the starting powders (Sigma Aldrich, ≥99.995%) into IPA and exfoliating for 3 h by using a bath sonication (Fisherbrand). The exfoliated dispersion is left to rest for 3 days to allow unexfoliated flakes to settle down by gravity. The supernatant is then collected for ink formulation. This is redispersed into IPA and re-exfoliated in a bath sonicator for 3 h, collecting the supernatant again. The process is then repeated. All collected supernatants are mixed and sonicated for 1 h to formulate the ReS_2 ink. Finally, the latter is placed into a vacuum oven at 40°C for 3 h to evaporate IPA and increase the concentration.

Upon production, solution-processed MS_2 inks (M = Mo, W, Re) are characterized to assess their concentration, quality and purity (Figure 4-1). UV-Vis spectroscopy is used to estimate the concentration of the three MS_2 dispersions. This gives ~4, 2 and 1 mg/ml for MoS_2, WS_2 and ReS_2, respectively[149]. The morphological features obtained by AFM imaging are compared to those obtained *via* spectroscopic investigation for MoS_2 and WS_2 flakes, the latter estimated from UV-Vis spectra as already reported in literature[82,150]. Remarkably, the average lateral size and thickness estimated by UV-Vis match the AFM analysis (Table 4-1). The UV-Vis spectra show the characteristic excitonic transitions for the three MS_2. In MoS_2 and WS_2, the peaks arise from direct-gap transitions at the K point of the Brillouin zone, resulting in absorption bands at 625 and 685 nm for MoS_2, and at 530 and 640 nm for WS_2 flakes[151]. Similarly, the ReS_2 spectra show an absorption band ~825 nm corresponding to the direct-gap transition[152]. In the typical Raman spectra recorded for the three MS_2, in-plane E_g modes and out-of-plane A_g modes are highlighted, corresponding to the two main peaks located ~384 cm^{-1} and 405 cm^{-1} for MoS_2, 352 cm^{-1} and 420 cm^{-1} for WS_2, 154 cm^{-1} and 218 cm^{-1} for ReS_2[152,153].
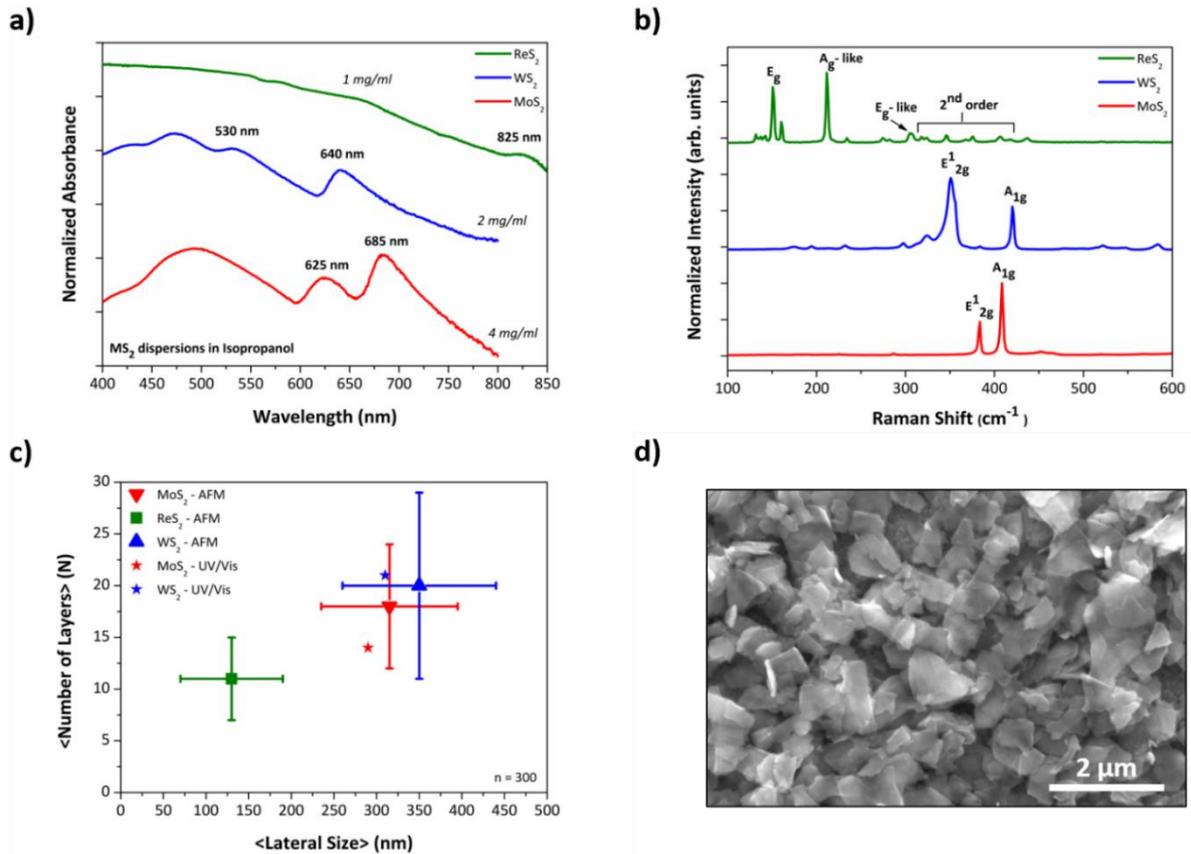
Figure 4-1 : a) UV-Vis spectra (solution) and **b)** Raman spectra (film) for solution-processed MS_2. **c)** Statistical AFM analysis performed on individual MS_2 flakes (300, overall) and comparison with values estimated *via* UV-Vis spectroscopy. **d)** Typical SEM image of drop-cast MoS_2 flakes.

TMD	$<N>$ AFM	$<L>$ AFM	$<N>$ UV-Vis	$<L>$ UV-Vis	Ref.
MoS_2	18 ± 6	315 ± 80 nm	14	290 nm	150
WS_2	20 ± 9	350 ± 90 nm	21	310 nm	82
ReS_2	11 ± 4	130 ± 60 nm	-	-	-

Table 4-1 : Morphological features of individual solution-processed MS_2 flakes and comparison between UV-Vis and AFM analysis. $<N>$ = average number of layers, $<L>$ = average lateral size.

The production of solution-processed MS_2 is carried out at *School of Physics, Trinity College Dublin*, by Prof. Jonathan Coleman's research group.

4.2. — *Thiolated molecules and noble metal salt precursors*

Thiols, also known as mercaptans (term introduced in 1832 by William Christopher Zeise, deriving from the Latin *mercurium captāns*, capturing mercury), are organosulfur compounds with the general form R-SH, where R represents an alkyl or other organic substituent. The term thiol is a blend of "thio-" and "alcohol", where the first word derives from the Greek *θεῖον* (*theion*), meaning "sulfur". Thiols are the sulfur analogue of alcohols, where an oxygen atom in the hydroxyl group is replaced by a sulfur atom in the sulfhydryl group. However, due to the similar electronegativity between sulfur and hydrogen atoms, thiols are less polar and have lower dipole moment than the corresponding alcohols. Moreover, sulfur is larger than oxygen, therefore the C-S bond lengths (ca. 180 pm) result 40 pm longer than a typical C-O bond. As a consequence, S-H bond is much weaker than O-H as reflected by the related bond dissociation energy (*e.g.*, it is 87 kcal/mol for CH_3-SH and 110 kcal/mol for CH_3-OH)[154]. Despite many similarities with hydroxyl compounds in terms of reactivity, thiols exhibit an extremely high aptitude to undergo oxidation reactions, especially in the presence of base, thereby forming organic disulfides, R-S-S-R. However, it is worth mentioning that the use of powerful oxidizing reagents (*e.g.*, sodium hypochlorite, hydrogen peroxide) leads to the formation of sulfonic acids, R-SO$_3$H, highly reactive strong acids commonly used in organocatalysis. As a consequence, thiols are generally employed under inert atmosphere, (*e.g.*, N_2-controlled atmosphere) ruling out, for instance, the presence of moisture and oxygen in order to hinder the formation of disulfide species and possible oxidation reactions.

Thiolated molecules (aliphatic or aromatic) can be employed as fundamental building blocks to form chemisorbed self-assembled monolayers (SAMs) on metal surfaces, particularly on Au, both from gas and liquid phase adsorption processes. A thiol molecule consists of three parts: (i) the sulfur headgroup, which forms a strong covalent bond with the metal substrates; (ii) the hydrocarbon chain (of variable length), which stabilizes the SAM through vdW interactions; (iii) the terminal group, which provides chemical functionality to the SAM and can be used to tailor the physicochemical properties of the solid surface. Since their discovery at the beginning of the 1980s by Nuzzo and Allara,[155] thiol and dithiol SAMs on metals have attracted considerable attention due to their ease of preparation and relatively high stability, strongly influenced by the strength of S-metal bond and vdW interactions. The energies related to each distinct part of the molecules have different orders of magnitude: 50 kcal/mol for the interaction between the S headgroup and the metal substrate (thiolate bond); 1-2 kcal/mol per methylene unit for the vdW interactions among the hydrocarbon chains; only few k_BT for the energies related to the terminal groups[156]. Owing to their inherent characteristics and versatility, during the last decades, thiolated molecules and related SAMs have been heavily employed in various technological applications, mainly concerning electronics. For instance,

thiolated molecules have been used as functional elements for single-molecule electronics[157,158], in order to investigate and tackle long-standing challenges, such as the precise geometry at the molecule-metal interface that can dominate the overall device performance. In addition, thiol-based SAMs have been used as active (semiconductor) and/or passive (dielectric) components in organic and biomolecular electronics[159,160], leading to new behaviors for applications such as ultra-sensitive label-free sensing, and low voltage operation (*viz*. low energy consumption) devices for major developments in forthcoming technologies.

In this thesis work (Chapter 5), we will capitalize on thiolated molecules with different structure (Figure 4-2), investigating the effects related to the number of thiol groups (mono- *vs*. dithiols) and molecular backbone (aliphatic *vs*. aromatic).
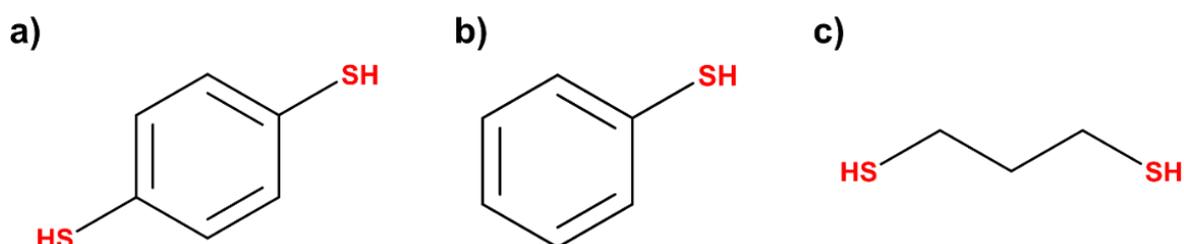

Figure 4-2 : Chemical structure of the thiolated molecular systems exploited in this thesis. **a)** 1,4-benzenedithiol (BDT). **b)** Thiophenol (TP). **c)** 1,3-Propanedithiol (PDT). The thiol (-SH) group is highlighted in red.

Transition metal chloride complexes are coordination complexes that consist of transition metal atoms coordinated to one or more chloride ligands. Usually, halides are good σ- and π-donors, and might be found both as terminal and bridging ligands (*e.g.*, the chloride ligands of aluminium chloride, $AlCl_3$, bridge two metal centres, leading to dimer formation, Al_2Cl_6, under ordinary conditions). Halides are weak field ligands due to their π-basicity, and because of small crystal field splitting energy they also form, when possible, high spin complexes for the first row transition series, unlike second and third series exhibiting low spin complexes. Homoleptic (all ligands are identical) metal halide complexes are known with several stoichiometries, but hexahalometallates and tetrahalometallates are predominant, showing octahedral and tetrahedral coordination, respectively. In this thesis work (Chapter 6), we will exploit transition metal tetrahalide complexes, whose features are reported below (Table 4-2).

Complex	Color	Electron configuration	Coordination
$[AuCl_4]^-$	Yellow	d^8	Square planar
$[PdCl_4]^{2-}$	Brown	d^8	Square planar
$[PtCl_4]^{2-}$	Pink	d^8	Square planar

Table 4-2 : Main properties for the transition metal tetrahalide complexes employed in this thesis work.

4.3. — *Multiscale characterization techniques*

The experimental data and resulting findings reported in this doctoral work rely on a long list of multiscale characterization techniques. To follow, the principal investigation methods are disclosed along with their operating conditions, taking advantage of a classification system that divides and gathers techniques with common features.

Spectroscopic characterizations

➢ UV-Vis absorption spectra are recorded on a JASCO v670 spectrometer using quartz cuvettes (light path = 10 mm) under ambient conditions.

➢ Raman spectra are recorded under ambient conditions with a Renishaw inVia spectrometer at 532 nm with a 100x objective (numerical aperture 0.85). The power is kept below 1 mW to avoid local heating and damage effects.

➢ X-ray photoelectron spectroscopy (XPS) is performed with a Thermo Scientific K-Alpha X-ray photoelectron spectrometer, operating with a base chamber pressure $\sim 10^{-9}$ mbar and an Al anode as X-ray source ($Al_{K\alpha}$ radiation, 1486.6 eV). The X-ray beam spot size is ~ 400 µm. Peak fitting is performed with constrains on the full width half maximum (FWHM) and the peak area ratio of the spin-orbit components.

➢ Photo-Electron Spectroscopy in Air (PESA) analysis is performed with a Riken Keiki AC-2 photoelectron spectrometer under ambient conditions.

➢ Nuclear magnetic resonance (NMR) analysis is performed with a Bruker Avance III HD 400 MHz, using cyclohexane-d_{12} as solvent. The MestreNova software is used to process the data.

Morphological, structural and surface characterizations

➢ Scanning electron microscopy (SEM) is performed with a Quanta FEG 450, operating with a chamber pressure $\sim 10^{-6}$ torr and gun pressure $\sim 10^{-9}$ torr, working at 20-30 kV.

➢ High-angle annular dark-field (HAADF) aberration-corrected scanning transmission electron microscopy (AC-STEM) is carried out in a NION UltraSTEM200, operating at 60 kV. The probe convergence semi-angle is 35 mrad, with a probe diameter of 1.2 Å. The inner and outer collection angles of the HAADF detector are 85 and 185 mrad, respectively.

➢ X-ray diffraction (XRD) experiments are performed with a Rigaku Smartlab equipped with a rotating anode of $Cu_{K\alpha}$ radiation operating at 45 kV and 300 mA.

➢ Atomic force microscopy (AFM) is done with a Bruker Dimension Icon microscope in ambient conditions, operating in tapping mode and using TESPA-V2 tips with spring constant k = 42 N/m.

➢ The film thickness is measured with a KLA-Tencor Alpha-Step IQ profilometer operating in ambient conditions.

➢ Optical microscopy imaging is performed with an Olympus BX51 microscope operating under ambient conditions.

➢ Static water contact angle measurements are performed with a Krüss DSA 100 instrument, operating under ambient conditions.

➢ Dynamic light scattering (DLS) and Zeta-Potential measurements are performed with a Beckman Coulter "Delsa Nano Submicron Particle Size and Zeta Potential" instrument, in ambient conditions.

➢ Mechanical tests are performed with digital force gauge "Mark-10, M7-025E, 1N" coupled with the motorized test stand "Mark-10, ESM-303E", operating under ambient conditions.

Electrical characterizations

➢ The electrical properties of LG-TFTs are investigated under N_2 atmosphere (inside glovebox) using a PM5 Cascade Microtech probe station connected with a Keithley 2636A SourceMeter.

➢ Cyclic voltammetry (CV) experiments are performed using a CH Instruments 600E Series Electrochemical Analyzer/Workstation, under ambient conditions. A three-electrode cell set-up is used with an Ag/AgCl reference electrode and a Pt counter electrode.

➢ Temperature-dependent electrical characterizations are carried out using an Oxford Instruments Optistat DN-V cryostat, operating in the range 80-300 K (liquid N_2) coupled with a Keithley 2636 SourceMeter unit.

Theoretical calculations

The calculations are carried out using density functional theory (DFT), with the Perdew–Burke-Ernzerhof generalized gradient approximation (GGA) for the exchange-correlation energy functional and the augmented plane-wave (APW) method using the Vienna *ab initio* simulation package (VASP). Wave functions are expanded in plane waves up to a kinetic energy cutoff of 400 eV. The periodically repeated simulation cells include slabs with one substrate layer of a 8x6 supercell for the 2DMs. In all cases, the vacuum gap between the slab surface models is larger than 15 Å. Dispersion corrections are also taken into account through the standard D2 Grimme parametrization. Finally, in order to investigate the interaction between NPs and 2D substrates, icosahedral NPs with the diameter of about 1 nm are considered.

Theoretical simulations and calculations concerning MS_2 and metal NPs are performed at *Dresden University of Technology*, by Prof. Gianaurelio Cuniberti's research group.

Chapter 5 — Covalently interconnected TMD networks *via* defect engineering for high-performance electronic devices

5.1. — *Introduction*

Solution-processed semiconducting TMDs are at the centre of an ever-increasing research effort in printed (opto)electronics. However, device performance is limited by structural defects resulting from the exfoliation process and poor inter-flake electronic connectivity. In this project, we report a radically new molecular strategy to simultaneously heal V_S in solution-processed MS_2 (M = Mo, W, and Re) and increase the inter-flake electronic connectivity by means of dithiolated molecular systems. By using π-conjugated dithiolated molecules (HS-R-SH), we prove *via* diverse multiscale analysis the simultaneous: (i) healing of V_S to restore the MS_2 crystal structure and decrease the related stoichiometric deficiencies acting as charge scattering centres, (ii) the covalent bridging of adjacent flakes, resulting in an enhanced charge carrier transport across an interconnected network. We investigate and capitalize on the *in-situ* functionalization approach of TMDs, by exposing the inorganic materials to molecular bridges just after their deposition on a substrate. This is crucial for the formation of long-range percolation pathways which exhibit superior charge transport characteristics, likewise the bridging of disordered regions in polycrystalline structures of conjugated polymer chains[16].

Such an approach represents an innovative and universal functionalization method capable of improving the performance of devices based on solution-processed MS_2 for large-area electronic applications. We apply this strategy in LG-TFTs, fabricated by drop-casting MS_2 dispersions onto SiO_2/Si substrates pre-patterned with interdigitated Au IDEs, followed by exposure to aromatic and conjugated BDT molecules. This boosts the characteristics of the electrical devices by one order-of-magnitude, leading to SoA performance characterized by competing μ_{FE} and I_{ON}/I_{OFF}, along with the fastest switching speed reported to date for devices of this kind[17]. Improved water stability and mechanical robustness are other unique features exhibited by the covalently bridged MS_2 networks.

5.2. — *Device fabrication*

MS$_2$ inks (see their production and characterization in Chapter 4, Section 4.1) are drop-cast onto SiO$_2$/Si substrates with 2.5 µm-spaced Au IDEs for TFT measurements. The ink deposition is performed on the substrate placed onto a 110°C heated hot plate to assist the solvent (IPA) evaporation and the elimination of humidity traces during casting (Figure 5-1).

Figure 5-1 : a) Illustration of the ink deposition and *in-situ* functionalization to produce MS$_2$ networks *via* BDT treatment. **b)** Sketch of V$_S$ healing mechanism in MoS$_2$ films by means of dithiolated molecules and related inter-flake networking.

Morphological characterizations (SEM and AFM) of the deposited materials show a large(µm)-scale uniform coverage of the electrodes (important to enable charge percolation pathways), high local disorder, thickness = 700 ± 100 nm over a 500 µm sampling distance, and average root-mean-square roughness R$_{rms}$ = 95 ± 10 nm over a 25 µm^2 area. MS$_2$ networks are formed by bridging adjacent flakes and taking advantage of the higher defect density at the edge sites

with respect to basal planes. In this regard, we performed HAADF-STEM analysis (Figure 5-2) investigating the Mo-Mo distance for MoS_2 prepared by LPE, mechanical cleavage (MC) and CVD, as the amount and kind of defects depend on the synthesis/production method[28]. The Mo-Mo distance in the basal plane is similar for all samples; however, at the edges of LPE-MoS_2 the Mo-Mo distance shortens by ~30 pm with respect to that on the basal plane. This is due to a higher defect density that can originate because of V_S mainly located at the MoS_2 edges[161]. Ultimately, the latter feature is crucial for the molecular bridging of adjacent flakes and formation of covalently interconnected TMD networks.
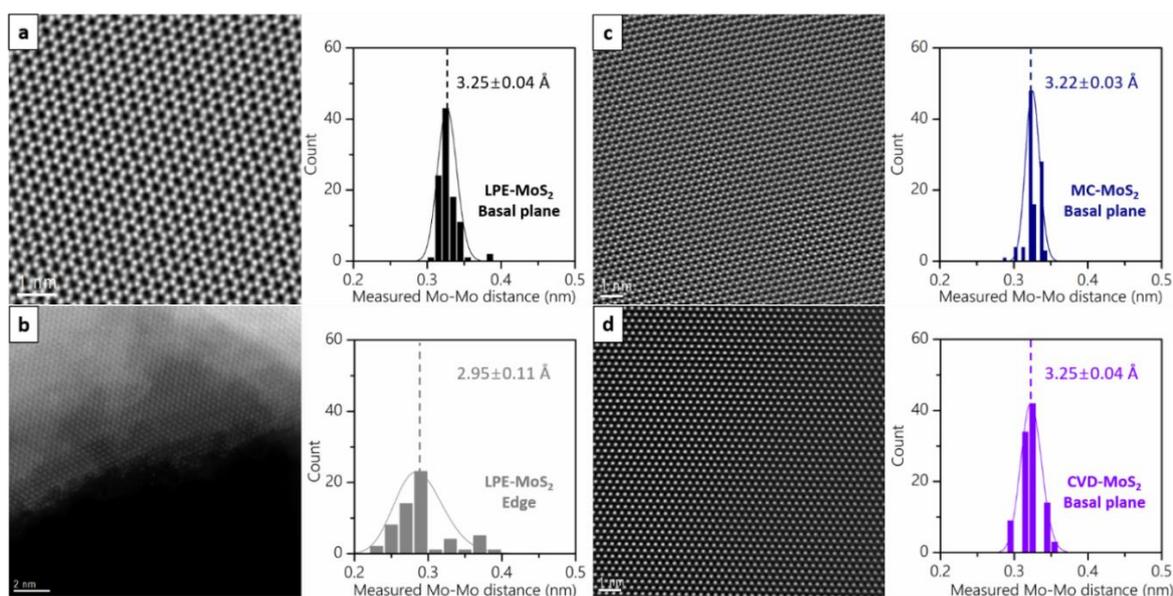
Figure 5-2 : HAADF-STEM images and related histograms of Mo-Mo distance for the **a)** basal plane of LPE-MoS_2, **b)** edge of LPE-MoS_2, **c)** basal plane of MC-MoS_2 and **d)** basal plane of CVD-MoS_2. The histograms show a similar average Mo-Mo distance for the basal plane of all samples, with a significant decrease ~30 pm for the edge of LPE-MoS_2, pointing to a higher defect density.

MS_2 thin films are functionalized in a N_2-filled glovebox, exploiting a 50 mM saturated solution of BDT in anhydrous hexane to produce covalently-linked MS_2 networks. The whole BDT solution preparation (powder weighing and dissolution) is carried out under N_2-controlled atmosphere to avoid thiol oxidation reactions induced by impurities[162]. The coated slides are soaked in BDT solution at room temperature for 24 h inside a sealed container, followed by rinsing in hexane, and annealing onto hot plate at 90°C for 30 min. No significant morphological variations are detected after thiol exposure, and the network features remain similar to those of the pristine films. Ultimately, the functionalization process is designed to simultaneously heal V_S in MS_2 films and covalently bridge adjacent flakes, thereby promoting their modification at the molecular level.

5.3. — *Results and discussion*

In order to assess the effects of the *in-situ* functionalization with BDT molecules, we carried out an in-depth analysis by making use of various independent, complementary and multiscale techniques. At first, we performed morphological and structural investigations highlighting no remarkable differences between films and networks (*viz.*, before and after BDT treatment, respectively). AFM and SEM imaging (Figure 5-3) show no changes, since both films and networks exhibit $R_{rms} = 95 \pm 10$ nm and no molecular aggregates or macroscopic post-functionalization effects are observed.
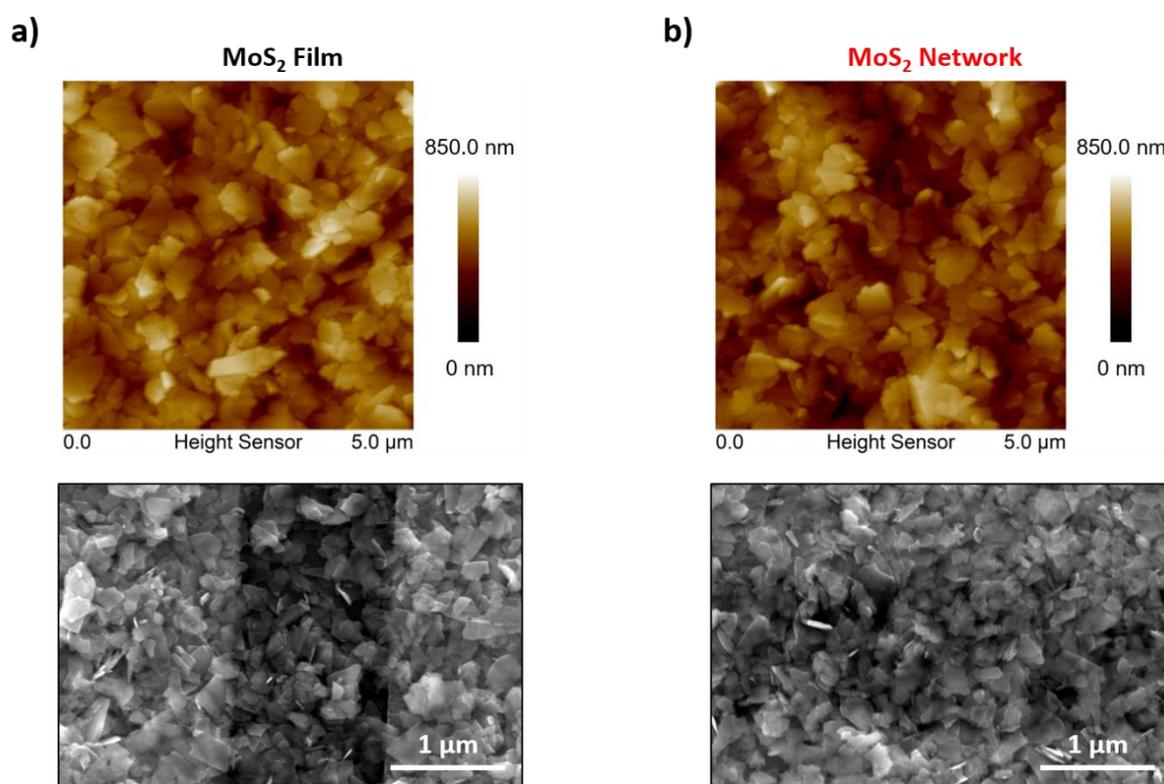
Figure 5-3 : AFM (top) and SEM (bottom) images for **a)** MoS_2 films and **b)** MoS_2 networks. No significant changes are observed upon BDT functionalization. The SEM images are recorded in-between Au IDEs of pre-patterned SiO_2/Si substrates.

XRD analysis was then used to detect any possible changes due to BDT functionalization. The two diffractograms in Figure 5-4 display the same characteristic peaks at 14.5° and 29°, corresponding to the (002) and (004) planes of hexagonal MoS_2, respectively[163]. Therefore, no structural changes are observed upon BDT exposure (*e.g.*, intercalation), indicating a preserved crystal structure. We speculate the same rationalizations apply to WS_2 and ReS_2 (XRD data not reported).
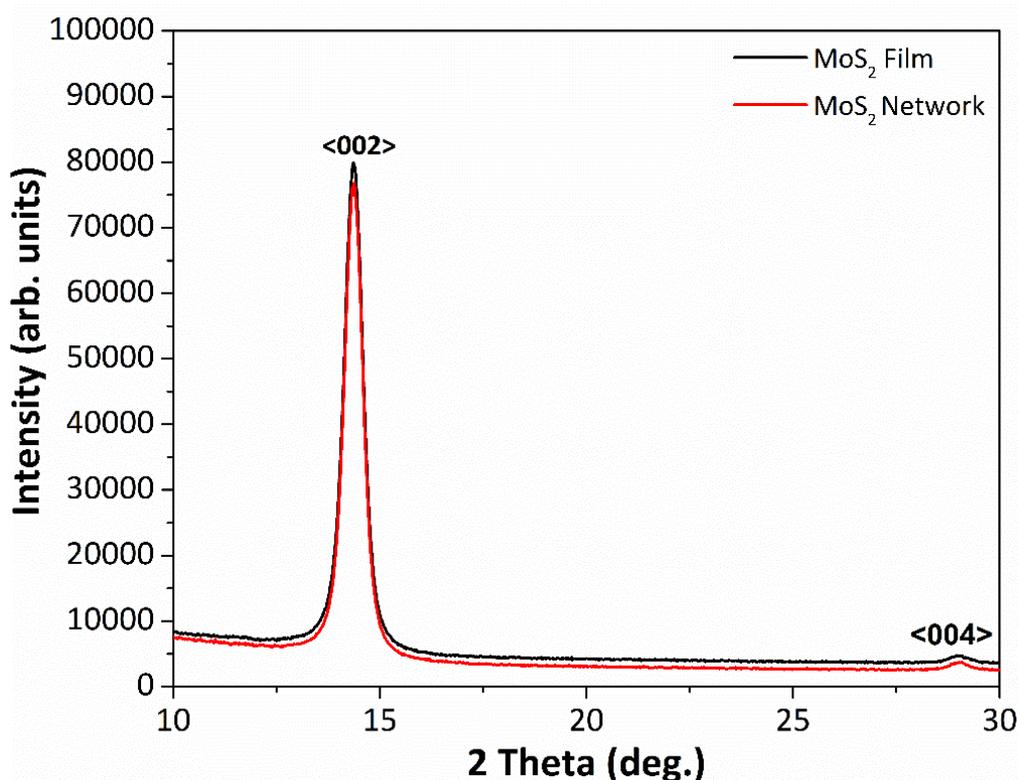
Figure 5-4 : Comparison of MoS_2 diffractograms obtained for films (black) and networks (red), displaying the characteristic peaks related to the (002) and (004) crystallographic planes.

We also exploited spectroscopic techniques to evaluate the network formation promoted by dithiolated molecular linkers. XPS measurements provide evidence for the MS_2 chemical functionalization, as illustrated in Figure 5-5 by the S2p high-resolution spectra of drop-cast solution-processed MS_2 before (as film) and after (as network) BDT treatment. For instance, the MoS_2 S2p spectrum displays two main peaks at ~162.3 and ~163.5 eV, assigned to the $S2p_{3/2}$ and $S2p_{1/2}$ components[164], respectively. However, an additional component can be deconvoluted at ~161.5 eV and ascribed to defects, *e.g.* vacancy neighbouring S atoms[164,165]. Such a minority component at lower binding energies is due to the charge localized on S, that, once S is desorbed, can be redistributed on the first neighbouring atoms, enhancing Coulomb screening[164]. The substroichiometric MoS_{2-x} component at ~161.5 eV is related to unsaturated S ligands[165], such as V_S, and decreases from 8.0 ± 0.5 % to 5.0 ± 0.5 % upon BDT treatment, proving how the exposure to thiolated molecules leads to a decrease of chalcogen vacancy defects in solution-processed MoS_2. Since different S ligands have minimal differences in binding energies, their identification in XPS spectra is not always straightforward, and most literature focuses just on MoS_2.

Nevertheless, we extended such an accurate analysis to WS_2 and ReS_2 as well, by monitoring the evolution of the component (singlet) ascribed to the substroichiometric MS_{2-x} materials (defects component) located ~1 eV lower than the $S2p_{3/2}$ component. As reported in Figure 5-5, the defects component decreases upon BDT exposure, thereby confirming a lower defect density in solution-processed MS_2 networks.
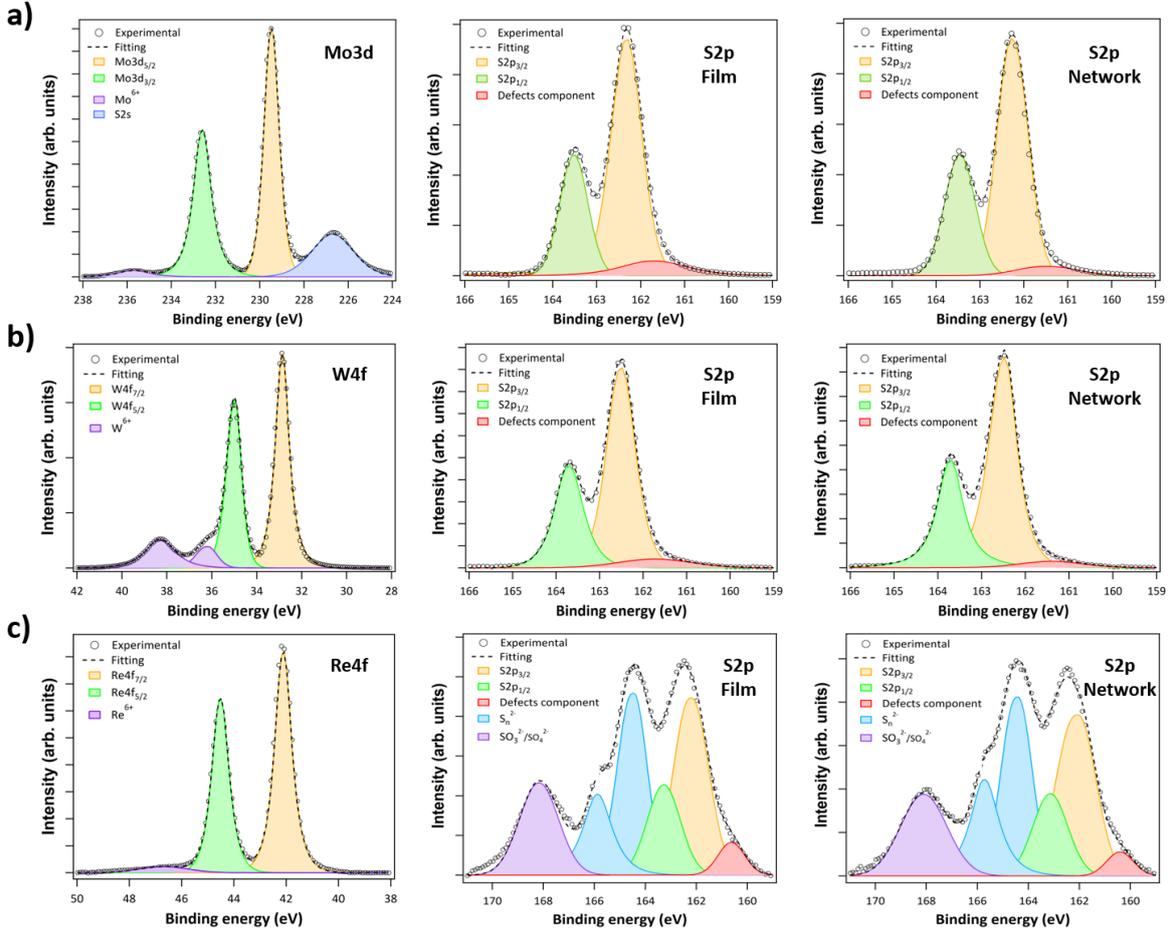

Figure 5-5 : a) MoS_2, with Mo3d (left) and S2p regions, the latter for film (middle) and network (right). **b)** WS_2, with W4f (left) and S2p regions, the latter for film (middle) and network (right). **c**, ReS_2, with Re4f (left) and S2p regions, the latter for film (middle) and network (right).

The ratio of the defects component area (A_{DC}) to the overall S2p region area (A_{S2p}) decreases after BDT exposure for all three materials, even though solution-processed MoS_2 shows the largest variation of A_{DC}/A_{S2p} upon network formation (Table 5-1). We believe that MoS_2 exhibits such a behaviour since it is the material, amongst the three under study, with the best trade-off between high-defectiveness and lower degree of oxidation, as reported in Figure 5-5.

TMD	A_{DC}/A_{S2p} Film	A_{DC}/A_{S2p} Network
MoS$_2$	8.0 ± 0.5 %	5.0 ± 0.5 %
WS$_2$	6.0 ± 0.5 %	4.0 ± 0.5 %
ReS$_2$	4.0 ± 0.5 %	3.0 ± 0.5 %

Table 5-1 : Defects component weight in high resolution XPS S2p spectra for MS$_2$ films and networks.

XPS spectra of WS$_2$ display two additional components (doublet) at ~36 eV and ~38 eV in the W4f region (besides the W4f$_{7/2}$ and W4f$_{5/2}$ components located at ~33 eV and ~35 eV, respectively), ascribed to W atoms with a 6+ oxidation state[166]. Similar results are observed in the Re4f and S2p regions of the ReS$_2$ spectra, where many additional intense components are observed and ascribed to oxidized species, such as Re atoms with a 6+ oxidation state, polysulphides (doublet), sulphite and sulphate groups (singlet) coming from the oxidation reactions occurring during the exfoliation procedures[167,168]. ReS$_2$ is produced by sonicating the starting crystals in IPA, which can promote stronger oxidation reactions than NMP used for MoS$_2$ and WS$_2$. Figure 5-6 compares the O1s XPS regions of MoS$_2$ and ReS$_2$, indicating higher amount of oxygen (from half to one order-of-magnitude) in ReS$_2$ than MoS$_2$. Additionally, the O1s region of ReS$_2$ displays a broader peak, whose components can be fitted and deconvoluted considering the oxidation species present in the material upon exfoliation. The C-O components in Figure 5-6 are assigned to external contaminants, such as solvent traces and adsorbates. Finally, MoS$_2$ has less oxidized V_S than WS$_2$ and ReS$_2$, therefore it is more prone to undergo V_S healing reactions, although BDT treatment effects are evident in all three materials.
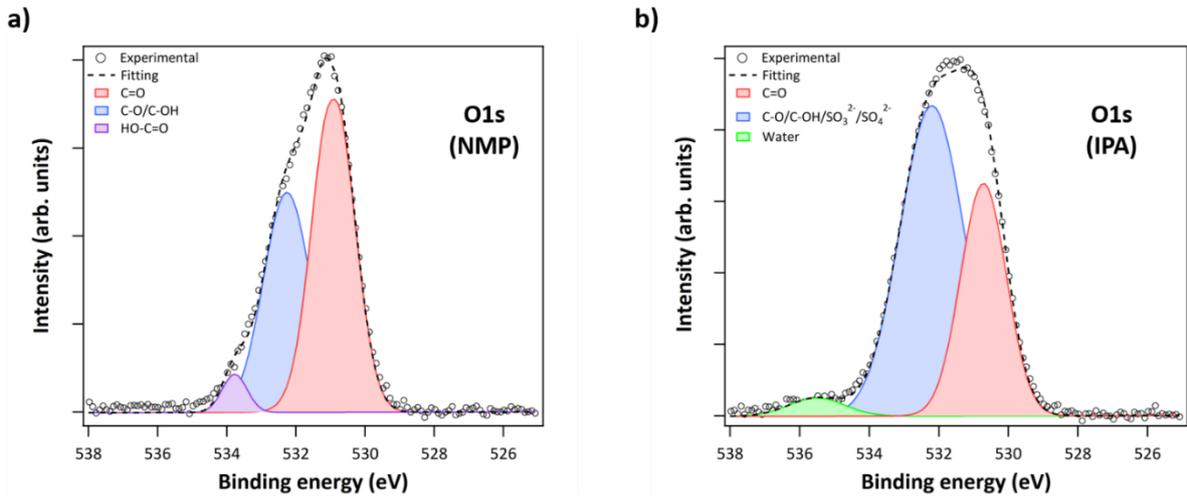
Figure 5-6 : Solution-processed **a)** MoS_2 and **b)** ReS_2 produced by sonicating the starting bulk material in NMP and IPA, respectively.

To confirm the effects of thiol functionalization, we surveyed the evolution of the Sulfur/Metal (S/M) XPS ratio of MS_2 before and after exposure to BDT molecules. Figure 5-7 shows an increase of S/M upon treatment, supporting the V_S healing mechanism and the decrease of defect density once thiolated molecules are employed.
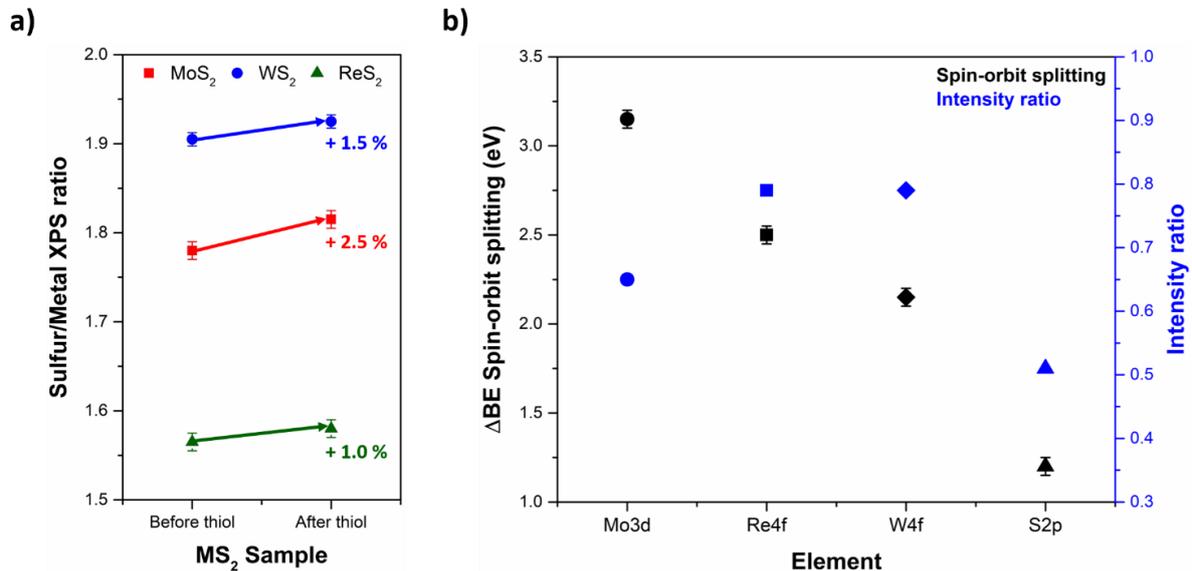

Figure 5-7 : a) Sulfur/Metal XPS ratio before and after exposure to BDT molecules for MoS_2, WS_2 and ReS_2. **b)** Summary of the XPS constraints (spin-orbit splitting and intensity ratio) implemented for the fitting of Mo3d, Re4f, W4f and S2p regions, before and after exposure to BDT molecules.

For the sake of clarity, we implemented the following constraints in the XPS fitting and analysis procedure: (i) Mo3d, spin-orbit splitting = 3.15 ± 0.05 eV and intensity ratio = 0.65; (ii) Re4f, spin-orbit splitting = 2.50 ± 0.05 eV and intensity ratio = 0.79; (iii) W4f, spin-orbit splitting = 2.15 ± 0.05 eV and intensity ratio = 0.79; (iv) S2p, spin-orbit splitting = 1.20 ± 0.05 eV and intensity ratio = 0.51.

In addition to XPS, we also capitalized on Raman spectroscopy to support the network formation once dithiolated molecules are employed for the V_S healing process. Raman spectra indicate that FWHM of E^1_{2g} and A_{1g} peaks for MoS_2 spectra decreases upon thiol exposure (Figure 5-8). This might be due to the reduction of defect density and, in particular, to the attenuation of defect-activated modes[169]. We perform a strong statistical analysis by collecting ~2000 spectra and mapping a total area of ~6000 µm^2. Figure 5-9 shows that, even though both films and networks are continuous, the latter exhibit higher homogeneity. The mapping gives a significant (~10 %) decrease of FWHM for both E^1_{2g} and A_{1g} peaks upon BDT exposure: E^1_{2g} FWHM decreases from 2.95 ± 0.20 cm^{-1} (films) to 2.50 ± 0.10 cm^{-1} (networks), while A_{1g} FWHM from 3.15 ± 0.15 cm^{-1} (films) to 2.85 ± 0.10 cm^{-1} (networks), consistent with previous observations when defect density is reduced[169]. We also observe a blue shift of both E^1_{2g} and A_{1g} peaks: from 382.60 ± 0.30 cm^{-1} (films) to 383.20 ± 0.25 cm^{-1} (networks) and from 407.80 ± 0.30 cm^{-1} (films) to 408.40 ± 0.25 cm^{-1} (networks), respectively (Figure 5-10). Such small variations are in agreement with the suppression of defects-activated modes and rule out any charge transfer phenomena (doping) due to BDT molecules[170].
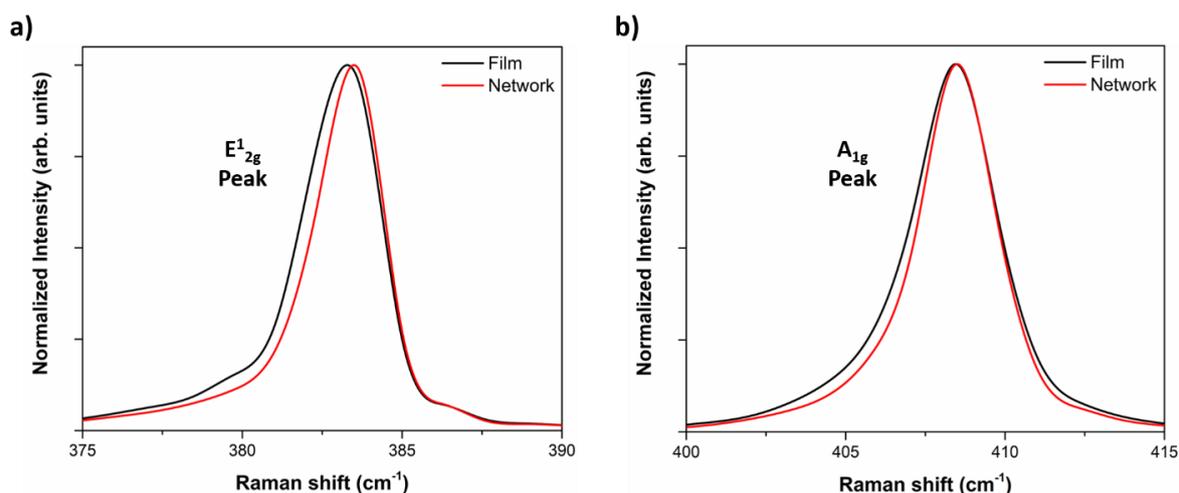

Figure 5-8 : Comparison between **a)** E^1_{2g} and **b)** A_{1g} peaks for pristine MoS_2 films and networks.

We also probed the $I(E^1_{2g})/I(A_{1g})$ before and after exposure to thiolated molecules. Figure 5-10 indicates that $I(E^1_{2g})/I(A_{1g})$ increases from 0.46 ± 0.04 (films) to 0.55 ± 0.04 (networks), consistent with previous reports indicating a lower defect density for higher $I(E^1_{2g})/I(A_{1g})$[171].
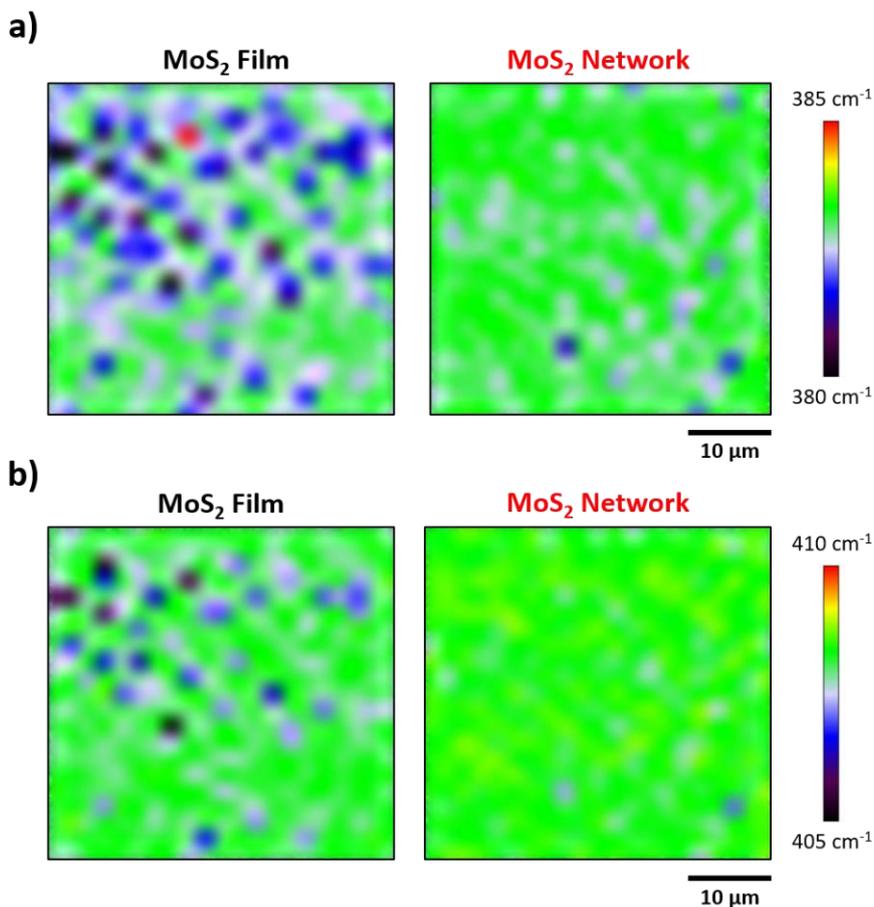

Figure 5-9 : Raman mapping of **a)** Pos(E^1_{2g}) and **b)** Pos(A_{1g}) for MoS₂ films and networks. Each map contains 441 spectra and covers 1600 μm².
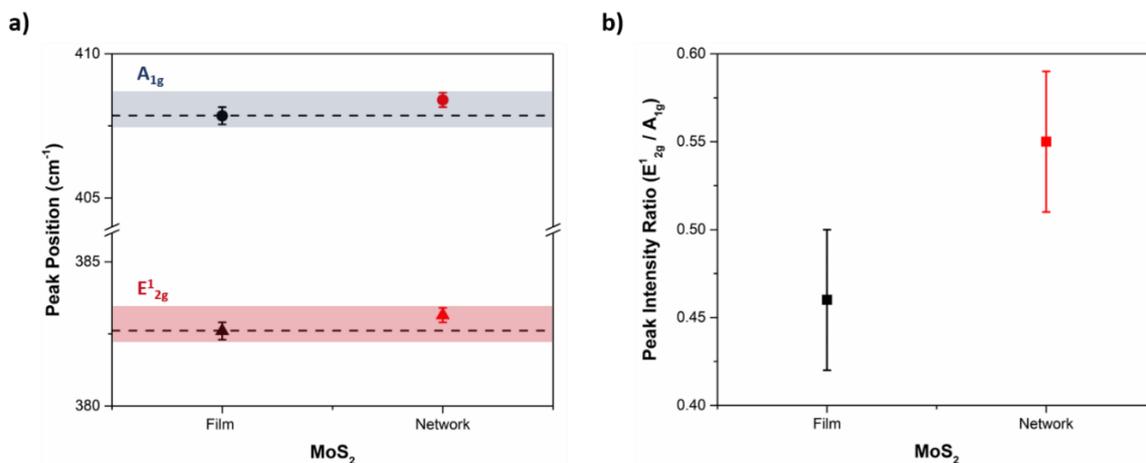

Figure 5-10 : Fitted **a)** Pos(E^1_{2g}) and Pos(A_{1g}) and **b)** $I(E^1_{2g})/I(A_{1g})$ for MoS₂ films and networks.

Additional evidence of the network formation come from the distinctive characteristic and macroscopic properties of BDT-treated MS$_2$ samples. Pristine MoS$_2$ films on electrode-free SiO$_2$/Si substrates are hydrophilic systems, with an average static water contact angle (WCA) of 53 ± 2° in agreement with literature[172], although the material production and deposition technique might be responsible for small fluctuations around these values[173]. Upon functionalization, MoS$_2$ networks are strongly hydrophobic as evidenced by an average WCA of 121 ± 2°, where the free aromatic and non-polar ring of BDT molecules remain exposed to the samples' surface increasing its hydrophobicity.

Moreover, the network formation in BDT-functionalized MoS$_2$ samples improves the material stability in water (Figure 5-11). For MoS$_2$ pristine films we observe detachment and floating of the material upon water exposure, while for MoS$_2$ networks the sample integrity is preserved. In fact, the solvation process is hindered within MoS$_2$ networks (less soluble than isolated free single flakes), consistent with the covalent interconnectivity promoted by dithiolated linkers. Such a feature is of primary importance for the fabrication of robust devices operating in aqueous environment[7].
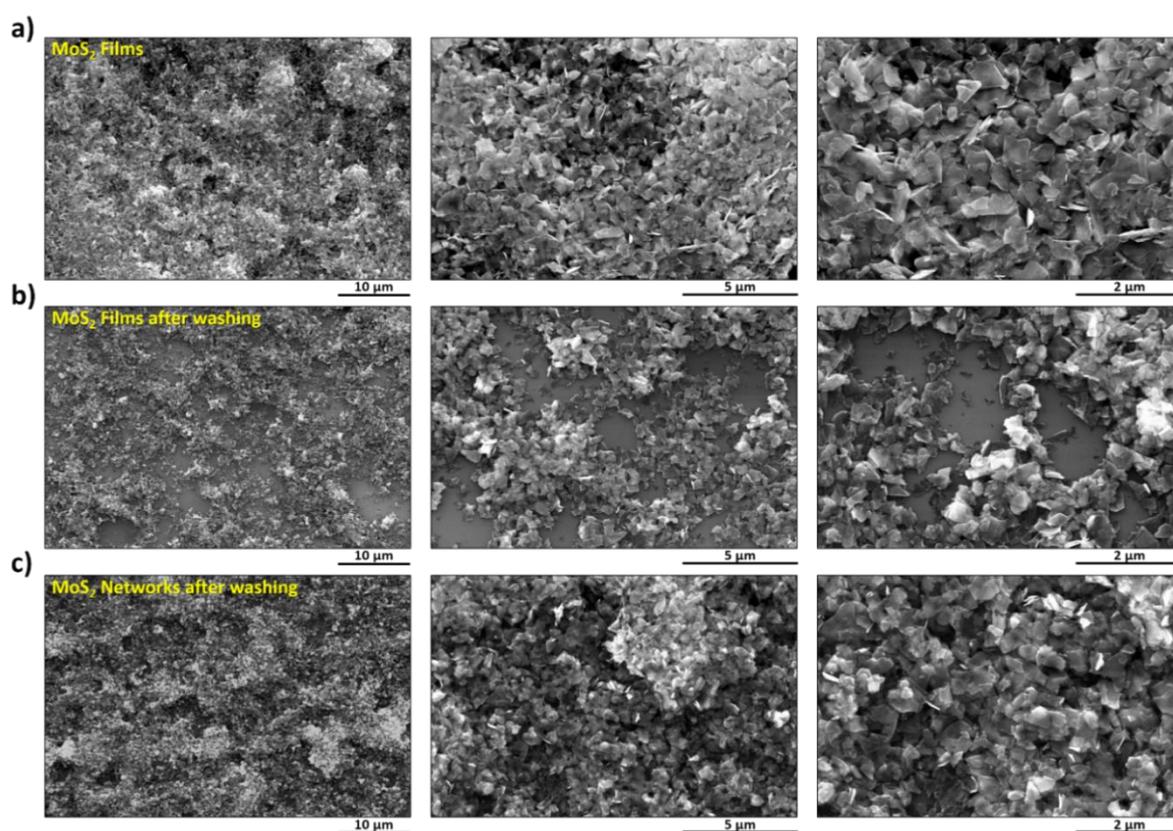
Figure 5-11 : SEM images at different magnifications of **a)** MoS$_2$ pristine films **b)** MoS$_2$ pristine films after water exposure and **c)** MoS$_2$ networks after water exposure.

We then investigated the mechanical robustness and consequent electrical stability of MoS_2 films and networks deposited onto flexible polyethylene terephthalate (PET) substrates. The deposition on PET slides (2 cm x 4 cm) occurs *via* dry transfer from a polytetrafluoroethylene (PTFE) membrane filter (Φ = 25 mm). In particular, after filtering 2 ml of MoS_2 dispersion at 0.6 mg/ml, the filters are pressed against the PET substrates for 1h, with a laboratory manual press. Then, IDEs are placed onto the film surface by shadow mask evaporation approach, having 5 nm of Cr adhesive layer and 75 nm of Au. For the production of networks, MoS_2 films are exposed to BDT before the electrode fabrication step.
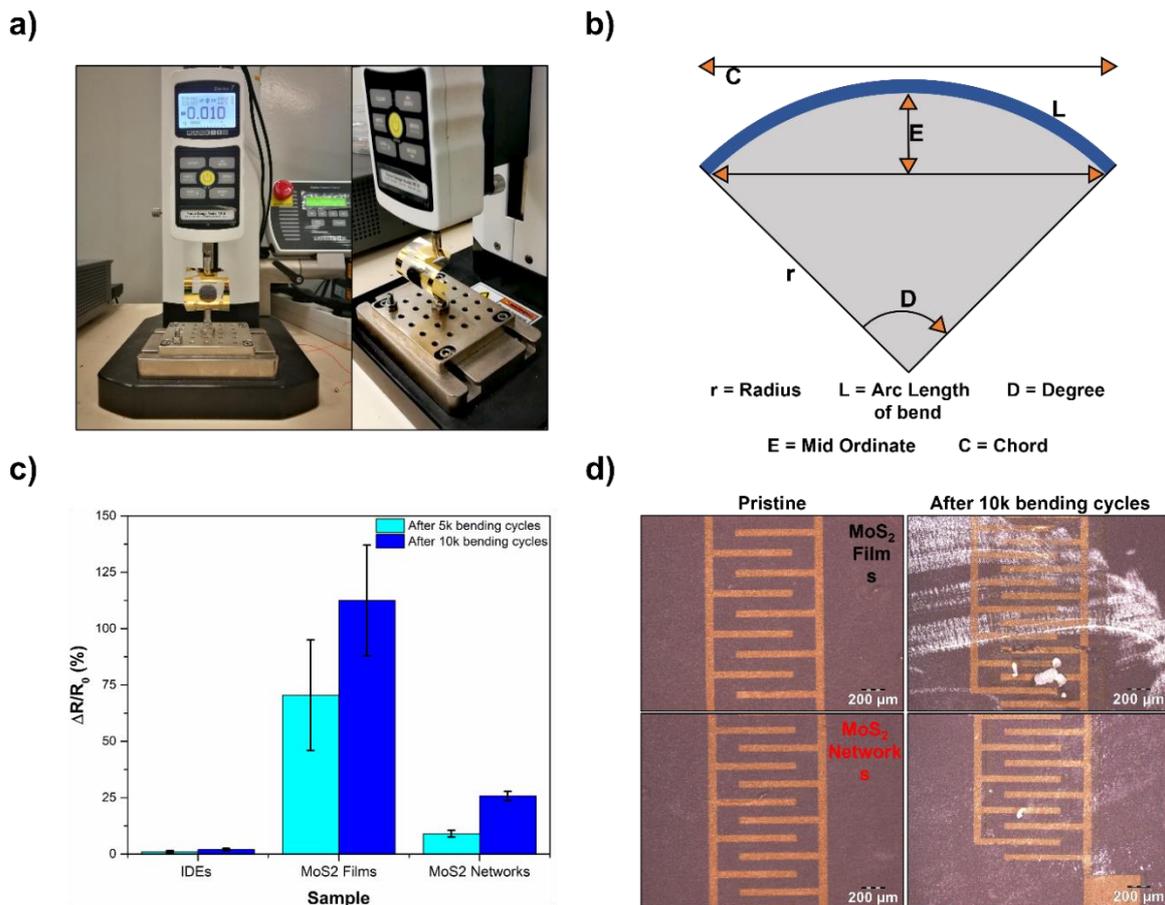
Figure 5-12 : a) Experimental setup. **b)** Sketch of the samples subjected to bending deformation. **c)** Variation of the relative channel resistance $\Delta R/R_0$ of bare IDEs, MoS_2 films, and MoS_2 networks upon 5k and 10k bending cycles, along with related **d)** optical images of MoS_2 films and networks before (left) and after (right) mechanical deformation.

Concerning the mechanical investigation, we set an overall deformation of 2 cm, bending radius (r) = 1 cm and degree of bend (D) = 210°. As shown in Figure 5-12, the electrical resistance (R) of the samples increases upon multiple (5k and 10k) bending cycles due to crack formation within both MoS_2 films and networks. However, MoS_2 networks exhibit superior

robustness, characterized by significantly lower variations of relative channel resistance ($\Delta R/R_0$) with respect to pristine films. This outcome supports the network formation, whereby a covalent interconnected system exhibits superior mechanical robustness, fatigue resistance, and electrical properties.

In order to corroborate the exclusive network formation in solution-processed TMDs upon exposure to dithiolated molecules, we performed analogous multiscale characterizations on MoS_2 samples treated with monothiolated TP molecules (Figure 5-13), keeping constant the equivalent concentration of functional thiol groups as in BDT case. Therefore, an identical *in-situ* protocol was used for the functionalization steps, soaking the samples within a 100 mM solution of TP in anhydrous hexane under N_2-controlled atmosphere.
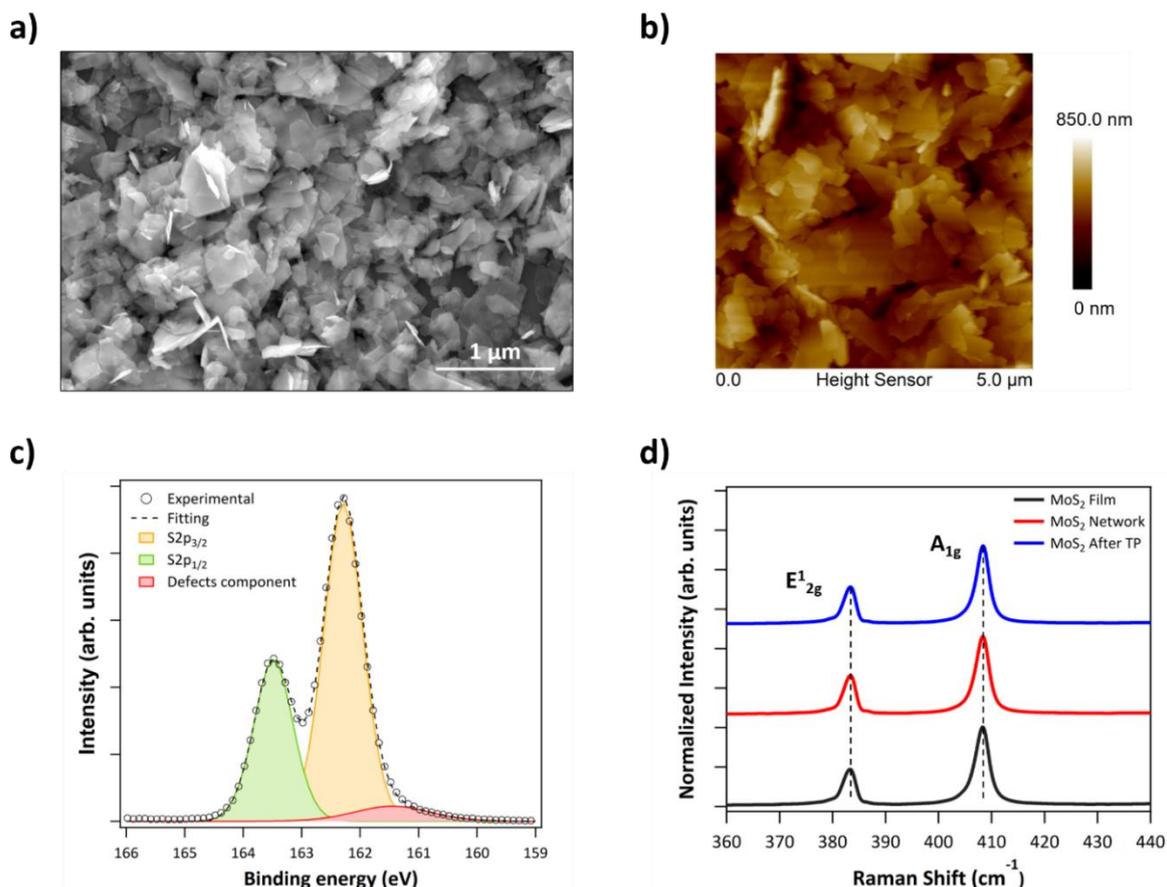
Figure 5-13 : a) SEM image, **b)** AFM image and **c)** HR-XPS S2p spectrum of MoS_2 upon TP exposure. **d)** Raman spectra of MoS_2 films, networks and TP-functionalized films.

Morphological and structural characterizations, based on AFM and SEM imaging, indicate minor differences between pristine films, networks and TP-functionalized films, as expected for a molecular-level chemical functionalization. XPS confirms the V_S healing process, since

the defects component deconvoluted from the S2p high-resolution spectra decreases upon TP exposure. The ratio of the defects component area to the overall S2p region diminishes after functionalization, from 8.0 % to 5.0 % analogously to the BDT case. This confirms the decrease of defect density when thiolated molecules are employed to heal V_S in solution-processed MS_2. Another evidence of V_S healing mechanism comes from the Raman analysis. In fact, FWHM of E^1_{2g} and A_{1g} characteristic modes decreases upon thiol exposure, both for MoS_2 networks and TP-functionalized films. Ultimately, the treatment with thiolated molecules promotes the healing of V_S, thereby attenuating the characteristic defect-activated modes[169].

Static water contact angle measurements show a shift of the average value upon thiol exposure, both for BDT and TP (Figure 5-14). Due to the similar molecular structure of the two functionalizing agents — they differ just for one thiol group — a similar hydrophobic nature is expected for BDT-linked networks and TP-functionalized films. The results are summarized in Table 5-2 and support the network formation along with increased connectivity due to the bridging of adjacent flakes (after BDT), since the presence of free thiol groups would have shifted the samples towards a more hydrophilic character[174]. MoS_2 films are not stable in water and detachment is observed. Thus, contact angle measurements are performed recording the values during the initial stage of the wetting procedure (< 30 s) on fresh samples to ensure repeatability and reproducibility.
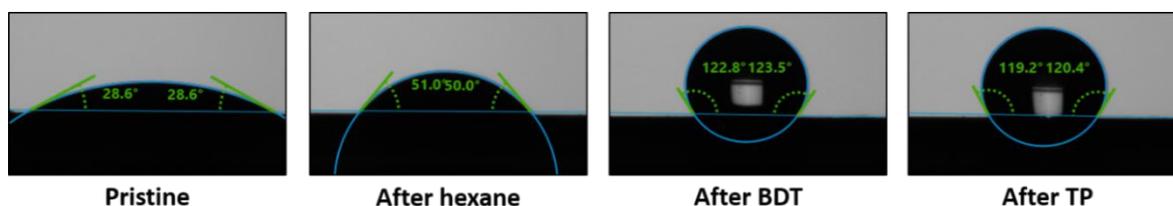

Figure 5-14 : Optical images with contact angle analysis of pristine MoS_2 films and upon thiol exposure, both BDT and TP molecules. An additional test is performed to rule out undesired effects due to the reaction solvent (hexane).
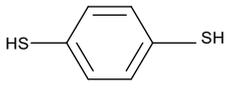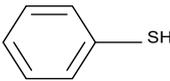
MoS$_2$ (Drop-cast)	Average WCA (°)
Pristine (Film)	30 ± 3
After hexane	53 ± 2
After BDT (Network)	121 ± 2
After TP	117 ± 2

Table 5-2 : Static water contact angle for MoS$_2$ films upon different treatments. The standard deviation values, for each sample, are estimated from 10 independent measurements.

Similarly to the pristine systems, TP-functionalized MoS$_2$ films display poor water stability and film detachment is observed. Therefore, dithiolated molecules, such as BDT, are needed for network formation and production of water-stable materials. Once the MoS$_2$ flakes are linked, they behave as interconnected system, less soluble and able to withstand solvation processes promoted by the aqueous environment. We believe that the same observations arising from the results of TP-functionalized MoS$_2$ samples can be extended to WS$_2$ and ReS$_2$, due to the similar reactivity and physicochemical properties of these systems[41,175].

To further investigate the reaction between MoS$_2$ and thiols (BDT and TP), we performed NMR analysis mimicking the same operating conditions employed for the network formation. Hence, we carried out the reaction under N$_2$-controlled atmosphere, at room temperature and using a non-polar solvent. MoS$_2$ (3 mg, 0.02 mmol) is sonicated in cyclohexane-d_{12} (2 ml) for 10 min prior to adding BDT (15 mg, 0.10 mmol) and stirring the solution for 24h. At the same time, a control experiment in absence of MoS$_2$ is performed. Figure 5-15 shows the NMR spectra related to the reaction between MoS$_2$ and BDT acquired 1, 2, 4, 16, and 24h after the addition of thiolated molecules. No disulfide species are formed under any circumstances[176], ruling out any dimerization reaction and supporting the functionalization reaction as main pathway governing the V$_S$ healing process[124,130]. Analogous results are obtained for TP.
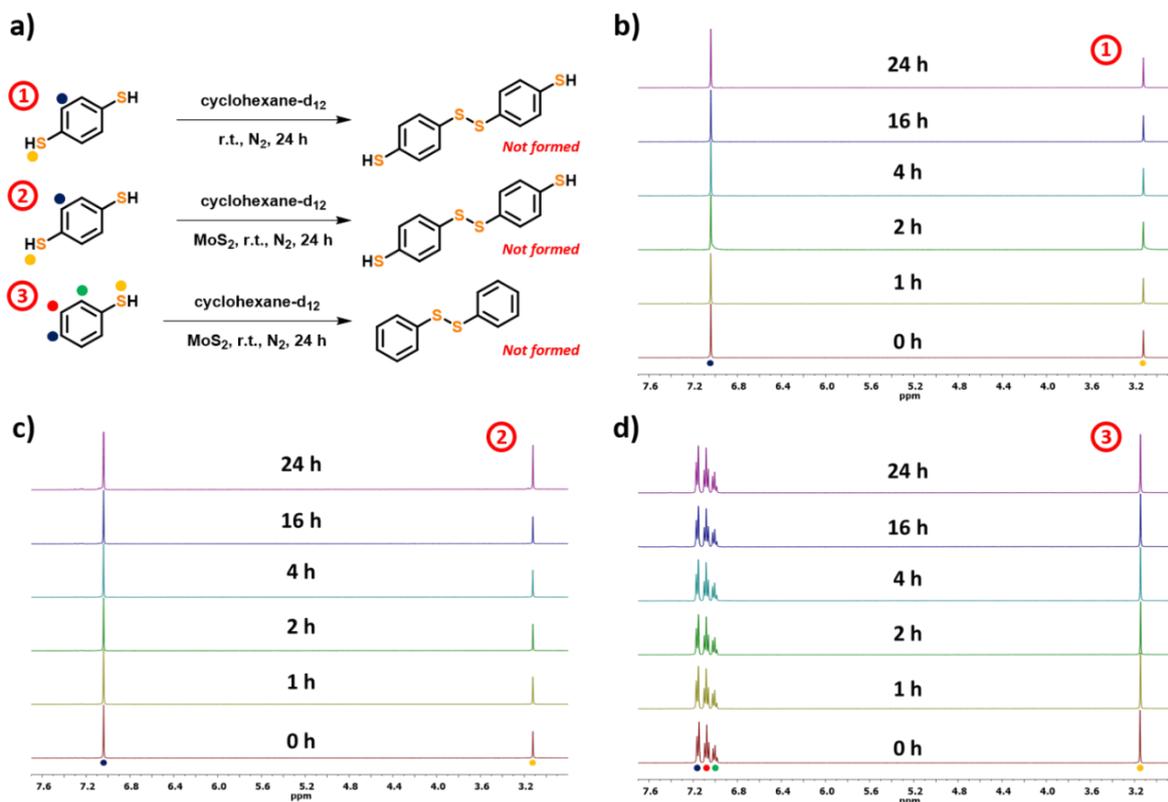
Figure 5-15 : a) Tested reactions between MoS_2 and thiolated molecules under exam (TP and BDT). Related NMR spectra at different time intervals for **b)** BDT without MoS_2 (control experiment), **c)** MoS_2 + BDT and **d)** MoS_2 + TP.

The core of this project aims to explore the effects of network formation on electrical devices based on covalently interconnected TMD networks. The covalent bridging of individual MS_2 flakes with π-conjugated molecules is expected to improve the material's electrical properties, especially its electrical connectivity, where long-range electronic delocalization is advocated[16]. Dielectrically-gated TFTs based on solution-processed TMDs show poor current switching (I_{ON}/I_{OFF} < 10)[18], encouraging one to focus on TFTs where the semiconductor layer is electrolytically gated by means of an ionic liquid (IL) solution, exploiting the inherent disorder and related porosity of the deposited materials. For LG-TFTs based on solution-processed TMD flakes, the liquid dielectric penetrates the internal free volume of the semiconducting material, thus gating the device volumetrically[17]. We thus investigated the performance of TFTs based on pristine MoS_2 films and networks (Figure 5-16). All our LG-TFT measurements are performed under N_2-controlled inert atmosphere (inside glovebox), to avoid side effects of environmental adsorbates, such as water and oxygen, that can induce strong p-doping[19].
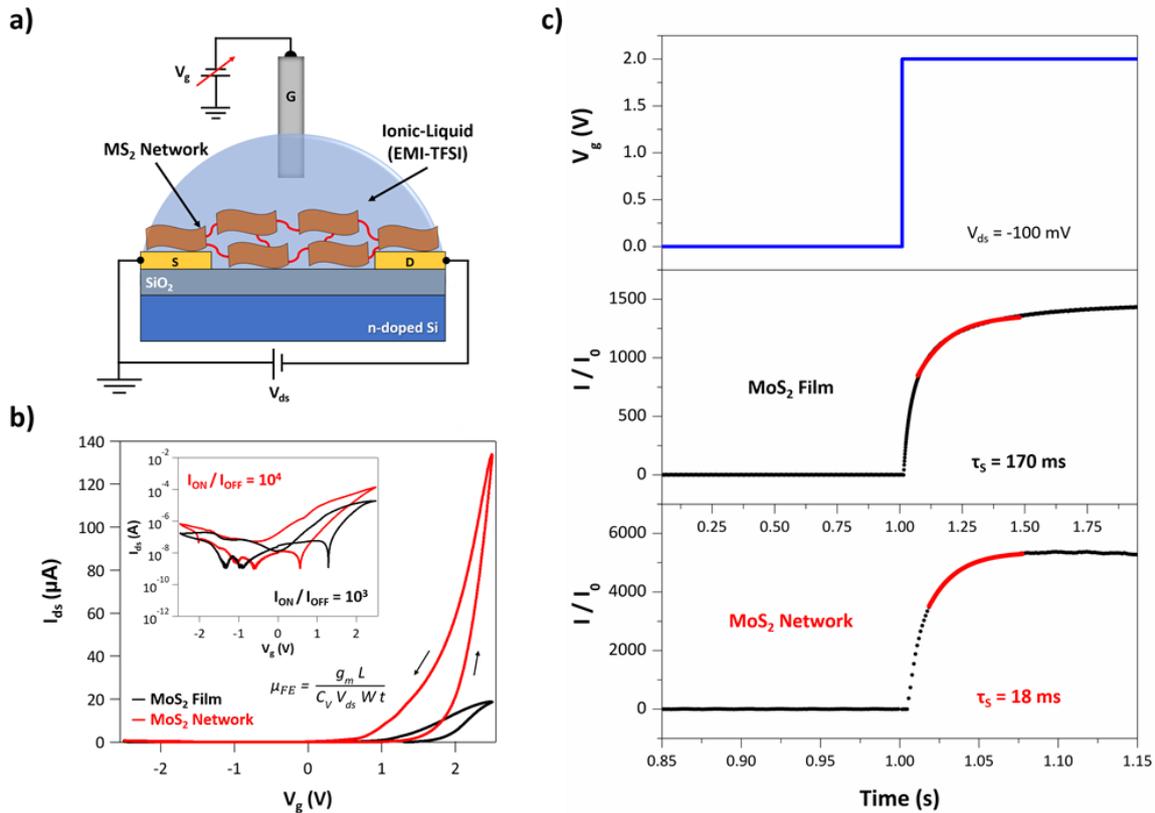
Figure 5-16 : a) LG-TFT geometry. **b)** Transfer curves for MoS_2 films and networks with V_{ds} = -100 mV and V_g sweeping from -2.5 V to +2.5 V. *Inset:* log-scale current characteristics and equation to calculate μ_{FE}. **c)** LG-TFT switching characteristics under V_g step and corresponding time-dependent normalized current response (I/I_0). The red line delimits the range in which a non-linear fitting can be used to extrapolate τ_S.

Figure 5-16 displays the typical transfer curves (I_{ds} *vs.* V_g) of LG-TFTs based on MoS_2 films and networks. Both show n-type transfer characteristics, with the latter featuring an overall superior performance. In particular, MoS_2 networks exhibit higher μ_{FE} up to 10^{-2} cm^2 V^{-1} s^{-1} and I_{ON}/I_{OFF} ratios up to 10^4, one order-of-magnitude greater than pristine MoS_2 films. No significant differences in threshold voltage (V_{TH}) are observed upon bridging of flakes, proving that BDT linkers mainly affect the conductivity of the networks in terms of μ_{FE} and not the charge carrier density (doping effect)[177]. Likewise, a similar outcome is observed for the τ_S of LG-TFTs based on MoS_2 films and networks, while applying a step-like V_g stimulus and measuring the device time-dependent current response. Here, τ_S is ~170 ms for MoS_2 films and ~18 ms for the networks, meaning that covalently interconnected systems result in one order-of-magnitude faster devices, with SoA switching performance for transistors of this kind[17]. The reproducible 10-fold enhancement of the device performance observed for MoS_2 networks supports the considerations envisaged for interconnected systems by dithiolated and π-conjugated linkers, unachievable for monothiolated TP molecules that, instead, do not allow network formation.

In order to prove an extensive penetration of functionalizing molecules through the whole film, we evaluated the electrical properties of MS_2 films exposed to BDT by measuring back-gated TFTs, probing the charge carrier transport at the device SiO_2 bottom interface. As shown in Figure 5-17, the exposure to dithiolated molecules promotes an enhancement of electrical performance comparable to that reported in Figure 5-16, namely the μ_{FE} increases by one order-of-magnitude with respect to pristine films. This is consistent with V_S passivation and interflake bridging by BDT molecules *via* diffusion throughout the whole film. Figure 5-17 also shows the typical limitations of TMD back-gated TFTs (*e.g.*, low current ratios, scant absolute μ_{FE}, large hysteresis), supporting our choice to focus on LG-TFTs to assess the network formation.
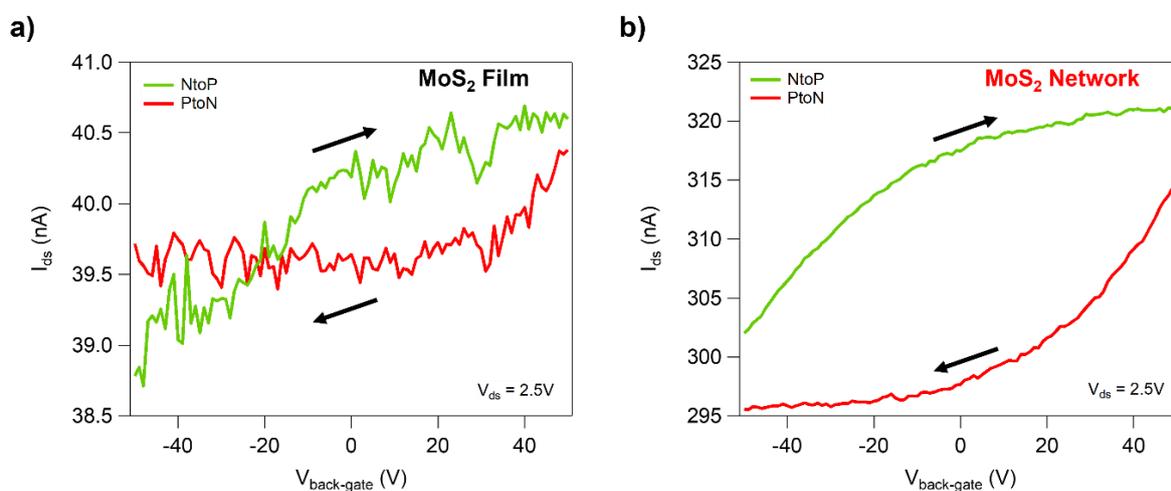

Figure 5-17 : Transfer curves for MoS_2 TFTs based on **a)** films and **b)** networks in back-gate configuration. All curves are recorded at V_{ds} = 2.5 V and sweeping $V_{back-gate}$ from -50 to + 50 V.

Moreover, to probe the excess of thiolated molecules during the functionalization steps, we measured the TFT characteristics of MoS_2 samples exposed to two rounds of BDT. No significant changes in μ_{FE} are observed upon a second exposure to BDT (Table 5-3), confirming that one functionalization step, under our experimental conditions, is sufficient to saturate and heal V_S, maximizing the number of molecules used to bridge adjacent flakes.

Sample	μ_{FE} / $\mu_{FE, Film}$
MS$_2$ Film	1
After BDT (1st functionalization)	10 ± 1
After BDT (2nd functionalization)	10 ± 1

Table 5-3 : Variations of μ_{FE} for MoS$_2$-based TFTs before and after single and double exposure to BDT.

The network formation results in an enhancement of the electrical properties for MoS$_2$ LG-TFTs, however such an improvement is also reproducible in WS$_2$ and ReS$_2$-based devices, proving that the V$_S$ healing process (using dithiolated molecules) represents a universal strategy to form TMD interconnected systems with enhanced performance (Table 5-4).

TMD	Polarity	μ_{FE} (cm^2 V^{-1} s^{-1})		I$_{ON}$/I$_{OFF}$		V$_{TH}$ (V)	
		Film	Network	Film	Network	Film	Network
MoS$_2$	n-type	10^{-3}	10^{-2}	10^3	10^4	1.9 ± 0.1	1.8 ± 0.1
WS$_2$	n-type	10^{-3}	10^{-2}	10^3	10^4	2.0 ± 0.1	1.9 ± 0.1
ReS$_2$	n-type	10^{-4}	10^{-3}	10^3	10^4	1.8 ± 0.1	1.8 ± 0.1

Table 5-4 : Electrical properties of MS$_2$-based LG-TFTs. Measurements are performed under N$_2$ controlled atmosphere, recording I$_{ds}$ while sweeping V$_g$ between -2.5 and +2.5 V with V$_{ds}$ = 100 mV.

Table 5-4 shows minimal variations of V$_{TH}$ upon BDT exposure. Our functionalization approach is applied on drop-cast TMD thin films with high defect density, complexity, and disordered nature, whereby grain boundaries and edges dominate the overall charge carrier transport. Therefore, despite our functionalization strategy enhances the overall electrical performance of MS$_2$ networks by bridging adjacent flakes thanks to dithiolated linkers, V$_S$ represent a limited share of the overall sample defectiveness, and it is just one of many factors responsible for the hysteretic behaviour of our devices.

The overall electrical device performance is assessed by the figures of merit (FOM) reported in Table 5-4. In particular, μ_{FE} is calculated from the transfer curves (I$_{ds}$ *vs.* V$_g$) as[17]:

$$\mu_{FE} = \frac{g_m \, L}{C_V \, V_{ds} \, W \, t}$$

where g_m is $(\partial I_{ds}/\partial V_g)_{MAX}$, L is the channel length (2.5 μm), C_V is the volumetric capacitance, V_{ds} is the source-drain voltage, W is the channel width (10^4 μm), and t is the film/network thickness. To estimate C_V, we performed CV using a three-electrode cell set-up with a Ag/AgCl reference electrode and a Pt-wire counter electrode. The electrochemical measurements for MoS_2 and WS_2 are already reported in ref.[17], hence the ReS_2 measurements are done with the same procedure. ReS_2 is spray-coated onto ITO-coated glass to form the working electrode (A ~ 2.3 cm^2, t ~ 400 nm), and then it is submerged within the ionic liquid EMI-TFSI (degassed for 12h in a vacuum oven at 70°C). Finally, CV is performed in a small voltage window (-0.2 V to +0.2 V) under ambient conditions at different scan rates (Figure 5-18).
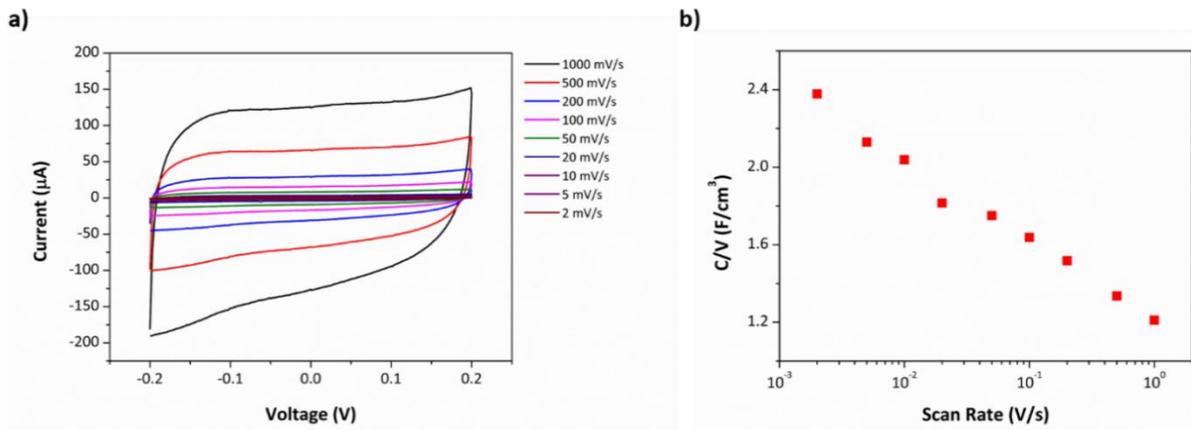
Figure 5-18 : a) Cyclic voltammograms recorded for ReS_2 films at different scan rates. **b)**, Scan rate dependence on sample capacitance.

From the voltammograms, C_V is calculated as:

$$\frac{C}{V} = \frac{1}{A\, t\, \Delta V\, (\frac{dV}{dt})} \int_{-0.2}^{0.2} I\, dV$$

where ΔV is the voltage window and dV/dt is the scan rate in Figure 5-18. We estimated C_V ~2.1 F/cm^3 (at 5 mV/s), similar to 1.9 and 1.2 F/cm^3 already reported for MoS_2 and WS_2[17].

Furthermore, we tested the electrical properties of TP-functionalized MoS_2 films as well. These show a slight increase of performances upon thiol exposure due to the healing of V_S (Figure 5-19), although such a variation is not comparable with the enhancement recorded upon network formation. In fact, networks exhibit $μ_{FE}$ one order-of-magnitude higher than films, whereas TP-functionalized films show higher $μ_{FE}$ by only a factor 2-3.
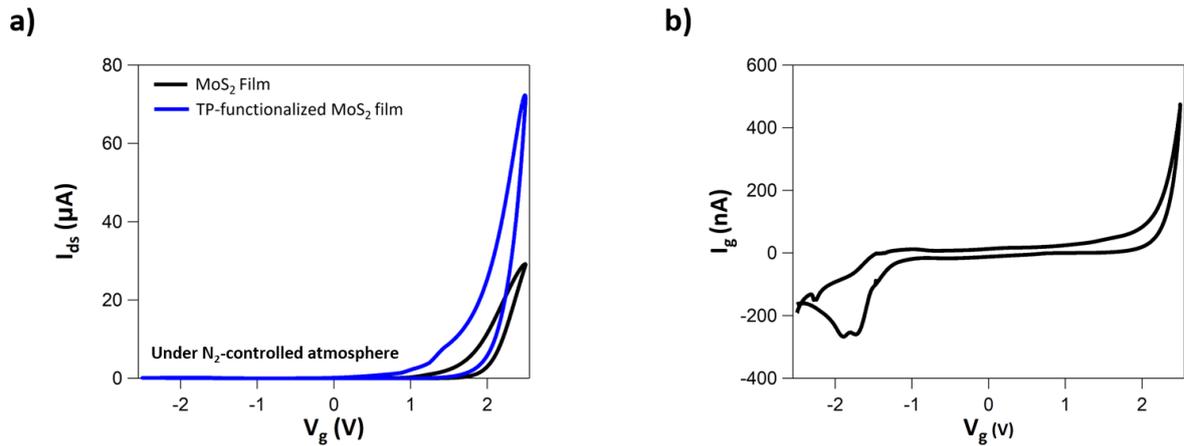
Figure 5-19 : a) Comparison between two typical transfer curves for pristine MoS₂ (black) and TP-functionalized MoS₂ (blue) films. **b)** Typical leakage curve for MoS₂ LG-TFTs. All curves are recorded for V_{ds} = -100 mV and sweeping V_g from -2.5 to +2.5 V.

To investigate the effects of the linker structure on the electrical performance of LG-TFTs, we explored the functionalization of MoS₂ films with benzene-1,4-diamine (PPD) and propane-1,3-dithiol (PDT). As for Figure 5-20, MoS₂ films exposed to PPD (*i.e.* conjugated core, but no thiol groups) exhibit no improvement of current compared to pristine samples, with only a mild decrease of hysteresis, likely due to the electrostatic screening of charge traps by free PPD trapped molecules within the film[178]. This confirms the need of thiol functional groups to form networks in defective solution-processed MS₂.
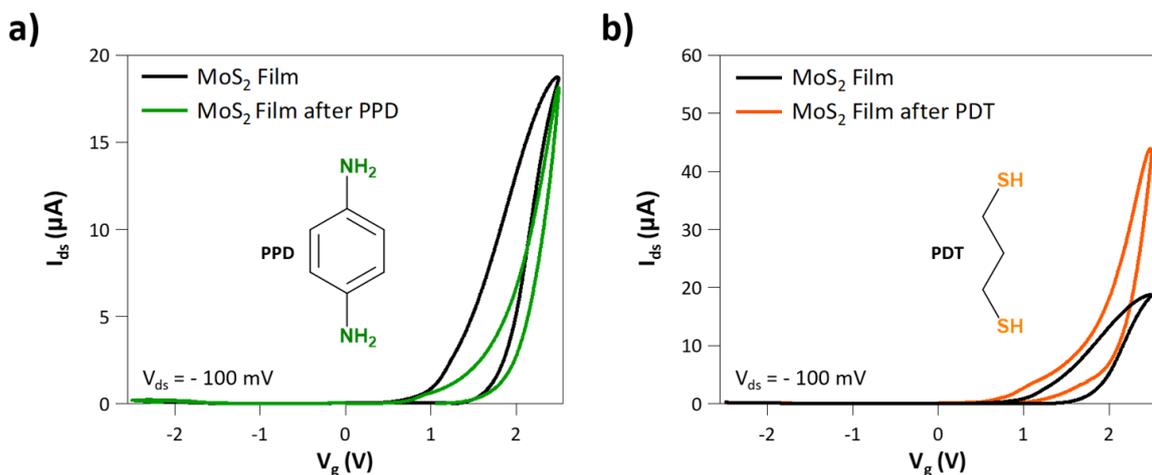

Figure 5-20 : Transfer curves for MoS₂ LG-TFTs **a)** before and after treatment with PPD and **b)** before and after treatment with PDT. All curves are recorded at V_{ds} = -100 mV, using EMI-TFSI as electrolyte and a Pt wire as gate electrode. The molecular structures of PPD and PDT are indicated.
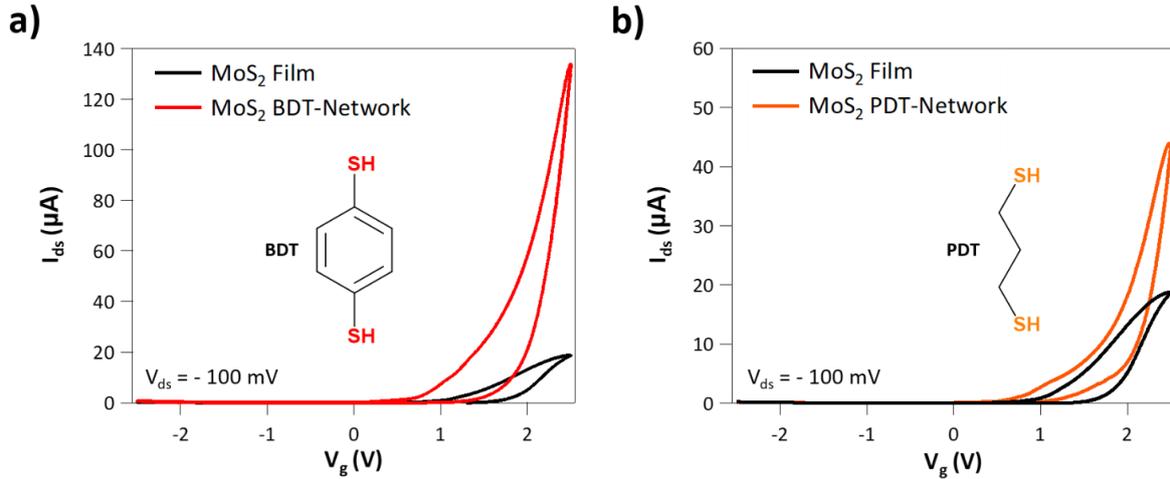
Figure 5-21 : Transfer curves for MoS$_2$ LG-TFTs **a)** before and after treatment with BDT linkers and **b)** before and after treatment with PDT linkers. All curves are recorded at V$_{ds}$ = -100 mV, using EMI-TFSI as electrolyte and a Pt wire as gate electrode. The molecular structures of BDT and PDT are also indicated.

LG-TFTs based on MoS$_2$ networks functionalized with PDT exhibit current and µ$_{FE}$ 2 to 3-times higher than pristine films (Figure 5-20). Nevertheless, the lack of a delocalized electron system in PDT molecules makes such a linker no rival for BDT, with one order-of-magnitude increase in the main figures of merit (Figure 5-21). This highlights the importance of interflake transport on the ultimate device performance.

In addition, we estimated the switching time for MoS$_2$-based LG-TFTs upon TP exposure and network formation. TP-functionalized films have τ$_S$ comparable to pristine ones, further highlighting the requirement of forming a covalently interconnected system to achieve high electrical device performance. τ$_S$ is calculated by fitting the device transient current (Figure 5-22), before reaching a steady-state response in the resulting I/I$_0$ *vs.* time curves, with the non-linear growth equation:
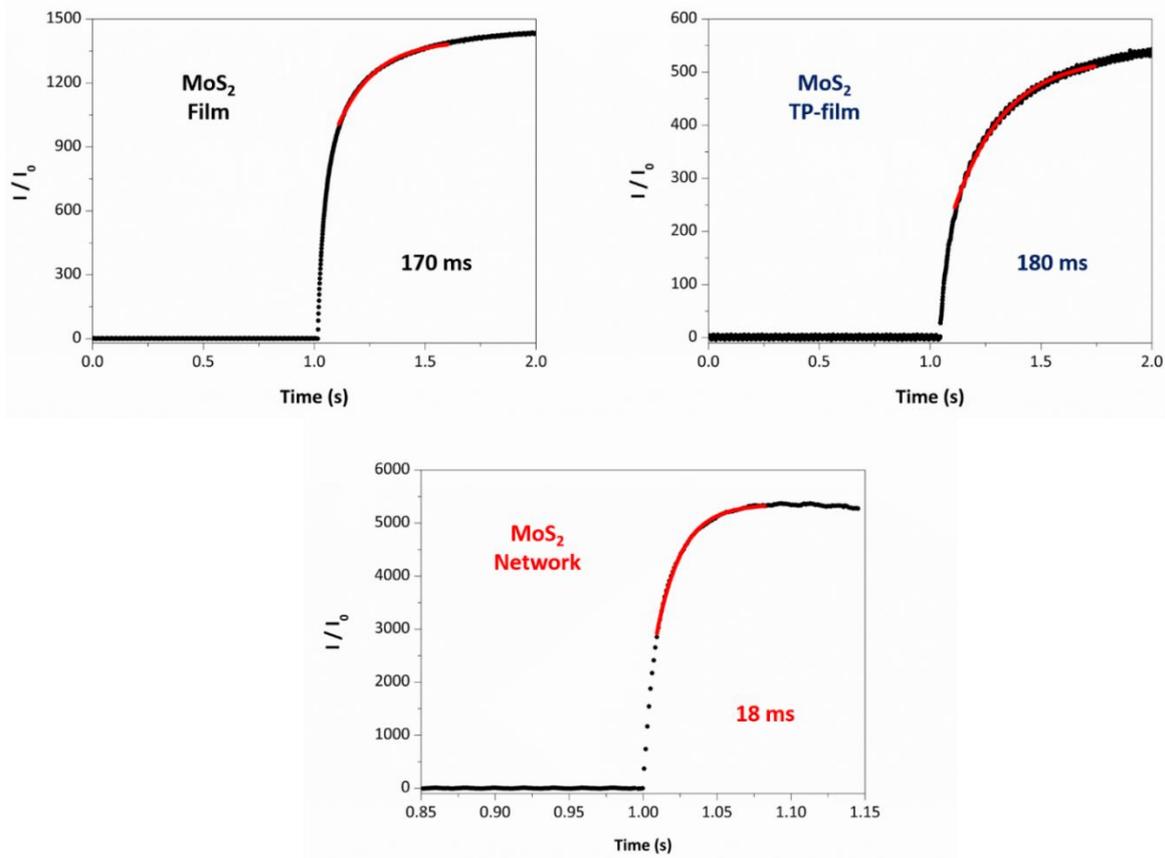
$$I = I_0 + A * e^{-\frac{(t-t_0)}{\tau_S}}$$

Figure 5-22 : Current *vs.* time curves (normalized to starting current I_0) for MoS_2 films (black), TP-functionalized films (blue) and networks (red) with related τ_S. The red line delimits the range in which a non-linear growth equation can be used to extrapolate τ_S.

To cast light on the charge transport mechanism responsible for the enhancement of electrical properties in MoS_2 networks, we evaluated their electrical characteristics (I-E) as a function of temperature (T) in high vacuum (10^{-6} Torr) (Figure 5-23). It is worth mentioning that such a formalism, related to the I-E analysis, is common in charge transport modelling[179]. The samples are prepared on SiO_2/Si substrates with pre-patterned Au IDEs, and the average field E is calculated from $V = E \times d$, where V is the applied bias voltage and *d* is the IDE channel distance (2.5 µm). The charge transport characteristics are measured with and without a back-gate voltage (V_G^{Back}) on the n^{++}-Si substrate. At room temperature, and with $V_G^{Back} = 0$, minor differences are found between the I-E traces of MoS_2 films and networks. For T ranging from 250 to 300 K, the current characteristics indicate Schottky emission as the dominant charge transport mechanism. In agreement with that, the formation of a Schottky barrier with height Φ_B at the metal/MoS_2 interface is already reported[180].
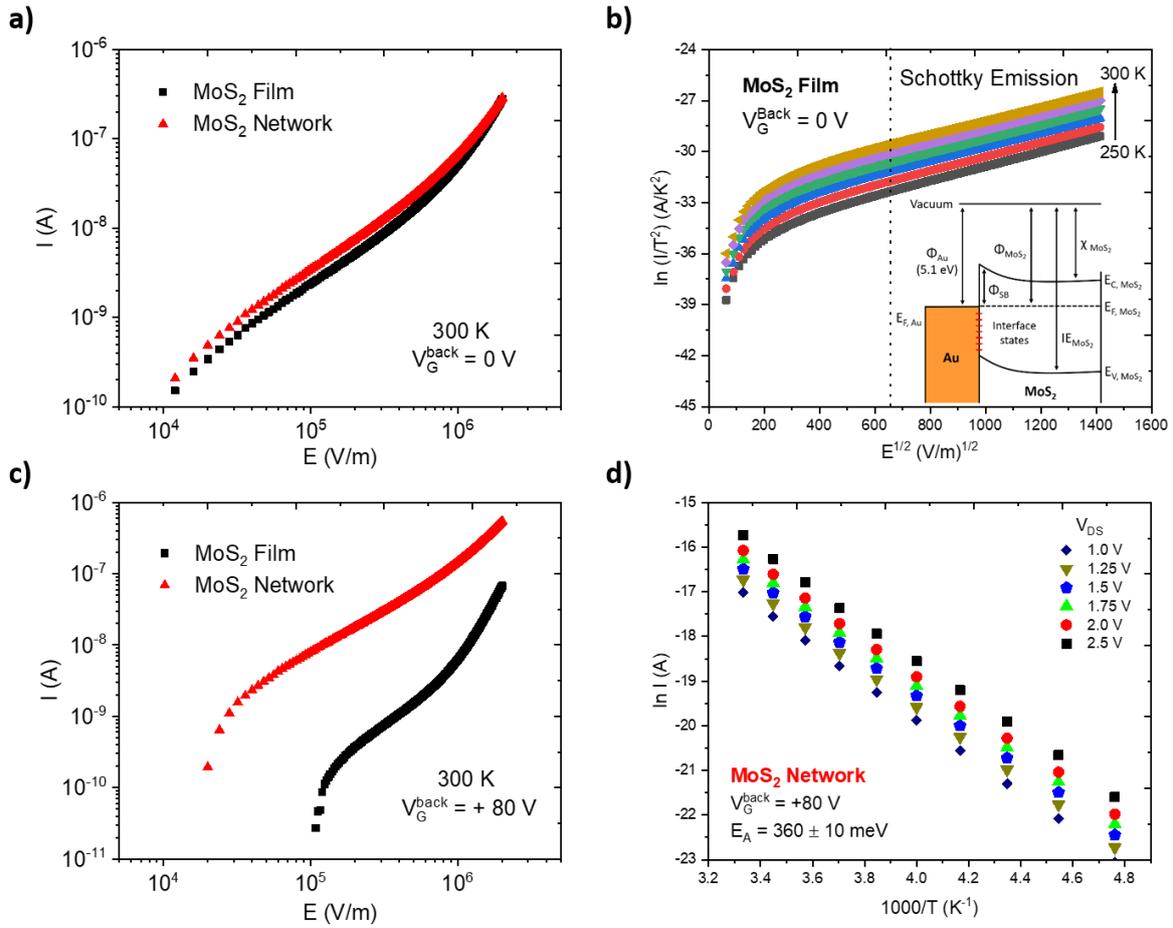
Figure 5-23 : a) 300K I-E curves for $V_G^{Back} = 0$ for MoS$_2$ films (black) and networks (red). **b)** Schottky plot for MoS$_2$ film for $V_G^{Back} = 0$ V. *Inset*: Band diagram for Au/MoS$_2$ Schottky barrier interface. **c)** 300K I-E characteristic with for $V_G^{Back} = +80$ V in MoS$_2$ films (black) and networks (red). **d)** Arrhenius plot for MoS$_2$ network for $V_G^{Back} = +80$ V.

We therefore adopted the thermionic emission formalism[179]:

$$I = A\,A^*\,T^2\,exp\left(\frac{-q\,(\phi_B - \sqrt{qE\,/\,4\pi\varepsilon_r\varepsilon_0})}{k_B T}\right)$$

where A is the charge injection area, A* is the effective Richardson constant, T is the absolute temperature, k_B is the Boltzmann constant, Φ_B is the Schottky barrier height, ε_r is the MoS$_2$ dielectric constant (ε_r ~4.8 for multilayer MoS$_2$ from ref.[181].) and ε_0 the vacuum permittivity. From that, we estimated, for the Au/MoS$_2$ interface, a $\Phi_B = 366 \pm 1$ meV for MoS$_2$ pristine films, $\Phi_B = 285 \pm 7$ meV for MoS$_2$ networks, and $\Phi_B = 288 \pm 16$ meV for TP-functionalized MoS$_2$ (Figure 5-24 and Figure 5-25).
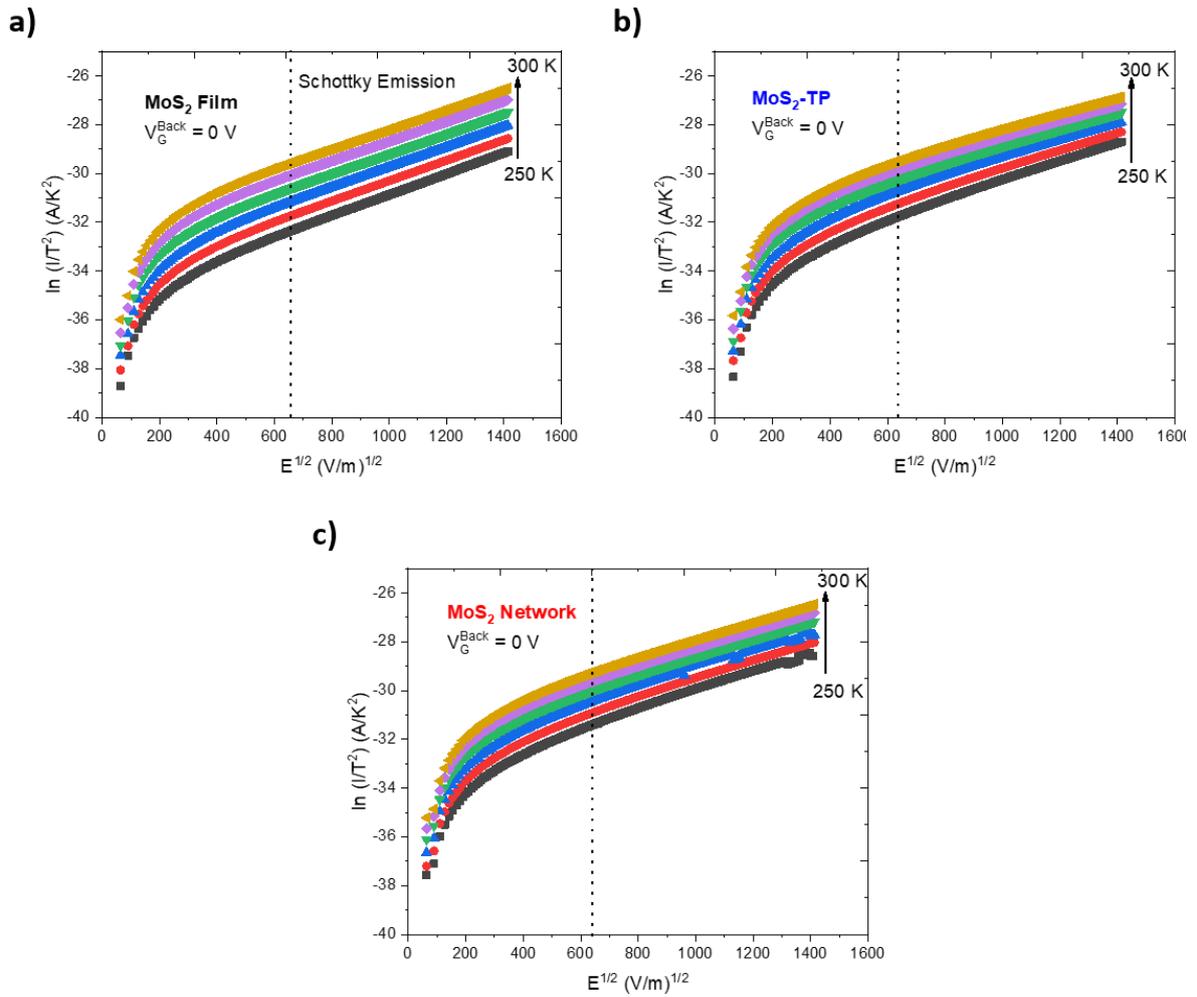
68

Figure 5-24 : Ln I(/T^2) *vs.* E$^{1/2}$ for **a**, MoS$_2$ pristine films **b**, TP-functionalized samples and **c**, MoS$_2$ networks in a T range 250-300 K without an external gate bias on the back electrode of Si/SiO$_2$/IDE test patterns.

Considering the slope of ln (I/T^2) *vs.* E$^{1/2}$ curves reported in Figure 5-24, we extrapolated Φ_B from the Arrhenius plots as in Figure 5-25.
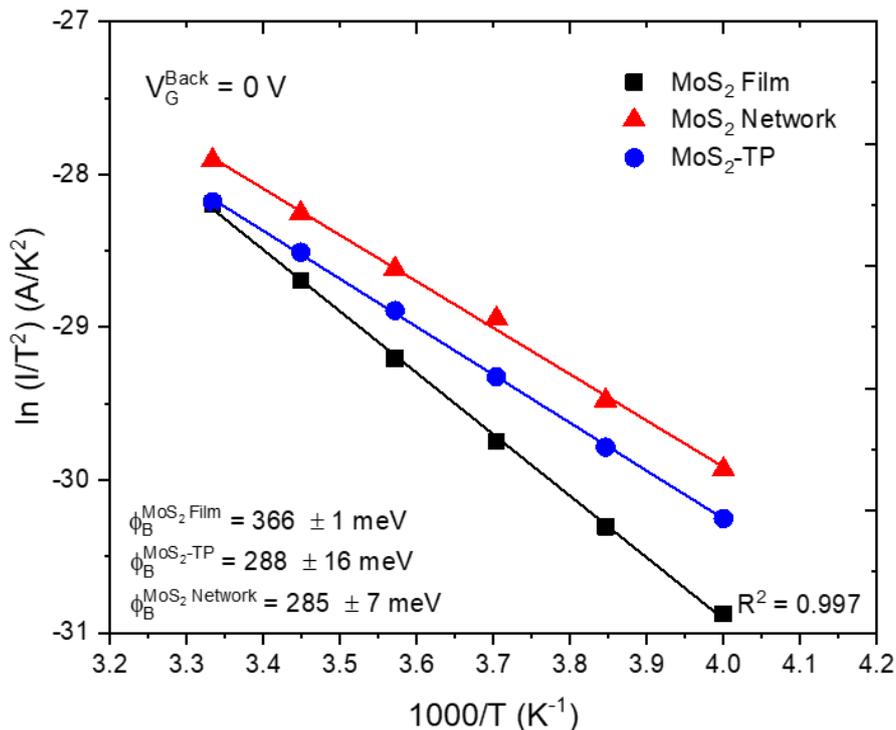
69

Figure 5-25 : Φ_B calculated from the Schottky formalism for MoS_2 pristine films, TP-functionalized samples and MoS_2 networks. The errors in Φ_B correspond to the standard deviation of values calculated at different E.

Such a reduction of Φ_B upon both thiol functionalization (BDT and TP) points to either a modification of the Au work-function (Φ_{WF}) and/or healing of Au/MoS_2 interface states[182]. Measurements of Φ_{WF} for Au electrode surfaces by PESA, before and after thiol treatment, reveal a small decrease from 5.11 ± 0.02 eV (bare Au) to 4.97 ± 0.10 eV and 4.93 ± 0.07 eV for BDT and TP, respectively (Table 5-5).

Au Electrodes	Work function (eV)
Bare	5.11 ± 0.02
After Hexane	4.90 ± 0.05
After BDT solution	4.97 ± 0.10
After TP solution	4.93 ± 0.07

Table 5-5 : Work function from PESA for Au electrodes in pristine case, after solvent (hexane) exposure and after thiol treatment with BDT and TP molecules. The mean value and standard deviation are estimated from 10 measurements for each sample.

Such a small change in the Φ_{WF} is consistent with the passivation of Au/MoS$_2$ interfaces states — due to the healing of V$_S$ in the material — as the main cause of Φ_B reduction in thiol functionalized samples[182]. Such a small Φ_{WF} reduction, as well as similar values found for BDT and TP-functionalized samples, cannot explain the enhanced device performance exhibited by MoS$_2$ networks in LG-TFTs.

As for LG-TFTs, the superior electrical performance of MoS$_2$ networks arise when the Schottky barrier is attenuated by the application of a V_G[183]. In fact, under high V_G^{Back} = +80 V, a ~10-fold current difference is observed for MoS$_2$ networks when compared to films, especially at intermediate fields (E= 10^5-10^6 V/m), a condition that mimics the LG-TFT operating parameters (E ~10^5 V/m). For T = 250-300 K and E = 1 MV/m, MoS$_2$ films and networks have a thermally-activated current response (Figure 5-26) with significantly different E$_A$, *i.e.* 512 ± 12 meV and 360 ± 10 meV, respectively.
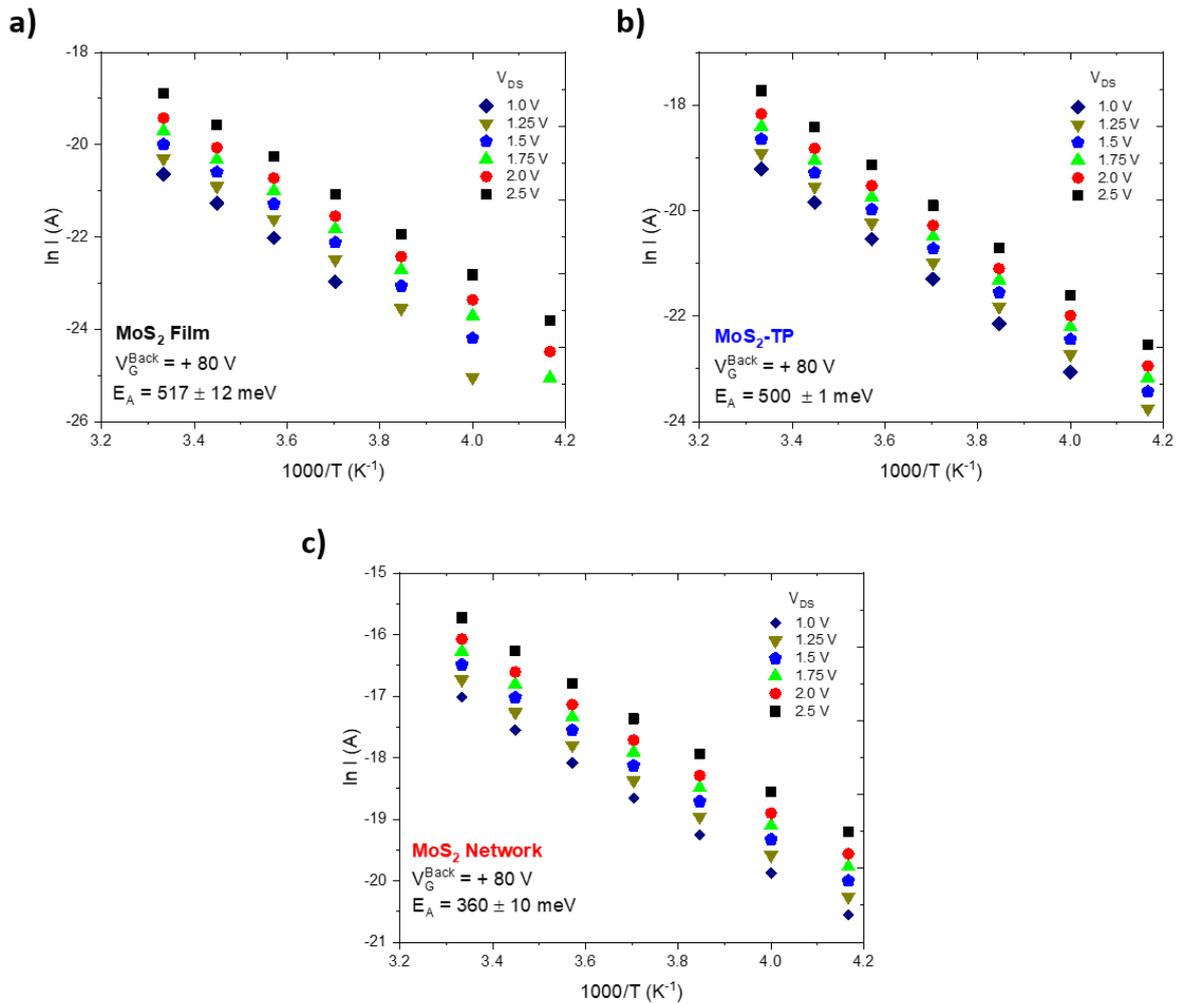

Figure 5-26 : Ln I *vs*. 1000/T for V_G^{back} = + 80 V in **a)** MoS$_2$ films **b)** TP-functionalized samples and **c)** MoS$_2$ networks. E$_A$ is calculated from the curve slope with errors associated to different applied bias on the IDEs (from 1-2.5 V, *i.e.*, E = 4 x 10^5 – 1 x 10^6 V/m).

E_A of hundreds of meV reflect the energy necessary to overcome the inter-flake barriers in MoS_2 systems[184], rather than low-energy (tens of meV) intra-flake conduction states[184]. By sweeping V_G^{Back} from -60 to +60 V, the T-dependent charge carrier mobility µ(T) of films and networks follows an Arrhenius relation, with lower E_A for networks (Figure 5-27). Hence, as inter-flake processes appear to be the limiting factor for charge transport within TMD thin-films[19], a reduced E_A points out an improved bulk connectivity among adjacent flakes (network formation). E_A for TP-functionalized samples (500 ± 1 meV) are only slightly smaller than the values found for pristine MoS_2 films, revealing a reduction of trap states caused by the V_S healing mechanism, without any further improvement due to the inter-flake connectivity.
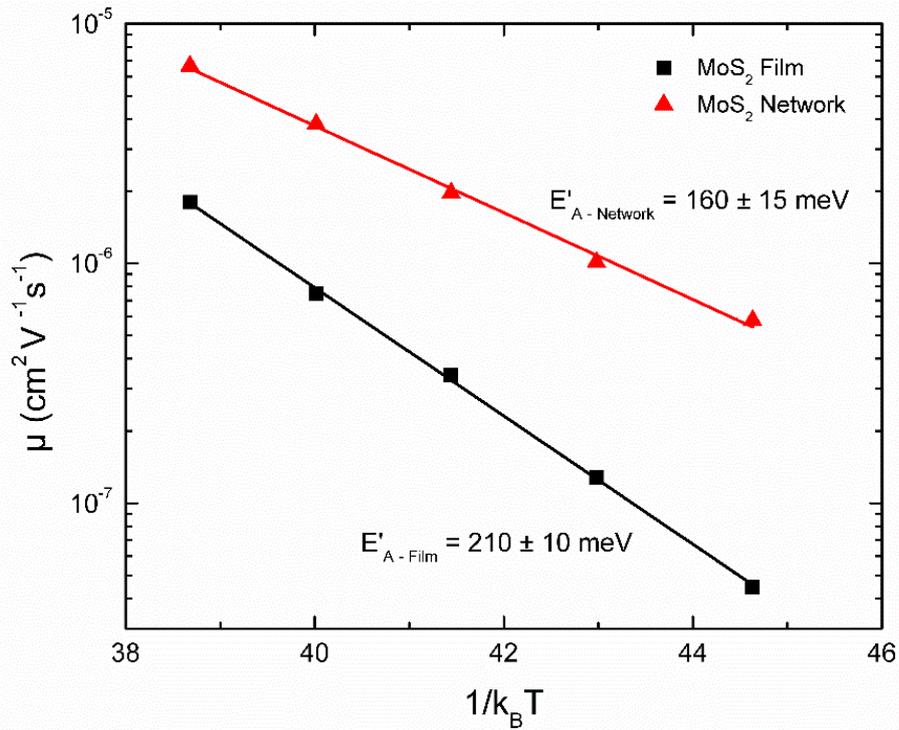

Figure 5-27 : Mobility Arrhenius plots for electrical devices based on MoS_2 films and networks in back-gated configuration. The mobility is extracted from the transfer curves for V_{ds} = 5 V and sweeping V_G^{back} from – 60 to + 60 V.

As a general counter proof, to support our proposed mechanism, we also performed MoS_2 *ex-situ* functionalization (Figure 5-28) by adding BDT molecules directly to the dispersion prior to film casting. The results confirm the need of the *in-situ* approach to produce long-range covalently interconnected TMD networks. In fact, the functional *ex-situ* inks have poor stability and start to aggregate within 30-45 min after mixing/sonication. Nevertheless, these inks present excellent patternability for IDEs, promoting an accurate deposition of the material in the contact area.
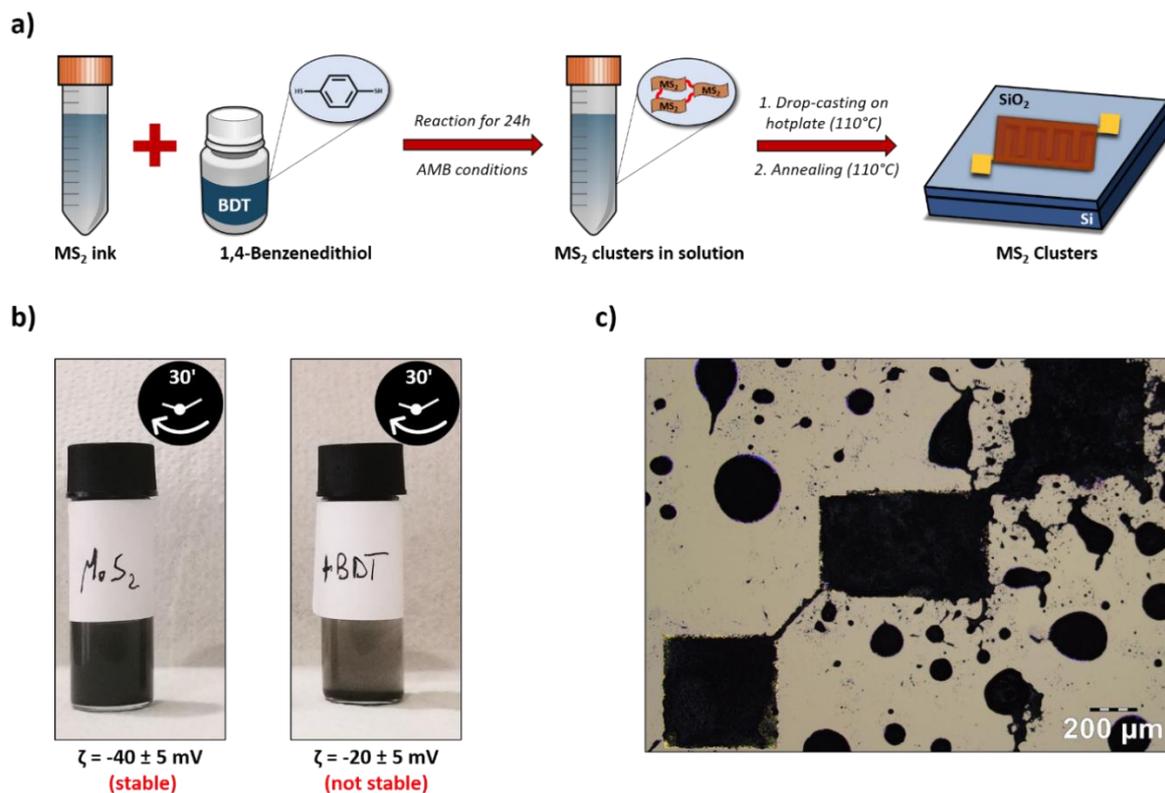
Figure 5-28 : a) Schematic illustration for the *ex-situ* functionalization of MS$_2$ inks with BDT. **b)** Outcome of stability test for pristine and BDT-functionalized MoS$_2$ ink, along with the related zeta potential values. **c)** Optical image of a IDE device covered with BDT-functionalized MoS$_2$ ink *via ex-situ* approach.

To further study the *ex-situ* reaction of MoS$_2$ with BDT, we performed dynamic light scattering (DLS) measurements (Figure 5-29). These results endorse the network formation by BDT molecules. However, the formation of a long-range network only happens when the layered materials are previously deposited on a surface (*in-situ*), where no precipitation can occur thereby hampering the flake bridging process.
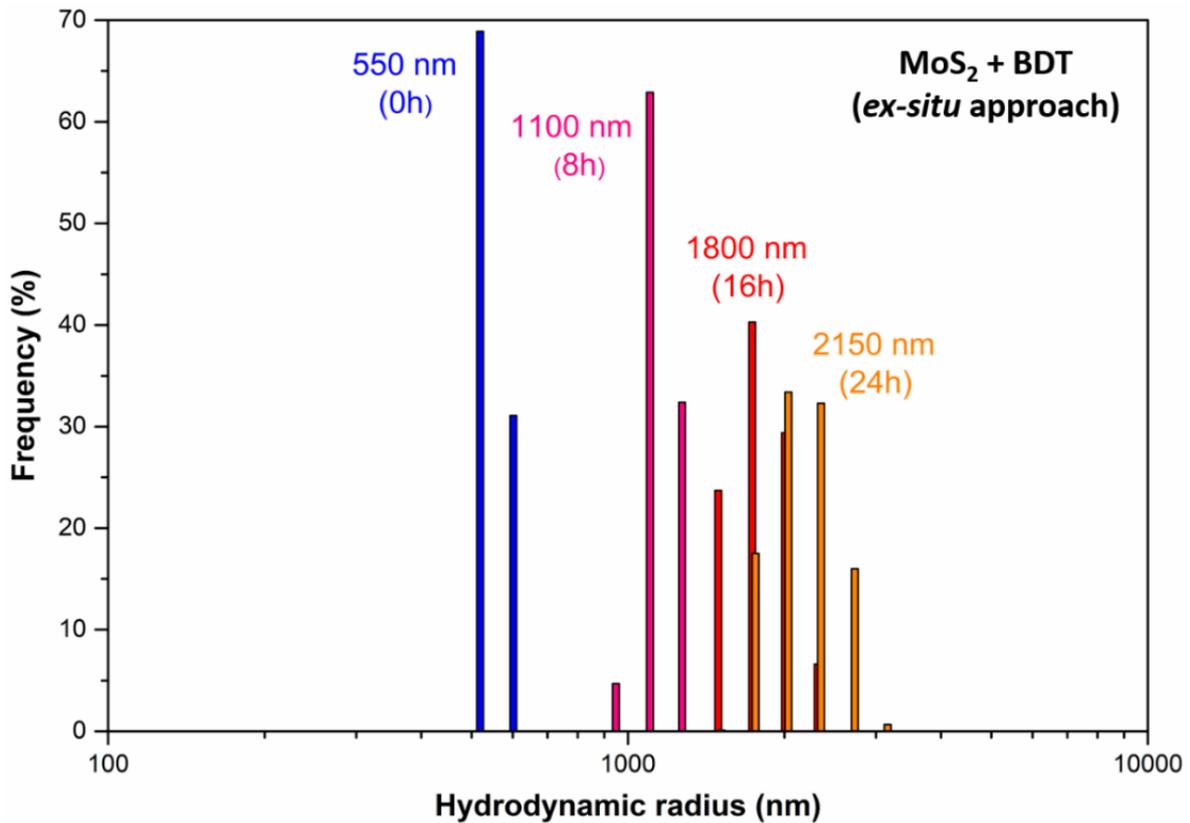
Figure 5-29 : Hydrodynamic radius of MoS₂ flakes dispersed in IPA and functionalized *ex-situ* with BDT molecules. Each sample is prepared by collecting 500 µl of the ink, successively subjected to 1:100 dilution and sonication/mixing steps.

Ex-situ BDT-functionalized MoS$_2$ films exhibit poor electrical performance, with μ_{FE} one order-of-magnitude lower than pristine MoS$_2$ films along with identical I_{ON}/I_{OFF}. As reported in Figure 5-30, AFM and SEM image show MoS$_2$ clusters embedded in an organic matrix, very likely produced by thiol oxidation reactions occurring within the solution exposed to ambient conditions. This prevents an optimal deposition onto IDEs and network formation, giving detrimental effects on electrical performance[185] (Table 5-6).

Static water contact angle measurements on *ex-situ* BDT-functionalized MoS$_2$ films show a decreased average value, with a consistent shift towards a more hydrophilic behaviour. In particular, *ex-situ* functionalized samples present an average contact angle ~96 ± 2°, different from the 121 ± 2° of *in-situ* samples. From the excellent patternability of the *ex-situ* functional inks towards Au IDEs and all other gathered information, we concluded that the material mainly consists of MoS$_2$ clusters embedded in a matrix presenting free thiol groups[174].
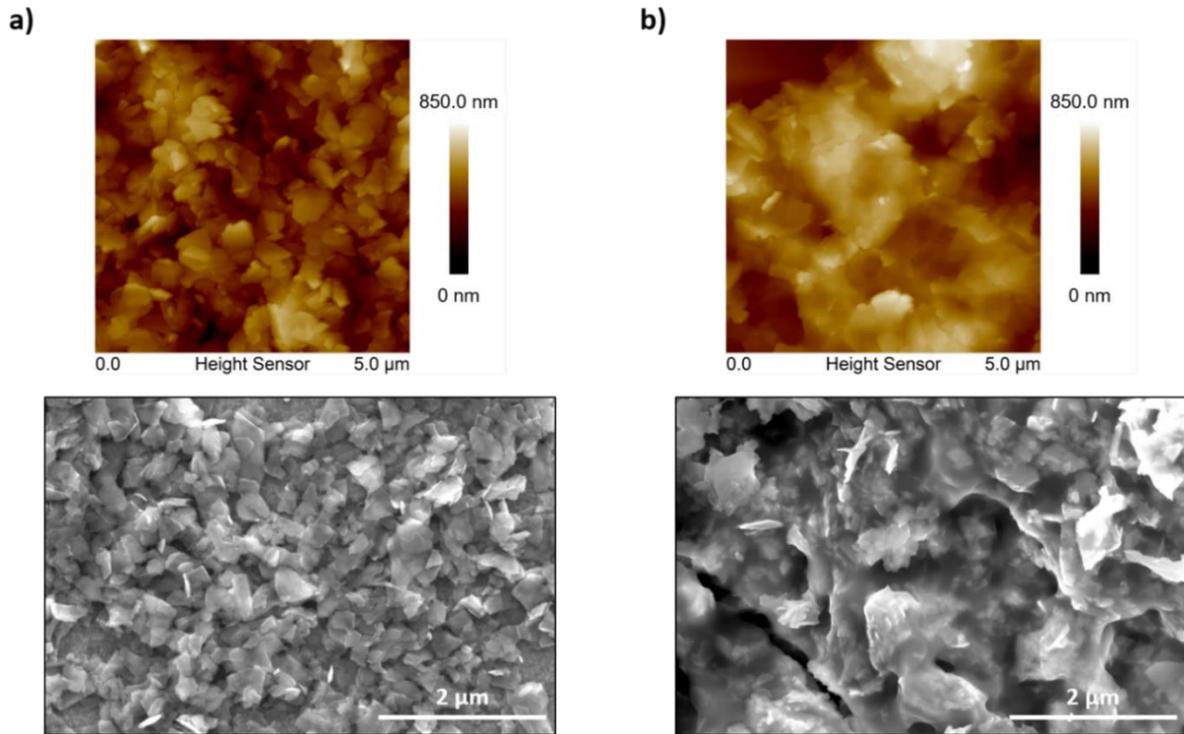
Figure 5-30 : AFM (top) and SEM (bottom) images taken for MoS$_2$ films functionalized **a)** *in-situ* and **b)** *ex-situ* with BDT.

Device figure of merit	MoS$_2$ Film	MoS$_2$ Clusters (*ex-situ*)	MoS$_2$ Network (*in-situ*)
μ_{FE} (cm^2 V^{-1} s^{-1})	10^{-3}	10^{-4}	10^{-2}
I_{ON}/I_{OFF}	10^3	10^3	10^4
V_{TH} (V)	1.9 ± 0.1	1.8 ± 0.1	1.8 ± 0.1

Table 5-6 : Summary of the electrical performance of MoS$_2$ films, networks and clusters, assessed according to the main device figures of merit in LG-TFTs : μ_{FE}, I_{ON}/I_{OFF} and threshold voltage (V_{TH}).

5.4. — *Conclusions*

We reported a universal and simple route to produce covalently interconnected TMD networks by exploiting defect engineering in solution-processed layered materials. We used π-conjugated dithiolated molecules to bridge adjacent MS_2 flakes, forming networks characterized by substantially different physicochemical properties (improved electrical characteristics, water stability, and mechanical robustness). The bridging of neighbouring flakes at the molecular level improves the charge transport across the network, thereby leading to superior device performances. LG-TFTs show a reproducible one order-of-magnitude increase in the main figures of merit, leading to SoA field-effect mobility (10^{-2} cm^2 V^{-1} s^{-1}) and I_{ON} / I_{OFF} ratio (10^4), along with the fastest switching time (18 ms) reported for devices of this kind[17,186]. Our findings pave the way for the development of high-performance, large-area and printed electronics based on solution-processed TMDs. The network formation results in water-stable and mechanically robust MS_2-based devices, that could be exploited in (bio)sensing[34], (photo)catalisyis[7], and flexible optoelectronics[187]. Finally, with an appropriate molecular design of the bridging linkers, one might endow the TMD networks with diverse functionalities, tuning the final properties *on demand* according to the envisioned applications.

Chapter 6 — Defect-driven selective decoration of TMDs with noble metal NPs for hybrid multifunctional materials

6.1. — *Introduction*

The ever-growing diffusion of solution-processed semiconducting TMDs in a great variety of applications keeps pushing the research on 2DMs beyond its limits. However, their inherent structural defects and properties still limit the range of applicability and performance of related devices. In this project, we report a functionalization strategy targeting the production of hybrid systems based on MS_2 (*i.e.*, MoS_2, WS_2) and noble metal NPs. The overall process is driven by galvanic displacement mechanism, whereby the spontaneous electron transfer from 2D crystals to metal salt precursors (*i.e.*, tetrahalide complexes) triggers the selective decoration of the flake edges with NPs, where a higher defect density (mainly V_S) is observed[15]. We exploited a variety of complementary multiscale characterization techniques (both theoretical and experimental) to unravel the subtle details of the reaction steps and the physicochemical properties of resulting hybrid materials. Our approach exhibits many notable advantages, since it exploits a one-pot (single step), green (aqueous solutions, no harsh conditions) and zero-waste synthesis, by which the material preparation can be achieved in less than 1 h. Moreover, the use of 2D structures has multiple benefits: TMD flakes simultaneously behave as reducing agents, scaffolds (no molecular likers are required to bind the metal nanostructures), and stabilizers for the growing NPs, promoting the formation of well-defined and direct interfaces between the two components of the hybrid system.

We employ this functionalization strategies to produce multifunctional hybrid materials based on solution-processed MS_2 and metal NPs, characterized by unique properties and enhanced performance. We test our systems for electrocatalysis and sensing applications, focusing on SERS and photothermal response, highlighting the effects induced by the presence of metal NPs at the flake edges. Preliminary data show that the presence of PdNPs induces a colossal enhancement of device performance for HERs, confirming the well-known activity of such a metal[188]. Likewise, hybrid systems comprising AuNPs exhibit increased SERS activity and photothermal response with respect to pristine TMDs, providing distinct evidence of the crucial role played by the *in-situ* grown hot spots (so called because of the surrounding highly intense electromagnetic field) as performance-enhancing elements[189,190].

6.2. — *Sample preparation*

The hybrid materials are synthesized by growing noble metal NPs at the reactive edges of solution-processed TMD flakes *via* galvanic displacement mechanism.

For this purpose, aqueous dispersions of MS_2 (*i.e.*, MoS_2, WS_2) and noble metal tetrahalide complexes (*i.e.*, $HAuCl_4$, K_2PdCl_4, K_2PtCl_4) are mixed together, under vigorous stirring and solvent boiling conditions. In order to optimize the reaction, three main parameters need to be tuned: the concentration ratio of 2DMs over metal salt precursors, the presence of external reducing agents, and the reaction temperature. First of all, in a total volume of 5 ml and under boiling conditions (T = 100 °C), the effects of two different concentration ratios are tested (namely, MoS_2/Au 1.5:1 and 2.5:1) by imaging the resulting hybrid materials *via* STEM. Figure 6-1 shows that 1.5:1 ratio returns AuNPs with average size of 20 nm, while 2.5:1 ratio yields AuNPs with average size of 10 nm. Therefore, upon decreasing the Au salt concentration, the resulting NPs decorating the TMD flake edges are smaller but exhibit a higher load. Moreover, considering the NP size evolution as a function of the concentration ratio, it results that the halving of Au salt concentration leads to NPs with halved size, highlighting a stoichiometric growth mechanism.
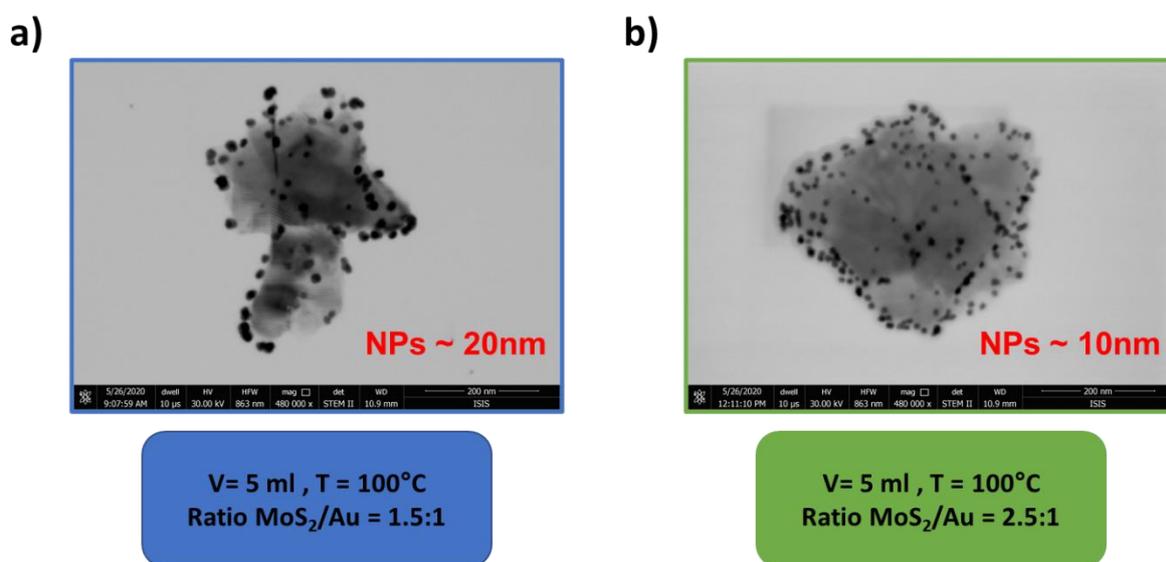
a)

b)

Figure 6-1 : STEM images, recorded under the same scanning conditions, of MoS_2/Au hybrid materials synthesized with **a)** 1.5:1 and **b)** 2.5:1 concentration ratio.

The need of an external reducing agent is also investigated: if the synthesis is performed, under the same operating conditions, in presence or in absence of the reducing agent trisodium citrate, no remarkable variations are recorded in STEM images of MoS_2/Au systems (Figure 6-2). Ultimately, the inherent properties of TMDs allow them to act as efficient reducing agents.
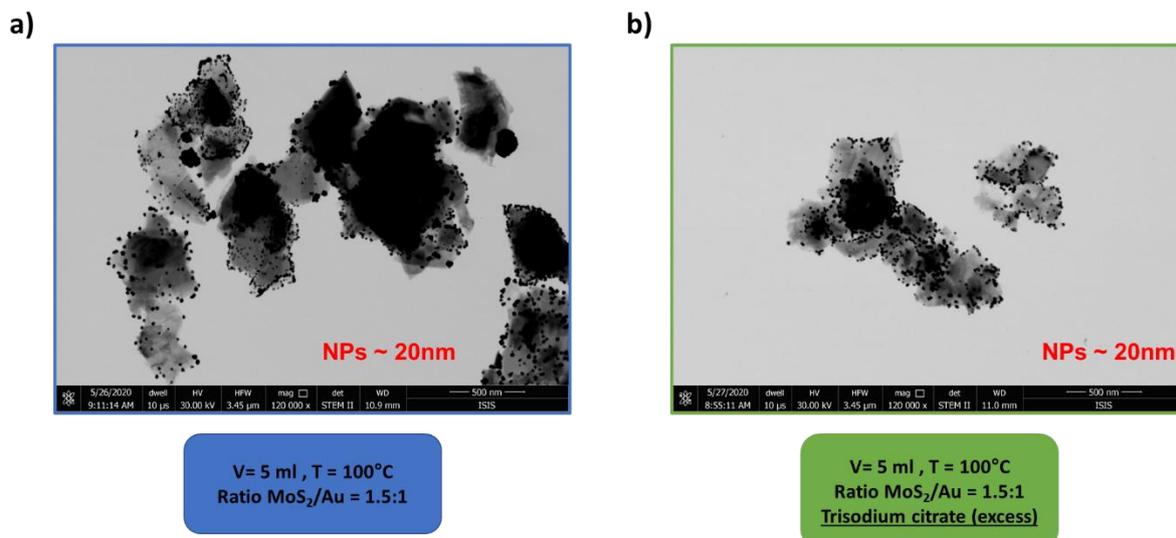
a)

b)

Figure 6-2 : STEM images, recorded under the same scanning conditions, of MoS$_2$/Au hybrid materials synthesized **a)** in absence and **b)** in presence of trisodium citrate.

Furthermore, the influence of the reaction temperature on the production of the hybrid materials is explored as well. In particular, the synthesis of MoS$_2$/Au systems is performed at four different temperatures, keeping constant all the aforementioned parameters (Figure 6-3).
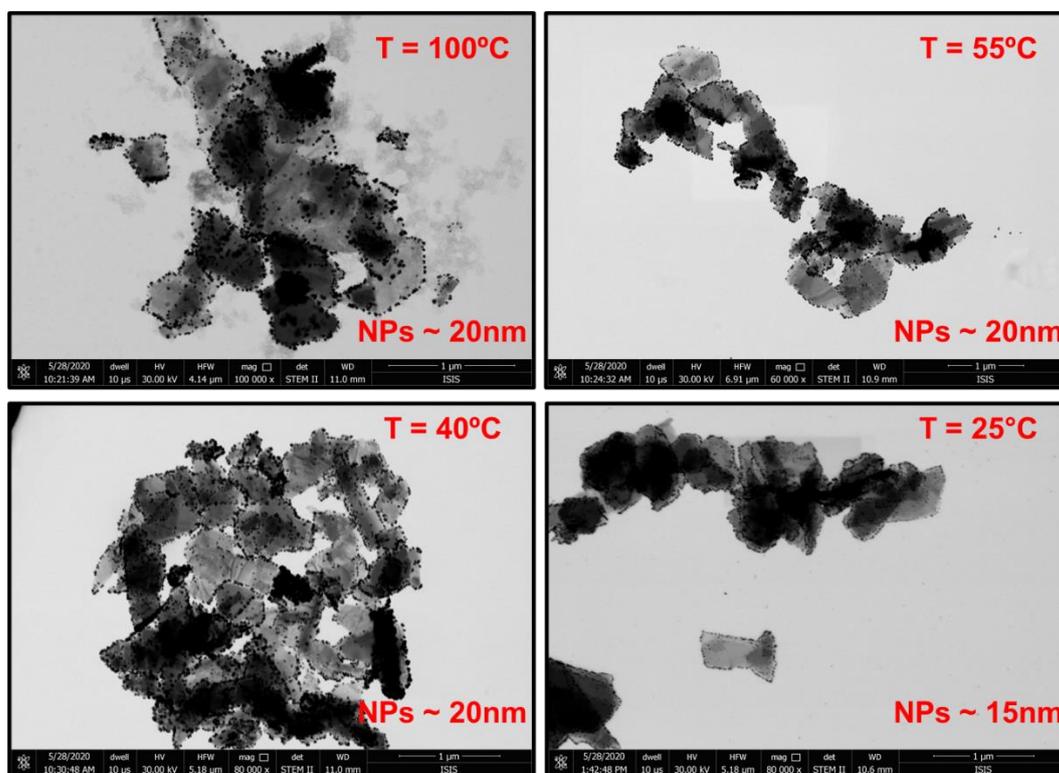

Figure 6-3 : STEM images, recorded under the same scanning conditions, of MoS$_2$/Au hybrid materials synthesized at different reaction temperature.

Figure 6-3 reveals only minimal changes upon temperature variation, and no harsh conditions are required to promote the growth of NPs. Ultimately, the presence in solution of TMD flakes, under ambient conditions, results suitable and efficient in reducing the metal salt precursor under investigation, thereby forming edge-decorated hybrid materials.

Finally, the overgrowth mechanism is explored *via* seed-mediated growth method. In particular, already formed MoS_2/Au hybrid systems (ratio 2.5:1) are exposed to a second round of Au salt precursor (maintaining the exact same operating conditions and 2DM/Au concentration ratio). As displayed in Figure 6-4, the NPs experience a size increase from 10 nm to 20 nm, also confirmed by UV-Vis spectra where the localized-surface plasmon band of the NPs becomes more evident in the overgrowth case, pointing to larger plasmonic nanostructures (highlighted by the black arrow). Such a result corroborates the stoichiometric growth mechanism driving the formation of the hybrid materials under investigation, where the size of NPs can be finely tailored *on demand* by adjusting the operating conditions.
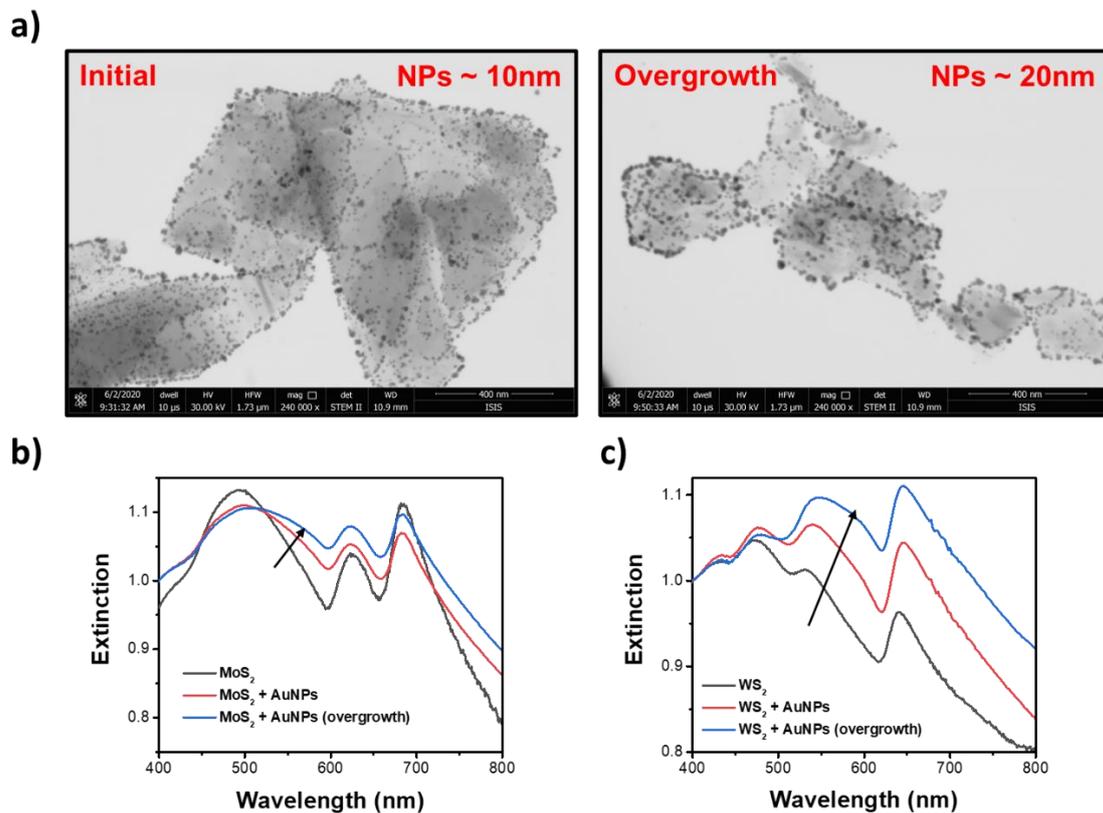

Figure 6-4 : a) STEM images, recorded under the same scanning conditions, of MoS_2/Au hybrid systems at initial condition and after overgrowth reaction. **b)** UV-Vis spectra for MoS_2/Au and **c)** WS_2/Au hybrid materials at different steps. The black arrow highlights the plasmon band of AuNPs.

To conclude, the reaction optimization for MS_2/Au lays out the guidelines for the production of hybrids materials based on Pd and PtNPs, where identical operating conditions are adopted.

6.3. — *Results and discussion*

As already mentioned in the previous sections of Chapter 6, the formation of hybrid materials based on solution-processed MS_2 and noble metal NPs occurs *via* galvanic displacement mechanism. The reaction takes place only if the E° of the metal salt precursor lies below the χ of the 2DM under investigation, thanks to an electron transfer process from the latter to the former, thereby forming metal NPs at the flake edges[137]. Such a phenomenon can be summarized in the following 3 main steps: (i) galvanic displacement triggering the formation of initial metal nuclei by electron transfer from the 2DM to the noble metal salt precursor; (ii) electrochemical Ostwald ripening process determining the growth of larger metal NPs and dissolution of smaller ones; (iii) diffusion and coalescence of metal NPs close to V_S. Remarkably, the presence of V_S plays a fundamental role in all stages of the mechanism, since they create new favorable adsorption sites for metal nuclei and greatly enhance their diffusion towards vacancy sites[20].

To further deepen and understand the reaction mechanism, some golden rules of electrochemistry result fundamental. For a redox reaction to be spontaneous, the E° of the oxidizing agent needs to be higher than the E° of the reducing agent. If so, the standard redox potential of the cell, E°$_{cell}$, results positive as follows:

$$E°_{cell} = E°_{cathode} - E°_{anode} > 0$$

where E°$_{cathode}$ refers to the reduction reaction, while E°$_{anode}$ refers to the oxidation reaction. When E°$_{cell}$ is positive, the standard Gibbs free energy, ΔG°, of the overall reaction results negative, highlighting a thermodynamic spontaneous process as follows:

$$\Delta G° = -nFE°_{cell}$$

where n represents the moles of electrons transferred in the reaction and F represents the Faraday constant (quantity of electrical charge contained in 1 mole of electrons, that is 96,500 Coulomb/mole of e⁻).

Ultimately, for a general redox reaction:

$$A_{red} + B_{ox} \rightarrow A_{ox} + B_{red}$$
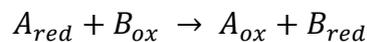
in order to assess its spontaneity, one shall refer to the two half-reactions (reduction reactions) involved in the process:

$$A_{ox} + ne^- \rightarrow A_{red} \quad (E°_1)$$
$$B_{ox} + ne^- \rightarrow B_{red} \quad (E°_2)$$
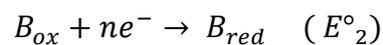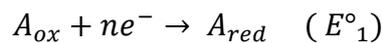
Finally, the calculation of the E°$_{cell}$ is crucial to understand and evaluate the direction (and spontaneity) of the redox reaction:

$$E°_{cell} = E°_2 - E°_1 > 0 \quad \text{Spontaneous}$$
$$E°_{cell} = E°_2 - E°_1 < 0 \quad \text{Not Spontaneous}$$

By taking into account the abovementioned observations regarding the electrochemistry facets lying beyond the galvanic displacement mechanism, we performed CV to assess the E° of the MS_2 and metal salt precursors under investigation (Figure 6-5). To this end, we analyzed all systems by using a GC working electrode (drop-casting the same amount of material in the case of MS_2, *i.e.*, 35 µl of aqueous dispersion at 0.5 mg/ml), upon cleaning and activation of the latter by carrying out 40 cyclic voltammograms in H_2SO_4 0.5 M. The fabrication of the electrolytic cell is then completed by using a Pt wire as counter electrode and Ag/AgCl (3.5 M KCl) as reference electrode, as well as aqueous solution of KCl 0.1 M as electrolyte.

Figure 6-5 : a) Schematic illustration of the reduction and oxidation reactions occurring in MoS_2 during a single step of CV. **b)** Cyclic voltammograms recorded for MoS_2 and **c)** WS_2 (drop-cast onto GC electrode), along with cyclic voltammograms recorded for aqueous solutions of **d)** $HAuCl_4$, **e)** K_2PdCl_4, and **f)** K_2PtCl_4. All measurements are performed using GC electrode as working electrode, Pt wire as counter electrode, Ag/AgCl (3.5 M KCl) as reference electrode, and aqueous solution of KCl 0.1 M as electrolyte.

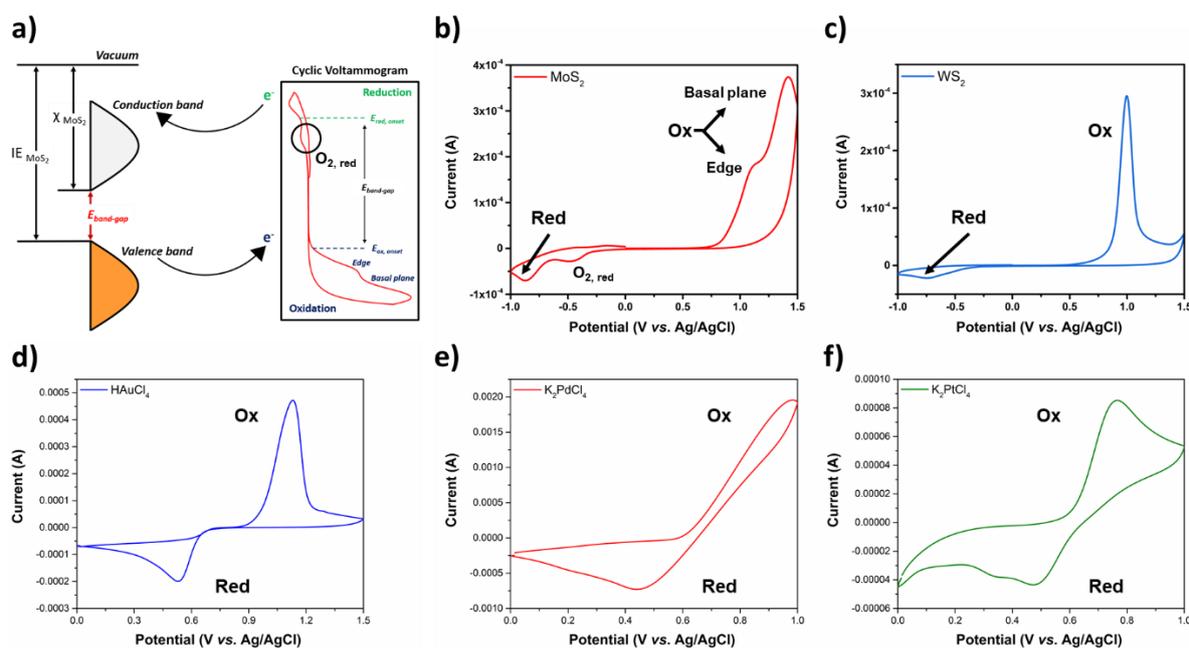The main results of the CV analysis are summarized in Table 6-1, as follows:

Material	Reduction reaction	E° (V *vs.* Ag/AgCl)
MoS_2	$MoS_2 + n\ e^- \rightarrow [MoS_2]^{n-}$	-0.85
WS_2	$WS_2 + n\ e^- \rightarrow [WS_2]^{n-}$	-0.75
$HAuCl_4$	$[AuCl_4]^- + 3\ e^- \rightarrow Au_{(s)} + 4\ Cl^-$	+0.55
K_2PdCl_4	$[PdCl_4]^{2-} + 2\ e^- \rightarrow Pd_{(s)} + 4\ Cl^-$	+0.45
K_2PtCl_4	$[PtCl_4]^{2-} + 2\ e^- \rightarrow Pd_{(s)} + 4\ Cl^-$	+0.48

Table 6-1 : CV experimental data obtained for MS_2 and noble metal salt precursors under investigation.

Considering the experimental values of E° obtained for the materials under exam, the galvanic displacement reaction results spontaneous for all combinations of MS_2 and metal precursors. Therefore, the production of hybrid systems based on solution-processed MoS_2/WS_2 and Au, Pd and PtNPs is expected under the operating conditions described beforehand.

In order to confirm such a prediction, we performed a meticulous HR-TEM investigation to examine the structural features of our hybrid materials. By taking advantage of the inherent higher resolution of this technique with respect to STEM, we observed a bimodal distribution in size for the edge-decorating AuNPs. In particular, we found out the simultaneous presence of larger (from 15 nm to 25 nm) and smaller (from 2 nm to 5 nm) nanostructures at the flake edges, as displayed in Figure 6-6.
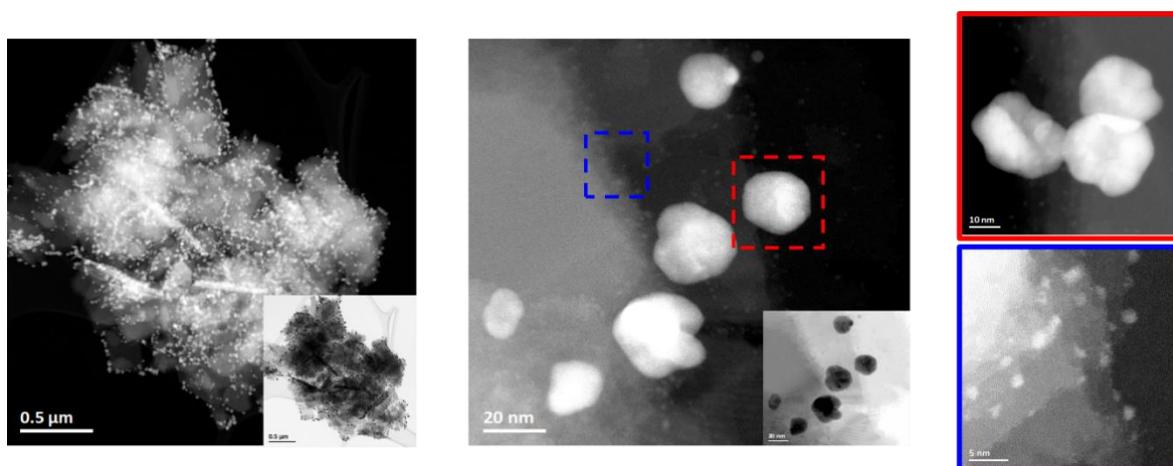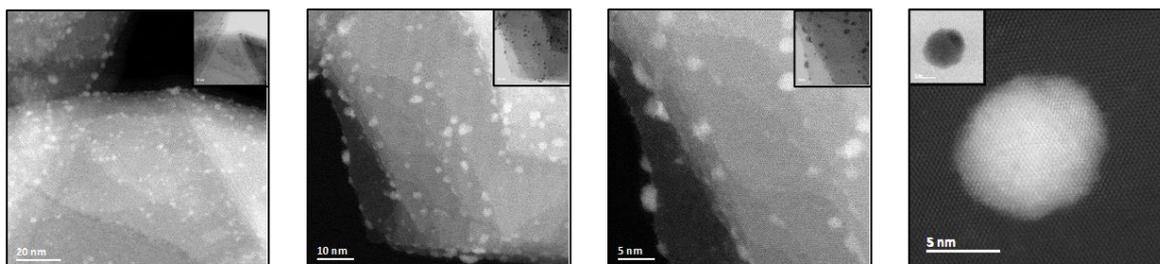

Figure 6-6 : HR-TEM images at different magnifications for MoS_2/Au hybrid materials. The presence of larger and smaller AuNPs at the flake edge is highlighted in red and blue, respectively.

We carried out a similar analysis on other hybrid systems, characterized by the presence of Pd and PtNPs at the edges. In this case, only smaller nanostructures (from 2 nm to 5 nm) are observed in HR-TEM images (Figure 6-7), highlighting a smaller load of NPs in the materials and, therefore, pointing to different thermodynamic and kinetic features involved in the galvanic displacement reaction.

PdNPs

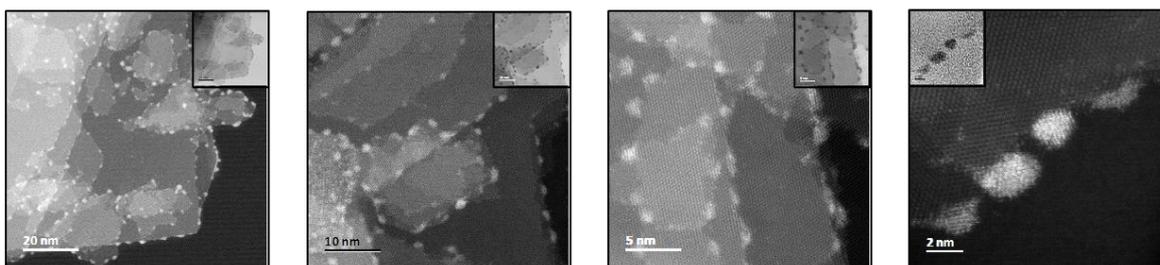
PtNPs

Figure 6-7 : HR-TEM images at different magnifications for MoS_2/Pd and MoS_2/Pt hybrid materials.

From the HR-TEM images recorded for all hybrid materials, we managed to get a better insight into the crystallinity of the *in-situ* grown NPs on MoS_2 edges. In this regard, the fast Fourier transform (FFT) images displayed in Figure 6-8 show the six diffraction spots in blue circles related to the [001] orientation of MoS_2, along with the diffraction spots in red circles related to the [111] orientation of Au, Pd and Pt. As already reported in literature, low-index facets of face-centred cubic (FCC) metals can grow with preferential orientation on the MoS_2 surface[11]. In fact, [111]$_{Au}$ has the lowest surface energy among low Miller index surfaces[191], which is typical for other FCC metals as well, such as Pd and Pt[192]. However, in the case of larger AuNPs, few other crystallographic orientations are also observed, namely [101]$_{Au}$ and [001]$_{Au}$, highlighting a polycrystalline structure.
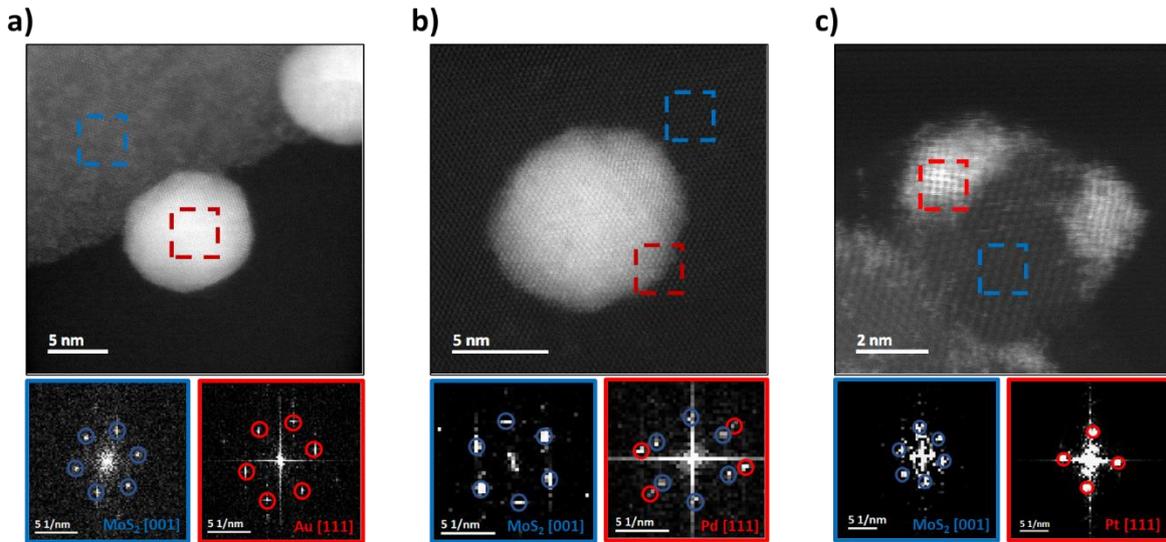
Figure 6-8 : HR-TEM and FFT images taken for hybrid systems based on MoS₂ and **a)** Au, **b)** Pd and **c)** PtNPs. The areas where the FFT analysis is performed are highlighted in blue for the 2DMs, while in red for the NPs.

To further corroborate these findings, we performed grazing incident X-ray diffraction (GIXD) on MoS₂/Au hybrid systems, which exhibited larger NPs and higher load. As shown in Figure 6-9, characteristic diffraction peaks of both MoS₂, *i.e.*, (102) and (103), and AuNPs, *i.e.*, (111), are observed, thereby confirming the composition of the materials under exam[193,194].

Figure 6-9 : GIXD diffractograms (incident angle, $\alpha_{inc.}$, 0.5°) of MoS₂ pristine (black) and MoS₂/Au hybrid materials (red). X-ray wavelength ($\lambda_{inc.}$) = 1.54 Å (CuKα), scanning time = 20 h.

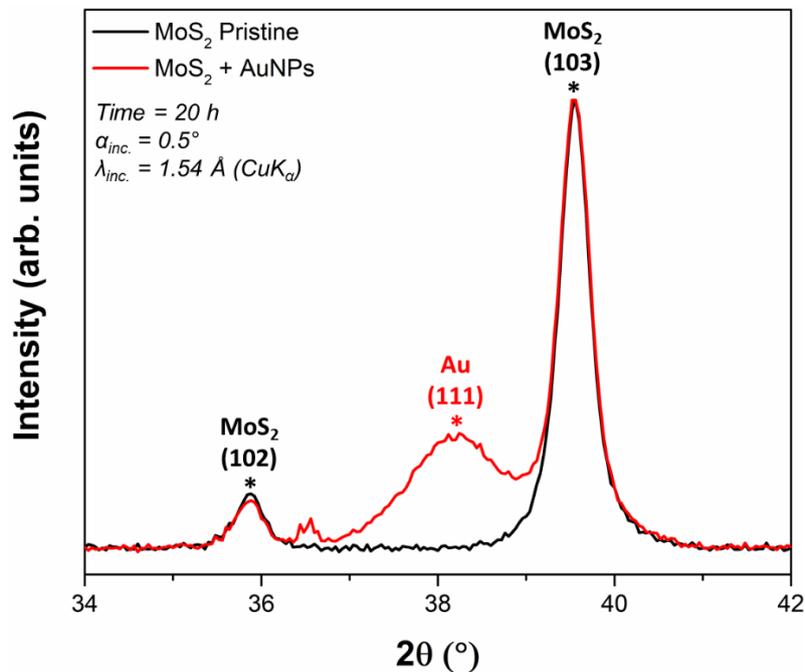XPS represents an additional chemical composition technique we exploited to investigate the hybrid systems synthesized *via* galvanic displacement mechanism. As shown in Figure 6-10, the HR-XPS spectra recorded in different regions confirm the presence of metal NPs, although some components related to higher oxidation states can be also deconvoluted, very likely due to the oxide formation during the reaction and/or residuals of the metal salt precursors.
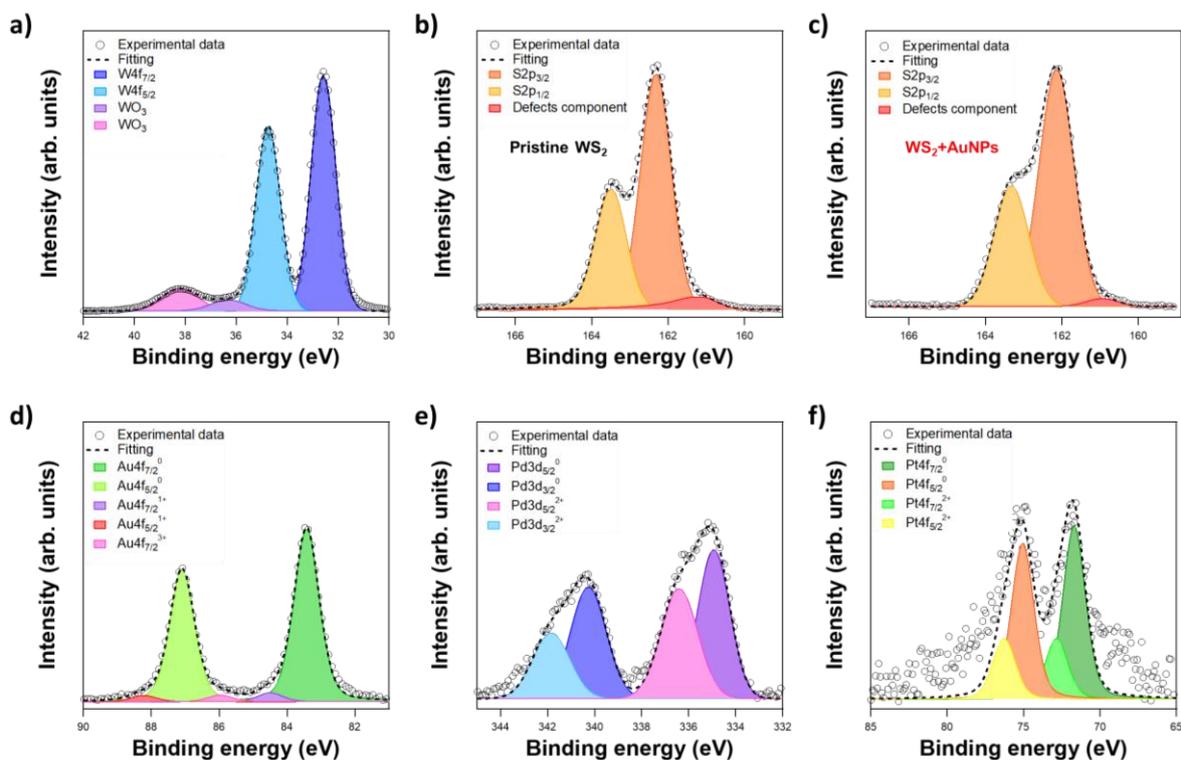

Figure 6-10 : HR-XPS spectra recorded in different regions, namely **a)** W4f, **b)** S2p for pristine and **c)** hybrid materials, **d)** Au4f, **e)** Pd3d and **f)** Pt4f.

For the sake of completeness, the binding energy values corresponding to the principal components reported in Figure 6-10, extrapolated from the fitting, are reported below:

$W4f_{7/2}$ = 32.6 eV, $W4f_{5/2}$ = 34.8 eV, $S2p_{3/2}$ = 162.2 eV, $S2p_{1/2}$ = 162.4 eV, $Au4f_{7/2}$ = 83.4 eV, $Au4f_{5/2}$ = 87.1 eV, $Pd3d_{5/2}$ = 334.9 eV, $Pd3d_{3/2}$ = 340.2 eV, $Pt4f_{7/2}$ = 71.7 eV, $Pt4f_{5/2}$ = 75.0 eV

It is worth mentioning that the XPS analysis and fitting procedures are performed keeping into account and respecting the constraints related to the atomic properties of each element, such as spin-orbit coupling and intensity ratio.

Finally, XPS investigation also provides an important evidence concerning the edge-decoration process. As already discussed in Chapter 5, defects are mainly located at the flake edges[15], thus the reported decrease of the defects component in S2p spectra of the hybrid materials is expected and offers an indirect proof of the supported reaction mechanism.

To shed further light on the galvanic displacement mechanism driving the production of hybrid systems based on solution-processed TMDs and noble metal NPs, we took advantage of theoretical calculations and simulations based on DFT, focussing on AuNPs as case study. The purpose of such an investigation aims to disclose the inherent features of each single step involved in the reaction mechanism (Figure 6-11), highlighting the crucial role played by defects (V_S) as well as supporting the experimental data reported and discussed beforehand.

1. Dissociative adsorption of HAuCl$_4$

2. Dimerization

3. Nanocrystal(s)

4. Nanoparticle(s)
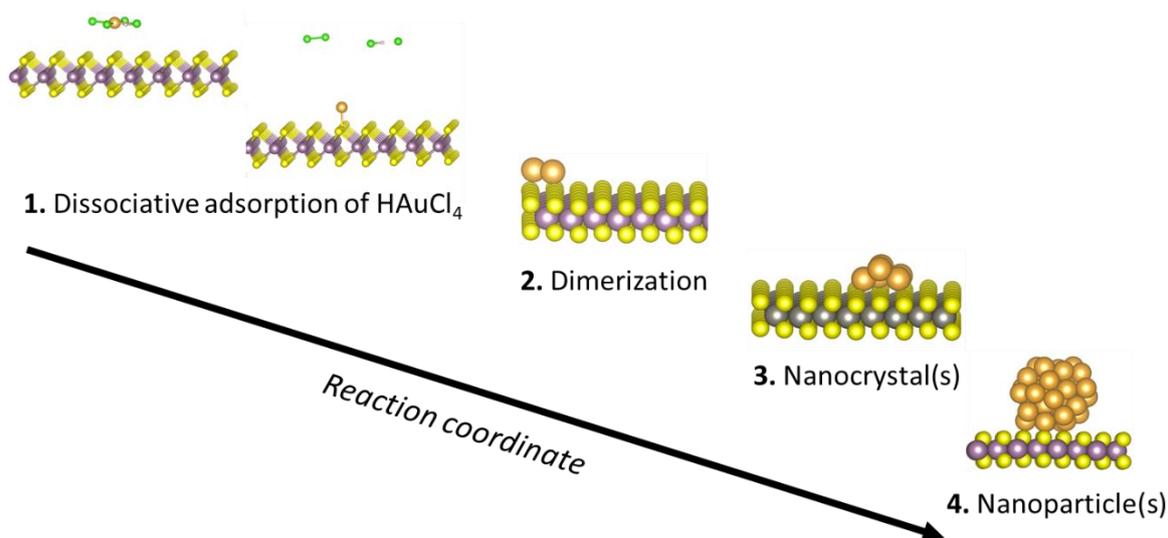
Reaction coordinate

Figure 6-11 : Illustration of the principal steps involved in the galvanic displacement reaction leading to the formation of hybrid systems based on MS$_2$ and AuNPs.

According to the roadmap illustrated in Figure 6-11, the first step entails the adsorption, dissociation and desorption of HAuCl$_4$ on MoS$_2$/WS$_2$. In this regard, the calculation of the characteristic energy involved in each step results crucial in understanding any difference between the two 2DMs (Figure 6-12, Figure 6-13). Moreover, focus is laid on the effects due to the presence of V_S on MS$_2$, evaluated by repeating the very same calculations with (V_S ~5%) and without vacancies. It is worth stressing that the presence of V_S strongly enhances the adsorption of the Au salt precursor, both for MoS$_2$ and WS$_2$, as reflected by a more negative energy value for such a process. Furthermore, the outcome of the calculations also highlights a remarkable difference between MoS$_2$ and WS$_2$ in terms of adsorption energy and dissociative + desorption energy (Table 6-2). In fact, if one considers the surface charge of MoS$_2$ and WS$_2$, amounting to -0.84e and -0.69e respectively, it is evident that the desorption probability is higher for MoS$_2$ (because of stronger repulsive interaction with electronegative species) with respect to WS$_2$, where Cl$_2$/HCl/Cl can remain stuck on its surface thereby hindering further HAuCl$_4$ adsorption. Ultimately, the adsorption, dissociation and desorption processes involved in the first reaction step are more favorable on MoS$_2$ than WS$_2$ substrates.

Adsorption of HAuCl$_4$ on MoS$_2$

Dissociation of HAuCl$_4$ from MoS$_2$
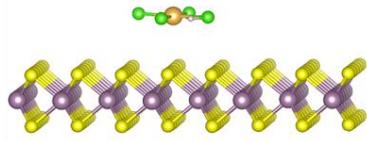
Without vacancy

Adsorption energy= **-0.55eV**
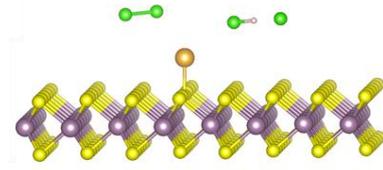
Dissociative+desorption energy= **3.63eV**

With vacancy
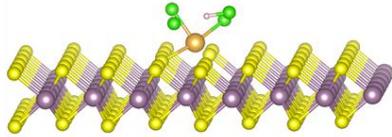
Adsorption energy= **-1.22eV**
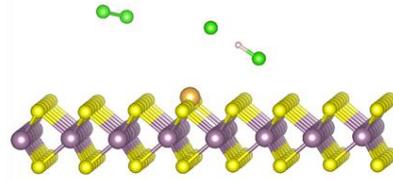
Dissociative+desorption energy= **1.25eV**

2 Chlorine atoms are spontaneously dissociated

Figure 6-12 : Calculation of the adsorption, dissociative and desorption energy for HAuCl$_4$ on MoS$_2$, with and without V$_S$.

Adsorption of HAuCl$_4$ on WS$_2$
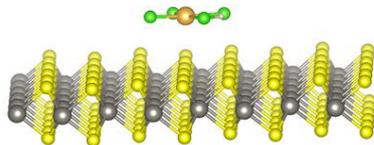
Dissociation of HAuCl$_4$ from WS$_2$

Without vacancy

Adsorption energy= **-0.75eV**
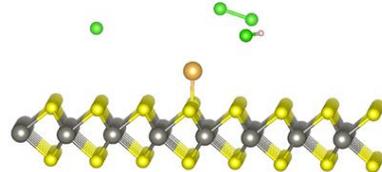
Dissociative+desorption energy= **4.10eV**

With vacancy
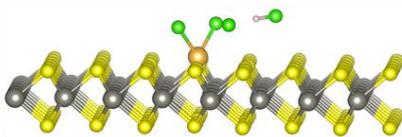
Adsorption energy= **-2.20eV**
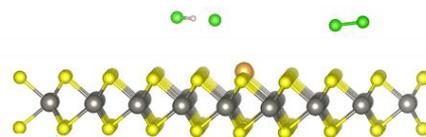
Dissociative+desorption energy= **3.43eV**

2 Chlorine atoms are spontaneously dissociated

Figure 6-13 : Calculation of the adsorption, dissociative and desorption energy for HAuCl$_4$ on WS$_2$, with and without V$_S$.

	MoS$_2$	WS$_2$
Adsorption energy	-1.22 eV	-2.20 eV
Dissociative + desorption energy	+1.25 eV	+3.43 eV

Table 6-2 : DFT calculations concerning the adsorption, dissociation and desorption of HAuCl$_4$ on MoS$_2$ and WS$_2$ with V$_S$ ~5%.

As a result of the initial step, Au single atoms are adsorbed on the MS$_2$ surface and they start growing while the reaction keeps progressing. By virtue of DFT calculations, the formation energy of Au nanostructures can be estimated as function of the number of constituent Au atoms (Figure 6-14). Interestingly, the largest variations of formation energy are recorded up to 5 Au atoms, until a steady state emerges. Moreover, it is worth mentioning that the presence of V$_S$ has a dramatic impact on the formation energy; in fact, under this condition, the reaction results more favorable, as highlighted by more negative values. However, this is evident up to the aforementioned threshold of 5 Au atoms, above which the clusters keep growing without any influence due to structural defects.
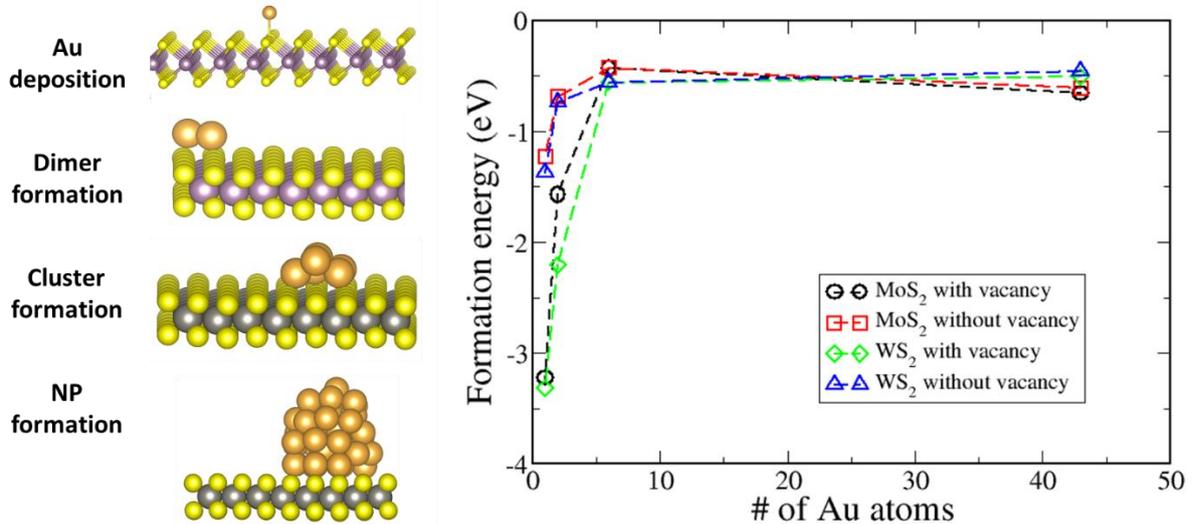
Figure 6-14 : DFT calculations of the formation energy of Au clusters on MoS$_2$ and WS$_2$ as a function of the number of constituent Au atoms. The very same calculations are carried out in presence and absence of V$_S$.

Once NPs are formed, to gain further insight into their effects on the electronic properties of 2DMs, we calculated the projected density of state (PDOS) for pristine MoS$_2$ and MoS$_2$/Au hybrid systems, with and without V$_S$ (Figure 6-15).
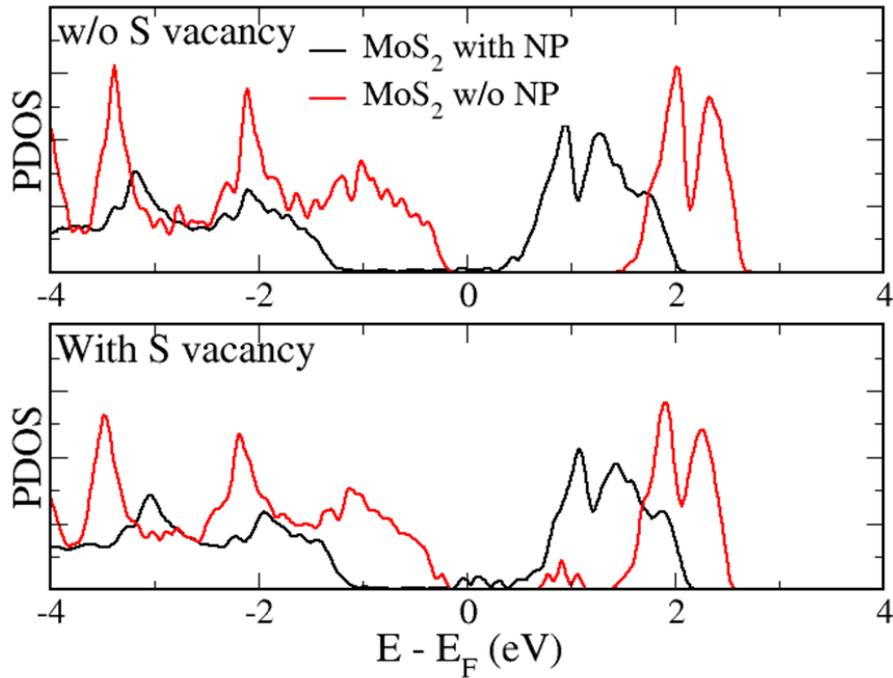
Figure 6-15 : PDOS calculated for pristine MoS_2 and MoS_2/Au hybrid materials, with and without V_S.

As displayed in Figure 6-15, the presence of AuNPs induces a shift of the bands towards lower energy, pointing out a charge transfer process leading to n-type doping. Interestingly, from the PDOS plots, it is also evident the presence of new states within the band-gap when V_S are taken into account, in agreement with some works already reported in literature[195].

Ultimately, the galvanic displacement reaction involves a preliminary charge transfer from the 2DM to the metal salt precursor, however, once NPs are formed, they induce a doping effect due to an inverse charge transfer process. To corroborate such a mechanism, we carried out the Bader charge analysis for MoS_2 (Table 6-3) under two different conditions, namely when interacting with $HAuCl_4$ and AuNPs. For the sake of clarity, looking at the MoS_2 charge, a positive sign indicates a loss of electrons and, therefore, a charge transfer from MoS_2 to the adsorbate. Conversely, a negative sign indicates a gain of electrons and charge transfer from the adsorbate to MoS_2.

	w/o V_S	with V_S
$MoS_2/HAuCl_4$	+0.10	+0.72
$MoS_2/AuNPs$	-0.27	-0.42

Table 6-3 : Bader charge analysis for MoS_2 when interacting with $HAuCl_4$ and AuNPs, with and w/o V_S.

Once all the main aspects of the galvanic displacement reaction are discussed from various points of view and the hybrid materials are thoroughly characterized by means of several multiscale techniques, the practical application of the latter in electrocatalysis and sensing can be investigated. In this regard, we performed some preliminary measurements, whose most relevant results and findings are reported below.

SERS represents a powerful tool for on-site detection in chemical and life science, owing to its inherent features (*e.g.*, fingerprint recognition, extremely high sensitivity) and to the recent technological advancements that lowered the cost of the instruments, improved the general performance and user-friendliness. Metal NPs are well-known plasmonic materials exploited in the fabrication of SERS substrates, because of their unique optical properties and ease of preparation. Moreover, such hot spots can markedly enhance the sensing capabilities of any SERS platform, allowing to reach extremely low limits of detection according to their density, size and geometry[196,197]. We fabricated SERS substrates (Figure 6-16) exploiting the hybrid materials produced by galvanic displacement reaction based on WS_2 and AuNPs (since Pd and PtNPs do not exhibit plasmon bands in the visible range and, therefore, no suitable laser lines are usually available in common instruments). To this end, we deposited WS_2/Au systems on SiO_2/Si substrates *via* layer-by-layer (LbL) approach, involving an alternate adsorption of polyelectrolytes and material under investigation, whose surface charge, established by Zeta potential analysis, results -28 mV. In particular, we employed poly(diallyldimethylammonium chloride), PDDA, and poly(acrylic acid), PAA, as positive and negative electrolyte, respectively. The substrates are dipped for 30 min in the aqueous solutions of the electrolytes at 1% v/v with the following order: PDDA, PAA, and PDDA; then, they are dipped for 30 min in aqueous solution of WS_2/Au 0.5 mg/ml, followed by multiple rinsing and drying under N_2 flow.
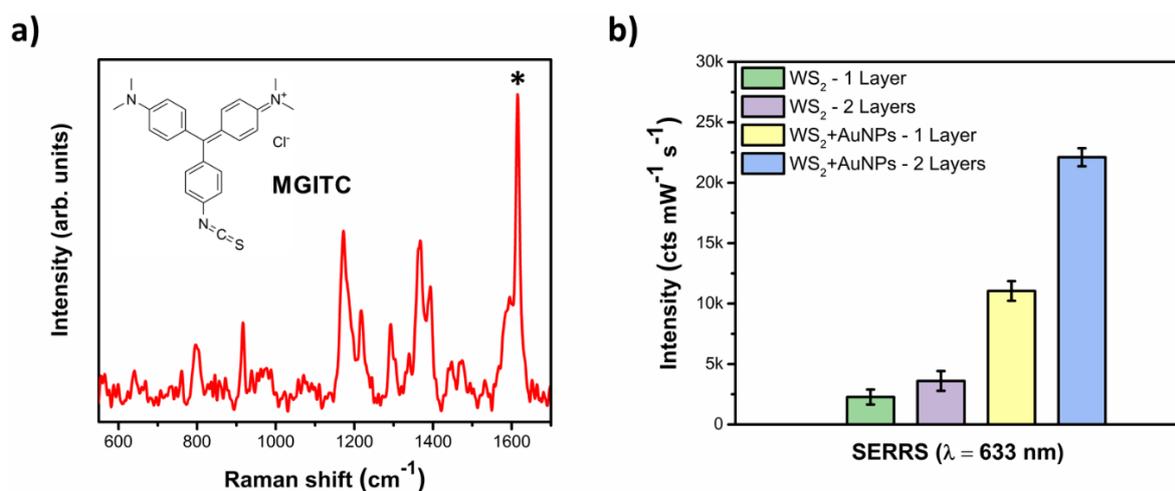

Figure 6-16 : a) Raman spectra of MGITC acquired by using a 633 nm laser line. The asterisk shows the peak used for the **b)** SERRS analysis performed on pristine WS_2 and WS_2/Au hybrid systems.

The very same procedure can be repeated to deposit a second layer of active material, in order to test the effects on the SERS response. In this regard, considering the selective location of the NPs at the flake edges and their small load compared to usual SERS substrates, we carried out the analysis by using a 633 nm laser line and selecting malachite green isothiocyanate (MGITC) as prototypical analyte, since it exhibits an adsorption maximum at ~630 nm[198]. Such a resonance condition (also known as surface-enhanced resonance Raman scattering, SERRS) boosts the response of the active material towards the specific analyte, since the energy of the incident photons matches the frequency of an electronic transition of the molecule. As reported in Figure 6-16, the presence of NPs in WS_2/Au hybrid material enhances the SERRS response towards MGITC (10^{-5} M, drop-cast onto the substrates) with respect to pristine WS_2 systems. Overall, the enhancement factor ranges from 6 to 10, confirming the crucial role played by the hot spots in the SERS mechanism, further highlighted by the higher response of the substrates made of 2 layers of active material.

Photothermal responsive materials have emerged as novel probes for on-site recognition, characterized by strong absorption, high photothermal conversion efficiency and photostability under laser irradiation for a certain time frame[199]. In this regard, we tested the aqueous colloidal dispersions obtained from the galvanic displacement reaction as photothermal sensors (Figure 6-17). In particular, by making use of a specific experimental set-up, we monitored the variation of the solution temperature when irradiated with a 808 nm laser line (spot size ~0.7 cm, power 501 mW, intensity 325 mW/cm^2). As displayed in Figure 6-17, the presence of NPs increases the photothermal response with respect to pristine materials (at equal concentration, *e.g.*, 100 µg/ml). In fact, their localized surface-plasmon resonance properties enhance the local electromagnetic field, resulting in stronger scattering and absorption of light. Hence, NPs serve as nanoscopic light-activated heaters, already exploited in many applications such as cancer therapy, imaging and sensing[200,201,202]. Moreover, the response of our active materials (both pristine and hybrid) scales linearly with concentration, even though this trend saturates at high concentrations (above 100-150 µg/ml) where parasitic effects, due to scattering phenomena, might interfere (Figure 6-18). In conclusion, MS_2/Au hybrid materials exhibit a superior photothermal response with respect to pristine ones, where the ΔT between the two systems, at equal concentration, ranges from 1.5 to 2.5°C.
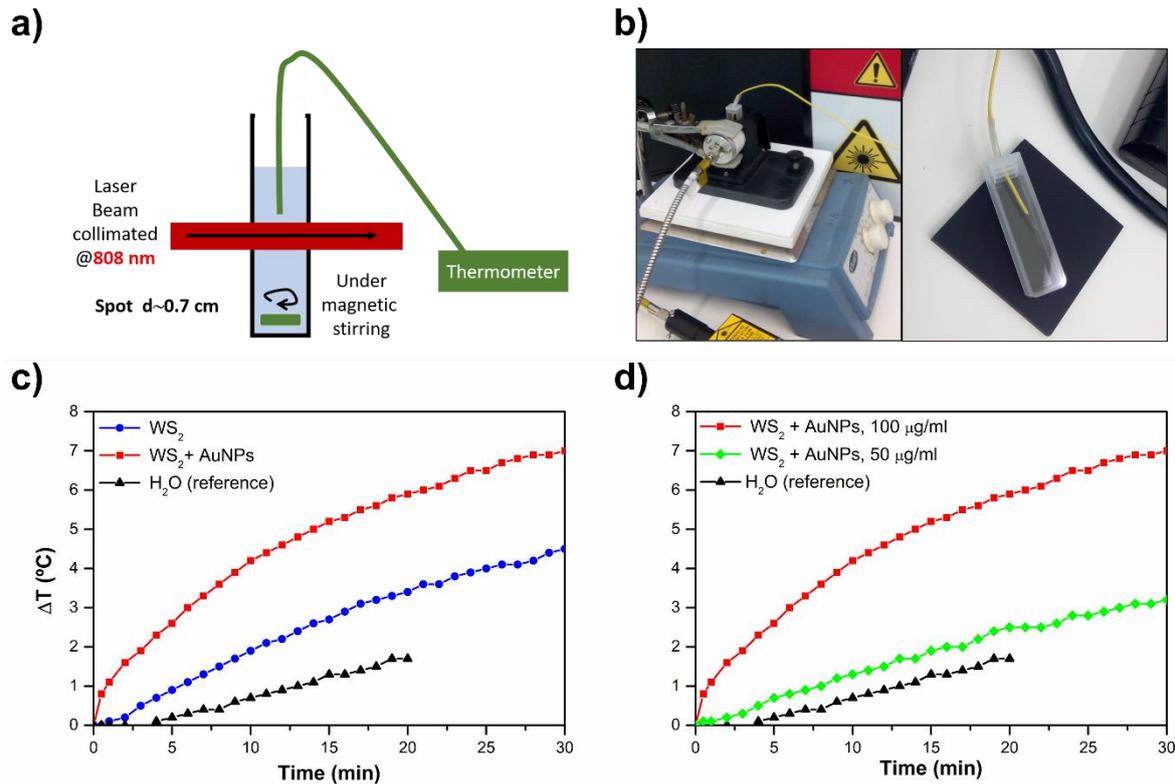
Figure 6-17 : a) Sketch and **b)** images of the experimental set-up used for the photothermal analysis. **c)** Photothermal response of pristine WS₂ and hybrid WS₂/Au compared to water, possessing both a concentration of 100 µg/ml. **d)** Photothermal response of hybrid WS₂/Au systems with different concentration.
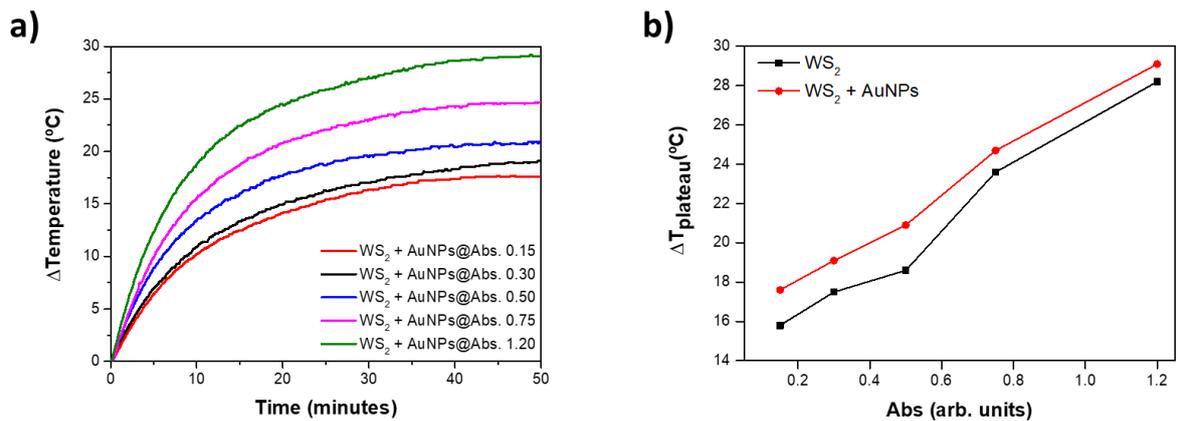
Figure 6-18 : a) Photothermal response of WS₂/Au hybrid materials with different absorbance (*viz.* concentration). **b)** Comparison of the photothermal response between pristine WS₂ and hybrid WS₂/Au as a function of different absorbance (*viz.* concentration).

During the ever-growing concern about climate change, pollution and decreasing availability of fossil fuels, the search for clean and renewable sources has become one of the greatest challenges for the sustainable development of our society[203,204,205]. In this regard, for energy-

related applications, two main cycles are considered: the water cycle and the carbon cycle. Central to the water cycle, is a series of hydrogen- and oxygen-related electrocatalytic processes. In particular, hydrogen has emerges as one the principal energy vectors for the development of groundbreaking technologies, boosting the progress of the future hydrogen economy[206]. To this end, we fabricated devices based on hybrid MS_2/NPs to test for HERs, by exploiting the same LbL protocol and CV set-up described above. More specifically, we deposited the active materials onto glass/ITO substrates, representing the working electrode of the electrolytic cell using a H_2SO_4 aqueous solution 0.5 M as electrolyte. The experimental results, displayed in Figure 6-19, highlight the crucial role played by NPs, which dramatically enhance the device performance, acting as reactive sites for the production of H_2 molecules. In particular, Pd and PtNPs exhibit higher catalytic activity compared to AuNPs, as pointed out by the higher current density and lower Tafel slope (extracted from the linear regime of the voltammogram). Such a key value, related to the device performance, results 145 mV/dec, 160 mV/dec, 250 mV/dec and 360 mV/dec for WS_2/Pt, WS_2/Pd, WS_2/Au and pristine WS_2 systems, respectively. These results are in agreement with the well-known volcano plot describing the catalytic activity of different metals for HERs[207]. Finally, we also performed electrochemical impedance spectroscopy (EIS)[208] to further investigate our systems and extract some key FOM, such as the solution resistance (R_S), charge transfer resistance (R_{ct}), and constant phase element (CPE). Amongst them, R_{ct} is the principal one as it refers to the electronic and ionic resistance at the electrode/electrolyte interface during the HER process. This value drastically drops in the presence of NPs, due to higher catalytic activity, passing from 24kΩ for pristine WS_2, to 3kΩ for WS_2/Au and 350Ω for WS_2/Pd (analysis on WS_2/PtNPs is work in progress).
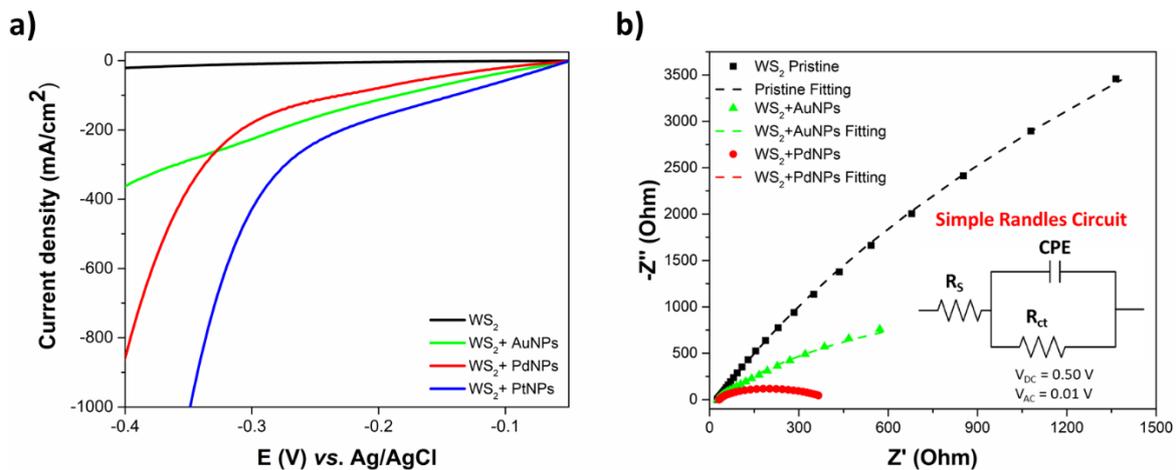
Figure 6-19 : a) HER and **b)** EIS plots for pristine WS_2 and hybrid WS_2/NPs systems.

6.4. — *Conclusions*

We developed an innovative functionalization reaction to produce hybrid systems based on solution-processed MS_2 and noble metal NPs, selectively decorating the flake edges. This strategy relies on the galvanic displacement reaction, promoted by V_S — mainly located at the peripheral defective regions of MS_2 — when a proper matching of $E°$ is achieved between 2DMs and metal salt precursors. The synthesis of such hybrid materials occurs under ambient conditions, in a single step and with no need of reducing agents, whose function is played by MS_2 also acting as scaffolds and stabilizers for the growing NPs. The resulting multifunctional MS_2/NPs systems show a remarkable potential applicability in SERS, photothermal sensing and electrocatalysis, as highlighted by the encouraging preliminary results collected from the various (theoretical and experimental) multiscale characterization techniques. In conclusion, the appropriate design of the functionalization reaction, affecting the nature, size and geometry of the NPs, could lead to the production of hybrid materials characterized by unique properties, tailoring their ultimate performance *à la carte* according to the envisioned applications.

Chapter 7 — General conclusion and outlooks

This doctoral thesis discussed the development of innovative and universal functionalization strategies for semiconducting solution-processed TMDs. In particular, by taking advantage of their inherent defectiveness, we devised two molecular chemistry approaches in order to produce hybrid systems with unique properties and enhanced performance in view of the envisioned applications. Among several options, the most appealing are certainly represented by flexible electronics, sensing and electrocatalysis, where the characteristic atomic thickness and high surface-to-volume ratio of 2DMs are crucial. From the second half of the 20th century, the abovementioned research areas have become indispensable part of the modern society, affecting industrial chemical processes, food products, environmental monitoring, healthcare, pharmaceuticals, and so on and so forth. Therefore, the evolution of SoA technologies based on TMDs remains one of the most sought-after topics within the current 2DM-oriented scientific community.

7.1. — *Summary*

Our first experimental project (Chapter 5) describes an original functionalization strategy for solution-processed MS_2, taking advantage of the inherent structural defects present in these materials upon the exfoliation steps. In particular, the V_S (mainly located at the flake edges) might be exploited as (re)active sites to carry out a chemical reaction targeting the simultaneous healing of defects and bridging of adjacent flakes. To this end, the use of dithiolated molecular systems results compulsory to form covalently interconnected networks, characterized by lower defect density and further unique features. Remarkably, the network formation turns out to be a performance-enhancing aspect for the electrical devices, which experience an increase of their main FOM (μ_{FE}, I_{ON}/I_{OFF}, τ_S) by one order-of-magnitude. In this regard, temperature-dependent electrical characteristics reveal that such an improvement can be principally ascribed to the decrease of inter-flake junction resistance, confirmed by the lower E_A related to the charge carrier transport within interconnected networks. Moreover, it is worth mentioning that SoA performance can only be achieved when π-conjugated dithiolated molecules (BDT) are employed, highlighting the crucial role played by the liker structure. In fact, covalent networks built by means of aliphatic dithiolated molecular systems (PDT) show a minimal improvement of their electrical characteristics, which cannot rival those attained with BDT due to the lack of a delocalized electron system. Finally, the bridging of adjacent flakes leads to additional remarkable properties, such as superior water stability and mechanical robustness, thereby paving the way for aqueous-based applications and flexible electronics.

Our second project (Chapter 6) describes an innovative functionalization strategy aiming to produce hybrid materials based on solution-processed MS_2 and noble metal NPs. By taking advantage of the inherent defectiveness such 2DMs, we succeeded in synthesizing selectively edge-decorated systems, since the peripheral flake regions are characterized by high density V_S that promote the adsorption of the metal salt precursors and the following controlled growth of NPs. The overall reaction is driven by galvanic displacement mechanism, whose *condicio sine qua non* entails a suitable matching of E° between the two systems involved in the process. MS_2 and noble metal tetrahalide complexes employed in this project match such a prerequisite, and the successful production of MoS_2/WS_2 and Au, Pd and PtNPs is thoroughly discussed and investigated. The resulting materials, whose performance is evaluated by various multiscale characterization techniques, exhibit remarkable potential applicability in SERS, photothermal sensing, and electrocatalysis. In fact, compared to pristine systems: (i) MS_2/Au show enhanced photothermal response by 1.5-2.5°C and improved SERS enhancement factor from 6- to10-fold; (ii) MS_2/Pt and Pd show drastically lower R_{ct} and Tafel slope as HER electrocatalysts.

7.2. — *Future perspectives*

In the last years, the scientific community has witnessed a tremendous progress in solution-processed TMDs, although few major challenges still need to be tackled (Figure 7-1).
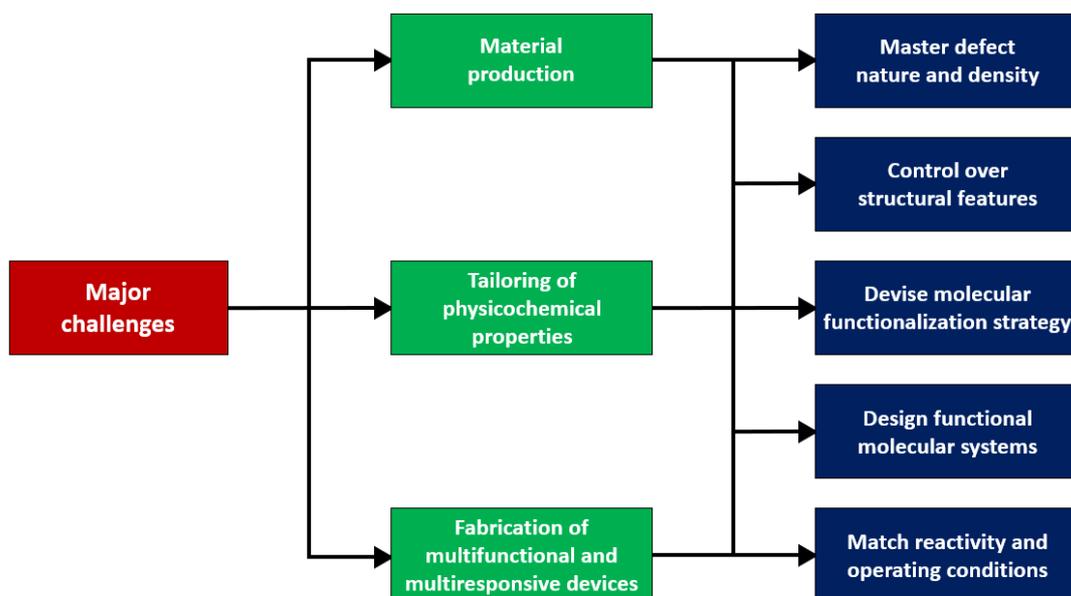

Figure 7-1 : Schematic illustration of the main challenges that need to be tackled in the forthcoming years to promote the progress in 2DM science and enable the development of innovative technologies based on solution-processed TMDs.

The relentless progress on the design of innovative functionalization strategies, based on molecular chemistry approaches, have supported and keeps supporting 2DM scientists in facing such hurdles. In this context, the projects reported in this doctoral thesis at Chapter 5 and Chapter 6 target the production of hybrid systems based on solution-processed TMDs *via* defect-engineering approaches. Covalently interconnected TMD networks and multifunctional materials based on TMDs&NPs show great potential in 2DM science (Figure 7-2), and some of their short- and long-term future perspectives are summarized below.

Covalently interconnected TMD networks. The work plan settled for the upcoming future entails an in-depth study and analysis concerning the reactivity of different dithiolated linkers used to form covalent networks. We already proved the influence of the linker structure on the electrical characteristics of the hybrid materials, though a meticulous investigation is required to assess its effects on other macroscopic properties, such as mechanical robustness, fatigue resistance and water stability. Interestingly, the fabrication of electrical devices with various architectures on different substrates (*e.g.*, Si, SiO_2/Si, PET, polyimide films) might promote the development of flexible digital electronics based on solution-processed TMDs. Moreover, the use of deposition techniques compatible with the industrial scale (*e.g.*, inkjet printing, roll-to-roll, spray coating) might stimulate the further progress of high-performance, large-area and printed TMD electronics. Finally, taking into consideration the intrinsic features of our universal functionalization strategy, we reckon captivating long-term outlook involving the formation of covalently interconnected networks endowed with specific functionalities according to the envisioned applications. For instance, dithiolated molecular systems bearing (supra)molecular (bio)receptor or light-sensitive units (*e.g.*, crown-ethers, azobenzenes, diarylethenes) would form networks with superior performance in sensing and optoelectronics.

Multifunctional materials based on TMDs&NPs. Future experiments aim to corroborate the galvanic displacement mechanism, by using noble metal salt precursors possessing a E° lower than MS_2, such as organometallic compounds. We undertake to complete and deepen the characterizations on the MS_2/NPs hybrid materials for SERS, photothermal sensing and electrocatalysis applications. In this regard, we target to explore the effects of different aspect ratios for the edge-decorating NPs, whose properties will be affected along with the overall materials performance. Moreover, we also intend to test the electrical properties of the hybrid systems, since the presence of metallic NPs at the flake edges might induce a drastic decrease of interflake resistance, similar to the formation of covalently interconnected networks. Finally, the hybrid systems show a great potential for SERS and photothermal applications, such as the detection of harmful analytes (*i.e.*, food, water), imaging and photothermal cancer therapy.
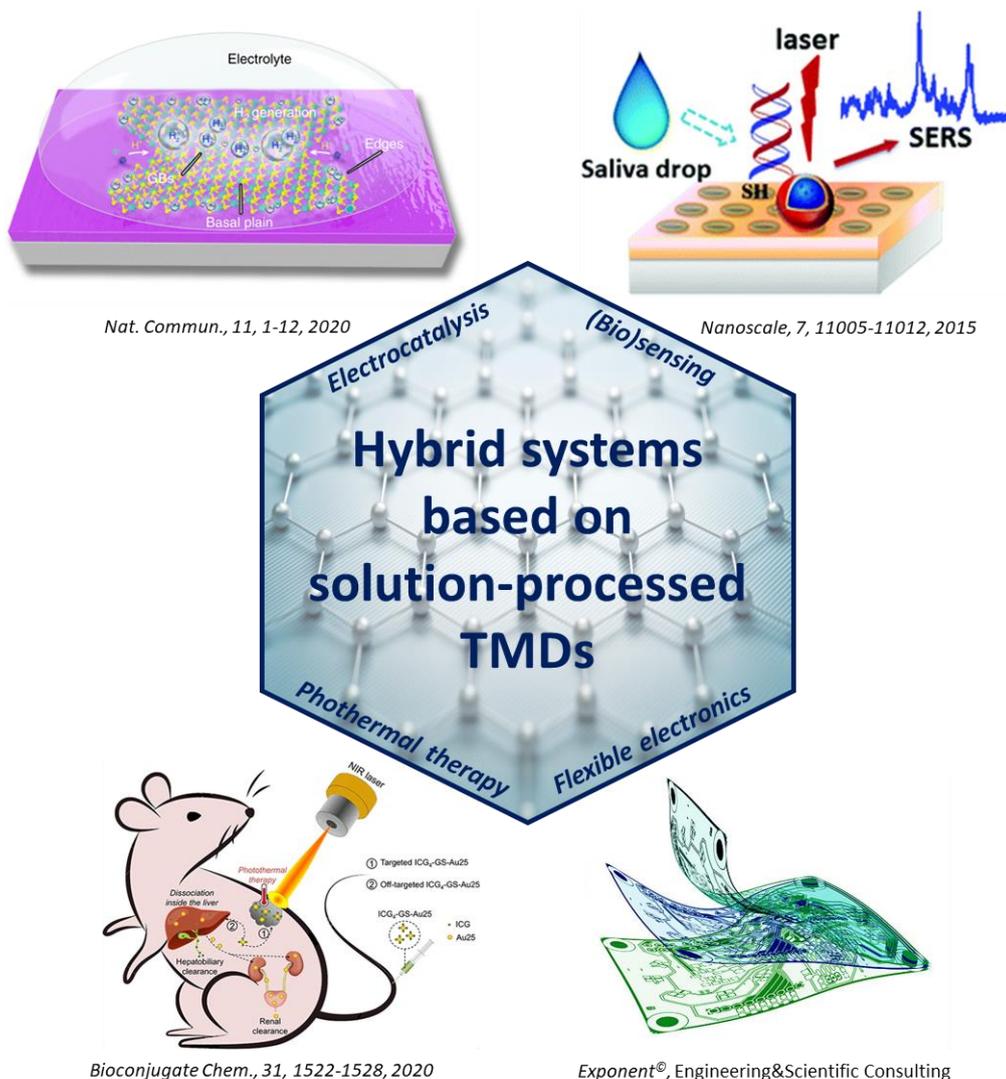
Figure 7-2 : Graphic illustration of the main research areas that would benefit from the TMD-based hybrid systems discussed in this doctoral work. The possible applications cover electrocatalysis, sensing and electronics, highlighting the unique versatility of such multifunctional materials.

All in all, the tuning of physicochemical properties achieved thanks to meticulously designed functionalization strategies could result in a smart and elegant alternative to develop original, cutting-edge and exotic hybrid technologies based on solution-processed TMDs. In particular, the forthcoming technological progress shall exploit the enormous potentiality of these emerging materials, flagship systems in 2DM science with extremely high potential for engaging and challenging applications in flexible and wearable (opto)electronics, (bio)sensing and (photo)catalysis.

References

1. Novoselov, K. S. *et al.* Electric field effect in atomically thin carbon films. *Science* **306**, 666–669 (2004).

2. Geim, A. K. & Novoselov, K. S. The rise of graphene. *Nat. Mater.* **6**, 183–191 (2007).

3. Novoselov, K. S. *et al.* Two-dimensional atomic crystals. *PNAS* **102**, 10451–10453 (2005).

4. Manzeli, S., Ovchinnikov, D., Pasquier, D., Yazyev, O. V. & Kis, A. 2D transition metal dichalcogenides. *Nat. Rev. Mater.* **2**, 17033 (2017).

5. Novoselov, K. S., Mishchenko, A., Carvalho, A. & Neto, A. H. C. 2D materials and van der Waals heterostructures. *Science* **353**, aac9439 (2016).

6. Mak, K. F. & Shan, J. Photonics and optoelectronics of 2D semiconductor transition metal dichalcogenides. *Nat. Photonics* **10**, 216–226 (2016).

7. Voiry, D., Yang, J. & Chhowalla, M. Recent strategies for improving the catalytic activity of 2D TMD nanosheets toward the hydrogen evolution reaction. *Adv. Mater.* **28**, 6197–6206 (2016).

8. Bertolazzi, S., Gobbi, M., Zhao, Y., Backes, C. & Samorì, P. Molecular chemistry approaches for tuning the properties of two-dimensional transition metal dichalcogenides. *Chem. Soc. Rev.* **47**, 6845–6888 (2018).

9. Yi, M. & Shen, Z. A review on mechanical exfoliation for the scalable production of graphene. *J. Mater. Chem. A* **3**, 11700–11715 (2015).

10. Park, J. H. *et al.* Defect passivation of transition metal dichalcogenides via a charge transfer van der Waals interface. *Sci. Adv.* **3**, e1701661 (2017).

11. Huang, X. *et al.* Solution-phase epitaxial growth of noble metal nanostructures on dispersible single-layer molybdenum disulfide nanosheets. *Nat. Commun.* **4**, 1444 (2013).

12. Liu, J. *et al.* Preparation of MoS_2-polyvinylpyrrolidone nanocomposites for flexible nonvolatile rewritable memory devices with reduced graphene oxide electrodes. *Small* **8**, 3517–3522 (2012).

13. Bonaccorso, F., Bartolotta, A., Coleman, J. N. & Backes, C. 2D-Crystal-based functional inks. *Adv. Mater.* **28**, 6136–6166 (2016).

14. Tsai, C. *et al.* Electrochemical generation of sulfur vacancies in the basal plane of MoS_2 for hydrogen evolution. *Nat. Commun.* **8**, 15113 (2017).

15. Ippolito, S. *et al.* Covalently interconnected transition metal dichalcogenide networks via defect engineering for high-performance electronic devices. *Nat. Nanotechnol.* **16**, 592–598 (2021).

16. Noriega, R. *et al.* A general relationship between disorder, aggregation and charge transport in conjugated polymers. *Nat. Mater.* **12**, 1038–1044 (2013).

17. Kelly, A. G. *et al.* All-printed thin-film transistors from networks of liquid-exfoliated nanosheets. *Science* **356**, 69–73 (2017).

18. Li, J., Naiini, M. M., Vaziri, S., Lemme, M. C. & Östling, M. Inkjet printing of MoS_2. *Adv. Funct. Mater.* **24**, 6524–6531 (2014).

19. Li, S.-L., Tsukagoshi, K., Orgiu, E. & Samorì, P. Charge transport and mobility engineering in two-dimensional transition metal chalcogenide semiconductors. *Chem. Soc. Rev.* **45**, 118–151 (2015).

20. Song, B. *et al.* In situ study of nucleation and growth dynamics of Au nanoparticles on MoS_2 nanoflakes. *Nanoscale* **10**, 15809–15818 (2018).

21. Lee, C., Wei, X., Kysar, J. W. & Hone, J. Measurement of the elastic properties and intrinsic strength of monolayer graphene. *Science* **321**, 385–388 (2008).

22. Geim, A. K. & Grigorieva, I. V. Van der waals heterostructures. *Nature* **499**, 419–425 (2013).

23. Han, J. H., Kwak, M., Kim, Y. & Cheon, J. Recent advances in the solution-based preparation of two-dimensional layered transition metal chalcogenide nanostructures. *Chem. Rev.* **118**, 6151–6188 (2018).

24. Backes, C. *et al.* Production and processing of graphene and related materials. *2D Mater.* **7**, 022001 (2020).

25. Ippolito, S., Ciesielski, A. & Samorì, P. Tailoring the physicochemical properties of solution-processed transition metal dichalcogenides via molecular approaches. *Chem. Commun.* **55**, 8900–8914 (2019).

26. Raccichini, R., Varzi, A., Passerini, S. & Scrosati, B. The role of graphene for electrochemical energy storage. *Nat. Mater.* **14**, 271–279 (2015).

27. Qin, H., Sorkin, V., Pei, Q.-X., Liu, Y. & Zhang, Y.-W. Failure in two-dimensional materials: defect sensitivity and failure criteria. *J. Appl. Mech.* **87**, (2020).

28. Lin, Z. *et al.* Defect engineering of two-dimensional transition metal dichalcogenides. *2D Mater.* **3**, 022002 (2016).

29. Wang, Q. H., Kalantar-Zadeh, K., Kis, A., Coleman, J. N. & Strano, M. S. Electronics and optoelectronics of two-dimensional transition metal dichalcogenides. *Nat. Nanotechnol.* **7**, 699–712 (2012).

30. Cai, X., Luo, Y., Liu, B. & Cheng, H.-M. Preparation of 2D material dispersions and their applications. *Chem. Soc. Rev.* **47**, 6224–6266 (2018).

31. Lembke, D. & Kis, A. Breakdown of high-performance monolayer MoS_2 transistors. *ACS Nano* **6**, 10070–10075 (2012).

32. Waldrop, M. M. The chips are down for Moore's law. *Nature News* **530**, 144 (2016).

33. Chia, X. & Pumera, M. Characteristics and performance of two-dimensional materials for electrocatalysis. *Nat. Catal.* **1**, 909–921 (2018).

34. Anichini, C. *et al.* Chemical sensing with 2D materials. *Chem. Soc. Rev.* **47**, 4860–4908 (2018).

35. Ping, J., Fan, Z., Sindoro, M., Ying, Y. & Zhang, H. Recent advances in sensing applications of two-dimensional transition metal dichalcogenide nanosheets and their composites. *Adv. Funct. Mater.* **27**, 1605817 (2017).

36. Jariwala, D., Sangwan, V. K., Lauhon, L. J., Marks, T. J. & Hersam, M. C. Emerging device applications for semiconducting two-dimensional transition metal dichalcogenides. *ACS Nano* **8**, 1102–1120 (2014).

37. Miró, P., Audiffred, M. & Heine, T. An atlas of two-dimensional materials. *Chem. Soc. Rev.* **43**, 6537–6554 (2014).

38. Yang, J.-F., Parakash, B., Hardell, J. & Fang, Q.-F. Tribological properties of transition metal di-chalcogenide based lubricant coatings. *Front. Mater. Sci.* **6**, 116–127 (2012).

39. Yang, H., Kim, S. W., Chhowalla, M. & Lee, Y. H. Structural and quantum-state phase transitions in van der Waals layered materials. *Nat. Phys.* **13**, 931–937 (2017).

40. Li, W., Qian, X. & Li, J. Phase transitions in 2D materials. *Nat. Rev. Mater.* 1–18 (2021).

41. Chhowalla, M. *et al.* The chemistry of two-dimensional layered transition metal dichalcogenide nanosheets. *Nat. Chem.* **5**, 263–275 (2013).

42. Chaves, A. *et al.* Bandgap engineering of two-dimensional semiconductor materials. *npj 2D Mater. Appl.* **4**, 1–21 (2020).

43. Splendiani, A. *et al.* Emerging photoluminescence in monolayer MoS_2. *Nano Lett.* **10**, 1271–1275 (2010).

44. Mak, K. F., Lee, C., Hone, J., Shan, J. & Heinz, T. F. Atomically thin MoS_2: a new direct-gap semiconductor. *Phys. Rev. Lett.* **105**, 136805 (2010).

45. Li, T. & Galli, G. Electronic properties of MoS_2 nanoparticles. *J. Phys. Chem. C* **111**, 16192–16196 (2007).

46. Yeh, P.-C. *et al.* Direct measurement of the thickness-dependent electronic band structure of MoS_2 using angle-resolved photoemission spectroscopy. *Phys. Rev. Lett.* **111**, 106801 (2013).

47. El Garah, M. *et al.* MoS_2 nanosheets via electrochemical lithium-ion intercalation under ambient conditions. *FlatChem* **9**, 33–39 (2018).

48. Lee, C. *et al.* Anomalous lattice vibrations of single- and few-Layer MoS_2. *ACS Nano* **4**, 2695–2700 (2010).

49. Elías, A. L. *et al.* Controlled synthesis and transfer of large-area WS_2 sheets: from single layer to few layers. *ACS Nano* **7**, 5235–5242 (2013).

50. Hoang, A. T., Qu, K., Chen, X. & Ahn, J.-H. Large-area synthesis of transition metal dichalcogenides via CVD and solution-based approaches and their device applications. *Nanoscale* **13**, 615–633 (2021).

51. Gong, C. *et al.* Metal contacts on physical vapor deposited monolayer MoS_2. *ACS Nano* **7**, 11350–11357 (2013).

52. Feng, Q. *et al.* Growth of $MoS_{2(1-x)}Se_{2x}$ (x = 0.41–1.00) monolayer alloys with controlled morphology by physical vapor deposition. *ACS Nano* **9**, 7450–7455 (2015).

53. Cai, Z., Liu, B., Zou, X. & Cheng, H.-M. Chemical vapor deposition growth and applications of two-dimensional materials and their heterostructures. *Chem. Rev.* **118**, 6091–6133 (2018).

54. Yu, Y. *et al.* Controlled scalable synthesis of uniform, high-quality monolayer and few-layer MoS_2 films. *Sci. Rep.* **3**, 1866 (2013).

55. Perkgoz, N. K. & Bay, M. Investigation of single-wall MoS_2 monolayer flakes grown by chemical vapor deposition. *Nano-Micro Lett.* **8**, 70–79 (2016).

56. Zhan, Y., Liu, Z., Najmaei, S., Ajayan, P. M. & Lou, J. Large-area vapor-phase growth and characterization of MoS_2 atomic layers on a SiO_2 substrate. *Small* **8**, 966–971 (2012).

57. Lin, Y.-C. *et al.* Wafer-scale MoS_2 thin layers prepared by MoO_3 sulfurization. *Nanoscale* **4**, 6637–6641 (2012).

58. Lin, S. *et al.* Tunable active edge sites in $PtSe_2$ films towards hydrogen evolution reaction. *Nano Energy* **42**, 26–33 (2017).

59. Song, J.-G. *et al.* Layer-controlled, wafer-scale, and conformal synthesis of tungsten disulfide nanosheets using atomic layer deposition. *ACS Nano* **7**, 11333–11340 (2013).

60. Cheng, L. *et al.* Ultrathin WS$_2$ nanoflakes as a high-performance electrocatalyst for the hydrogen evolution reaction. *Angew. Chem. Int. Ed.* **53**, 7860–7863 (2014).

61. Jeong, S., Yoo, D., Jang, J., Kim, M. & Cheon, J. Well-defined colloidal 2-D layered transition-metal chalcogenide nanocrystals via generalized synthetic protocols. *J. Am. Chem. Soc.* **134**, 18233–18236 (2012).

62. Chen, L. *et al.* One-pot synthesis of MoS$_2$ nanoflakes with desirable degradability for photothermal cancer therapy. *ACS Appl. Mater. Interfaces* **9**, 17347–17358 (2017).

63. Arul, N. S. & Han, J. I. Facile hydrothermal synthesis of hexapod-like two dimensional dichalcogenide NiSe$_2$ for supercapacitor. *Mater. Lett.* **181**, 345–349 (2016).

64. Ding, W. *et al.* Highly ambient-stable 1T-MoS$_2$ and 1T-WS$_2$ by hydrothermal synthesis under high magnetic fields. *ACS Nano* **13**, 1694–1702 (2019).

65. Nasilowski, M., Mahler, B., Lhuillier, E., Ithurria, S. & Dubertret, B. Two-dimensional colloidal nanocrystals. *Chem. Rev.* **116**, 10934–10982 (2016).

66. Jang, J. *et al.* Ultrathin zirconium disulfide nanodiscs. *J. Am. Chem. Soc.* **133**, 7636–7639 (2011).

67. Yoo, D., Kim, M., Jeong, S., Han, J. & Cheon, J. Chemical synthetic strategy for single-layer transition-metal chalcogenides. *J. Am. Chem. Soc.* **136**, 14670–14673 (2014).

68. Jung, W. *et al.* Colloidal synthesis of single-layer MSe$_2$ (M = Mo, W) nanosheets via anisotropic solution-phase growth approach. *J. Am. Chem. Soc.* **137**, 7266–7269 (2015).

69. Frindt, R. F. Single crystals of MoS$_2$ several molecular layers Thick. *J. Appl. Phys.* **37**, 1928–1929 (1966).

70. Chen, J., Duan, M. & Chen, G. Continuous mechanical exfoliation of graphene sheets via three-roll mill. *J. Mater. Chem.* **22**, 19625–19628 (2012).

71. Whittingham, M. S. & Gamble, F. R. The lithium intercalates of the transition metal dichalcogenides. *Mater. Res. Bull.* **10**, 363–371 (1975).

72. Joensen, P., Frindt, R. F. & Morrison, S. R. Single-layer MoS$_2$. *Mater. Res. Bull.* **21**, 457–461 (1986).

73. Zeng, Z. *et al.* An effective method for the fabrication of few-layer-thick inorganic nanosheets. *Angew. Chem. Int. Ed.* **51**, 9052–9056 (2012).

74. Benavente, E., Santa Ana, M. A., Mendizábal, F. & González, G. Intercalation chemistry of molybdenum disulfide. *Coord. Chem. Rev.* **224**, 87–109 (2002).

75. Leong, S. X. *et al.* 2H → 1T Phase change in direct synthesis of WS$_2$ nanosheets via solution-based electrochemical exfoliation and their catalytic properties. *ACS Appl. Mater. Interfaces* **9**, 26350–26356 (2017).

76. Hernandez, Y. *et al.* High-yield production of graphene by liquid-phase exfoliation of graphite. *Nat. Nanotechnol.* **3**, 563–568 (2008).

77. Witomska, S., Leydecker, T., Ciesielski, A. & Samorì, P. Production and patterning of liquid phase–exfoliated 2D sheets for applications in optoelectronics. *Adv. Funct. Mater.* **0**, 1901126.

78. Yao, Y. *et al.* Large-scale production of two-dimensional nanosheets. *J. Mater. Chem.* **22**, 13494–13499 (2012).

79. Han, C. *et al.* High-yield production of MoS$_2$ and WS$_2$ quantum sheets from their bulk materials. *Nano Lett.* **17**, 7767–7772 (2017).

80. Cunningham, G. *et al.* Solvent exfoliation of transition metal dichalcogenides: dispersibility of exfoliated nanosheets varies only weakly between compounds. *ACS Nano* **6**, 3468–3480 (2012).

81. O'Neill, A., Khan, U. & Coleman, J. N. Preparation of high concentration dispersions of exfoliated MoS$_2$ with increased flake size. *Chem. Mater.* **24**, 2414–2421 (2012).

82. Backes, C. *et al.* Production of highly monolayer enriched dispersions of liquid-exfoliated nanosheets by liquid cascade centrifugation. *ACS Nano* **10**, 1589–1601 (2016).

83. Pachauri, V., Kern, K. & Balasubramanian, K. Chemically exfoliated large-area two-dimensional flakes of molybdenum disulfide for device applications. *APL Materials* **1**, 032102 (2013).

84. Zhou, W. *et al.* Intrinsic structural defects in monolayer molybdenum disulfide. *Nano Lett.* **13**, 2615–2622 (2013).

85. Komsa, H.-P. & Krasheninnikov, A. V. Native defects in bulk and monolayer MoS$_2$ from first principles. *Phys. Rev. B* **91**, 125304 (2015).

86. Komsa, H.-P., Kurasch, S., Lehtinen, O., Kaiser, U. & Krasheninnikov, A. V. From point to extended defects in two-dimensional MoS$_2$: evolution of atomic structure under electron irradiation. *Phys. Rev. B* **88**, 035301 (2013).

87. Han, Y., Hu, T., Li, R., Zhou, J. & Dong, J. Stabilities and electronic properties of monolayer MoS$_2$ with one or two sulfur line vacancy defects. *Phys. Chem. Chem. Phys.* **17**, 3813–3819 (2015).

88. Zou, X., Liu, Y. & Yakobson, B. I. Predicting dislocations and grain boundaries in two-dimensional metal-disulfides from the first principles. *Nano Lett.* **13**, 253–258 (2013).

89. Schweiger, H., Raybaud, P., Kresse, G. & Toulhoat, H. Shape and edge sites modifications of MoS$_2$ catalytic nanoparticles induced by working conditions: a theoretical study. *J. Catal.* **207**, 76–87 (2002).

90. Miró, P., Ghorbani-Asl, M. & Heine, T. Spontaneous ripple formation in MoS$_2$ monolayers: electronic structure and transport effects. *Adv. Mater.* **25**, 5473–5475 (2013).

91. Crowne, F. J. *et al.* Blueshift of the A-exciton peak in folded monolayer 1H-MoS$_2$. *Phys. Rev. B* **88**, 235302 (2013).

92. Yan, W. *et al.* Strain and curvature induced evolution of electronic band structures in twisted graphene bilayer. *Nat Commun* **4**, 2159 (2013).

93. Kang, J., Li, J., Li, S.-S., Xia, J.-B. & Wang, L.-W. Electronic structural moiré pattern effects on MoS$_2$/MoSe$_2$ 2D heterostructures. *Nano Lett.* **13**, 5485–5490 (2013).

94. Rosenberger, M. R. *et al.* Twist angle-dependent atomic reconstruction and moiré patterns in transition metal dichalcogenide heterostructures. *ACS Nano* **14**, 4550–4558 (2020).

95. Shabani, S. *et al.* Deep moiré potentials in twisted transition metal dichalcogenide bilayers. *Nat. Phys.* **17**, 720–725 (2021).

96. Zande, A. M. van der *et al.* Grains and grain boundaries in highly crystalline monolayer molybdenum disulphide. *Nat. Mater.* **12**, 554–561 (2013).

97. Peimyoo, N. *et al.* Nonblinking, intense two-dimensional light emitter: monolayer WS$_2$ triangles. *ACS Nano* **7**, 10985–10994 (2013).

98.   Gong, Y. *et al.* Vertical and in-plane heterostructures from WS$_2$/MoS$_2$ monolayers. *Nat. Mater.* **13**, 1135–1142 (2014).

99.   Ji, Q., Zhang, Y., Zhang, Y. & Liu, Z. Chemical vapour deposition of group-VIB metal dichalcogenide monolayers: engineered substrates from amorphous to single crystalline. *Chem. Soc. Rev.* **44**, 2587–2602 (2015).

100.   Lee, J. *et al.* Defect-induced in situ atomic doping in transition metal dichalcogenides via liquid-phase synthesis toward efficient electrochemical activity. *ACS Nano* **14**, 17114–17124 (2020).

101.   Xie, J. *et al.* Defect-rich MoS$_2$ ultrathin nanosheets with additional active edge sites for enhanced electrocatalytic hydrogen evolution. *Adv. Mater.* **25**, 5807–5813 (2013).

102.   Schuler, B. *et al.* Large spin-orbit splitting of deep in-gap defect states of engineered sulfur vacancies in monolayer WS$_2$. *Phys. Rev. Lett.* **123**, 076801 (2019).

103.   Zhu, H. *et al.* Defects and surface structural stability of MoTe$_2$ under vacuum annealing. *ACS Nano* **11**, 11005–11014 (2017).

104.   Zhang, L. *et al.* Molecular beam epitaxy of two-dimensional vanadium-molybdenum diselenide alloys. *ACS Nano* **14**, 11140–11149 (2020).

105.   Chua, R. *et al.* Can reconstructed Se-deficient line defects in monolayer VSe$_2$ induce magnetism? *Adv. Mater.* **32**, 2000693 (2020).

106.   Cho, S. *et al.* Phase patterning for ohmic homojunction contact in MoTe$_2$. *Science* **349**, 625–628 (2015).

107.   Castellanos-Gomez, A. *et al.* Laser-thinning of MoS$_2$: on demand generation of a single-layer semiconductor. *Nano Lett.* **12**, 3187–3192 (2012).

108.   Chen, M. *et al.* Multibit data storage states formed in plasma-treated MoS$_2$ transistors. *ACS Nano* **8**, 4023–4032 (2014).

109.   Shim, J. *et al.* High-performance 2D rhenium disulfide (ReS$_2$) transistors and photodetectors by oxygen plasma treatment. *Adv. Mater.* **28**, 6985–6992 (2016).

110.   Wu, Z. *et al.* Defect activated photoluminescence in WSe$_2$ monolayer. *J. Phys. Chem. C* **121**, 12294–12299 (2017).

111.   Kang, N., Paudel, H. P., Leuenberger, M. N., Tetard, L. & Khondaker, S. I. Photoluminescence quenching in single-layer MoS$_2$ via oxygen plasma treatment. *J. Phys. Chem. C* **118**, 21258–21263 (2014).

112.   Nan, H. *et al.* Strong photoluminescence enhancement of MoS$_2$ through defect engineering and oxygen bonding. *ACS Nano* **8**, 5738–5745 (2014).

113.   Komsa, H.-P. *et al.* Two-dimensional transition metal dichalcogenides under electron irradiation: defect production and doping. *Phys. Rev. Lett.* **109**, 035503 (2012).

114.   Yoshimura, A., Lamparski, M., Kharche, N. & Meunier, V. First-principles simulation of local response in transition metal dichalcogenides under electron irradiation. *Nanoscale* **10**, 2388–2397 (2018).

115.   Zan, R. *et al.* Control of radiation damage in MoS$_2$ by graphene encapsulation. *ACS Nano* **7**, 10167–10174 (2013).

116.   Mitterreiter, E. *et al.* Atomistic positioning of defects in helium ion treated single-layer MoS$_2$. *Nano Lett.* **20**, 4437–4444 (2020).

117.   Thiruraman, J. P., Das, P. M. & Drndić, M. Irradiation of transition metal dichalcogenides using a focused ion beam: controlled single-atom defect creation. *Adv. Funct. Mater.* **29**, 1904668 (2019).

118.   Bertolazzi, S. *et al.* Engineering chemically active defects in monolayer MoS$_2$ transistors via ion-beam irradiation and their healing via vapor deposition of alkanethiols. *Adv. Mater.* **29**, 1606760 (2017).

119.   Tongay, S. *et al.* Defects activated photoluminescence in two-dimensional semiconductors: interplay between bound, charged and free excitons. *Sci. Rep.* **3**, 2657 (2013).

120.   Kim, T.-Y. *et al.* Irradiation effects of high-energy proton beams on MoS$_2$ field effect transistors. *ACS Nano* **8**, 2774–2781 (2014).

121.   Sim, D. M. *et al.* Controlled doping of vacancy-containing few-layer MoS$_2$ via highly stable thiol-based molecular chemisorption. *ACS Nano* **9**, 12115–12123 (2015).

122.   Liang, Q., Zhang, Q., Zhao, X., Liu, M. & Wee, A. T. S. Defect engineering of two-dimensional transition-metal dichalcogenides: applications, challenges, and opportunities. *ACS Nano* **15**, 2165–2181 (2021).

123.   Chou, S. S. *et al.* Ligand conjugation of chemically exfoliated MoS$_2$. *J. Am. Chem. Soc.* **135**, 4584–4587 (2013).

124.   Förster, A., Gemming, S., Seifert, G. & Tománek, D. Chemical and electronic repair mechanism of defects in MoS$_2$ monolayers. *ACS Nano* **11**, 9989–9996 (2017).

125.   Liu, T. *et al.* Drug delivery with PEGylated MoS$_2$ nano-sheets for combined photothermal and chemotherapy of cancer. *Adv. Mater.* **26**, 3433–3440 (2014).

126.   Nguyen, E. P. *et al.* Electronic tuning of 2D MoS$_2$ through surface functionalization. *Adv. Mater.* **27**, 6225–6229 (2015).

127.   Karunakaran, S., Pandit, S., Basu, B. & De, M. Simultaneous exfoliation and functionalization of 2H-MoS$_2$ by thiolated surfactants: applications in enhanced antibacterial activity. *J. Am. Chem. Soc.* **140**, 12634–12644 (2018).

128.   Presolski, S. *et al.* Functional nanosheet synthons by covalent modification of transition-metal dichalcogenides. *Chem. Mater.* **29**, 2066–2073 (2017).

129.   Chen, X., Berner, N. C., Backes, C., Duesberg, G. S. & McDonald, A. R. Functionalization of two-dimensional MoS$_2$: on the reaction between MoS$_2$ and organic thiols. *Angew. Chem. Int. Ed.* **55**, 5803–5808 (2016).

130.   Li, Q. *et al.* Towards a comprehensive understanding of the reaction mechanisms between defective MoS$_2$ and thiol molecules. *Angew. Chem. Int. Ed.* **56**, 10501–10505 (2017).

131.   Yu, X., Guijarro, N., Johnson, M. & Sivula, K. Defect mitigation of solution-processed 2D WSe$_2$ nanoflakes for solar-to-hydrogen conversion. *Nano Lett.* **18**, 215–222 (2018).

132.   Yu, X., Prévot, M. S. & Sivula, K. Multiflake thin film electronic devices of solution processed 2D MoS$_2$ enabled by sonopolymer assisted exfoliation and surface modification. *Chem. Mater.* **26**, 5892–5899 (2014).

133. Shahar, C. *et al.* Surface functionalization of WS$_2$ fullerene-like nanoparticles. *Langmuir* **26**, 4409–4414 (2010).

134. Kang, D.-H. *et al.* Controllable nondegenerate p-type doping of tungsten diselenide by octadecyltrichlorosilane. *ACS Nano* **9**, 1099–1107 (2015).

135. Ayán-Varela, M. *et al.* Aqueous exfoliation of transition metal dichalcogenides assisted by DNA/RNA nucleotides: catalytically active and biocompatible nanosheets stabilized by acid–base interactions. *ACS Appl. Mater. Interfaces* **9**, 2835–2845 (2017).

136. Chuang, M.-K., Yang, S.-S. & Chen, F.-C. Metal nanoparticle-decorated two-dimensional molybdenum sulfide for plasmonic-enhanced polymer photovoltaic devices. *Materials* **8**, 5414–5425 (2015).

137. Kim, J., Byun, S., Smith, A. J., Yu, J. & Huang, J. Enhanced electrocatalytic properties of transition-metal dichalcogenides sheets by spontaneous gold nanoparticle decoration. *J. Phys. Chem. Lett.* **4**, 1227–1232 (2013).

138. Yuwen, L. *et al.* General synthesis of noble metal (Au, Ag, Pd, Pt) nanocrystal modified MoS$_2$ nanosheets and the enhanced catalytic activity of Pd–MoS$_2$ for methanol oxidation. *Nanoscale* **6**, 5762–5769 (2014).

139. Raza, F. *et al.* Structuring Pd nanoparticles on 2H-WS$_2$ nanosheets induces excellent photocatalytic activity for cross-coupling reactions under visible light. *J. Am. Chem. Soc.* **139**, 14767–14774 (2017).

140. Sarkar, D. *et al.* Functionalization of transition metal dichalcogenides with metallic nanoparticles: implications for doping and gas-sensing. *Nano Lett.* **15**, 2852–2862 (2015).

141. Paredes, J. I. *et al.* Impact of covalent functionalization on the aqueous processability, catalytic activity, and biocompatibility of chemically exfoliated MoS$_2$ nanosheets. *ACS Appl. Mater. Interfaces* **8**, 27974–27986 (2016).

142. Zhou, L., He, B., Yang, Y. & He, Y. Facile approach to surface functionalized MoS$_2$ nanosheets. *RSC Adv.* **4**, 32570–32578 (2014).

143. Cheng, Z., He, B. & Zhou, L. A general one-step approach for in situ decoration of MoS$_2$ nanosheets with inorganic nanoparticles. *J. Mater. Chem. A* **3**, 1042–1048 (2014).

144. Zuo, P. *et al.* Metal (Ag, Pt)–MoS$_2$ hybrids greenly prepared through photochemical reduction of femtosecond laser pulses for SERS and HER. *ACS Sustainable Chem. Eng.* **6**, 7704–7714 (2018).

145. Zhu, C., Kwok, R. T. K., Lam, J. W. Y. & Tang, B. Z. Aggregation-induced emission: a trailblazing journey to the field of biomedicine. *ACS Appl. Bio Mater.* **1**, 1768–1786 (2018).

146. Sreeprasad, T. S., Nguyen, P., Kim, N. & Berry, V. Controlled, defect-guided, metal-nanoparticle incorporation onto MoS$_2$ via chemical and microwave routes: electrical, thermal, and structural properties. *Nano Lett.* **13**, 4434–4441 (2013).

147. Keyshar, K. *et al.* Experimental determination of the ionization energies of MoSe$_2$, WS$_2$, and MoS$_2$ on SiO$_2$ using photoemission electron microscopy. *ACS Nano* **11**, 8223–8230 (2017).

148.   Kajiwara, R., Asaumi, Y., Nakamura, M. & Hoshi, N. Active sites for the hydrogen oxidation and the hydrogen evolution reactions on the high index planes of Pt. *J. Electroanal. Chem.* **657**, 61–65 (2011).

149.   Paton, K. R. & Coleman, J. N. Relating the optical absorption coefficient of nanosheet dispersions to the intrinsic monolayer absorption. *Carbon* **107**, 733–738 (2016).

150.   Backes, C. *et al.* Edge and confinement effects allow in situ measurement of size and thickness of liquid-exfoliated nanosheets. *Nat. Commun.* **5**, 1–10 (2014).

151.   Mishra, A. K., Lakshmi, K. V. & Huang, L. Eco-friendly synthesis of metal dichalcogenides nanosheets and their environmental remediation potential driven by visible light. *Sci. Rep.* **5**, 15718 (2015).

152.   Rahman, M., Davey, K. & Qiao, S.-Z. Advent of 2D rhenium disulfide (ReS_2): fundamentals to applications. *Adv. Funct. Mater.* **27**, 1606129 (2017).

153.   Saito, R., Tatsumi, Y., Huang, S., Ling, X. & Dresselhaus, M. S. Raman spectroscopy of transition metal dichalcogenides. *J. Phys.: Condens. Matter* **28**, 353002 (2016).

154.   Lide, D. R. *CRC handbook of chemistry and physics*. **85**, *CRC Press* (2004).

155.   Allara, D. L. & Nuzzo, R. G. Spontaneously organized molecular assemblies. 1. Formation, dynamics, and physical properties of n-alkanoic acids adsorbed from solution on an oxidized aluminum surface. *Langmuir* **1**, 45–52 (1985).

156.   Vericat, C., Vela, M. E., Benitez, G., Carro, P. & Salvarezza, R. C. Self-assembled monolayers of thiols and dithiols on gold: new challenges for a well-known system. *Chem. Soc. Rev.* **39**, 1805–1834 (2010).

157.   Sun, L. *et al.* Single-molecule electronics: from chemical design to functional devices. *Chem. Soc. Rev.* **43**, 7378–7411 (2014).

158.   Su, T. A., Neupane, M., Steigerwald, M. L., Venkataraman, L. & Nuckolls, C. Chemical principles of single-molecule electronics. *Nat. Rev. Mater.* **1**, 1–15 (2016).

159.   Casalini, S., Bortolotti, C. A., Leonardi, F. & Biscarini, F. Self-assembled monolayers in organic electronics. *Chem. Soc. Rev.* **46**, 40–71 (2017).

160.   Singh, M., Kaur, N. & Comini, E. The role of self-assembled monolayers in electronic devices. *J. Mater. Chem. C* **8**, 3938–3955 (2020).

161.   Zhou, S. *et al.* Atomic structure and dynamics of defects in 2D MoS_2 bilayers. *ACS Omega* **2**, 3315–3324 (2017).

162.   Schilter, D. Thiol oxidation: a slippery slope. *Nat. Rev. Chem.* **1**, 1–1 (2017).

163.   Joensen, P., Crozier, E. D., Alberding, N. & Frindt, R. F. A study of single-layer and restacked MoS_2 by X-ray diffraction and X-ray absorption spectroscopy. *J. Phys. C: Solid State Phys.* **20**, 4043–4053 (1987).

164.   Donarelli, M., Bisti, F., Perrozzi, F. & Ottaviano, L. Tunable sulfur desorption in exfoliated MoS_2 by means of thermal annealing in ultra-high vacuum. *Chem. Phys. Lett.* **588**, 198–202 (2013).

165.   McIntyre, N. S., Spevack, P. A., Beamson, G. & Briggs, D. Effects of argon ion bombardment on basal plane and polycrystalline MoS_2. *Surf. Sci.* **237**, L390–L397 (1990).

166. Bouvard, O., Krammer, A. & Schüler, A. In situ core-level and valence-band photoelectron spectroscopy of reactively sputtered tungsten oxide films. *Surf. Interface Anal.* **48**, 660–663 (2016).

167. Borowiec, J. *et al.* Room temperature synthesis of ReS$_2$ through aqueous perrhenate sulfidation. *J. Phys.: Condens. Matter* **30**, 055702 (2018).

168. Steudel, R. Mechanism for the formation of elemental sulfur from aqueous sulfide in chemical and microbiological desulfurization processes. *Ind. Eng. Chem. Res.* **35**, 1417–1423 (1996).

169. Mignuzzi, S. *et al.* Effect of disorder on Raman scattering of single-layer MoS$_2$. *Phys. Rev. B* **91**, 195411 (2015).

170. Chakraborty, B. *et al.* Symmetry-dependent phonon renormalization in monolayer MoS$_2$ transistor. *Phys. Rev. B* **85**, 161403 (2012).

171. Bae, S. *et al.* Defect-induced vibration modes of Ar$^+$-irradiated MoS$_2$. *Phys. Rev. Appl.* **7**, 024001 (2017).

172. Park, S. Y. *et al.* Highly selective and sensitive chemoresistive humidity sensors based on rGO/MoS$_2$ van der Waals composites. *J. Mater. Chem. A* **6**, 5016–5024 (2018).

173. Chow, P. K. *et al.* Wetting of mono and few-layered WS$_2$ and MoS$_2$ films supported on Si/SiO$_2$ substrates. *ACS Nano* **9**, 3023–3031 (2015).

174. Marques, M. E., Mansur, A. A. P. & Mansur, H. S. Chemical functionalization of surfaces for building three-dimensional engineered biosensors. *Appl. Surf. Sci.* **275**, 347–360 (2013).

175. Chen, X. & McDonald, A. R. Functionalization of two-dimensional transition-metal dichalcogenides. *Adv. Mater.* **28**, 5738–5746 (2016).

176. Chen, X., McGlynn, C. & McDonald, A. R. Two-dimensional MoS$_2$ catalyzed oxidation of organic thiols. *Chem. Mater.* **30**, 6978–6982 (2018).

177. Wang, Y., Gali, S. M., Slassi, A., Beljonne, D. & Samorì, P. Collective dipole-dominated doping of monolayer MoS$_2$: orientation and magnitude control via the supramolecular approach. *Adv. Funct. Mater.* **30**, 2002846 (2020).

178. Shu, J. *et al.* The intrinsic origin of hysteresis in MoS$_2$ field effect transistors. *Nanoscale* **8**, 3049–3056 (2016).

179. Chiu, F.-C. A Review on conduction mechanisms in dielectric films. *Adv. Mater. Sci. Eng.* **2014**, 1–18 (2014).

180. Lee, K. *et al.* Electrical characteristics of molybdenum disulfide flakes produced by liquid exfoliation. *Adv. Mater.* **23**, 4178–4182 (2011).

181. Retamal, J. R. D., Periyanagounder, D., Ke, J.-J., Tsai, M.-L. & He, J.-H. Charge carrier injection and transport engineering in two-dimensional transition metal dichalcogenides. *Chem. Sci.* **9**, 7727–7745 (2018).

182. Sze, S. M. & Ng, K. K. Physics of semiconductor devices. *John Wiley&Sons* (2006).

183. Vladimirov, I. *et al.* Bulk transport and contact limitation of MoS$_2$ multilayer flake transistors untangled via temperature-dependent transport measurements. *Phys. Status Solidi A* **212**, 2059–2067 (2015).

184. Zeng, X., Hirwa, H., Metel, S., Nicolosi, V. & Wagner, V. Solution processed thin film transistor from liquid phase exfoliated MoS$_2$ flakes. *Solid-State Electron.* **141**, 58–64 (2018).

185. Simonetti, O. & Giraudet, L. Sub-threshold current in organic thin film transistors: influence of the transistor layout. *Org. Electron.* **14**, 909–914 (2013).

186. Higgins, T. M. *et al.* Electrolyte-gated n-type transistors produced from aqueous inks of WS₂ nanosheets. *Adv. Funct. Mater.* **29**, 1804387 (2019).

187. Akinwande, D., Petrone, N. & Hone, J. Two-dimensional flexible nanoelectronics. *Nat. Commun.* **5**, 5678 (2014).

188. Ren, W., Zhang, H. & Cheng, C. Ultrafine Pt nanoparticles decorated MoS₂ nanosheets with significantly improved hydrogen evolution activity. *Electrochim. Acta* **241**, 316–322 (2017).

189. Pérez-Jiménez, A. I., Lyu, D., Lu, Z., Liu, G. & Ren, B. Surface-enhanced Raman spectroscopy: benefits, trade-offs and future developments. *Chem. Sci.* **11**, 4563–4577 (2020).

190. Su, S. *et al.* Creating SERS hot spots on MoS₂ nanosheets with in-situ grown gold nanoparticles. *ACS Appl. Mater. Interfaces* **6**, 18735–18741 (2014).

191. Liu, S.-H., Saidi, W. A., Zhou, Y. & Fichthorn, K. A. Synthesis of {111}-faceted Au nanocrystals mediated by polyvinylpyrrolidone: insights from density-functional theory and molecular dynamics. *J. Phys. Chem. C* **119**, 11982–11990 (2015).

192. Wu, J. *et al.* Surface lattice-engineered bimetallic nanoparticles and their catalytic properties. *Chem. Soc. Rev.* **41**, 8066–8074 (2012).

193. Yang, J.-C. E. *et al.* The mechanistic difference of 1T-2H MoS₂ homojunctions in persulfates activation: structure-dependent oxidation pathways. *Appl. Catal., B* **297**, 120460 (2021).

194. Long, N. N. *et al.* Synthesis and optical properties of colloidal gold nanoparticles. *J. Phys.: Conf. Ser.* **187**, 012026 (2009).

195. Huang, Y. L. *et al.* Bandgap tunability at single-layer molybdenum disulphide grain boundaries. *Nat. Commun.* **6**, 6298 (2015).

196. Yuan, Y. *et al.* SERS-based ultrasensitive sensing platform: an insight into design and practical applications. *Coord. Chem. Rev.* **337**, 1–33 (2017).

197. Solís, D. M., Taboada, J. M., Obelleiro, F., Liz-Marzán, L. M. & García de Abajo, F. J. Optimization of nanoparticle-based SERS substrates through large-scale realistic simulations. *ACS Photonics* **4**, 329–337 (2017).

198. Kitching, H., Kenyon, A. J. & Parkin, I. P. The interaction of gold and silver nanoparticles with a range of anionic and cationic dyes. *Phys. Chem. Chem. Phys.* **16**, 6050–6059 (2014).

199. Xu, S., Bai, X. & Wang, L. Exploration of photothermal sensors based on photothermally responsive materials: a brief review. *Inorg. Chem. Front.* **5**, 751–759 (2018).

200. Jain, P. K., Huang, X., El-Sayed, I. H. & El-Sayed, M. A. Noble metals on the nanoscale: optical and photothermal properties and some applications in imaging, sensing, biology, and medicine. *Acc. Chem. Res.* **41**, 1578–1586 (2008).

201. Jakoboshn, K., Motiei, M., Sinvani, M. & Popovtzer, R. Towards real-time detection of tumor margins using photothermal imaging of immune-targeted gold nanoparticles. *Int. J. Nanomed.* **7**, 4707–4713 (2012).

202.   Tseng, S.-C. *et al.* Eco-friendly plasmonic sensors: using the photothermal effect to prepare metal nanoparticle-containing test papers for highly sensitive colorimetric detection. *Anal. Chem.* **84**, 5140–5145 (2012).

203.   Jin, H. *et al.* Emerging two-dimensional nanomaterials for electrocatalysis. *Chem. Rev.* **118**, 6337–6408 (2018).

204.   Seh, Z. W. *et al.* Combining theory and experiment in electrocatalysis: insights into materials design. *Science* **355**, (2017).

205.   Chu, S. & Majumdar, A. Opportunities and challenges for a sustainable energy future. *Nature* **488**, 294–303 (2012).

206.   Turner, J. A. Sustainable hydrogen production. *Science* **305**, 972–974 (2004).

207.   Tymoczko, J., Calle-Vallejo, F., Schuhmann, W. & Bandarenka, A. S. Making the hydrogen evolution reaction in polymer electrolyte membrane electrolysers even faster. *Nat. Commun.* **7**, 10990 (2016).

208.   Wang, S. *et al.* Electrochemical impedance spectroscopy. *Nat. Rev. Methods Primers* **1**, 1–21 (2021).

List of publications

Covalently interconnected transition metal dichalcogenide networks via defect engineering for high-performance electronic devices

<u>Stefano Ippolito</u>, Adam G. Kelly, Rafael Furlan de Oliveira, Marc-Antoine Stoeckel, Daniel Iglesias, Ahin Roy, Clive Downing, Zan Bian, Lucia Lombardi, Yarjan Abdul Samad, Valeria Nicolosi, Andrea C. Ferrari, Jonathan N. Coleman, Paolo Samorì

Nature Nanotechnology, 16, 592-598 (2021)

Asymmetric dressing of WSe$_2$ with (macro)molecular switches: fabrication of quaternary-responsive transistors

Haixin Qiu, <u>Stefano Ippolito</u>, Agostino Galanti, Zhaoyang Liu, Paolo Samorì

ACS Nano, 15, 10668-10677 (2021)

Effect of temperature and exfoliation time on the properties of chemically exfoliated MoS$_2$ nanosheets

Iwona Janica, Daniel Iglesias, <u>Stefano Ippolito</u>, Artur Ciesielski, Paolo Samorì

Chemical Communications, 56, 15573-15576 (2020)

Comparative effects of graphene and molybdenum disulfide on human macrophage toxicity

Hazel Lin, Ding-Kun Ji, Matteo Andrea Lucherelli, Giacomo Reina, <u>Stefano Ippolito</u>, Paolo Samorì, Alberto Bianco

Small, 16, 2002194 (2020)

Simultaneous non-covalent bi-functionalization of 1T-MoS$_2$ ruled by electrostatic interactions: towards multi-responsive materials

Daniel Iglesias, <u>Stefano Ippolito</u>, Artur Ciesielski, Paolo Samorì

Chemical Communications, 56, 6878-6881 (2020)

Functionalization of 2D materials with photosensitive molecules: from light-responsive hybrid systems to multifunctional devices

Yuda Zhao, <u>Stefano Ippolito</u>, Paolo Samorì

Advanced Optical Materials, 7, 1900286 (2019) – Cover page

Liquid-gated transistors based on reduced graphene oxide for flexible and wearable electronics

Rafael Furlan de Oliveira, Pietro Antonio Livio, Verónica Montes-García, <u>Stefano Ippolito</u>, Matilde Eredia, Pablo Fanjul-Bolado, María Begoña González García, Stefano Casalini, Paolo Samorì

Advanced Functional Materials, 29, 1905375 (2019)

Tailoring the physicochemical properties of solution-processed transition metal dichalcogenides via molecular approaches

<u>Stefano Ippolito</u>, Artur Ciesielski, Paolo Samorì

Chemical Communications, 55, 8900-8914 (2019)

Charge transport enhancement in supramolecular oligothiophene assemblies using Pt(II) centers as a guide

Amparo Ruiz-Carretero, Youssef Atoini, Tianyan Han, Alessandra Operamolla, <u>Stefano Ippolito</u>, Cataldo Valentini, Serena Carrara, Stephan Sinn, Eko Adi Prasetyanto, Thomas Heiser, Paolo Samorì, Gianluca Farinola, Luisa De Cola

Journal of Materials Chemistry A, 7, 16777-16784 (2019)

MoS_2 nanosheets via electrochemical lithium-ion intercalation under ambient conditions

Mohamed El Garah, Simone Bertolazzi, <u>Stefano Ippolito</u>, Matilde Eredia, Iwona Janica, Georgian Melinte, Ovidiu Ersen, Giovanni Marletta, Artur Ciesielski, Paolo Samorì

FlatChem, 9, 33-39 (2018) – Cover page

List of presentations

Oral

Covalently interconnected TMD networks via defect engineering for high performance electronic devices

Stefano Ippolito, Adam G. Kelly, Rafael Furlan de Oliveira, Marc-Antoine Stoeckel, Daniel Iglesias, Ahin Roy, Clive Downing, Zan Bian, Lucia Lombardi, Yarjan Abdul Samad, Valeria Nicolosi, Andrea C. Ferrari, Jonathan N. Coleman, Paolo Samorì

E-MRS Spring Meeting 2021, Virtual Conference, 31 May - 4 June 2021 (YRA - Symp. J)

Harnessing the charge transport in covalently interconnected TMD networks

Stefano Ippolito, Adam G. Kelly, Rafael Furlan de Oliveira, Marc-Antoine Stoeckel, Daniel Iglesias, Ahin Roy, Clive Downing, Zan Bian, Lucia Lombardi, Yarjan Abdul Samad, Valeria Nicolosi, Andrea C. Ferrari, Jonathan N. Coleman, Paolo Samorì

Graphene&2DM Industrial Forum 2021, Online Conference, 26-27 January 2021

Harnessing the charge transport through films of liquid-phase exfoliated TMDs

Stefano Ippolito, Adam G. Kelly, Zan Bian, Andrea C. Ferrari, Jonathan N. Coleman, Paolo Samorì

Graphene 2019 – International Conference, Rome (Italy), 25-28 June 2019

MoS_2 nanosheets via electrochemical lithium-ion intercalation under ambient conditions

Stefano Ippolito, Mohamed El Garah, Simone Bertolazzi, Matilde Eredia, Iwona Janica, Georgian Melinte, Ovidiu Ersen, Giovanni Marletta, Artur Ciesielski, Paolo Samorì

E-MRS Spring Meeting 2018, Strasbourg (France), 18-22 June 2018

Poster

MoS_2 nanosheets via electrochemical lithium-ion intercalation under ambient conditions

Stefano Ippolito, Mohamed El Garah, Simone Bertolazzi, Artur Ciesielski, Paolo Samorì

Graphene Week, San Sebastian (Spain), 10-14 September 2018

Graphene Winter Study, Obergurgl (Austria), 5-10 February 2018

Acknowledgements

"A story has no beginning or end:
arbitrarily one chooses that moment of experience
from which to look back or from which to look ahead"
(Graham Greene)

First and foremost, I would like to thank Prof. Paolo Samorì for accepting me as PhD student in his team conducting state-of-the-art research on fascinating and challenging topics. I feel grateful and lucky for the chance to work in such a stimulating environment, from which I learned and keep learning a lot about science and life. I thank him for the patience, trust and freedom he placed in me during the last 4 years.

I am also thankful to Prof. Artur Stefankiewicz, Prof. Felice Torrisi and Prof. Bernard Doudin for accepting to be part of my PhD jury and for investing their time to read and evaluate this doctoral work.

Many special thanks go to Dr. Simone Bertolazzi for being my supervisor during my master internship and first year of PhD. He taught me a lot, starting from important theoretical basis until advanced experimental techniques, from which I benefited throughout my PhD work.

I received strong support from friends and all members of the Nanochimie group, to whom I am deeply grateful. They joined and accompanied me in this journey, inspiring me, supporting me, and sharing with me great time both inside and outside the lab. I would like to thank Enrico, Matilde, Irene, Stefano, Cosimo, Fernando, Gosia, Veronica, Aldo, Stefania, Ye, Haixin, Nicholas, Sara, Pietro, Luca and Francesca for their scientific help and pleasant moments we shared together in Strasbourg. A special thanks goes to Rafael, from whom I received a strong and continuous support during the last laborious years. He has been an incredible supervisor from whom I learned the right aptitude to succeed in science. He taught me and shared a massive amount of knowledge, that I will always treasure. Most importantly, he has been and he still is a dear friend, despite any geographical distance.

Last but not least, I thank all the people in my family for their endless support. In particular, I would like to thank my father, who has always encouraged and supported me. I would not have come this far without him. Thank you.

Strasbourg, 3rd August 2021

Stefano (*Ippo*)

Stefano IPPOLITO

Ingénierie des défauts dans les semi-conducteurs 2D : fabrication de dispositifs hybrides multifonctionnels

Résumé

Ce travail de thèse vise à développer de nouvelles stratégies de fonctionnalisation basées sur des approches d'ingénierie des défauts pour les dichalcogénures de métaux de transition (TMD) traités en solution. Leurs défauts structurels inhérents, principalement les lacunes de soufre (V_S) situées aux bords des nanofeuillets, se comportent comme des sites (ré)actifs pour former des systèmes hybrides caractérisés par de nouvelles propriétés et des performances améliorées.

D'une part, l'utilisation de molécules dithiolées pour remédier aux V_S dans les TMD entraîne la formation de réseaux interconnectés de manière covalente, présentant des caractéristiques uniques et des performances électriques supérieures. En particulier, la fabrication de transistors à couche mince à grille liquide révèle une amélioration de leurs principaux facteurs de mérite d'un ordre de grandeur, conduisant à des dispositifs électriques de pointe.

D'autre part, les V_S s'avèrent également favoriser la croissance spontanée de nanoparticules (NP) de métaux nobles. En fait, grâce au mécanisme de déplacement galvanique, les bords des nanofeuillets de TMD peuvent être sélectivement décorés avec des Au, Pd et PtNP, ce qui conduit à des matériaux multifonctionnels avec des performances améliorées en électrocatalyse et en détection.

Mots-clés : *Ingénierie des défauts, traitement en solution, dichalcogénures de métaux de transition, dispositifs multifonctionnels, matériaux hybrides*

Résumé en anglais

This thesis work aims to develop new functionalization strategies based on defect engineering approaches for solution-processed transition metal dichalcogenides (TMDs). Their inherent structural defects, mainly sulfur vacancies (V_S) located at the flake edges, behave as (re)active sites to form hybrid systems characterized by new properties and enhanced performance.

On the one hand, the use of dithiolated molecules to heal V_S in TMDs entails the formation of covalently interconnected networks, presenting unique features and superior electrical performance. In particular, the fabrication of liquid-gated thin-film transistors reveals an improvement of their main figures of merit by one order-of-magnitude, leading to state-of-the-art electrical devices.

On the other hand, V_S are found to promote the spontaneous growth of noble metal nanoparticles (NPs) as well. In fact, thanks to the galvanic displacement mechanism, flake edges of TMDs can be selectively decorated with Au, Pd and PtNPs, leading to multifunctional materials with improved performance in electrocatalysis and sensing.

Keywords : *Defect engineering, solution processing, transition metal dichalcogenides, multifunctional devices, hybrid materials*